Correction of Atmospheric Water Vapour Effects on Repeat-Pass SAR Interferometry Using GPS, MODIS and MERIS Data

Zhenhong Li

Thesis submitted for the degree of
Doctor of Philosophy
of the University of London

Department of Geomatic Engineering

University College London

2005

ProQuest LLC
789 East Eisenhower Parkway
P.O. Box 1346
Ann Arbor, MI 48106-1346

Abstract

Over the last two decades, repeat-pass Interferometric Synthetic Aperture Radar (InSAR) has been a widely used geodetic technique for measuring the Earth's surface, including topography and deformation, with a spatial resolution of tens of metres. Like other astronomical and space geodetic techniques, repeat-pass InSAR is limited by the variable spatial and temporal distribution of atmospheric water vapour. The purpose of this thesis is to seek to understand and quantify the spatial and temporal variations in water vapour and to reduce its effects on repeat-pass InSAR using independent datasets such as Global Positioning System (GPS), the NASA Moderate Resolution Imaging Spectroradiometer (MODIS) and the ESA's Medium Resolution Imaging Spectrometer (MERIS) measurements.

The performance of different techniques including radiosondes, GPS, MODIS and MERIS for measuring precipitable water vapour (PWV) is assessed through inter-comparisons. It is shown that MODIS appears to overestimate water vapour against GPS and radiosondes. For the first time a GPS-derived correction model has been developed to calibrate the scale uncertainty of MODIS near IR water vapour product, and regional 1 km × 1 km water vapour fields have been produced with a standard deviation of up to 1.6 mm using a GPS/MODIS integrated approach, from which a zenith-path-delay difference map (ZPDDM) can be derived with an accuracy of 5 mm and a spatial resolution of 2 km. Based on analyses of the spatial structure of water vapour using spatial structure function, a GPS topography-dependent turbulence model (GTTM) has been developed to produce ZPDDMs with a standard deviation of 6.3 mm.

A water vapour correction approach has been successfully designed and incorporated into the ROI_PAC (version 2.3) software using the ZPDDMs provided by the GTTM and GPS/MODIS integrated models. The application of both correction models to ERS data over the Southern California Integrated GPS Network (SCIGN) shows that the order of water vapour effects on interferograms can be reduced from ~10 mm to ~5 mm using the GTTM or the GPS/MODIS integrated models. It is also demonstrated that the application of both correction models can improve InSAR processing such as phase unwrapping.

Declaration

I confirm that this is my own work and the use of all material from other sources has been properly and fully acknowledged.

Zhenhong Li

The text of Sections 4.1, 5.2 and 5.3 is, in part, a reformatted version of material appearing in: Li, Z., J.-P. Muller, and P. Cross, Comparison of precipitable water vapor derived from radiosonde, GPS, and Moderate-Resolution Imaging Spectroradiometer measurements, *Journal of Geophysical Research*, 108 (D20), 4651, doi:10.1029/2003JD003372, 2003. The dissertation author was the primary researcher and author, whilst the co-authors listed in this publication directed and supervised the research which forms the basis for these sections (Copyright by the American Geophysical Union).

The text of Sections 5.1, 5.4 and 5.5 is, in part, a reformatted version of material appearing in: Li, Z., J.-P. Muller, P. Cross, P. Albert, J. Fischer, and R. Bennartz, Assessment of the potential of MERIS near-infrared water vapour products to correct ASAR interferometric measurements, *International Journal of Remote Sensing*, under review, 2004. The dissertation author was the primary researcher and author, the second and third co-authors listed in this publication directed and supervised the research, whilst the remaining authors provided MERIS near IR water vapour products for this research.

The text of Chapter 6 is, in part, a reformatted version of material appearing in: Li, Z., E.J. Fielding, P. Cross, and J.-P. Muller, Interferometric synthetic aperture radar (InSAR) atmospheric correction: GPS Topography-dependent Turbulence Model (GTTM), *Journal of Geophysical Research*, under review, 2005. The

dissertation author was the primary researcher and author, whilst the co-authors listed in this publication directed and supervised the research which forms the basis for this chapter.

The text of Chapter 7 is, in part, a reformatted version of material appearing in: Li, Z., J.-P. Muller, P. Cross, and E.J. Fielding, Interferometric synthetic aperture radar (InSAR) atmospheric correction: GPS, Moderate Resolution Imaging Spectroradiometer(MODIS), and InSAR integration, *Journal of Geophysical Research*, 110 (B3), B03410, doi:10.1029/2004JB003446, 2005. The dissertation author was the primary researcher and author, whilst the co-authors listed in this publication directed and supervised the research which forms the basis for this chapter (Copyright by the American Geophysical Union).

Acknowledgements

This research is supported by an Overseas Research Student Award (ORS) and a UCL Graduate School Research Scholarship. This work is also linked to the Centre for the Observation and Modelling of Earthquakes and Tectonics (COMET), a NERC Earth Observation Centre of Excellence, and the ENVISAT project 853 (HAZARDMAP) which is co-funded by the EU-CLOUDMAP2 project under contract EVG1-CT-2000-00033.

First and foremost, I would like to express my greatest thanks to my supervisors, Prof. Jan-Peter Muller and Prof. Paul Cross, for their creative guidance, constructive criticism and constant encouragement throughout my PhD program and invaluable time during the writing up of this thesis. I am also grateful to my examiners, Prof. Allen Dodson and Dr. Jianguo Liu, for constructive comments that improved this thesis.

I owe special thanks to a few individuals whose contribution to this project was in some way immense. An enormous debt is owed to Marek Ziebart for being there whenever I needed advice, both for my research (particularly GIPSY) and in general. Andy Smith from Phoenix Systems provided free licences to use his PulSAR package for one and half years, and answered countless questions on SAR and interferometric processing, which helped me to gain valuable experience with InSAR. Eric Fielding from JPL and Tim Wright from Oxford assisted me with the JPL/Caltech ROI_PAC package, and I benefited enormously from their vast knowledge, expertise and experience. They were never too busy to help, and their suggestions were crucial to the success of the GPS/InSAR integration approach that has been successfully incorporated into the ROI_PAC software in this thesis. I am additionally grateful to Eric as my co-author, for the published articles that grew out of his input to Chapters 6 and 7. I also gratefully acknowledge Peter Albert from Freie Universität Berlin (now Germany's National Meteorological Service, the Deutscher Wetterdienst (DWD)) for providing their MERIS near IR water vapour products.

Special mention must go to Prof. Jingnan Liu, my former supervisor at Wuhan University, for arousing my initial interest in SAR interferometry back in 1998. I always remember his words: "Do something difficult!" I would also like to thank Prof. Guansong Wang, Prof. Caijun Xu, and Dr. Yanxiong Liu for their continuous assistance and general encouragement.

There are too many people at UCL to thank individually for their friendship, support and help. John Arthur and Gordon Bentley provided me with strong encouragement and great help when I applied for scholarships for my PhD program, the success of which made this research possible. I am grateful to Catherine Naud for her assistance with IDL and her ruthless proofreading of my first JGR paper, to Ant Sibthorpe for his careful reading for this thesis and several of my previous published papers, to Mike Dunderdale for his assistance with numerous IT difficulties, and to Gunho Sohn for his recommendation to the CTES program. I also like to thank Sima Adhya, Reda Ali, Pantelis Michalis, Lawrence Lau, and Peter Arrowsmith for useful discussion and all the good times at UCL in the last 3 years.

Finally, I reserve my most heartfelt appreciation and thanks for my family. I am grateful to my parents and my sisters for supporting my seemingly endless education and sharing in my struggles and successes, and to Wei for her loving support and patience while the evenings and weekends were taken from her by this thesis.

Contents

List of Figures

List of Tables

List of Acronyms

2-DInSAR	Two-pass Differential InSAR
2D	Two-Dimensional
2D-SSF	2D Spatial Structure Function
3-DInSAR	Three-pass Differential InSAR
AMSL	Above Mean Sea Level
ARM	Atmospheric Radiation Measurement Program
ASAR	Advanced Synthetic Aperture Radar
ASTER	Advanced Spaceborne Thermal Emission and Reflection Radiometer
BLUE	Best Linear Unbiased Estimator
CGPS	Continuous GPS
CMF	Cosecant Mapping Function
D-PAF	German Processing and Archiving Facility
DEM	Digital Elevation Model
DTM	Digital Terrain Model
DEOS	Delft Institute for Earth-Oriented Space Research
DInSAR	Differential Interferometric SAR
ECMWF	European Centre for Medium-range Weather Forecasts
FFT	Fast Fourier Transform
FOV	Field of View
FR	Full Resolution
FUB	Freie Universität Berlin
GASP	GPS Atmosphere Sounding Project
GFZ	GeoForschungsZentrum Potsdam
GMT	Greenwich Mean Time
GPS	Global Positioning System
HIRS	High resolution Infrared Radiation Sounder
IDW	Inverse Distance Weighting
IIDW	Improved Inverse Distance Weighting

IGS	International GPS Service
InSAR	SAR Interferometry (or Interferometric SAR)
IRM	Interferometric Radar Meteorology
IWV	Integrated Water Vapour
JPL	Jet Propulsion Laboratory
LOS	Line of Sight
MDOP	Multiple Data Ordering Page
MERIS	Medium Resolution Imaging Spectrometer
MODIS	Moderate Resolution Imaging Spectroradiometer
MSL	Mean Sea Level
MWR	Microwave Radiometer
NASA	National Aeronautics and Space Administration
NED	National Elevation Dataset
NGA	National Geospatial-intelligence Agency
NRT	Near Real Time
NWMF	Niell Wet Mapping Function
NWM	Numerical Weather Model
PWV	Precipitable Water Vapour
RAR	Real Aperture Radar
RMS	Root Mean Square
RR	Reduced Resolution
SAR	Synthetic Aperture Radar
SCIGN	Southern California Integrated GPS Network
SIR-C	Shuttle Imaging Radar satellite
SLC	Single-Look Complex
SRTM	Shuttle Radar Topography Mission
SSF	Spatial Structure Function
TEC	Total Electron Content
TECU	Total Electron Content Unit
TID	Travelling Ionospheric Disturbance
USGS	U.S. Geological Survey
VLBI	Very Long Baseline Interferometry
VTEC	Vertical Total Electron Content

ZHD	Zenith Hydrostatic Delay
ZPDDM	Zenith-Path-Delay Difference Map
ZTD	Zenith Total Delay
ZWD	Zenith Wet Delay

Chapter 1

Introduction

Spaceborne repeat-pass Synthetic Aperture Radar Interferometry (InSAR) provides a new tool to map global topography with metre-scale accuracy and to detect surface displacement with sub-centimetre accuracy and tens of metres spatial resolution [*Zebker and Goldstein*, 1986; *Gabriel et al.*, 1989; *Massonnet and Feigl*, 1998; *Bürgmann et al.*, 2000; *Rosen et al.*, 2000]. A major source of error for repeat-pass InSAR is the phase delay (especially the part due to water vapour) in radio signal propagation through the atmosphere. The research reported in this thesis is an attempt to understand how water vapour affects repeat-pass InSAR, to assess the potential and limitations of different water vapour products to correct InSAR measurements, and to seek integration methods to correct InSAR measurements for water vapour effects.

1.1 Background

Applications of Radar interferometry can be traced back to the 1970s. *Rogers and Ingalls* [1969] first applied interferometry to radar to remove the north/south ambiguity in the range/range rate of radar echoes from the planet Venus with Earth-based antennas. Later, *Zisk* [1972] first applied the same method to measure the topography of the moon where the radar antenna directionality was high, so there was no ambiguity. It was *Graham* [1974] who first applied Radar interferometry to an airborne radar to obtain Earth topography using amplitude fringes with optical processing techniques. To overcome the inherent difficulties of inverting amplitude fringes to obtain topography, digital processing techniques were developed using both the complex amplitude and phase information recorded by the SAR sensors. *Zebker and Goldstein* [1986] first reported the application of such a system with an airborne platform to produce interferograms that led to a topographic map with an accuracy between 10 and 30 m over an area of 10 × 11 km. The first application of interferometry with a spaceborne platform to produce topographic maps using

L-band SAR images from the short-lived SEASAT mission, with a 3-day repeat-pass mode, was demonstrated by Goldstein and his colleagues [*Goldstein et al.*, 1988; *Li and Goldstein*, 1990].

Goldstein and Zebker [1987] developed a new interferometric SAR technique, dubbed "along-track interferometry " (ATI), to measure ocean currents with two antennas separated in the azimuth direction parallel to the platform line of flight. It was shown that the ATI technique was capable of measuring tidal motions in the San Francisco bay area with an accuracy of several cm/s (loc. cit.). For repeat-pass InSAR, if the flight track exactly repeats itself so that there is no cross-track shift, and no consequent sensitivity to topography, radial motions can also be measured directly as with an ATI system [*Rosen et al.*, 2000]. It was *Goldstein* and his colleagues again who first demonstrated the use of the repeat-pass InSAR for velocity mapping of the Rutford ice stream in Antarctica [*Goldstein et al.*, 1993].

An extension of the InSAR technique is Differential Interferometric SAR (DInSAR) in which two interferograms are made from two or more SAR images taken at different times. *Gabriel et al.* [1989] first reported the application of the DInSAR technique to mapping the surface deformation of agricultural fields over a large area in California to centimetre-level accuracy using SEASAT data. In this approach, two interferograms were required: one, a so-called topographic interferogram, was assumed to contain the signature of topography only, whilst the other, a so-called deformation interferogram, measures topography and changes. The phase differences in the topographic interferogram were scaled to match the frequency of variability in the deformation interferogram and subtracted from the deformation interferogram, yielding a differential interferogram [*Gabriel et al.*, 1989]. *Massonet et al.* [1993] detected the 1992 Landers earthquake signature using the European Space Agency (ESA) ERS-1 satellite data while removing the topographic phase signature using a reference Digital Elevation Model (DEM). *Zebker et al.* [1994] developed the so-called three-pass method, and its application to the 1992 Landers earthquake showed good agreements with independent Global Positioning System (GPS) and Electronic Distance Measurement (EDM) data.

It is believed that a single-pass interferometric configuration has a number of advantages over a repeat-pass system for topography mapping [*Klees and*

Massonnet, 1999; *Mather*, 2004]. Firstly, single-pass SAR images are acquired under identical conditions at the same time, thus they are highly correlated, whilst the repeat-pass InSAR is limited by the temporal change in backscatter properties of the surface between the first and the second data acquisition, which is usually referred to as temporal decorrelation. Secondly, atmospheric conditions are similar for single-pass SAR images, whilst the repeat-pass SAR images exhibit artifacts due to temporal and spatial variations of the atmosphere, including the ionosphere and the troposphere [*Massonnet and Feigl*, 1995; *Hanssen*, 2001]. The Shuttle Radar Topography Mission (SRTM) is the most exciting example of the application of the single-pass InSAR technique. SRTM was launched in February 2000 and collected topographic data for 80 percent of the Earth's land surfaces, creating the first-ever near-global data set of land elevations [*Rabus et al.*, 2003; *JPL*, 2004]. However, with the great success of spaceborne SAR missions since the 1990s, including ERS-1/2, JERS-1, Radarsat, and ENVISAT, the most exciting application of SAR interferometry is the use of repeat-pass InSAR for surface change detection. There have been a wealth of studies on repeat-pass InSAR and its applications to land subsidence mapping [*Carnec et al.*, 1996; *Massonnet et al.*, 1997; *Fielding et al.*, 1998; *Carnec and Fabriol*, 1999; *Buckley*, 2000; *Buckley et al.*, 2003], earthquake research [*Peltzer and Rosen*, 1995; *Massonnet and Feigl*, 1995; *Price and Sandwell*, 1998; *Wright et al.*, 2003; *Talebian et al.*, 2004], volcano mapping [*Massonnet et al.*, 1995; *Rosen et al.*, 1996; *Lu et al.*, 1997], and glacier and polar ice studies [*Hartl et al.*, 1994; *Joughin et al.*, 1995; *Kwok and Fahnestock*, 1996].

It should be noted that, like the Global Positioning System (GPS), signal delays observed by SAR images can be used to derive precipitable water vapour (PWV) in the atmosphere. *Tarayre and Massonnet* [1996] first suggested that InSAR might be a new remote sensing tool for the study of tropospheric turbulence and ionospheric phenomena. *Hanssen* [2001] developed the Interferometric Radar Meteorology (IRM) technique to study PWV with a spatial resolution of 20 m and an accuracy of ~2 mm over most land and ice areas.

1.2 Atmospheric effects on InSAR measurements

As mentioned in Section 1.1, in the case of topography mapping and surface change detection, the use of repeat-pass InSAR is mainly limited by two effects: temporal decorrelation and atmospheric effects [*Klees and Massonnet*, 1999]. Here, the temporal decorrelation is defined as the temporal change in the backscatter property of the surface between SAR image acquisitions, which makes the gathering of sound phase information more difficult or even impossible. Temporal decorrelation is the highest for water surfaces and lowest for desert or other arid areas with low vegetation. Temporal decorrelation is not just a strong limitation on the accuracy of repeat-pass data however [*Zebker and Villasenor*, 1992], it can also be a means for understanding the nature of the surface. For instance, *Liu et al.* [2001] applied temporal decorrelation to reveal the distribution of migrating sand dunes, ephemeral lakes, erosion of river channels, etc.

It is well known that radar signals suffer from propagation delays when they travel through the atmosphere (with uncertainties mainly due to water vapour in the troposphere). Moreover, the state of the atmosphere is not identical when two images are acquired at different times for repeat-pass InSAR. Therefore, any difference in path delays between these two acquisitions results in additional shifts in phase signals. Based on their physical origin, there are two types of atmospheric signals [*Hanssen*, 2001]. The first is due to turbulent mixing that results from turbulent processes in the atmosphere and is largely uncorrelated with topography. The second signal is caused by a change in the vertical stratification of the troposphere between the lowest and highest elevations in the area. This signal is highly correlated with topography.

Massonnet et al. [1994] first identified atmospheric effects in repeat-pass InSAR measurements when they studied the 1992 Landers earthquake. *Goldstein* [1995] found that the interferogram acquired over the Mojave Desert in California by the Shuttle Imaging Radar satellite (SIR-C) contained one-way path delays[1] with a peak value of 2.8 cm and a root mean square (RMS) error of ~0.3 cm. *Massonnet and Feigl* [1995] reported that a 25-by-20-km kidney-shaped anomaly in interferograms

[1]: In this thesis, atmospheric delay is stated as an excess path length due to propagation delays in the atmosphere compared with the straight-line geometrical path length in vacuum (Equation 3.3.2).

over the Landers, California earthquake might be due to ionospheric effects. This kidney-shaped feature contained one close fringe, which indicated a range change of about 2.8 cm; but *Hanssen* [2001] argued that the magnitude of these effects is too large to be accounted for by ionospheric effects due to the spatial scale of the ionospheric disturbances, but a localized water vapour or cloud distribution could provide a more plausible explanation.

Rosen et al. [1996] reported that two-way path delays due to atmospheric refractivity anomalies were found at the level of a 12 cm peak-to-peak amplitude in the line of sight (LOS) direction over Kilauea Volcano, Hawaii. *Zebker et al.* [1997] suggested that a 20% spatial or temporal change in relative humidity could result in a 10-14 cm error in deformation measurement retrievals, independent of baseline parameters, and possibly 80-290 m of error in derived digital elevation models (DEM) for those interferometric pairs with unfavourable baseline geometries.

A series of 26 ERS tandem SAR interferograms was investigated to assess the heterogeneous effects of the atmosphere on the interferometric phase observations in the Netherlands [*Hanssen*, 1998]. The study showed that the RMS values of the atmospheric effects ranged from 0.5 to 3.6 radians, which implied that the observed phase values ranged from 0.3 to 2.3 phase cycles (one cycle corresponds to 2.8 cm path delay) at a 95% significance level with a Gaussian distribution. The phase error however reached 4 cycles during thunderstorms.

With JERS-1 data, apparent water vapour signatures with a peak-to-peak path delay of up to 16 cm along a cross section of c.140 km were observed over the Izu Peninsula, Japan, which made it impossible to derive reliable estimates of small deformation from only one interferogram [*Fujiwara et al.*, 1998]. *Rigo and Massonnet* [1999] found that atmospheric variations greatly increased the noise in the interferograms to about 2-3 times the level of the coseismic signal of the 1996 Pyrenean earthquake in France using ERS-1/2 data. The atmospheric variation reached 2.8 cm range change whilst the total change across the coseismic fault was only 1.3 cm.

Lyons and Sandwell [2003] found that atmospheric delays observed from interferograms ranged from −1.5 cm to +1.5 cm, independent of the time span between images, over the southern San Andreas using ERS data. Atmospheric

ripples with wavelengths of 15-20 km and 2-3 km were identified and were attributed to atmospheric gravity waves.

1.3 Research objectives

This thesis focuses on atmospheric effects on InSAR measurements and the possibility of reducing these water vapour effects using independent datasets including GPS, the NASA Moderate Resolution Imaging Spectroradiometer (MODIS) and the ESA's Medium Resolution Imaging Spectrometer (MERIS) data.

The key questions addressed in this study are as follows:

1. How does water vapour affect InSAR measurements? What is the requirement for the accuracy of individual independent datasets if they are to be used to reduce the atmospheric effects? What is the accuracy of the water vapour product derived from each independent dataset? Are these sufficiently accurate for correcting InSAR measurements?
2. What spatial interpolator appears best to take into account the spatial structure of water vapour variation as well as topography? Is there any demonstrable improvement when interpolating 2D GPS water vapour fields using such a spatial interpolator over commonly used interpolation methods such as Inverse Distance Weighting (IDW)?
3. Is it possible to produce regional 2D 1 km × 1 km water vapour fields through the integration of GPS and MODIS data? What is the accuracy of the output?
4. Presently, different calibration methods usually compare between unwrapped phases and independent datasets or models, rather than correct InSAR measurements. Is it possible to design a true integration approach that not only reduces atmospheric effects on interferograms, but also improves InSAR processing such as phase unwrapping?
5. How can a particular correction method be assessed? Is there any improvement after water vapour correction using methods developed in this thesis?

1.4 Research approach

In order to assess whether they are sufficiently accurate to correct InSAR measurements, cross-correlation analysis was applied in time and/or in space to different independent techniques, viz. GPS, MODIS and MERIS. The advantage of the cross-correlation method lies in the ease with which systematic biases and/or scale factors can be detected.

To assess water vapour effects on interferograms and validate different correction methods, ERS-1/ERS-2 Tandem data were selected whenever available, because they were just one day apart, and there should be no significant deformation signals in the interferograms. Since water vapour values are temporally uncorrelated when their temporal interval is greater than 1 day [*Emardson et al.*, 2003], the water vapour effects on Tandem interferograms are not necessarily less than those on long-term interferograms. The phase remaining in the Tandem interferograms after removing the known topographic and baseline effects should be almost entirely due to changes in the atmosphere between the two acquisitions.

Both the NASA Terra platform and ERS-2 satellite fly in a near-polar sun-synchronous orbit, and both have a descending node across the equator at 10:30 am local time. Therefore, there is spatial overlap in the swaths of ERS-2 and MODIS, and ERS-2 data were used to test Terra MODIS-derived correction methods. The Medium Resolution Imaging Spectrometer (MERIS) and the Advanced Synthetic Aperture Radar (ASAR) are on board the ESA ENVISAT satellite and these two datasets can be acquired simultaneously during daytime. Hence ASAR data can be used to validate the MERIS-derived correction model. However, due to the limited data availability during this study, the MERIS near IR water vapour product was not used to correct ASAR measurements in this thesis. It should be noted that, since both MODIS and MERIS near IR water vapour retrieval algorithms rely on observations of water vapour absorption of near IR solar radiation reflected by land, water surfaces and clouds, they are sensitive to the presence of clouds. Hence, water vapour from MODIS or MERIS is only useful under cloud free conditions.

The Southern California Integrated GPS Network (SCIGN) is the densest regional GPS network in the world with station spacing varying from only a few kilometres

to tens of kilometres; the frequency of cloud free conditions is also high in southern California (Section 5.5; *Li et al.*, 2005). Additionally, GPS data from SCIGN is freely available on the web. Therefore, SCIGN was selected as the principal test area.

1.5 Outline

Chapter 2 reviews Synthetic Aperture Radar (SAR) theory and its interferometric processing, including a physically intuitive understanding of InSAR principles. Some issues related to interferometric processing are discussed with examples over SCIGN.

Chapter 3 reviews the theory of atmospheric delays induced in SAR images by water vapour, dry air, hydrometeors, and other particulates. This is to provide a better understanding of how the atmosphere affects SAR images and its interferometric processing. Furthermore, a concise review of different atmospheric correction approaches proposed to date is given.

Chapter 4 provides a review of four techniques including GPS, radiosonde, MODIS, and MERIS, from which water vapour products can be derived. This chapter is not intended to exhaustively cover each technique, but serves as a general reference for the principles and the current status of each technique. Chapter 5 is dedicated to the assessment of the accuracy of each technique for monitoring water vapour by validation through inter-comparisons with independent data sets.

Chapters 6 and 7 present the main findings of this study. In Chapter 6, for the purpose of water vapour correction, a novel approach is described to integrate water vapour fields with interferometric processing. Moreover, using only GPS data, a topography-dependent turbulence model (GTTM) is developed to produce zenith-path-delay difference maps (ZPDDM) for InSAR atmospheric correction. The application of GTTM to ERS Tandem data shows that the GTTM can reduce water vapour effects on interferograms significantly. In Chapter 7, GPS and MODIS data are integrated to provide regional water vapour fields with high spatial resolution of 1 km × 1 km, and a water vapour correction model based on the resultant water vapour fields is successfully incorporated into the Jet Propulsion Laboratory (JPL) /California Institute of Technology (Caltech) ROI_PAC software. The advantage of

this integration approach is that only one continuous GPS station is required within a 2,030 km × 1,354 km MODIS scene. Application to ERS-2 repeat-pass data over the Los Angeles area shows this integration approach not only helps discriminate geophysical signals from atmospheric artefacts, but also reduces water vapour effects significantly, which is of great interest to a wide community of geophysicists.

Finally, conclusions and recommendations for future research are given in Chapter 8.

Chapter 2

Synthetic Aperture Radar and Interferometric processing

This chapter begins with a brief introduction to Synthetic Aperture Radar (SAR), followed by a description of the key elements in the formation of a complex SAR image, also known as a *single-look complex image* (SLC), and a discussion of the properties of SLC images. Then the InSAR geometry and its mathematical models for interferometric processing, including differential interferometry, are presented. Given the fact that the JPL/Caltech ROI_PAC package was used in this study, demonstrations on its SAR and InSAR processors are given as well as an investigation of some of the main technical issues related.

2.1 Synthetic Aperture Radar (SAR) imaging

Imaging sensor systems are usually classified as passive or active according to their modes of operation. Passive sensors make use of the radiation naturally emitted or reflected by the Earth's surface (or any other observed surface), while active sensors are equipped with a transmitter and receive signals backscattered from the illuminated surface. The principal limitations of passive sensors are represented by the lack of an independent source of radiation and by the presence of clouds or fog over the area of interest. Active sensors are independent from external sources (e.g. sunlight), and their frequency bands drastically reduce the impact of clouds, fog, and rain on the obtained images. Imaging active sensors therefore allow day and night and all-weather imaging, and are mostly realized by radar systems [*Franceschetti and Lanari*, 1999].

Radar sensors that operate in a side looking mode can be divided into two groups: Real Aperture Radar (RAR) and Synthetic Aperture Radar (SAR). RAR depends on the beamwidth determined by the actual antenna, and SAR depends on signal processing to achieve a much narrower beamwidth in the along-track direction than that attainable with a real antenna. Figure 2.1 shows the schematic geometry of a

SAR system. For a more complete discussion of the principles of SAR, refer to *Curlander and McDonough* [1991] and *Franceschetti and Lanari* [1999].

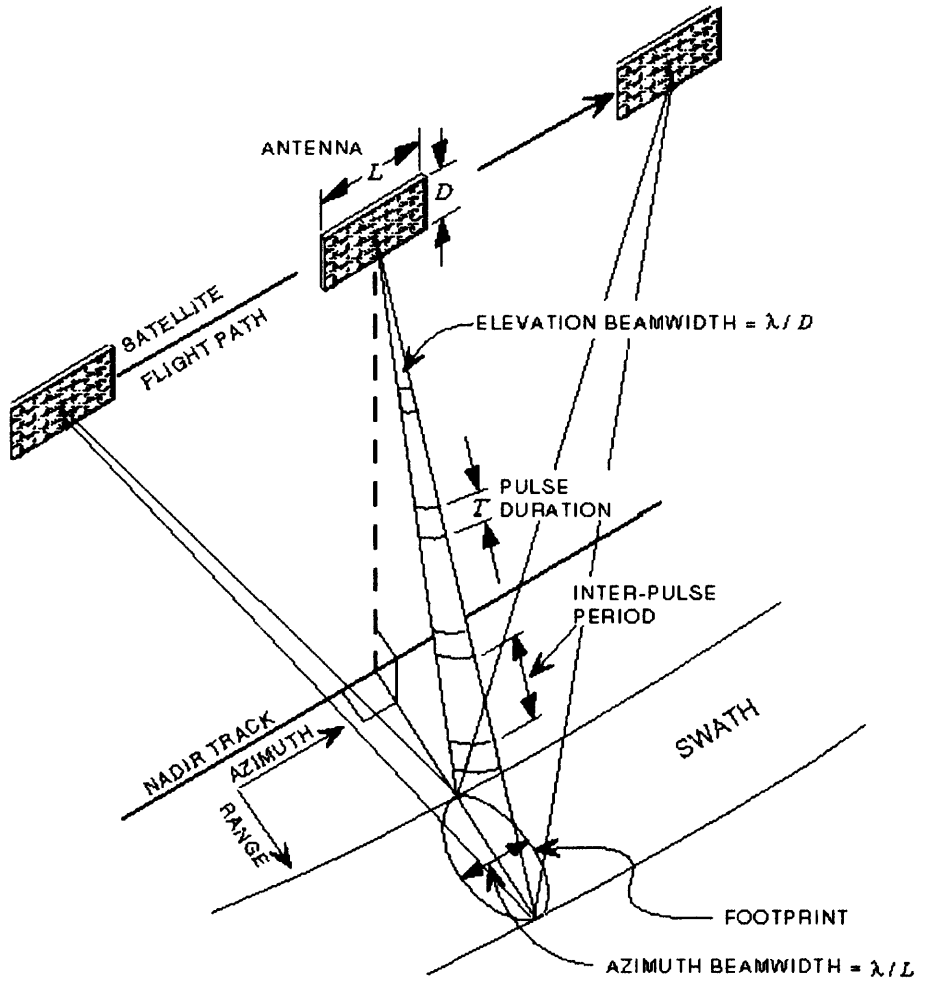

Figure 2.1 Geometry of a right looking SAR with a rectangular antenna (adapted from *Olmsted*, 1993).

2.1.1 Range and azimuth resolutions

For radar sensors, the slant range resolution is defined as the minimum spacing between two objects in the line from the radar to the centre of the ground footprint that can be individually detected:

$$\Delta r_s = \frac{cT}{2} \qquad (2.1.1)$$

where c is the speed of light, T is the pulse duration and a factor of 2 accounts for the two-way propagation. In order to achieve a resolution of a few metres, a very short pulse duration is required. For instance, a pulse duration with an order of 10^{-8}

seconds is required for a resolution of 5 m. This means that improvement of the resolution requires a reduction of the pulse width and a high transmit peak power. A way to circumvent this limitation is to use high bandwidth phase coded waveforms such as chirp pulses with a frequency bandwidth of W. After reception, a procedure called range compression can be applied to the received signals, and a temporal resolution of $1/W$ can be obtained. Therefore, the range resolution is given by:

$$\Delta r_s = \frac{c}{2W} \tag{2.1.2}$$

The ground range resolution of the radar, Δr_g, is defined as the minimum separation of two points on the ground surface in the direction perpendicular to the antenna trajectory that can be separately identified, and given by:

$$\Delta r_g = \frac{\Delta r_s}{\sin\eta} = \frac{c}{2W\sin\eta} \tag{2.1.3}$$

where η is the incidence angle which is the angle between the radar beam and the normal to the Earth's surface at a particular point of interest.

ERS has a frequency bandwidth of 18.96 MHz, and the incidence angles range from 19.35° at the near range to 26.50° at the far range [*Olmsted*, 1993]. Thus, the ground range resolution ranges from 26 m at the near range to 18 m at the far range.

Two objects at a given range can be discriminated only if they are not within the radar beam at the same time. Hence, the azimuth resolution Δx is related to the antenna azimuth beamwidth λ/L by means of the relationship:

$$\Delta x = \frac{R\lambda}{L} \tag{2.1.4}$$

where R is the slant range and L is the effective antenna dimension along the track (the azimuth direction). For a RAR, L is coincident with its physical length. If the 10 m antenna on ERS was adopted as a RAR with a typical value of $R = 850\ km$, the azimuth resolution would be of the order of kilometres (about 4.8 km). In other words, in order to get an azimuth resolution of 20 m for ERS, an antenna of about 2.4 km would be required. Such an antenna is clearly technically unfeasible. Fortunately, a very large antenna can be synthesized by moving a real one of limited

dimension along a reference path, and such an antenna is usually referred to as a Synthetic Aperture Radar (SAR). A SAR records the received echoes coherently. As the moving antenna passes by the image point, the Doppler frequency shift of the received (returned) signal from the point and the round trip time of the signal can be used together to discriminate image points in the azimuth direction. The received echoes can be combined to synthesize a larger antenna aperture and thus achieve much finer resolution:

$$\Delta x = \frac{L}{2} \tag{2.1.5}$$

This means that the azimuth resolution is half of the physical antenna length and is independent of range and wavelength. For ERS, use of the synthetic aperture improves the azimuth resolution by three orders of magnitude, from 4.8 km to 5 m.

2.1.2 Overview of the ROI_PAC SAR processor

In the raw SAR data, the signal energy from a point target is spread in range and azimuth, and the purpose of SAR processing (or focusing) is to collect the dispersed energy into a single pixel in the output image, i.e. a single look complex (SLC) image. This processing should be phase preserving for further interferometric processing. To date, there are two major categories of SAR focusing techniques: range-Doppler and wavenumber domains [*Bamler*, 1992]. The range-Doppler algorithm is applied in the ROI_PAC V2.3, a Repeat Orbit Interferometry Package developed at JPL/Caltech, which has been used for producing all SAR image products from raw radar signal data used in this thesis. This section provides an overview of the ROI_PAC SAR Processor. For a full description of the methodology of the ROI_PAC, see *Buckley* [2000].

Figure 2.2 shows the basic ROI_PAC SAR Processor architecture. Except for parameter extraction, this range-Doppler processor consists of three steps: range compression, range migration, and azimuth compression. It processes radar signals in a sequence of overlapping blocks of pulses due to CPU limitations. For each block of data, there will be several azimuth lines at the beginning and the end which will be resolved with less than the full Doppler bandwidth, and only those azimuth lines which are processed with the full Doppler bandwidth can be written as output.

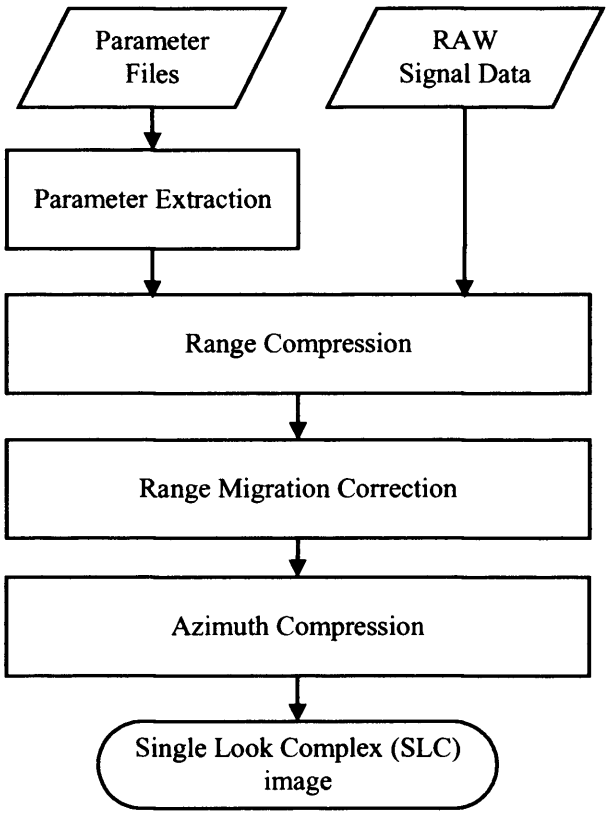

Figure 2.2 Basic ROI_PAC SAR processor architecture

Two types of parameters, radar system parameters and satellite orbit ephemeris, are required in SAR processing. The first type includes pulse repetition frequency, sampling frequency, pulse length, chirp slope, and wavelength, whilst the second includes the satellite body-fixed position and velocity, the height above the reference surface, and the Earth's radius. Satellite orbit ephemerides can be extracted from the SAR Leader files or some SAR archival facilities, including DEOS (Delft Institute for Earth-Oriented Space Research) and D-PAF (German Processing and Archiving Facility), and will be discussed further in Section 2.3.2.

To reduce the peak power of the radar transmitter associated with a short pulse, the radar emits a long frequency-modulated chirp. When the chirp returns to the radar, the raw signal data consists of the complex reflectivity of the surface convolved with the chirp. The objective of range compression is to recover the complex reflectivity by deconvolution of the chirp with a range reference function that is calculated from a replica of the transmitted pulse. This process is performed on each range line of SAR data, and can be done efficiently by the use of the Fast Fourier Transform (FFT).

After range compression, a point target will appear as a hyperbolic-shaped reflection in the azimuth direction because of: 1) the changing distance to the point target as the satellite moves along its track; 2) an elliptical orbit; and 3) Earth rotation. Prior to focusing the image in the azimuth direction, a range migration correction is required to adjust the point target response to a constant value. The range migration correction amounts to an interpolation of the range-compressed data and can be implemented using an eight-point sinc (i.e. sine cardinal) function interpolator [*Buckley*, 2000].

Azimuth compression is a procedure analogous to range compression, which deals with the phase shift of the target as it moves along trajectory (azimuth direction). This procedure involves generation of a frequency-modulated chirp in azimuth based on the knowledge of the spacecraft orbit, and then the chirp is Fourier transformed into Doppler space and mulitiplied by each column of range-migrated data. Finally, the product is inverse Fourier transformed to yield a focused SAR image.

It should be noted that the raw signal data will generally have different Doppler histories, and the ROI_PAC SAR processor needs to process the raw data to the same Doppler [*Buckley*, 2000].

2.1.3 Properties of SAR images

After SAR focusing, the radar image is a two-dimensional matrix carrying an amplitude and a phase associated with each image pixel. The amplitude is a measure of target reflectivity, and a function of radar observation parameters (including frequency, polarisation, and incidence angle) and surface parameters (including roughness, geometric shape and dielectric properties of the target). Of these, surface roughness plays a key role, and the amplitude varies with the type of terrain. Urban areas usually show strong amplitudes, forest areas show intermediate amplitudes, whilst smooth surfaces (e.g. calm water) show low ones. The significance of the phase of an image pixel is that the phase encodes changes at the surface as well as a term proportional to the two-way range from the platform to the gound. The ground surface represented by a pixel in a radar image is large compared to the radar wavelength, and typically contains hundreds of individual elementary targets, each with a different complex reflection coefficient, that contribute to the phase. Each of these targets can

cause a phase rotation or delay, which leads to different complex returns. Since it is dependent on the sum of hundreds of unkown complex numbers, the resultant phase by itself is thus a random and not a meaningful parameter.

However, if a repeat acquisition is made, then there is a correlation between the phases of corresponding image pixels; if the repeat acquisition is made with exactly the same orbital geometry, then equivalent image points would be expected to have identical complex pixel values, provided that the ground scattering characteristics remain unchanged. If the repeat orbit is parallel to the first orbit but spatially separated, there remains a correlation between the phase values, but with a phase shift corresponding to the overall difference in range to the pixel phase centre. The phases only become meaningful when two different radar images of the same target are compared.

2.2 SAR Interferometry and Differential Interferometry

Interferometric Synthetic Aperture Radar (SAR Interferometry, or InSAR) is a method by which the phase differences of two SAR images are used to reconstruct highly accurate Digital Elevation Models (DEM) and/or to detect surface deformation. The interested reader may consult *Graham* [1974], *Zebker and Goldstein* [1986], *Goldstein et al.* [1988], *Zebker et al.* [1992], and *Bürgmann et al.* [2000] on the generation of DEMs, and *Goldstein and Zebker* [1987], *Massonet et al.* [1993], *Zebker et al.* [1994], and *Hanssen* [2001] on the detection of surface deformation. A parallel-ray approximation is usually applied to derive a mathematical model of InSAR, which ignores a small term expressing the phase part relative to the distance in the line of sight (i.e. the second term in Equation (2.2.4)) and makes the derivation much simpler. In this section, the parallel-ray approximation method is discussed, whilst the mathematical model of InSAR is derived in a more logical way.

2.2.1 Phase measurements

Consider two radar systems observing the same target from two positions, S_1 and S_2, respectively, as illustrated in Figure 2.3. The measured phase at each of the two SAR images may be taken as equal to the sum of a propagation part proportional to

the round-trip distance travelled and a scattering part due to the interaction of the wave with the surface. If each resolution element on the ground behaves the same for each observation and no ground movement between the two radar observations occurs, then calculating the difference in the phases removes dependence on the scattering mechanism and provides a quantity dependent only on geometry. If the two path lengths are taken to be ρ and $\rho+\delta\rho$, the measured phase difference ϕ will be [*Zebker et al.*, 1994]:

$$\phi = \frac{4\pi}{\lambda}\delta\rho \qquad (2.2.1)$$

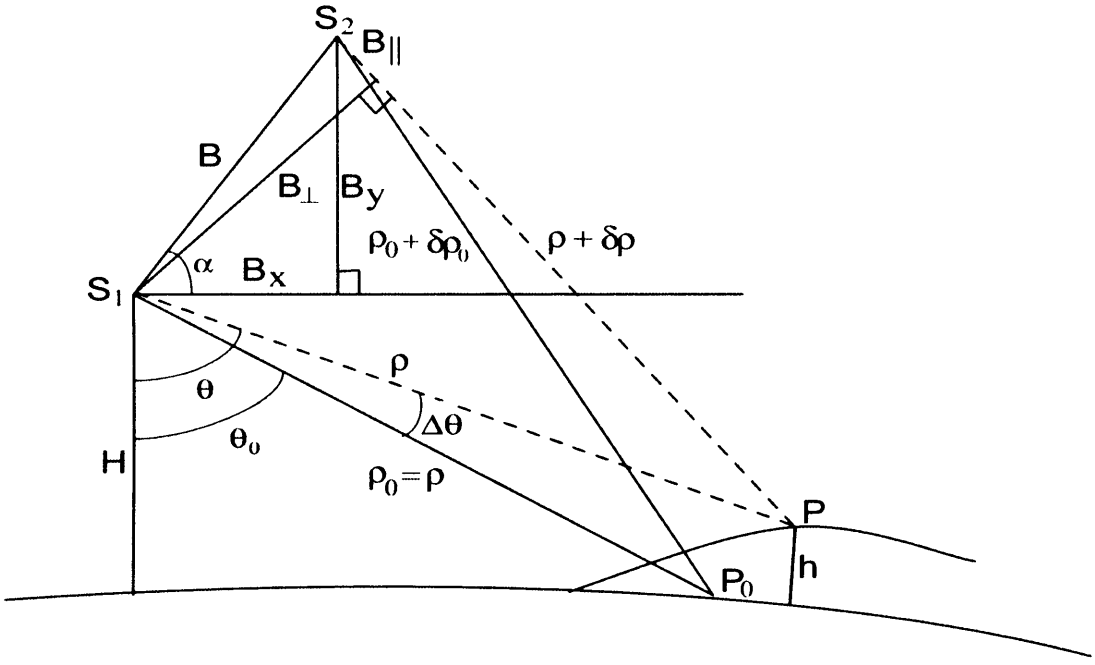

Figure 2.3 Geometry of InSAR. S_1 and S_2 are two radar sensors, H is the height of S_1, P is a point on the surface with a height of h and a range of ρ from S_1 (or a range of $\rho+\delta\rho$ from S_2), and P_0 is a corresponding point on the reference ellipsoid with the same distance ρ from S_1 as P. α is the angle of the baseline with respect to the horizontal at S_1, θ is the look angle, and $\Delta\theta$ is the angular distortion due to the presence of topography. B is the baseline, $B_\perp$ the perpendicular component, $B_{||}$ the parallel component, B_x the horizontal component, and B_y the vertical component.

In Figure 2.3, recalling the law of cosines, then

$$(\rho+\delta\rho)^2 = \rho^2 + B^2 - 2\rho B\sin(\theta-\alpha) \qquad (2.2.2)$$

where B is the baseline length, ρ is the distance from the radar system S_1 to a point on the ground, θ is the look angle, and α is the angle of the baseline with respect to the horizontal at the radar system. Equation (2.2.2) can be rearranged to give

$$2\rho\delta\rho+\delta\rho^2 = B^2 - 2\rho B\sin(\theta-\alpha) \qquad (2.2.3)$$

In the case of spaceborne geometries, e.g. ERS-1/2, $\rho \approx 8\times10^5 m$, $\delta\rho < B \approx 1\times10^3 m$, then $\delta\rho << \rho$; In the case of airborne NASA CV990 geometry demonstrated by *Zebker et al.* [1986], the aircraft elevation was from $8\times10^3 \sim 14\times10^3 m$, and the incidence angle from $25° \sim 55°$, then the distance ρ was $8.8\times10^3 \sim 24.4\times10^3 m$, since $\delta\rho < B = 11m$, still gives $\delta\rho << \rho$. Therefore, the term of order $\delta\rho^2$ can be ignored, giving:

$$\begin{aligned}\delta\rho &= -B\sin(\theta-\alpha)+\frac{B^2}{2\rho} \\ &= -B_{\|}+\Delta\end{aligned} \qquad (2.2.4)$$

In the case of airborne NASA CV990, the second term on the right hand side of Equation (2.2.4): $\Delta = \frac{B^2}{2\rho} \le \frac{11^2}{2\times8.8\times10^3} m = 0.6mm$, the wavelength was 24.5 cm, then $\frac{\Delta}{\lambda} \le \frac{0.6}{245} = \frac{1}{408}$, which is largely beyond the cycle-slicing limit, i.e. resolving phase differences smaller than about one tenth of a cycle is difficult [*Massonnet and Feigl*, 1998]. The second term can therefore be ignored:

$$\delta\rho = -B\sin(\theta-\alpha) = -B_{\|} \qquad (2.2.5)$$

As a consequence, the parallel-ray approximation method can be applied to derive a mathematical model for InSAR in this case. The interested reader can refer to *Zebker and Goldstein* [1986].

In the case of spaceborne ERS geometries, one can obtain $\Delta = \frac{B^2}{2\rho} \le \frac{(1\times10^3)^2}{2\times8\times10^5} m = 0.625m$. The wavelength is 5.66 cm, then $\frac{\Delta}{\lambda} \le \frac{0.625}{0.0566} = 11$. This indicates that the ratio can be up to 11. Even when the baseline is 100 m, the ratio is about 0.1, equal to the cycle-slicing limit. This indicates that the second term of Equation (2.2.4) can be neglected only when the baseline is shorter than 100 m.

Due to the Earth's curvature, the interferogram phases would exist even in the absence of topography. The "curved Earth" effect has to be removed from the interferogram.

In Figure 2.3, the phase difference ϕ_0 due to the range difference $\delta\rho_0$ from P_0 on the reference ellipsoid to the two radar sensors is:

$$\begin{aligned}\phi_0 &= \frac{4\pi}{\lambda}\delta\rho_0 \\ &= \frac{4\pi}{\lambda}\left(-B_{\|_0} + \Delta_0\right)\end{aligned} \qquad (2.2.6)$$

where subscript 0 represents values relative to P_0 in this section.

The phase corrected for the "curved Earth" effect, denoted ϕ_{flat}, is given by

$$\begin{aligned}\phi_{flat} &= \phi - \phi_0 \\ &= \frac{4\pi}{\lambda}(\delta\rho - \delta\rho_0) \\ &= \frac{4\pi}{\lambda}\left(-B_{\|_0} + B_{\|_0} + \Delta - \Delta_0\right)\end{aligned} \qquad (2.2.7)$$

For the last two terms on the right hand side of Equation (2.2.7):

$$\begin{aligned}\delta\Delta &= \Delta - \Delta_0 \\ &= \frac{B^2}{2\rho} - \frac{B^2}{2\rho_0} \\ &= \frac{B^2}{2\rho\rho_0}(\rho_0 - \rho) \\ &= 0 \qquad (\because \rho_0 = \rho)\end{aligned} \qquad (2.2.8)$$

and then:

$$\begin{aligned}\phi_{flat} &= \frac{4\pi}{\lambda}\left(-B_{||} + B_{||_0}\right) \\ &= -\frac{4\pi}{\lambda}\left(B\sin(\theta-\alpha) - B\sin(\theta_0-\alpha)\right)\end{aligned} \tag{2.2.9}$$

Noting that the angular change $\Delta\theta = \theta - \theta_0$ is small, e.g. approximately 1° for a 5 km height difference, one can obtain:

$$\begin{aligned}\varphi_{flat} &= -\frac{4\pi}{\lambda} B\cos(\theta_0-\alpha)\Delta\theta \\ &= -\frac{4\pi}{\lambda} B_{\perp_0}\Delta\theta\end{aligned} \tag{2.2.10}$$

where $B_{\perp_0} = B\cos(\theta_0-\alpha)$ and θ_0 are the values relative to the reference ellipsoid.

2.2.2 SAR Interferometry and topographic mapping

In Figure 2.3, if the height of the satellite above the reference ellipsoid is known, one can obtain the geometric equation:

$$h = H - \rho\cos\theta \tag{2.2.11}$$

$$\frac{dh}{d\theta} = \rho\sin\theta \tag{2.2.12}$$

The derivative of Equation (2.2.10) with a look angle θ, taking into account $\Delta\theta = \theta - \theta_0$, gives the relationship between a change in phase measurements and a change in the look angle, θ:

$$\frac{d\varphi_{flat}}{d\theta} = -\frac{4\pi}{\lambda} B_{\perp_0} \tag{2.2.13}$$

Combining Equations (2.2.12) and (2.2.13), one can obtain:

$$\begin{aligned}\frac{dh}{d\varphi_{flat}} &= \frac{dh}{d\theta}\frac{d\theta}{d\varphi_{flat}} \\ &= -\frac{\lambda}{4\pi}\frac{\rho\sin\theta}{B_{\perp_0}}\end{aligned} \tag{2.2.14}$$

and finally the equation to convert phase to height:

$$h = -\frac{\lambda}{4\pi}\frac{\rho\sin\theta}{B_{\perp_0}}\varphi_{flat} \tag{2.2.15}$$

The altitude of ambiguity, h_a, is defined as the magnitude of topography that results in a single fringe, a 2π phase shift. Inserting $\phi = 2\pi$ in Equation (2.2.15) gives:

$$h_a = \left| \frac{\lambda}{2} \frac{\rho \sin\theta}{B_{\perp_0}} \right| \tag{2.2.16}$$

The smaller the altitude of ambiguity, the more sensitive the interferogram phase is to height variations. Since λ is a system parameter and ρ and θ vary only slightly over a full scene, the sensitivity is obviously scaled by the perpendicular baseline $B_{\perp_0}$. The larger the perpendicular baseline $B_{\perp_0}$, the more sensitive the interferogram phase is to topography. In the case of ERS-1/2, the magnitude of h_a can vary from infinity to values of the order of 10 m with the perpendicular baseline ranging from 0 m to 1000 m.

2.2.3 Three-pass Differential Interferometry and deformation mapping

Now consider a second interferogram acquired over the same area but at a different time with a different baseline B' and baseline orientation α', thus a different $B'_{\perp_0}$. If no deformation occurs in the second interferogram, one can obtain from Equation (2.2.10):

$$\varphi'_{flat} = -\frac{4\pi}{\lambda} B'_{\perp_0} \Delta\theta \tag{2.2.17}$$

Examination of the ratio of the "Earth Flattened" phases in Equation (2.2.10) and (2.2.17) yields

$$\frac{\varphi_{flat}}{\varphi'_{flat}} = \frac{B_{\perp_0}}{B'_{\perp_0}} \tag{2.2.18}$$

This means that the ratio of the "Earth Flattened" phases is equal to the ratio of the perpendicular baselines, independent of the topography.

If ground deformation is assumed to displace each resolution element between observations for the second interferogram in a coherent manner, then, in addition to the phase dependence on topography, there is a phase change due to the radar line of sight component of the displacement $\Delta\rho$. If the second interferogram shares an

orbit with the previous pair, i.e. ρ and $\Delta\theta$ are unchanged, and the "Earth Flattened" phase ϕ'_{flat} is:

$$\begin{aligned}\varphi'_{flat} &= -\frac{4\pi}{\lambda}\left(B'_{\perp_0}\Delta\theta - \Delta\rho\right) \\ &= -\frac{4\pi}{\lambda}B'_{\perp_0}\Delta\theta + \frac{4\pi}{\lambda}\Delta\rho\end{aligned} \tag{2.2.19}$$

Combining Equation (2.2.10) and (2.2.19), one can obtain:

$$\varphi'_{flat} - \frac{B'_{\perp_0}}{B_{\perp_0}}\varphi_{flat} = \frac{4\pi}{\lambda}\Delta\rho \tag{2.2.20a}$$

and

$$\Delta\rho = \frac{\lambda}{4\pi}\left(\varphi'_{flat} - \frac{B'_{\perp_0}}{B_{\perp_0}}\varphi_{flat}\right) \tag{2.2.20b}$$

This important equation shows how to determine the displacement $\Delta\rho$ without requiring the exact values of the look angle θ and the topographic information using 3 SAR images (three-pass method, or 3-DInSAR). The main advantage of the three-pass method is that no information other than SAR images is required. However, there are some limitations for the three-pass DInSAR method: 1) The unwrapped phases are required in Equation (2.2.20b), and the phases in the first interferogram must be unwrapped before being used to remove topographic contributions in the second interferogram. Phase unwrapping is a source of error in InSAR processing, and its performance depends on two factors: the SNR of the interferogram and the interferometric fringe spacing [*Zebker et al.*, 1994]; 2) the three-pass method assumes that there is no deformation in the first interferogram, which is not always the case; 3) There are often atmospheric contributions in this first interferogram, which might lead to large errors; 4) The probability of finding three mutually coherent images is smaller than that of finding two such images, since the three-pass method usually requires that all three images be acquired by the same satellite (or the same type of satellite such as ERS-1 and ERS-2) in the same orbital track. Therefore, a two-pass method is usually preferred when a precise DEM is available.

2.2.4 Two-pass Differential Interferometry and SRTM DEM

The two-pass differential method (2-DInSAR) has been widely used to extract deformation on the basis of two SAR images as well as a Digital Elevation Model (DEM), as described by *Massonnet et al.* [1993] and *Massonnet and Feigl* [1998]. In the case of the two-pass approach, with known imaging geometry, DEM data is mapped from an orthogonal cartographic or geographic coordinate system to SAR image coordinates, and then an interferogram can be synthesized. The simulated interferogram can be applied to remove the topographic phase, pixel by pixel, to leave only the phase due to deformation if there are no atmospheric and other effects.

The availability of high resolution DEMs, necessary for this two-pass approach, has been a major limitation for applications before the release of the data from the Shuttle Radar Topography Mission (SRTM). SRTM collected data over most of the world's land surface between 60 degrees north latitude and 54 degrees south latitude (which is about 80% of all the land on the Earth), during its ten days of operation in February 2000. This radar system included two types of antenna panels, C-band and X-band, and the near-global DEMs were made by the Jet Propulsion Laboratory (JPL) from the C-band radar data. The X-band radar data were used to create slightly higher resolution DEMs but without the global coverage. The SRTM data has a spatial resolution of 30 metres and a vertical absolute accuracy of less than 7 metres [*Farr and Kobrick*, 2000]. The horizontal datum is WGS84, and the vertical datum is the WGS84 EGM96 geoid [*NIMA*, 1997].

2.2.5 Overview of the ROI_PAC InSAR processor

The ROI_PAC V2.3, a Repeat Orbit Interferometry Package developed at JPL/Caltech, was used to produce the differential interferometric products shown in this thesis. This package was developed using Fortran and C programming languages and is controlled by Perl scripts. An excellent reference for the ROI_PAC is David Schmidt's website on the ROI_PAC[1]. This section is not intended to be a complete manual, but rather a concise introduction to the ROI_PAC. The interested reader can also refer to *Buckley* [2000].

[1]: http://www.seismo.berkeley.edu/~dschmidt/ROI_PAC/, 21 November 2004.

The main objectives of the ROI_PAC are DEM generation and differential InSAR product generation from repeat-pass interferometry. The ROI_PAC can work using both the three-pass mode and the two-pass mode. Since a DEM with high resolution and good accuracy is available for the study sites used here, the two-pass approach is employed in this thesis.

Figure 2.4 shows the main processing steps to generate a differential InSAR product using the ROI_PAC with the two-pass mode. The processing chain elements can be summarised as follows:

A. Knowledge of a set of range and azimuth offset measurements for each block is required to co-register the reference and slave SLC images. An amplitude normalized cross-correlation procedure is performed to obtain the coarse offsets in the range and azimuth direction. After culling based on specified thresholds, the correlation procedure is repeated to achieve fine offsets, which are used to determine a functional mapping to resample the slave image to the reference image.

B. Based on the affine transformation determined in the previous step, the slave image is resampled to the reference image, whilst conserving the phase content of the pixels. If M is the complex reference image and S is the co-gridded complex slave image, then the complex interferogram is defined as MS^*, where the asterisk denotes complex conjugation.

C. A precise estimate of the interferometric baseline is required in the Interferogram flattening & Topography removal step. Baselines can be determined from the registration offsets or from orbit ephemeredes which are usually found to be in error, leaving residual tilts in the flattened interferograms [*Massonnet and Feigl*, 1998; *Buckley*, 2000; *Wright*, 2000].

D. The purpose of Interferogram flattening & Topography removal is to remove the interferometric phase due to the effects of the ellipsoid Earth surface and topography from the interferogram.

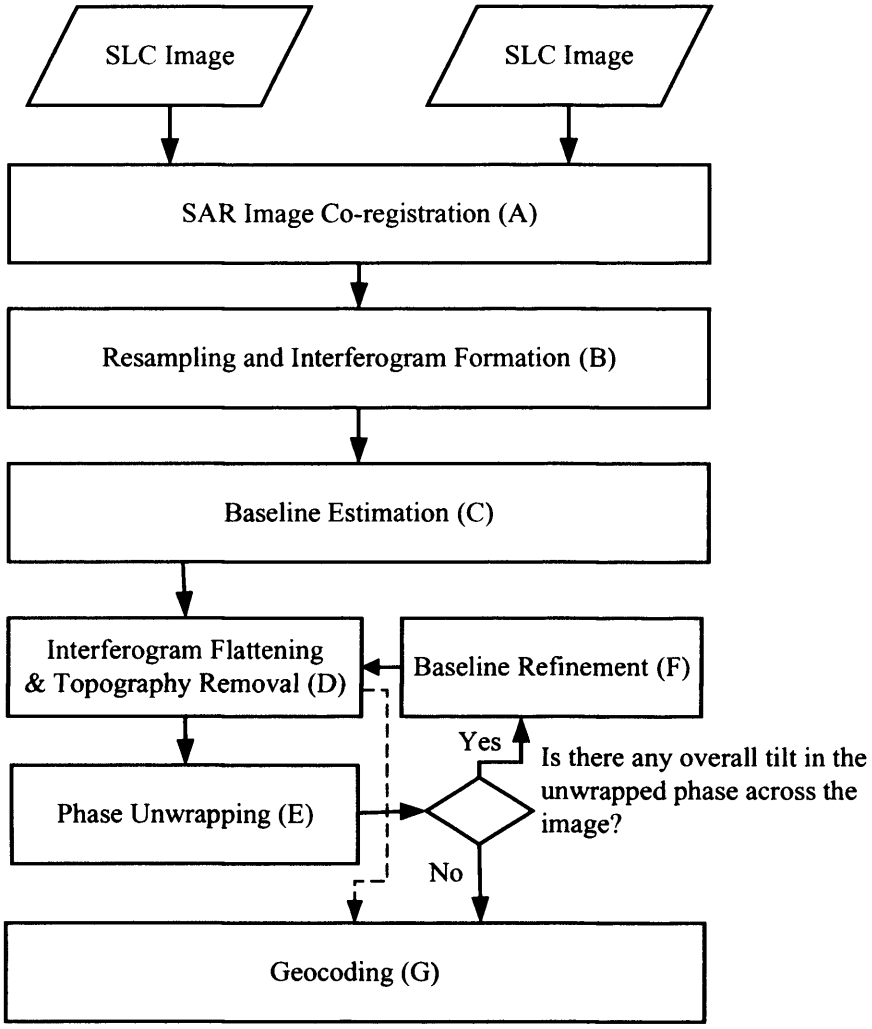

Figure 2.4 Two-pass differential InSAR processing architecture

E. The phase of the radar echoes may only be measured modulo 2π ; however, it is the absolute interferometric phase that is needed to obtain the topographic height or amount of deformation. *Ghiglia and Pritt* [1998] presented a very detailed review of two-dimensional phase unwrapping algorithms with source codes for the implementation. There are two main algorithmic approaches to phase unwrapping: residue-based algorithms [e.g. *Goldstein et al.*, 1988] and least squares algorithms [e.g. *Zebker and Lu*, 1998]. The residue-based algorithm developed by *Goldstein et al.* [1988] is used in this thesis due to its popularity in the scientific community. The Goldstein algorithm connects nearby phase residues with branch cuts so that the residues are balanced, and is implemented in three steps: residue identification, residue connection, and integration [*Goldstein et al.*, 1988; *Ghiglia and Pritt*, 1998].

F. If there is an overall tilt in the unwrapped phase across the image, the baseline can then be refined using the unwrapped phase and an independent DEM. This will be further investigated in Section 2.3.3. The refined baseline can be used to remove the topographic contribution from the original interferogram, and no further phase unwrapping is required.

G. The geocoding procedure maps the unwrapped phase values from the radar coordinate system into the DEM-based coordinate system, and converts the unwrapped phase values to deformation distances (viz. scale the unwrapped phase by $\lambda/4\pi$).

2.3 Technical issues related to the ROI_PAC InSAR processor

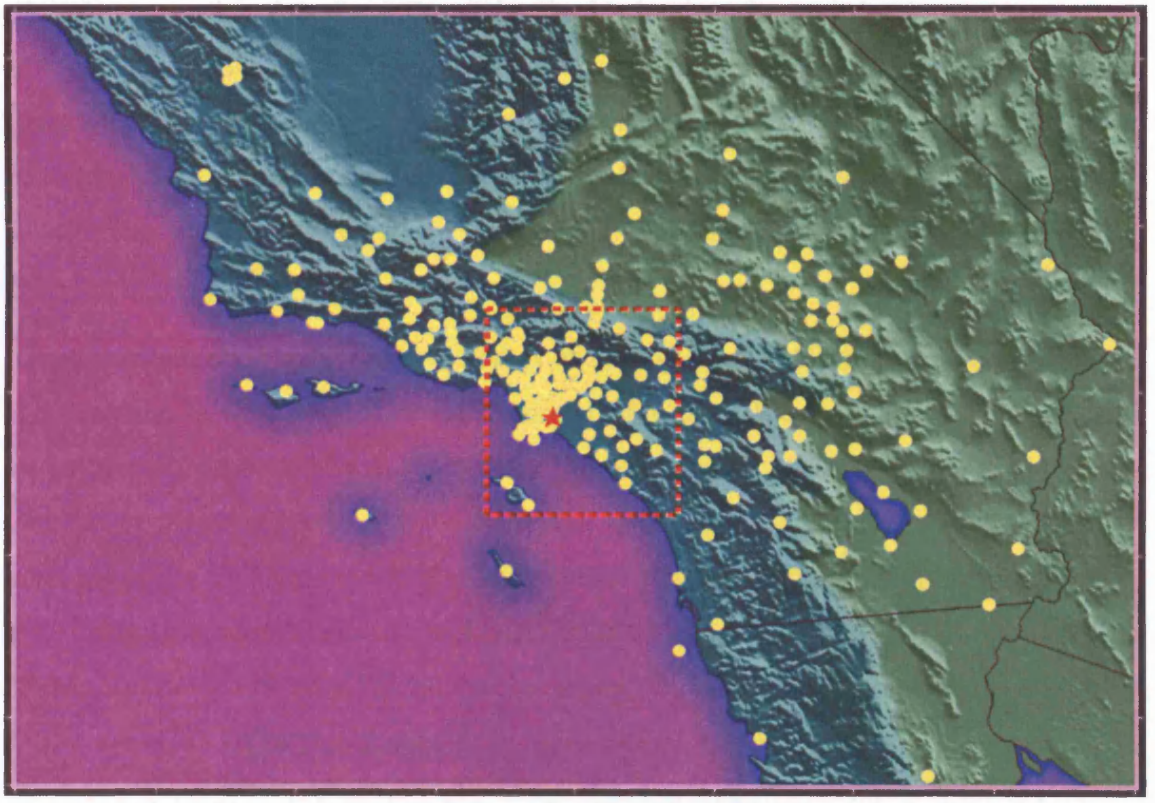

Figure 2.5 The locations of GPS stations (shown as yellow circles) over the SCIGN region (adapted from an SCEC[1] image). The dashed red box is the area of interest shown in Figure 2.6, and the red star represents the city of Long Beach.

In order to understand the ROI_PAC InSAR processor further, some technical issues are investigated in this section. As mentioned in Section 1.4, the Los Angeles

[1]: http://www.scec.org/scign/images/stationmap.jpg, 21 September 2004.

metropolitan region is selected as the principal test site in this thesis. Figure 2.5 shows the Southern California Integrated GPS Network (SCIGN), the densest regional GPS network in the world, whose stations are distributed throughout southern California with an emphasis on the greater Los Angeles metropolitan region.

2.3.1 SRTM DEM

In order to remove topographic contributions from interferograms, a SRTM DEM with a spatial resolution of 30 m was used in this study. The Shuttle Radar Topography Mission (SRTM) is a joint project between the National Geospatial-intelligence Agency (NGA) and the National Aeronautics and Space Administration (NASA). The planned objective of this project was to produce digital topographic data for 80% of the Earth's land surface (all land areas between 60° north and 56° south latitude), with data points located every 1-arc-second (approximately 30 metres) on a latitude/longitude grid. The absolute vertical accuracy of the elevation data is claimed to be less than 7 metres [*Farr and Kobrick*, 2000]. Two typical problems are likely to be encountered when using the SRTM DEM:

The first problem is noisy water surfaces as well as poorly defined coastlines. Since the coastline is well defined in the National Elevation Dataset (NED[1]), a seamless raster product produced by the U.S. Geological Survey (USGS), the NED DEM was used to produce a mask of the ocean that was then applied to mask the water surfaces of the SRTM DEM. It should be noted that the horizontal datum for NED is the North American Datum of 1983 (NAD83) [*Gesch et al.*, 2002], whilst the SRTM DEM uses the WGS-84 ellipsoid. In this study, for the comparison with the SRTM DEM, the NED DEM was converted to the WGS-84 system.

The second problem is missing data in the SRTM DEM, which is indicated by an elevation of –32,768. The simplest solution is to set the missing values as zero when used in the ROI_PAC software since the ROI_PAC package will ignore zero values by default. If the missing data areas are relatively small, interpolation methods can be used to fill in the holes. If the missing data areas are quite large, independent

[1]: http://gisdata.usgs.gov/NED, 23 November 2004.

source data sets, such as ASTER (Advanced Spaceborne Thermal Emission and Reflection Radiometer[1]) and NED DEMs, should be used to fill in the missing pixels. In the test area, since there are very few missing pixels, an interpolation method was applied to fill in the missing data using the ENVI 4.0 software.

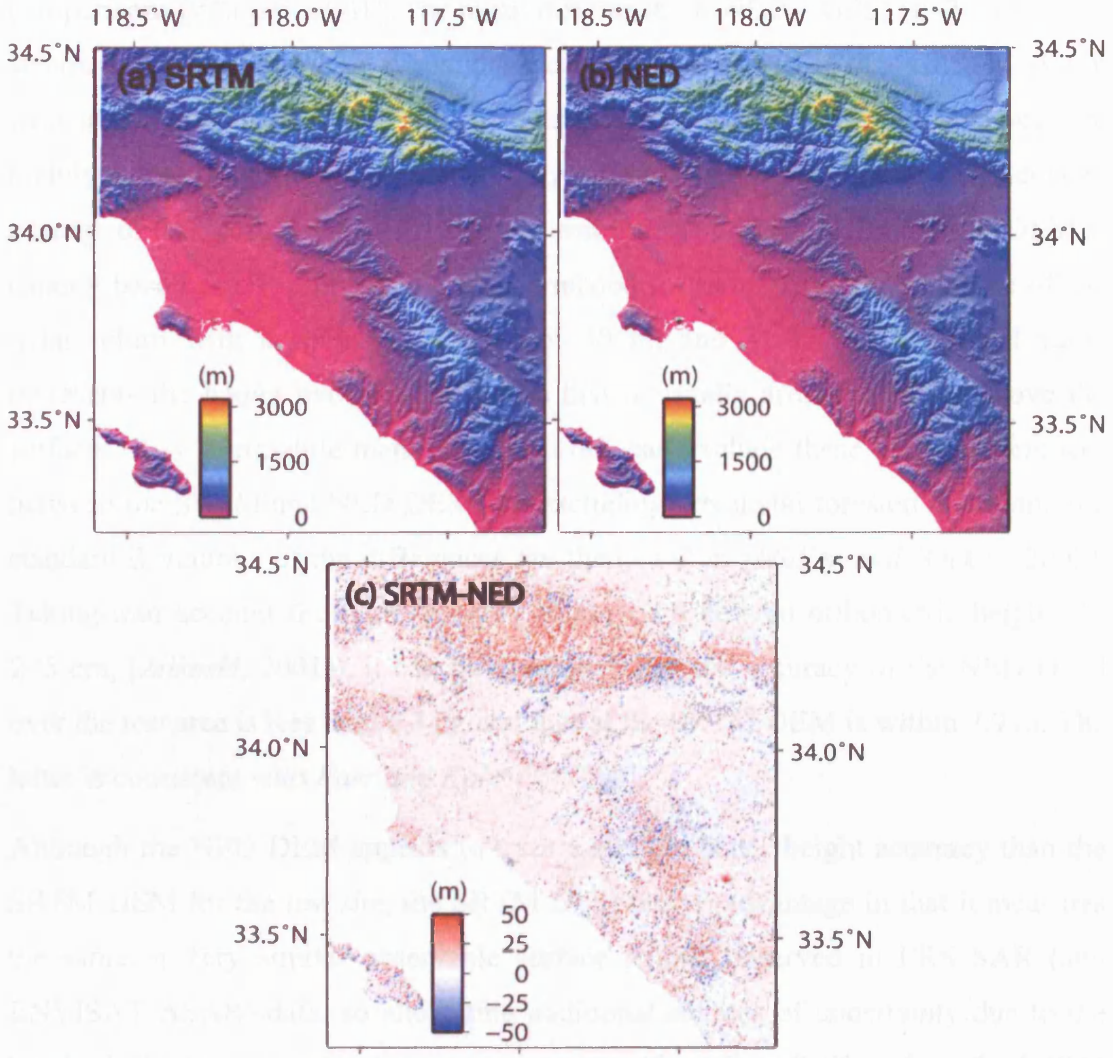

Figure 2.6 Hill-shaded topographic map of the area of interest. a) SRTM DEM with a spatial resolution of 30 m; b) NED DEM with a spatial resolution of 30 m; c) Difference: SRTM - NED.

Figure 2.6 shows the SRTM DEM after masking ocean surfaces and filling in the missing values, the NED DEM and their difference (SRTM – NED). The mean difference was 1.8 m with a standard deviation of 7.9 m. In order to assess the absolute accuracy of these two DEMs for the test areas, they were compared with

[1]: http://asterweb.jpl.nasa.gov, 23 November 2004.

GPS-derived heights over 100 CGPS stations. It should be noted that the SRTM DEM is referenced to the WGS84 geoid, and the NED DEM used in this study to the North American Vertical Datum 1988 (NAVD88), so that GPS-derived ellipsoid heights had to be converted to orthometric heights using geoid heights before comparisons [*Zilkoski*, 2001]. The mean difference of (NED – GPS) is –3.2 m with a standard deviation of 6.3 m, whilst the mean difference of (SRTM – GPS) is –3.4 m with a standard deviation of 7.9 m. The differences between these data sets are mainly due to the different levels that they refer to: 1) The NED DEM represents an average of the "bare Earth" with a spatial resolution of 30 m; 2) The SRTM DEM is canopy based, i.e. it represents a height related to the average phase centre of the radar return with a spatial resolution of 30 m; and 3) The GPS-derived value represents the height over a GPS station that is usually around 1 metre above the surface[1]. It is worthwhile mentioning that one can exclude these height differences between the SRTM and NED DEMs by excluding urban and forested areas, and the standard deviations of the differences are then ~1-2 m [*Muller and Backes*, 2003]. Taking into account the high accuracy of the GPS-derived orthometric heights (< 2~5 cm, [*Zilkoski*, 2001]), it can be concluded that the accuracy of the NED DEM over the test area is less than 6.3 m, and that of the SRTM DEM is within 7.9 m. The latter is consistent with *Farr and Kobrick* [2000].

Although the NED DEM appears to have a slightly better height accuracy than the SRTM DEM for the test site, the SRTM DEM has an advantage in that it measures the same or very similar observable surface to that observed in ERS SAR (and ENVISAT ASAR) data, so alleviating additional sources of uncertainty due to the height difference between phase centres and the "bare Earth". Therefore, the SRTM DEM was selected to remove the topographic contribution to phase in interferograms in this thesis.

2.3.2 Comparison between Delft ODR and D-PAF PRC orbits

Knowledge of satellite position comes to play a key role when removing the component due to the ellipsoidal Earth in an interferogram. In the InSAR community, two sources of precise orbit state vectors are usually used: one is available at the German Processing and Archiving Facility (D-PAF) with a radial

[1]: http://www.scign.org/arch/sdb_monument.htm, 12 December 2004.

accuracy of about 8-10 cm, consisting of the satellite ephemeris (position and velocity vectors) including time tag, given in a well defined reference frame, together with the nominal satellite attitude information and a radial orbit correction [*Ries et al.*, 1999]. The other is provided by the Delft Institute for Earth-Oriented Space Research (DEOS), containing the longitude, latitude, and altitude of the nominal centre-of-mass of the satellite in the GRS80 reference frame, every 60 seconds with a radial accuracy of 5-7 cm but without velocity vectors [*Scharroo and Visser*, 1998].

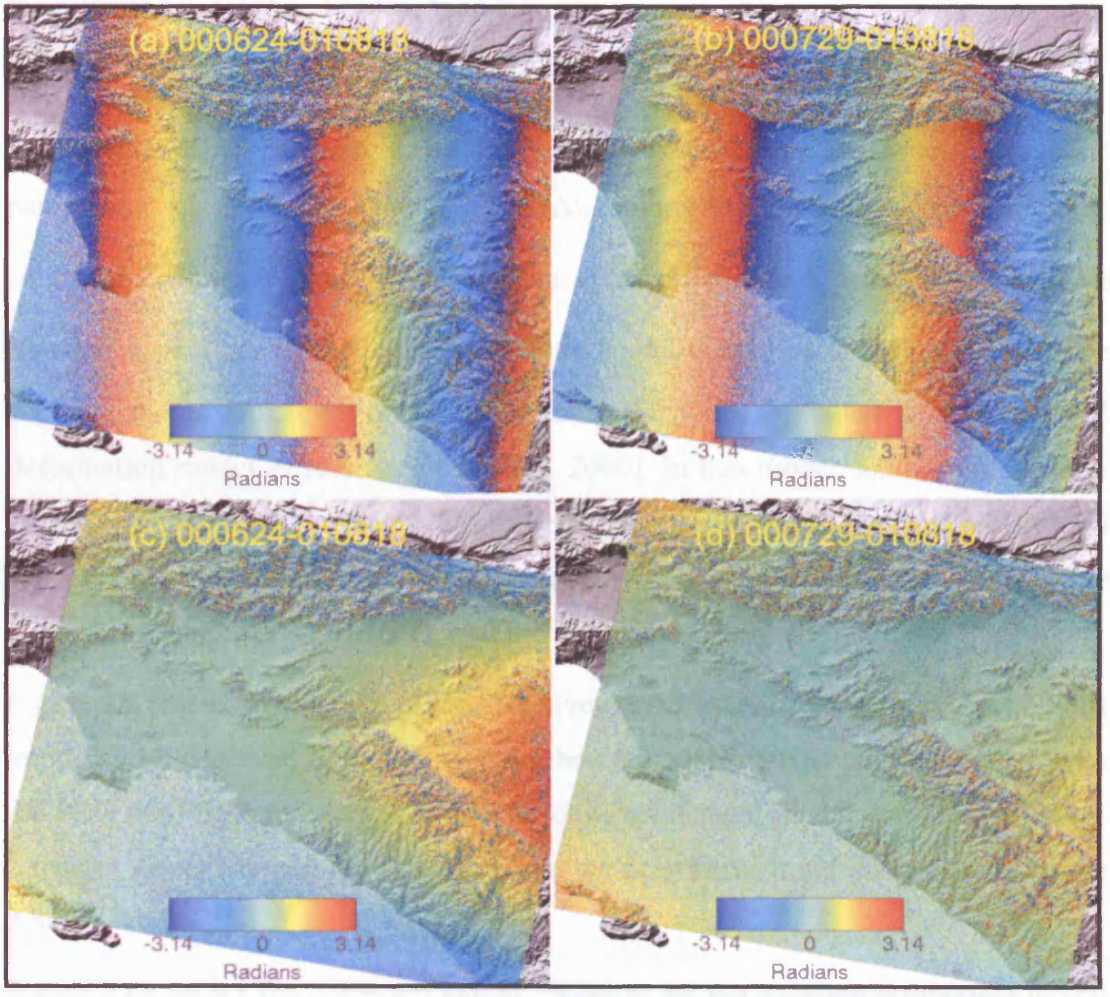

Figure 2.7 Difference between PRC and Delft (ODR) orbits (PRC-ODR) for ERS-2 track 170, frame 2925. The collected dates of the master and slave images are given in the upper of each interferogram with a format of YYMMDD (e.g. 010818 is read as 18 August 2001): (a) & (b) without baseline correction; (c) & (d) with baseline correction.

The differences between these two precise orbit products are shown in Figure 2.7. The differences were up to 2~3 near-linear fringes (Figures 2.7a and 2.7b) when the baseline was estimated from precise orbits. This means that residual fringes can remain even with two such precise orbits, and there are significant differences in the interferograms when using different orbit products. Fortunately, these fringes were near linear and parallel to the satellite track, and further action, e.g. a linear model or Fourier Transforms, can be applied to remove the near-linear trends. When the baseline was refined using unwrapped phase with a precise DEM (see Section 2.3.3), the differences decreased to less than 0.5 fringes.

2.3.3 Application of baseline refinement

In the ROI_PAC package, a baseline model is developed with seven baseline parameters: along-track constant offset Δs_0, along-track scaling factor k, range constant offset $\Delta\rho_0$, cross-track baseline b_{c0} and its rate of change $\dot{b}_c$, vertical baseline b_{h0} and its rate of change $\dot{b}_h$. This model is applied to refine the baseline estimate to the mm level of precision using the DEM provided and an optional deformation model as reference [*Buckley*, 2000]. In this model, azimuth offsets are estimated in the registration process, range offsets come from either the registration process or the unwrapped phase, and the baseline parameters are estimated from the azimuth offsets, the range offsets, and the unwrapped phase.

Figure 2.8 shows an example of the effectiveness of baseline correction. An obvious trend can be observed from SW to NE when the baseline was only estimated from the PRC orbit (Figure 2.8a). After the baseline refinement model was applied, about 2 fringes were removed (Figure 2.8d), and the near linear trend disappeared (Figure 2.8c).

Figure 2.8d shows the corrected values produced by the baseline refinement model using the unwapped phase shown in Figure 2.8b. It should be noted that the baseline refinement model also generated the corrected values for areas with low coherence, e.g. the San Gabriel Mountains in the north and the ocean in the southwest. It is also worth noticing that the two fringes in the bottom left in Figure 2.8d appear as parabolas. The most likely possibility is that there was no unwrapped phase over the ocean due to low coherence over water surfaces (Figure 2.8b).

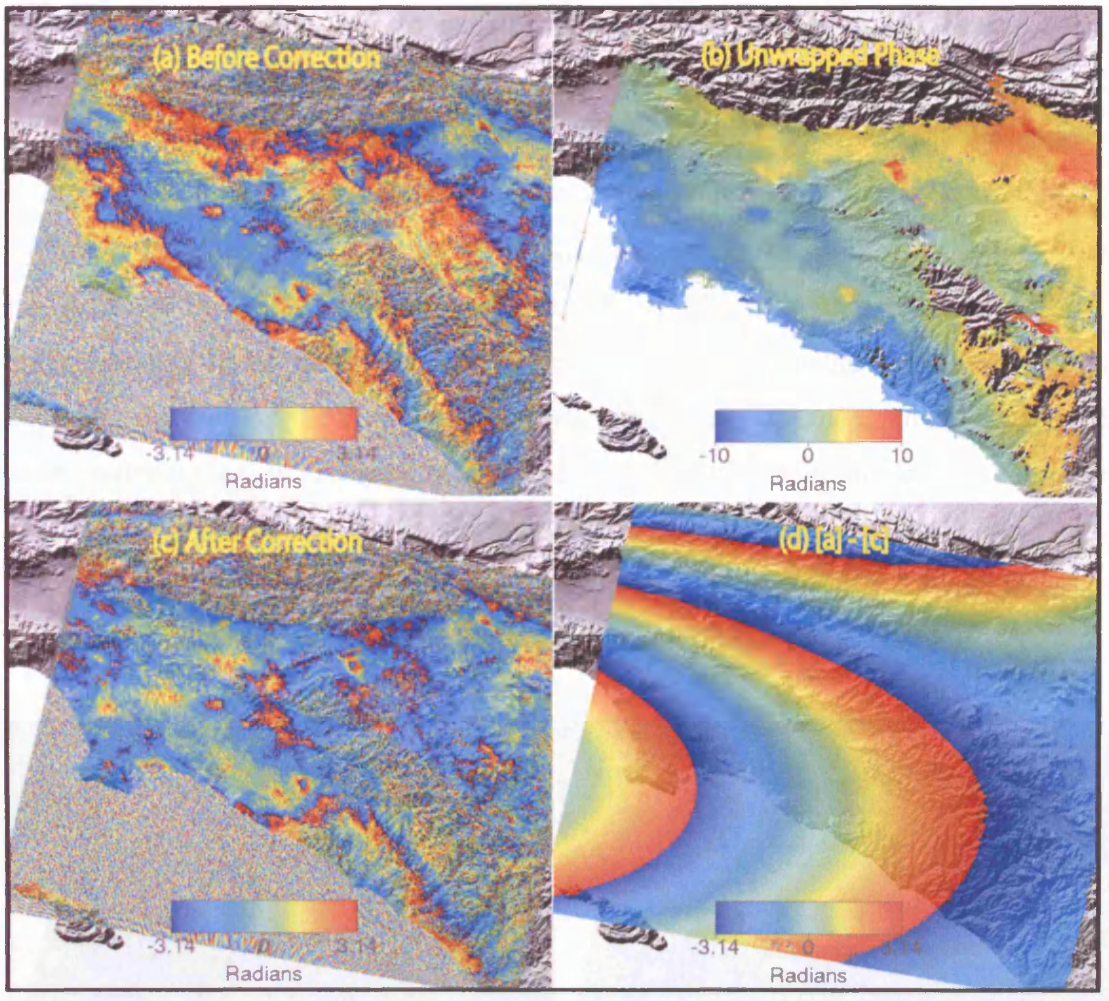

Figure 2.8 Example of baseline correction for Interferogram 000624-010818. a) before baseline correction, i.e. baseline only estimated from PRC orbits; b) unwrapped phase with the baseline estimated from PRC orbits; c) after baseline correction, i.e. baseline refined using unwrapped phase; d) difference image: before – after.

2.3.4 Application of filtering algorithm

There are several sources of phase noise in interferograms, such as thermal noise, baseline geometry, temporal decorrelation, instability of SAR sensors, uncertainty of image processing, etc. These factors not only degrade fringe visibility but also preclude accurate phase unwrapping.

Phase noise in interferograms is usually reduced by a complex multilook approach, in which the interferogram data in a specified window are simply averaged [*Goldstein et al.*, 1988; *Hanssen*, 2001]. *Webley* [2003] reported that the coarser sampling, i.e. 5×20 pixels, showed a better data quality in the interferogram than an averaging window of 1×4 pixels. Generally, the coarser the sampling, the smoother the data. Unfortunately, this approach leads to a loss of spatial resolution. So, a balance needs to be made between filtering effects and spatial resolution, which depends on the application of interferograms. For instance, in the case of deformation mapping, 2 looks in range and 10 looks in azimuth are a reasonable choice for a typical pixel of 4 m along track and 20 m across [*Massonnet and Feigl*, 1998]; in the case of water vapour mapping, larger multilooks, e.g. 8 looks in range and 40 looks in azimuth, might be better [*Hanssen*, 2001].

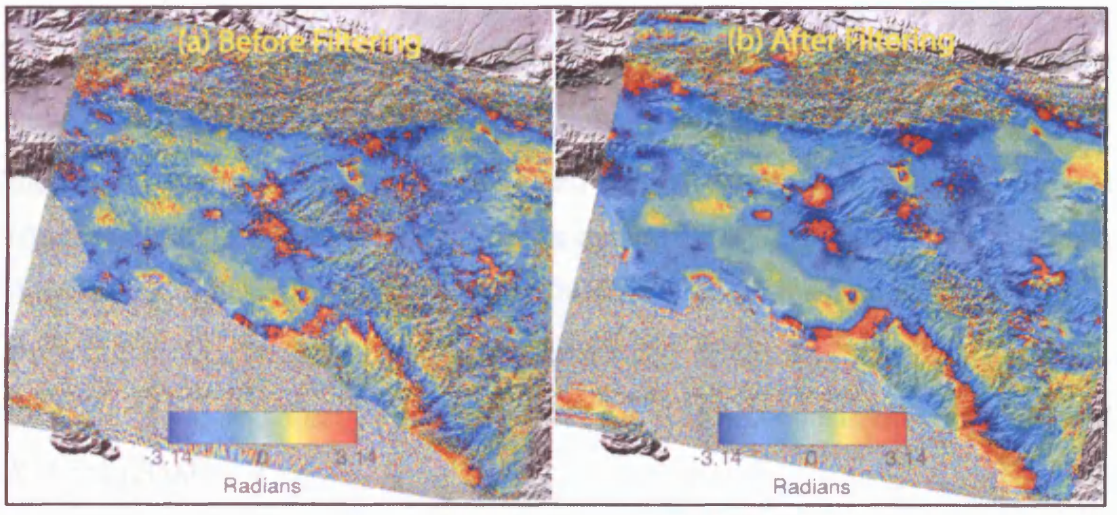

Figure 2.9 Application of filtering algorithm to Interferogram 000624-010818. a) Geocoded interferogram as output by ROI_PAC. Each pixel is 160 by 160 m; b) Filtered interferogram with a power spectrum filter ($\alpha = 0.8$) [*Goldstein and Werner*, 1998].

Apart from complex multilooking, an adaptive power spectrum filter proposed by *Goldstein and Werner* [1998] is applied widely [e.g. *Wright*, 2001; *Feigl et al.*, 2002]. Based on smoothing the power spectrum of the interferogram $Z(u,v)$ in a moving window with the intensity of the spectrum, this power spectrum filter is

sensitive to the local phase noise and the phase gradient. The local power spectrum of the filtered interferogram $Z'(u,v)$ is expressed as:

$$Z'(u,v) = \left|Z(u,v)\right|^{1+\alpha} \qquad (2.4.1)$$

where α is a parameter, varying from 0 to 1, that controls the strength of the filter: no filtering occurs if α is zero and the filtering is stronger if α is larger. The spatial resolution of this filter adapts to the local phase slope such that regions with high correlation are strongly filtered, while regions with low correlation are weakly filtered. In addition, regions of incoherence (at high frequency) are preserved. Therefore, the filter improves the signal to noise ratio of interferograms. Figure 2.9 shows an example of this power spectrum filter with a significant improvement in fringe visibility.

2.4 Conclusions

This chapter has presented the InSAR geometry and the associated mathematical models for the retrieval of topography and surface deformation mapping. Several technical issues concerning the application of the ROI_PAC package have also been discussed in this chapter, from which the following conclusions can be drawn:

1) A comparison between GPS and SRTM DEM shows that the accuracy of the SRTM DEM is less than 7.9 m in the test area, which is consistent with *Farr and Kobrick* [2000].

2) There is no significant difference between the two main precise orbit products, i.e. ODR and PRC orbits, after near-linear trends are removed;

3) The baseline refinement technique employed in the ROI_PAC package can significantly reduce (if not completely remove) the near linear trends in interferograms;

4) Filtering improves the signal to noise ratio and fringe visibility of interferograms.

Chapter 3 will now discuss atmospheric effects on InSAR processing, which is the main thrust of this research.

Chapter 3

Atmospheric effects on repeat-pass InSAR

Numerous error sources that affect phase measurement quality may also increase the noise level or introduce systematic errors (biases) in the estimated topography and deformation fields. These include instrument noise, satellite orbit error, atmospheric disturbances, temporal decorrelation, residual topographic signals in differential interferograms, and processing errors [*Zebker et al.*, 1997; *Massonnet and Feigl*, 1998; *Klees and Massonnet*, 1999; *Bürgmann et al.*, 2000; *Hanssen*, 2001; *Li et al.*, 2004]. A full description of InSAR's error sources is beyond the scope of this thesis, and interested readers are referred to *Hanssen* [2001]. This chapter focuses primarily on microwave propagation delay induced by the atmosphere, especially atmospheric water vapour, which is the principal motivation for this study. An introduction is given to the composition and structure of the atmosphere, followed by a detailed demonstration of atmospheric refractivity and its effects on the products of repeat-pass InSAR. This chapter also covers the impact of dry air, hydrometeors[1], and other particulates on interferograms.

3.1 The influence of uncertainties of phase measurements

The uncertainties in phase measurements result primarily from atmospheric effects (mainly the wet delay due to water vapour), satellite orbit error, and temporal decorrelation, which in turn lead to the statistical variation of each point in both DEMs and deformation maps [*Zebker et al.*, 1994]. In order to evaluate atmospheric effects on repeat-pass InSAR, the influence of the phase measurement uncertainties on topography mapping of repeat-pass InSAR, and deformation mapping of 2-DInSAR needs to be estimated.

[1]: A hydrometeor is defined as any product of condensation or deposition of atmospheric water vapour formed in the free atmosphere or at the Earth's surface. Hydrometeor can also be any water particle blown by the wind from the Earth's surface [*AMS*, 2000].

For simplicity, the basic mathematical models for repeat-pass InSAR are given again as follows (see Equations (2.2.1) and (2.2.4)):

$$\begin{aligned}\varphi &= \frac{4\pi}{\lambda}\delta\rho \\ &= \frac{4\pi}{\lambda}\left(-B\sin(\theta-\alpha)+\frac{B^2}{2\rho}\right)\end{aligned} \tag{3.1.1}$$

where φ is the measured interferometric phase without removing the component due to the ellipsoidal Earth, and $\delta\rho$ is the extra path length of the SAR sensors' second pass, relative to the first pass, which results in a phase shift.

If there is no deformation between these two passes, the phase shift can be expressed as (see Equation (2.2.10)):

$$\varphi_{flat} = -\frac{4\pi}{\lambda}B_{\perp_0}\Delta\theta \tag{3.1.2}$$

where φ_{flat} is the interferometric phase after removing the component due to the ellipsoidal Earth, $B_{\perp_0}$ is the perpendicular component of the baseline referenced to the ellipsoidal Earth, and $\Delta\theta = \theta - \theta_0$ (see Figure 2.3).

If there is any change ($\Delta\rho$) in the slant range direction during these two passes, the phase shift can be expressed as:

$$\begin{aligned}\varphi_{flat} &= \frac{4\pi}{\lambda}(\delta\rho+\Delta\rho) \\ &= \frac{4\pi}{\lambda}\left(-B_{\perp_0}\Delta\theta+\Delta\rho\right)\end{aligned} \tag{3.1.3}$$

The relationship between the height and the phase is:

$$h = H - \rho\cos\theta \tag{3.1.4}$$

Based on the above equations, the uncertainties of repeat-pass topography mapping and two-pass surface deformation mapping are estimated respectively.

3.1.1 The influence of path variations on phase measurements

In Figure 2.3, consider that signals propagate through the atmosphere, and the two path lengths are assumed to be $\rho+\Delta d_1$ and $\rho+\delta\rho+\Delta d_2$, where Δd_1 and Δd_2 are

additional path delays, e.g. atmospheric delays, the measured phase difference ϕ can be rewritten as:

$$\begin{aligned}\phi &= \frac{4\pi}{\lambda}\left(\delta\rho + \left(\Delta d_2 - \Delta d_1\right)\right) \\ &= \frac{4\pi}{\lambda}\left(\delta\rho + \Delta d\right)\end{aligned} \tag{3.1.5}$$

where Δd is the total path variation due to path delays, e.g. atmospheric delays. On the one hand, if there were no variation in atmospheric conditions between observations, the two atmospheric phase delays would cancel out except for a very slight difference in path resulting from a tiny change in incidence angle across the interferometer baseline (i.e. $\Delta d \approx 0$) [*Zebker et al.*, 1997]. On the other hand, if the atmospheric variation were homogeneous for the whole SAR scene, it would lead to a biased interferometric phase. Since in interferometry phase differences are measured, the atmosphere-induced phase bias is eliminated. However, for most of the areas in the world, atmospheric variation is inhomogeneous [*Hanssen*, 1998]. For further discussion see Sections 5.1 and 6.1.

Differentiation of (3.1.5) with respect to the path variation Δd yields the phase measurement uncertainty:

$$\sigma_\varphi = \frac{4\pi}{\lambda}\sigma_{\Delta d} \tag{3.1.6}$$

For ERS-1/2 with a wavelength of 5.66 cm, a path variation of half the wavelength (2.83 cm) could lead to a phase uncertainty of 2π radians (viz. 1 fringe).

3.1.2 The influence on repeat-pass topography mapping

Differentiation of (3.1.2) and (3.1.4) with respect to φ yields the following two equations:

$$\begin{cases} -\dfrac{4\pi}{\lambda} B_{\perp_0} \dfrac{\partial\theta}{\partial\varphi} = \dfrac{\partial\varphi_{flat}}{\partial\varphi} = 1 \\ \dfrac{\partial h}{\partial\varphi} = \rho\sin\theta\dfrac{\partial\theta}{\partial\varphi} \end{cases} \tag{3.1.7}$$

Thus, one can derive height error as a function of phase error for topography mapping:

$$\begin{aligned}\sigma_h &= \frac{\lambda}{4\pi}\frac{\rho\sin\theta}{B_{\perp_0}}\sigma_\varphi \\ &= \frac{1}{2\pi}\left(\frac{\lambda}{2}\frac{\rho\sin\theta}{B_{\perp_0}}\right)\sigma_\varphi \\ &= \frac{h_a}{2\pi}\sigma_\varphi\end{aligned} \qquad (3.1.8)$$

where σ_φ is the phase error in the interferogram in radians, σ_h is the resultant height error, and h_a is the altitude of ambiguity (Equation (2.2.16)). It is clear that the phase error results in less topographic uncertainty with a smaller altitude of ambiguity. For instance, a phase error of 1.25 radians (0.2 fringes) could lead to a height uncertainty of 9 m with a 45 m altitude of ambiguity (i.e. a perpendicular baseline of 200 m), whilst it could lead to a height uncertainty of 4.4 m with an altitude of ambiguity of 22 m (i.e. a perpendicular baseline of 400 m). It should be kept in mind that a large baseline will result in low correlation between the SAR images.

3.1.3 The influence on two-pass deformation mapping

Differentiation of (3.1.3) with respect to φ yields an estimate of the error in deformation as a function of the error in the phase estimate:

$$\sigma_{\Delta\rho} = \frac{\lambda}{4\pi}\sigma_{\varphi_{flat}} = \frac{\lambda}{4\pi}\sigma_\varphi \qquad (3.1.9)$$

A phase error of 1.25 radians (0.2 fringes) could therefore lead to a deformation uncertainty of 0.56 cm.

In order to assess the atmospheric effects, Equations (3.1.6), (3.1.8) and (3.1.9) can be easily used to transform path variations to the influences they hold over topography and/or deformation mapping in the following sections.

3.2 Introduction to the atmosphere

3.2.1 Composition of the atmosphere

The Earth's atmosphere is a mixture of many discrete gases, each with its own physical properties, in which varying quantities of tiny solid and liquid particles are suspended [*Lutgens and Tarbuck*, 2004]. The major atmospheric gas components are summarized in Table 3.1 [*Lutgens and Tarbuck*, 2004]. As shown in Table 3.1, two gases, nitrogen and oxygen, make up 99.03% of the volume of clean, dry air. The remaining 1 percent of dry air is mostly the inert gas argon (0.934%) plus tiny quantities of a number of other gases.

Table 3.1 Composition of the atmosphere near the Earth's surface[1]

Constituent	Symbol	Percent by volume
Nitrogen	N_2	78.084
Oxygen	O_2	20.946
Argon	Ar	0.934
Carbon dioxide	CO_2	0.037
Neon	Ne	0.00182
Helium	He	0.000524
Methane	CH_4	0.00015
Krypton	Kr	0.000114
Hydrogen	H_2	0.00005
Water vapour	H_2O	0-4
Aerosols		0.000001[2]

[1]: Modified from Lutgens and Tarbuck [2004].

[2]: From Ahrens [2000].

The composition of the Earth's atmosphere is not constant: it varies from time to time and from place to place. One important example is water vapour. Water vapour may account for up to 4% of the atmosphere in warm tropical areas, whilst its concentration may decrease to a mere fraction of a percent in cold arctic areas. Carbon Dioxide (CO_2) is another good example: measurements of CO_2 at Hawaii's

Mauna Loa Observatory shows that the CO_2 concentration has risen more than 15% since 1958 [*Ahrens*, 2000; *Lutgens and Tarbuck*, 2004]. It should be kept in mind that in addition to dry air and water vapour, there are also some solid and liquid particles suspended within the atmosphere, such as hydrometeors and other particles.

3.2.2 Structure of the atmosphere

Due to the Earth's gravity, the atmosphere is, to first order, horizontally stratified. Without much simplification, the atmosphere can be divided into a series of layers by its representative temperature profile or by its electrical properties. Typical mid-latitude profiles of temperature and ion density are given in Figure 3.1.

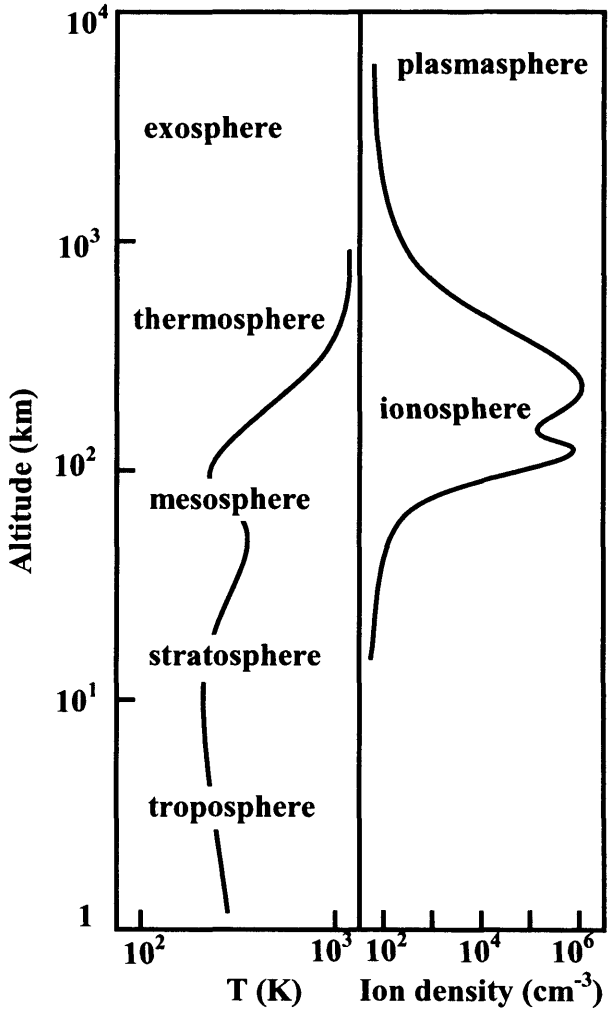

Figure 3.1 Schematic structure and ion density of the atmosphere (adapted from *Rees* [1989])

The bottom layer, where the air temperature decreases with altitude, is known as the troposphere. The rate at which the temperature decreases with height is called the temperature lapse rate. Its average value is 6.5°C per kilometre. The troposphere is on average around 12 km thick, ranging from an excess of 16 km in the tropics, to 9 km or less in Polar Regions. All the weather that we are primarily interested in occurs in the troposphere. The troposphere contains 80% of the atmosphere's mass [*Mason et al.*, 2001], and contains 99% of the atmosphere's water vapour [*Mocker*, 1995]. The top of the troposphere is marked by the tropopause.

Above the tropopause lies the stratosphere, which extends to about 50 km. Throughout the stratosphere, the temperature gradually increases with height until it reaches about 0°C at an altitude of 50 km. The primary reason for temperature increase with altitude is that most of the ozone is contained in the stratosphere: ultraviolet (UV) light interacting with the ozone causes the temperature to increase. The boundary between the stratosphere and the next layer, the mesosphere, is called the stratopause.

Above the stratopause, the temperature again decreases with altitude. The temperature drops to about -90°C near the top of the mesosphere where the mesopause is located, some 80 km above the Earth's surface.

Above the mesopause is the thermosphere, where oxygen molecules (O_2) absorb energetic solar rays which warm the air. In the thermosphere the temperature increases with height (>1000°C).

On top of the thermosphere, about 500 km above the Earth's surface, lies the exosphere. The boundary between these two is very diffuse, and molecules in the exosphere have enough kinetic energy to escape the Earth's gravity and thus fly off into space.

The outer part of the mesosphere and the whole of the thermosphere are also referred to as the ionosphere, since fairly large concentrations of ions and free electrons exist in this region. Ions are atoms and molecules that have lost (or gained) one or more electrons. The ionosphere is composed of D, E, F1 and F2 layers, extending from a height of about 50 km to 1500 km above the Earth's surface (Table 3.2). Each layer has different rates of production and loss of free electrons. As

shown in Figure 3.1 and Table 3.2, the electron density increases with altitude, but only up to a certain height where a maximum density is reached. This increase in the electron density is mainly due to a reduction in the absorption of UV light by the decreasing numbers of gas molecules with altitude, leading to the ionisation of more gas molecules. Above the certain height, the electron density begins to decrease due to fewer gas molecules being available for ionization [*Odijk*, 2002]. From Table 3.2, it is clear that the peak electron density occurs in the F2 layer, with its maximum usually at a height of 200-400 km [*Spilker and Parkinson*, 1996; *Odijk*, 2002]. The electron density changes by one to two orders of magnitude between day and night, with a peak around 2 pm local time, and a nadir at midnight. The electron density also varies with geographic location, certain solar activities, and geomagnetic disturbances [*Schaer*, 1999].

Table 3.2 Horizontal layers in the ionosphere (adapted from Odijk [2002] and Schaer [1999])

Layer	Height (km)	Typical electron density (m^{-3})		Remarks
		Day	Night	
D	80~90	10^{10}	-	Disappear at night
E	90~140	10^{11}	5×10^{9}	Sporadic electrons at c. 120 km
F1	140~200	5×10^{11}	-	Goes up into F2 at night
F2	200~∞	10^{12}	10^{11}	Maximum density at c. 350 km

3.3 Microwave propagation delay due to the troposphere

The atmosphere affects the velocity of microwave signals. This is referred to as refraction. Since the velocity and the ray bending of light varies between different media, the refractive index (n) for any medium is often introduced:

$$n = \frac{c_0}{c} \tag{3.3.1}$$

where c_0 is the speed of light in vacuum and c is the speed of light in the medium. In clear air, the refractive index is only slightly greater than unity at sea level, typically $n \approx 1.0003$, and much closer to unity at the upper end of the troposphere. For simplicity, the refractive index is expressed in terms of refractivity N where

$N = 10^6 \times (n-1)$. Atmospheric effects on microwave signals can be stated in terms of an increase in travel path length. The excess path length due to signal delays in the atmosphere compared with the geometrical path length in vacuum, or atmospheric delay, is expressed as [*Davis*, 1985]:

$$\Delta L = \int_S [n-1]ds + S - G = 10^{-6} \int_S N ds + S - G \qquad (3.3.2)$$

where s is the position along the curved ray path $S = \int_S ds$, and G is the straight line path. The first term in Equation (3.3.2) is the delay of the signal due to its reduced propagation velocity caused by the refractive index. The second and third terms are the "geometric delay" caused by the bending of the signal. The geometric delay can be ignored for rays with elevation angles above 15°, but has to be taken into account for lower angles since it is on the order of 10 cm for an elevation angle of 5°.

In particular, for a signal coming from the zenith direction, assuming a spherically symmetric atmosphere, the atmospheric zenith total delay (ZTD) can be given as:

$$ZTD = \int_{H_0}^{H} [n-1]dh = 10^{-6} \int_{H_0}^{H} N dh \qquad (3.3.3)$$

where H_0 is the geocentric height of the site above the geoid, and H is the geocentric height of the troposphere above the geoid.

As demonstrated in Section 3.1.2, the atmosphere of the Earth can be divided into different parts depending on which aspect of the atmosphere is of interest. In our case, the behaviour of the propagation of microwave radiation is considered, and the atmosphere is commonly divided into the neutral atmosphere (including troposphere, tropopause, and stratosphere) and the ionosphere, a methodology also adopted here. In the neutral atmosphere, microwave delays are induced by refractivity of gases (including dry air and water vapour), hydrometeors, and other particulates, which is dependent on their permittivity and concentration, as well as forward scattering from hydrometeors and other particulates [*Solheim et al.*, 1999]. In the following sub-sections, delays in the neutral atmosphere are discussed including: 1) refractive delays induced by dry air and water vapour, 2) refractive delays induced by cloud and fog, 3) refractive delays induced by aerosols and

volcanic ash, 4) scattering delays induced by rain. Phase advance due to the ionosphere is discussed in Section 3.4.

3.3.1 Tropospheric refractive delays (I): induced by dry air and water vapour

The neutral atmosphere (troposphere, tropopause, and stratosphere) is a non-dispersive medium, and its impact on microwaves does not depend on the frequency of the signal. Since about 80% of the atmosphere's mass is found in the troposphere, which stretches to about 16 km above the equator and about 9 km above the poles [*Mason et al.*, 2001], the overall effect of the neutral atmosphere is, therefore, referred to as the tropospheric effect.

The refractivity of dry air and water vapour is a function of its temperature, pressure, and water vapour pressure. It is usually described by empirical formulas, e.g. [*Thayer*, 1974]:

$$N = k_1 \frac{p_d}{T} Z_d^{-1} + k_2 \frac{p_w}{T} Z_w^{-1} + k_3 \frac{p_w}{T^2} Z_w^{-1} \qquad (3.3.4)$$

where k_i are refractivity constants, and have the following values suggested by *Bevis et al.* [1994]: $k_1 = 77.60 \pm 0.05\ [K\,hPa^{-1}]$, $k_2 = 70.4 \pm 2.2\ [K\,hPa^{-1}]$, and $k_3 = (3.739 \pm 0.012) \times 10^5\ [K^2\,hPa^{-1}]$; p_d and p_w are the partial pressures of the dry gases and water vapour, respectively, in hPa; T is the absolute temperature in degrees Kelvin; Z_d^{-1} and Z_w^{-1} are the inverse compressibility factors (corrections for non ideal-gas behaviour) for the dry air and water vapour respectively, and have nearly constant values that differ from unity by a few parts per thousand [*Owens*, 1967]. The refractivity can be computed as accurately as 0.02% considering the uncertainties of the constants in Equation (3.3.4) [*Davis et al.*, 1985]. The first term on the right hand side of Equation (3.3.4) represents the effect of the induced dipole moment of the dry constituents, and is usually called the dry refractivity (N_d). The second term represents the effect of the induced dipole moment of water vapour, whilst the third term represents the dipole moment of the water molecule. The last two terms are called the wet refractivity (N_w^d). Thus

$$N = N_d + N_w^d \qquad (3.3.5)$$

It should be noted that integration of the refractivity in the form given in Equations (3.3.4) and (3.3.5) requires knowledge of the profiles of both the wet and dry constituents.

Alternatively, the refractivity can be expressed as [*Davis et al.*, 1985]:

$$\begin{aligned} N &= k_1 R_d \rho + k_2' \frac{p_w}{T} Z_w^{-1} + k_3 \frac{p_w}{T^2} Z_w^{-1} \\ &= k_1 R_d \rho + k_2' R_v Z_w^{-1} + k_3 R_v \frac{Z_w^{-1}}{T} \end{aligned} \tag{3.3.6}$$

where ρ is the total mass density of the air, R_d and R_v are the specific gas constants for dry air and water vapour, and $k_2' = k_2 - (R_d/R_v)k_1 = 17 \pm 10\ [KhPa^{-1}]$. It should be noted that the first term on the right hand side of Equation (3.3.6) depends only on surface pressure and not on the wet/dry mixing ratio, which is called the hydrostatic refractivity (N_h), whilst the remaining two terms form the wet refractivity (N_w), which depends solely on water vapour distribution. Thus

$$N = N_h + N_w \tag{3.3.7}$$

In terms of Equations (3.3.5) and (3.3.7), the tropospheric delay can be separated into a dry (or hydrostatic) and wet delay component. It is important to remember the basic differences in the definition of the total refractivity as given by Equations (3.3.5) and (3.3.7), since in the second one, the hydrostatic refractivity includes a significant contribution from water vapour (due to the non-dipole component of water vapour refractivity) as well as the largest contribution of the dry air [*Bevis et al.*, 1992; *Ifadis and Savvaidis*, 2001]. The formulation of Equations (3.3.6) and (3.3.7) is useful, as knowledge of water vapour content is not required for the hydrostatic component unlike the dry component formalism.

Using Equations (3.3.6) and (3.3.7) in Equation (3.3.3), the zenith tropospheric delay can be expressed as:

$$\begin{aligned} ZTD &= 10^{-6} \int (N_h + N_w)\, dh \\ &= 10^{-6} \left(k_1 R_d \int \rho dh + \int \left(k_2' \frac{p_w}{T} Z_w^{-1} + k_3 \frac{p_w}{T^2} Z_w^{-1} \right) dh \right) \\ &= ZHD + ZWD \end{aligned} \tag{3.3.8}$$

The zenith hydrostatic delay can be obtained using ground pressure measurements [*Saastamoninen*, 1972]:

$$ZHD = (0.002277 \pm 0.0024)\frac{P_s}{f(\varphi, H)} \qquad (3.3.9a)$$

or [*Davis et al.*, 1985]:

$$ZHD = (0.0022768 \pm 0.0005)\frac{P_s}{f(\varphi, H)} \qquad (3.3.9b)$$

$$f(\phi, H) = 1 - 0.00266\cos(2\varphi) - 0.00028H \qquad (3.3.9c)$$

where ZHD is the zenith hydrostatic delay in *mm*, P_s is the surface pressure in hPa, φ is the latitude of the site in degrees, and H is the station height in *km* above the geoid. The hydrostatic delay in the zenith direction is typically around 2.3 m. Taking into account the uncertainties in the physical constants and in the calculation of the mean value of gravity, but not accounting for the error in the surface pressure, the uncertainty is 0.5 mm [*Davis et al.*, 1985]. The sensitivity of the hydrostatic delay to an error in the measurement of surface pressure is 2.3 $mm \cdot hPa^{-1}$. If the surface pressure is measured with an accuracy better than 0.4 hPa, the zenith hydrostatic delay can be estimated with an accuracy of 1 *mm* or better [*Bevis et al.*, 1992]. Actually, the uncertainty in the surface pressure is usually less than 0.2 hPa, thus the combined uncertainty in the zenith hydrostatic delay is less than 1 *mm* [*Niell et al.*, 2001].

The wet delay is much smaller than the hydrostatic delay, varying roughly from 0 to 30 cm between the poles and the equator and from a few cm to about 20 cm during the year at mid-latitudes [*Elgered*, 1993]. However, it is the most highly variable (both spatially and temporally) component of delay and is not easy to determine using surface measurements. Based on surface meteorological measurements, a number of different models to determine ZWD have been proposed. The most common and simplest models are based on the assumption of the linear decrease in temperature with height and the relationship between total pressure and water vapour partial pressure [*Saastamoinen*, 1972]:

$$ZWD = 0.002277\left(\frac{1255}{T_0} + 0.05\right)e_0 \qquad (3.3.10)$$

where T_0 is surface temperature in degrees Kelvin and e_0 is surface water vapour partial pressure in hPa.

Some improved models take into account seasons, latitudes and type of climates [e.g. *Baby et al.*, 1988]. More complex models estimate humidity and temperature profiles with statistical regression, and then use numerical integration method to compute the refractivity [e.g. *Askne and Nordius*, 1987]. However, ZWD can only be derived with an accuracy of around 2~5 cm using surface meteorological measurements [*Baby et al.*, 1988].

3.3.2 Tropospheric refractive delays (II): induced by cloud and fog

Cloud is defined as a visible aggregate of minute water droplets and/or ice particles in the atmosphere above the Earth's surface, and fog is defined as water droplets suspended in the atmosphere in the vicinity of the Earth's surface that affect visibility [*AMS*, 2000]. Cloud differs from fog only in that fog is close (within a few metres) to the Earth's surface. Therefore, for simplicity, the term cloud will refer to cloud and/or fog hereafter in the thesis, unless otherwise noted.

Refractivity in cloud droplets is due to displacement of charge in the dielectric medium. The droplets are too small to cause much scattering, and phase delays induced by them can be approximated based on permittivity. The dielectric refractivity can be related to the liquid water content W, independent of the shape of the cloud droplets, using the Clausius-Mossotti equation [*Liebe et al.*, 1989; *Solheim et al.*, 1999]:

$$N_{cloud} = \frac{3}{2} \times \frac{W}{\rho_w} \times \mathrm{Re}\left(\frac{\varepsilon - 1}{\varepsilon + 2}\right) = 1.45 \times W \qquad (3.3.11)$$

where ρ_w is the density of liquid water ($\sim 1\ g \cdot cm^{-3}$), ε is the permittivity of water, and $\mathrm{Re}\left(\frac{\varepsilon - 1}{\varepsilon + 2}\right)$ is the real part of $\frac{\varepsilon - 1}{\varepsilon + 2}$. The permittivity of liquid water can be computed with a new double-Debye formulation [*Liebe et al.*, 1989]:

$$\varepsilon = \frac{\varepsilon_0 - \varepsilon_p}{1 + i\left(\frac{f}{f_p}\right)} + \frac{\varepsilon_0 - \varepsilon_s}{1 + i\left(\frac{f}{f_s}\right)} + \varepsilon_s \qquad (3.3.12)$$

with $k = \frac{300}{T + 273.15} - 1$, $\varepsilon_0 = 77.66 + 103.3k$, $\varepsilon_p = 5.48$, $\varepsilon_s = 3.51$,

$f_p = 20.09 - 142k + 293k^2$, and $f_s = 590 - 1500k$.

where T is the temperature in degrees Celsius, and f is the frequency in GHz.

Although the permittivity of liquid water ranges from 62-*i*39 ($T = -4°C$) to 72-*i*16 ($T = 30°C$) at a frequency of $f = 5.3GHz$, the approximation of Equation (3.3.12) can be within 1% for C-band microwave since the permittivity dominates both the numerator and the denominator.

From Equation (3.3.3) and (3.3.12), if the thickness of a cloud layer is L in km, the zenith path delay can be given by:

$$ZCD[in\ mm] = N_{cloud} L = 1.45 \times W \times L \qquad (3.3.13)$$

where ZCD represents the Zenith Cloud Delay in mm.

Table 3.3 Liquid water content in clouds (after *Hanssen* [1998])

Type of clouds	Liquid water content (g/m^3)	Zenith Delay Rate (mm/km)
Stratiform clouds	0.05-0.25	0.1-0.4
Small cumulus clouds	0.5	0.7
Cumulus congestus and cumulonimbus	0.5-2.0	0.7-3.1
Ice clouds	< 0.1	< 0.1

The maximum of the liquid water content is usually found at 2 km above the cloud base and then decreases towards the top of the cloud, which may be several kilometres higher [*Hall et al.*, 1996]. *Hanssen* [1998] listed the liquid water content of clouds, and their corresponding zenith delays (Table 3.3). According to *Hanssen* [1998; 2001], owing to their large spatial coverage and small delay rates, stratiform and ice clouds do not appear to cause large phase disturbances. However, the other

two types could result in significant phase delays as a result of their relatively limited horizontal size together with a large vertical thickness and liquid water content.

As a numerical example, a cumulonimbus with $W \approx 1 g/m^3$, assuming a cloud thickness of 3 km, results in a zenith cloud delay of 4.4 mm.

3.3.3 Tropospheric refractive delays (III): induced by aerosols and volcanic ash

An aerosol is a colloidal system in which the dispersed phase is composed of either solid or liquid particles, and in which the dispersion medium is some gas, usually air [*AMS*, 2000]. Based on an assumption that the condensation nucleus of the aerosol does not affect the permittivity of the aerosol droplet, the phase delay induced by aerosols is proportional to the density of water. *Solheim et al.* [1999] stated that aerosols induce path delays of less than 0.1 mm due to their limited vertical extent (hundreds of metres) and low normal concentrations ($\leq 1\ g/m^3$).

Volcanoes are of concern to DInSAR, so volcanic ash is also discussed here. Volcanic ash consists of airborne particulates including rock, mineral, and volcanic glass fragments. *Adams et al.* [1996] estimated the dielectric constants of volcanic ash and found that the reflectivity factor is $k = \left|\frac{\varepsilon - 1}{\varepsilon + 2}\right|^2 = 0.39$, regardless of composition or wavelength from 4 to 19 GHz. Taking into account the typical density of ash particles ($2.6 g/cm^3$), and using the Clausius-Mossotti equation, the refractivity can be given by:

$$N = \frac{3}{2}\frac{W}{\rho_w}\frac{\varepsilon_0 - 1}{\varepsilon_0 + 2} = 1.5 \cdot \frac{W}{2.6} \cdot 0.39^{\frac{1}{2}} = 0.36 \times W \qquad (3.3.14)$$

The amount of ash varies from 0.0002 to 0.04 g/m^3 , so the maximum zenith delay rate could be up to 0.01 mm/km [*Solheim et al.*, 1999].

3.3.4 Tropospheric scattering delays induced by rain

Forward scattering from large particles such as rain, hail, and snow may also induce phase delays [*Solheim et al.*, 1999]. This phenomenon is the aggregate effect of scattering by a population of particles which are encountered along the wave

propagation path. Since rain is the most disturbing phenomenon from the point of view of propagation, it is discussed here.

Raindrops with a radius up to 1 mm can legitimately be considered as spheres, which is generally reasonable for moderate rain. Beyond that, i.e. for heavy rain, they are better described as oblate spheroids [*Brussaard and Wa*tson, 1995]. The ratio of the horizontal to vertical axis r can be related approximately to the equivoluminal drop diameter D (in millimetres) by [*Preuppacher and Beard*, 1970]:

$$r = 1.03 - 0.062D \tag{3.3.15}$$

The raindrop size distribution is commonly assumed to have an exponential form [*Marshall and Palmer*, 1948]:

$$N(D) = N_0 e^{-\Lambda D} \tag{3.3.16}$$

where N_0 and Λ are experimentally determined constants, and $N(D)$ is the number concentration per cubic metre per size interval in millimetres. It is widely accepted that:

$$N_0 = 8\times10^3 m^{-3} mm^{-1} \tag{3.3.17}$$

$$\Lambda = 4.1 R^{-0.21} mm^{-1} \tag{3.3.18}$$

where R is the rain rate in mm/hr.

For microwaves at C-Band, the Rayleigh scattering approximation can be invoked to estimate the forward scattering amplitude[1] [*van de Hulst*, 1957]. In accordance with *Tranquilla and Al-Rizzo* [1994], the forward scattering amplitude can be calculated as:

$$f_h = \frac{k^2 D^3}{24} \frac{(\varepsilon_r - 1)}{1 + L_h(\varepsilon_r - 1)} \tag{3.3.19a}$$

$$f_v = \frac{k^2 D^3}{24} \frac{(\varepsilon_r - 1)}{1 + L_h(\varepsilon_r - 1)} \left[1 + \cos^2\beta \frac{(\varepsilon_r - 1)(L_h - L_v)}{1 + L_v(\varepsilon_r - 1)} \right] \tag{3.3.19b}$$

---

[1]: The assumption for Rayleigh scattering is that $2\pi r/\lambda \ll 1$, meaning that the radius r of the particle is much smaller than the wavelength λ. *Kerker* [1969] concluded that the upper limit of the radius could be taken to be $r = 0.05\lambda$, with an error of less than 4% for a single scatter.

where subscripts h and v indicate horizontal and vertical polarization respectively, $k = 2\pi/\lambda$ is the wave number, λ is the wavelength, ε_r is the relative permittivity of water drops, β is the inclined angle of the microwave with respect to the horizontal plane, L_h and L_v are geometrical factors given, for an oblate spheroidal scatter, by

$$L_h = \frac{1}{2}[1 - L_v] \tag{3.3.20a}$$

$$L_v = \frac{1}{e^2}\left[1 - \sqrt{\frac{1-e^2}{e^2}}arc(\sin e)\right] \tag{3.3.20b}$$

where e is the eccentricity of the particle. The relationship between e and r can be given by:

$$e = \sqrt{1 - r^2} \tag{3.3.21}$$

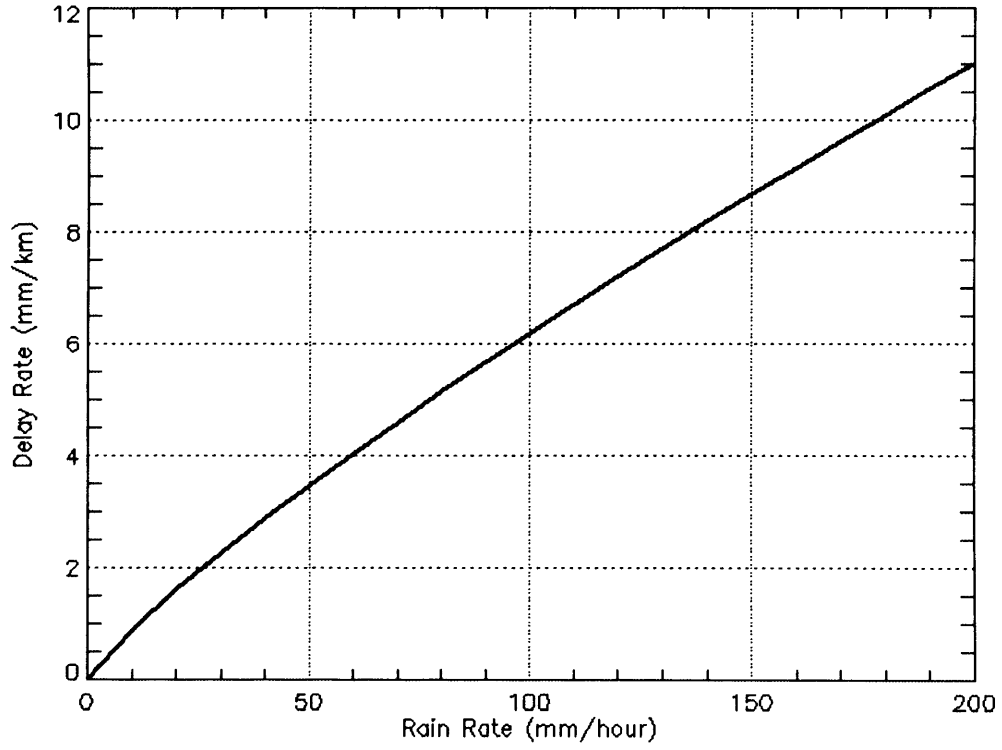

Figure 3.2 C-band Path delay due to forward scattering in rain.

Assuming that the propagation path is uniformly filled with scatterers, the phase delay due to rain can be written as:

$$ZRD_{h,v} = 10^{-3}\frac{2\pi}{k^2}\int \mathrm{Re}\left(f_{h,v}(D)\right)N(D)dD \qquad (3.3.22)$$

where $ZRD_{h,v}$ is the propagation phase in mm/km, $\mathrm{Re}(f_{h,v}(D))$ means the real part of the forward scattering amplitude for horizontal or vertical polarization.

As shown in Figure 3.2, the heavier the rain rate, the stronger the effects on the C-band signals. Light rain of a rate of 20 mm/hr causes a phase delay rate of 2 mm/km, whilst heavy rain of a rate of 200 mm/hr causes a delay rate of 11 mm/km.

3.3.5 Mapping functions and tropospheric slant delay

Maximum path delays induced by dry air and tropospheric constituents in the zenith direction are summarized in Table 3.4. In order to determine tropospheric delays at a certain elevation angle ξ, referred to as slant path delays, without the use of a ray-tracing method for the evaluation of Equation (3.3.2), which would require the knowledge of a three-dimensional refractivity field of the atmosphere, some assumptions need to be made to evaluate slant path delays. In particular, one can assume that the path delay in an arbitrary direction is related to the path delay at zenith, or zenith tropospheric delay, through the use of mapping functions [*Davis et al.*, 1985]:

$$STD = ZHD \times m_h(\xi) + ZWD \times m_v(\xi) \qquad (3.3.23)$$

where STD is the total slant delay, $m_h(\xi)$ and $m_w(\xi)$ are the respective mapping functions and ξ is the elevation angle at the ground station.

The simplest mapping function is $1/\sin(\xi)$, which is based on an assumption of a plane-parallel refractive medium, a poor approximation for low elevations owing to the curvature of the atmosphere. A number of more elaborate mapping functions have been proposed: e.g. *Davis et al.* [1985], *Niell* [1996; 2000], and *Ifadis and Savvaidis* [2001]. These functions use either site location and surface meteorology measurements or only site location and time of year. More recently, it has been shown that the use of *in situ* data from a numerical weather model can provide a significant improvement in the mapping functions [*Niell*, 2001; *Niell and Petrov*,

2003]. Taking into account the azimuthal asymmetry of the atmospheric delays, some previous studies have derived gradient mapping functions [*Davis et al.*, 1993; *MacMillian*, 1995; *Chen and Herring*, 1997; *Bar-Sever et al.*, 1998]. A full review of mapping functions is beyond the scope of this thesis. Instead, the widely used Niell Mapping Functions [*Niell,* 1996] are adopted in this thesis.

Table 3.4 Maximum zenith path delays induced by atmospheric constituents (adapted from *Solheim et al.* [1999])

Source	Diameter ($\leq mm$)	Surface Delay ($\leq mm/km$)	Scale Height (km)	Maximum Zenith Delays ($\leq mm$)
Dry air	10^{-7}	290	8	2320
High water vapour	10^{-7}	140	2.7	378
Low water vapour	10^{-7}	15	2.7	40
Cloud	0.1	8	5	40
Radiation fog	0.05	0.2	0.5	0.1
Advection fog	0.05	0.3	1	0.3
Haze	0.001	0.02	2	0.04
Drizzle	0.5	0.2	1.5	0.3
Steady rain[1]	4	2	3	6
Heavy rain[1]	6	11(C Band)	6	66
Hail[2]	20	5(C Band)	6	30
Snow[3]	15	1(C Band)	3	3
Aerosols	0.01	0.1	0.5	0.05
Sand	1	18	1	18
Volcanic ash	0.2	0.01	4	0.04

[1]: Steady rain corresponds to about 20 mm/hr, and heavy rain corresponds to 200 mm/hr

[2]: $r = 0.8$; $\rho = 0.9\, g \cdot cm^{-3}$; $\mathrm{Re}(\varepsilon_r) = 3.17$ [Tranquilla and Al-Rizzo, 1994]

[3]: $r = 0.8$; $\rho = 0.2\, g \cdot cm^{-3}$; $\mathrm{Re}(\varepsilon_r) = 1.33$ [Vivekanandan et al. 1993]

The Niell Hydrostatic mapping function depends on the latitude (φ) and height above sea level (H_s) of the site as well as the day of the year (DoY):

$$m_h(\xi)=\frac{1+\dfrac{a}{1+\dfrac{b}{1+c}}}{\sin\xi+\dfrac{a}{\sin\xi+\dfrac{b}{\sin\xi+c}}}+\Delta M_h(\xi)H_s \qquad (3.3.24a)$$

$$\Delta M_h(\xi)=\frac{1}{\sin\xi}-\frac{1+\dfrac{a_{ht}}{1+\dfrac{b_{ht}}{1+c_{ht}}}}{\sin\xi+\dfrac{a_{ht}}{\sin\xi+\dfrac{b_{ht}}{\sin\xi+c_{ht}}}} \qquad (3.3.24b)$$

$$g(\varphi_i,DoY)=g_{avg}(\varphi_i)+g_{amp}(\varphi_i)\cos\left[2\pi\frac{DoY-28}{365.25}\right] \qquad (3.3.24c)$$

where $a_{ht},b_{ht},c_{ht}=$constants , $g_{avg}(\varphi_i),g_{amp}(\varphi_i)=$constants for a given tabular latitude and a given coefficient $a,b,$ or c . The coefficients $a,b,$ and c can be obtained from Equation (3.3.24c) using the latitude and the day of the year.

The Niell wet mapping function depends only on the site latitude:

$$m_w(\xi)=\frac{1+\dfrac{a}{1+\dfrac{b}{1+c}}}{\sin\xi+\dfrac{a}{\sin\xi+\dfrac{b}{\sin\xi+c}}} \qquad (3.3.25)$$

where the coefficients $a,b,$ and c can be obtained using a linear interpolation in latitude.

At low elevation angles ξ, the mapping function increases sharply with view zenith angles θ, the complement value of elevation angles ($\theta=90^0-\xi$). The typical values are about 2 at 30° ($\theta=60^0$), 4 at 15° ($\theta=75^0$), 6 at 10° ($\theta=80^0$), and 10 at 5° ($\theta=85^0$). Fortunately, the mapping function increases slowly with the view angle θ at high elevation angles, and different mapping functions agree closely with each other, even the simplest mapping function $1/\sin\xi=1/\cos\theta$ (Designated CMF hereafter). Figure 3.3 shows the relative difference of CMF with respect to the Niell

Wet Mapping Function (NWMF) at the HERS IGS GPS station that is located at 50.90°N, 0.32°E, 50.9 m above mean sea level (AMSL) in East Sussex, UK. For a satellite with a view zenith angle of 23° (e.g. ERS-1/2), the relative difference is only up to 0.1%, indicating that even CMF can be employed at low view zenith angles (i.e. at high elevation angles), particularly in ERS SAR processing.

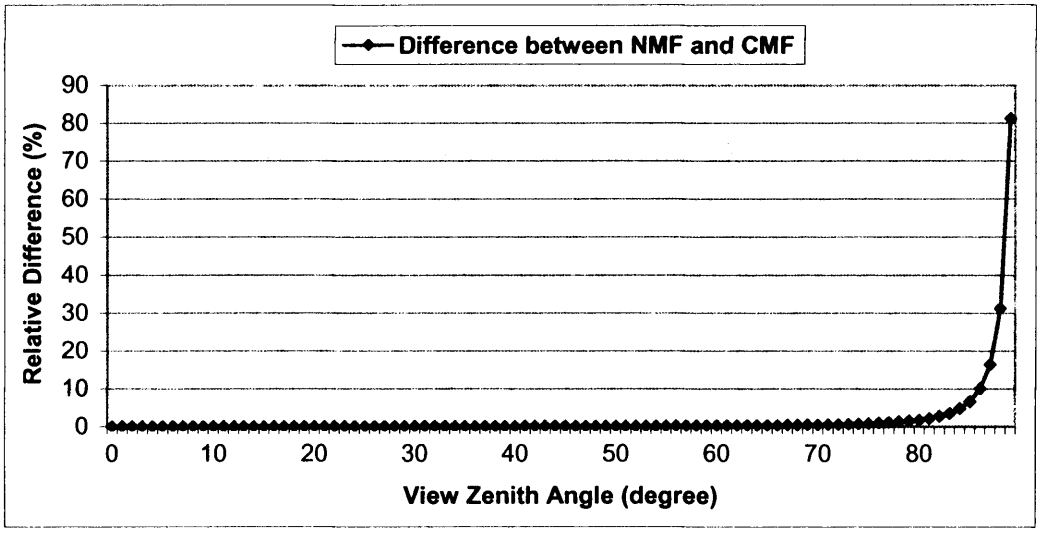

Figure 3.3 Relative differences between the Cosecant Mapping Function (CMF) and the Niell Wet Mapping Function (NWMF) at the HERS IGS GPS station at a latitude of 50.9°. The relative difference is 0.1% at a view zenith angle of 23°, 0.3% at 65° and 0.4% at 70°. The accuracy of the CMF with respect to the NWMF decreases to 1% at 77°.

Under "normal" conditions (i.e. with a surface temperature of 15°C, and a surface pressure of 1013.25 hPa), the Saastamoinen hydrostatic zenith delay is 2.31 m, and the Saastamoinen wet zenith delay is 0.17 m with a total zenith delay of 2.48 m over the HERS IGS GPS station. For the ERS-1/2 satellites with a nominal view zenith angle θ of 23° (i.e. $\xi = 67^0$), the hydrostatic slant delay is about 2.50 m, and the wet slant delay is about 0.19 m with a total slant delay of 2.69 m.

3.4 Microwave propagation delay due to the ionosphere

3.4.1 Variation of ionospheric free electron density

The ionosphere is characterized by the presence of free (negatively charged) electrons and positively charged atoms and molecules called ions. Since the

ionization is driven by the Sun's radiation, the state of the ionosphere is determined primarily by the intensity of solar activity. The electron density changes by one to two orders of magnitude between day and night, with a peak around 2 pm local time, and a nadir at mid-night. As one of the most notable phenomena characterizing solar activity, sunspots appear periodically in groups on the solar surface, and their number influences the electron density. Figure 3.4 shows the progression of the current solar cycle (no. 23). The last so-called solar minimum was in October 1996, and the recent solar maximum consisted of two maxima (the first and largest, in July 2000, and the second in August 2001). The electron density also shows a large dependence on latitude in a geomagnetic reference frame, and the size and variability of the electron density are usually relatively low at geomagnetic mid-latitude regions (about 20°~70° on both sides of the geomagnetic system).

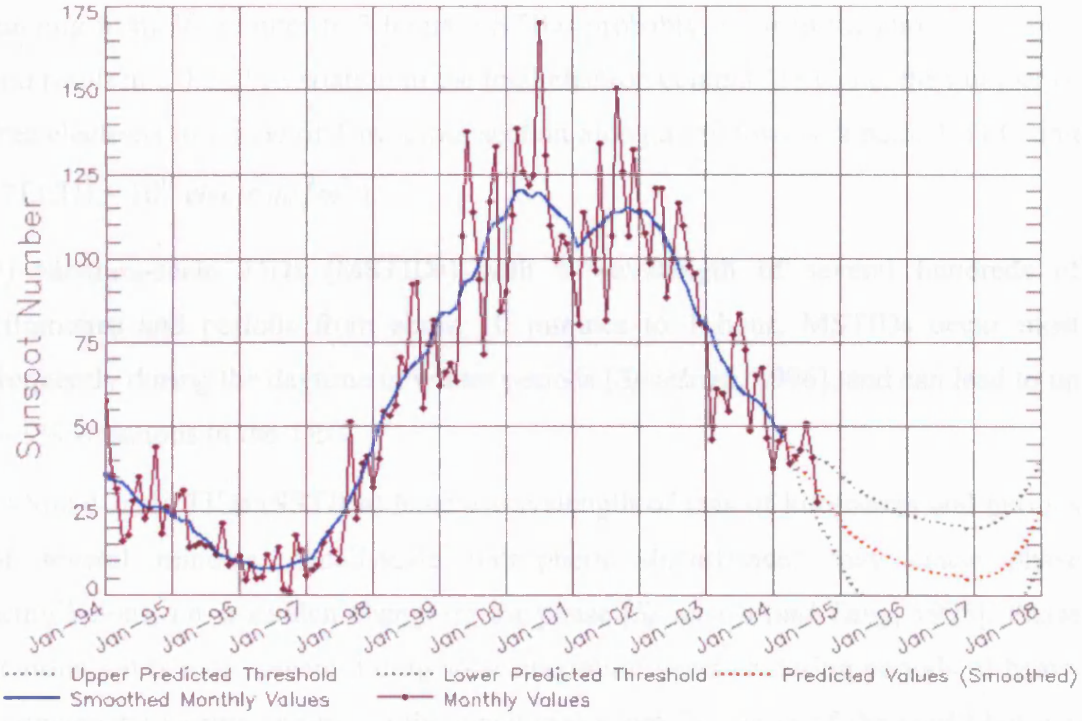

Figure 3.4 Progression of solar cycle 23: measured and predicted sunspot numbers with data till 30 September 2004 (from NOAA Space Environment Center (SEC), USA[1])

The ionosphere can be divided into a number of layers, historically labelled D, E, F1 and F2, which have different characteristics (Table 3.2). In the D layer the

[1]: http://www.sec.noaa.gov/SolarCycle/, 3 November 2004.

atmosphere is still dense, and atoms (and/or molecules) that have been ionized recombine quickly. Therefore, the D layer is only weakly ionized, and the level of ionization is directly related to solar radiation that begins at sunrise, disappears at sunset, and generally varies with the sun's elevation angle. The E layer has a little more ionization. Small patches of extremely dense ionization can often be observed within the E layer, which is known as 'sporadic E (Es)'. In the F1 and F2 layers, the electrons and ions recombine slowly due to low pressure. The peak electron density occurs in the F2 layer.

So-called Travelling Ionospheric Disturbances (TIDs) may cause variation in the electron density. A TID is a ripple or wave in the electron density that propagates horizontally, and three types of TIDs can be discriminated [*Schaer*, 1999]:

1) Large-scale TIDs (LSTIDs) with a wavelength larger than 1000 km and periods ranging from 30 minutes to 3 hours. LSTIDs probably occur in the auroral regions, and result in a 0.5-5% variation in the total electron content (TEC, i.e. the number of free electrons in a tube of 1 m^2 cross section along a microwave's path; 1 TEC unit (TECU) = 10^{16} $electrons/m^2$).

2) Medium-scale TIDs (MSTIDs) with a wavelength of several hundreds of kilometres and periods from about 10 minutes to 1 hour. MSTIDs occur most frequently during the daytime in winter periods [*Spoelstra*, 1996], and can lead to up to 8% variations in the TEC.

3) Small-scale TIDs (SSTIDs) have a wavelength of tens of kilometres and periods of several minutes. Small-scale ionospheric disturbances may cause phase scintillations, i.e. a sudden change in the phase [*Spoelstra and Yang*, 1995]. Phase scintillation is more severe during solar maximum years or during periods of heavy geomagnetic storms, mainly in the equatorial anomaly region of the world but can also occur in the auroral regions. In mid-latitude regions however, the occurrence of ionospheric scintillation is extremely rare: it happens only once or twice during an 11-year solar cycle [*Klobuchar and Doherty*, 1998].

3.4.2 Zenith phase advance due to the ionosphere

The ionosphere affects radio propagation from extremely low frequencies (<3 kHz) to super high frequencies (30 GHz). In contrast to the neutral atmosphere, the

ionosphere is dispersive. That is, the refractive index is a function of the frequency of the signal.

To examine the propagation effects on microwave signals travelling through the ionosphere, the refractive index of the medium must be specified. To an accuracy of better than 1%, the phase refractive index of the ionosphere can be given with a first-order form as follows [*Klobuchar*, 1996]:

$$\begin{aligned} n &\approx 1-\frac{e^2}{8\pi^2 m_e \varepsilon_0}\frac{N_e}{f^2} \\ &\approx 1-40.3\frac{N_e}{f^2} \end{aligned} \qquad (3.4.1)$$

where N_e is the electron density in m^{-3}, e is elementary charge, m_e is the mass of an electron , ε_0 is the permittivity of a vacuum, and f is the frequency of the microwave signal, in Hz.

From Equation (3.4.1), it is clear that the phase refractive index in the ionosphere is less than unity, so there is no delay but an advance in the zenith direction relative to that in a vacuum. Therefore, the phase advance in the zenith direction can be given by:

$$\begin{aligned} ZPA &= -\frac{40.3}{f^2}\int_H N_e \\ &= -\frac{40.3}{f^2} VTEC \end{aligned} \qquad (3.4.2)$$

where ZPA is zenith phase advance (or 'delay'), and VTEC is the vertical total electron content in $electrons/m^2$, expressed as the number of free electrons in a vertical column with 1 m^2 cross section along a microwave ray path. It is clear that, to first-order, phase advance depends on the square of the frequency, so ionospheric effects on InSAR measurements should be ~17 times less at C-band ($f_C = 5.29\ GHz$ for ERS-1/2) than at L-band ($f_L = 1.275\ GHz$ for JERS-1).

3.4.3 Mapping functions and slant phase advance

TEC varies also with the view zenith angle θ: the higher the view zenith angle, the longer the path length through the ionosphere and the higher the TEC. Similar to

tropospheric delays, a mapping function (or obliquity factor) is usually employed to relate the oblique path TEC (OTEC) to the VTEC. For simplicity, two assumptions are made as follows [*Misra and Enge*, 2001]: 1) The ionosphere may be considered as a thin shell surrounding the Earth; 2) There are no lateral electron gradients. As shown in Figure 3.5, the zenith angle ζ at the Earth's surface is slightly greater than the zenith angle ζ' at the intersection of the line of sight with the spherical shell at height h_I. Based on the sine law, the ionospheric obliquity factor $m_I(\varepsilon)$ for zenith angle ζ can be written as [*Misra and Enge*, 2001]:

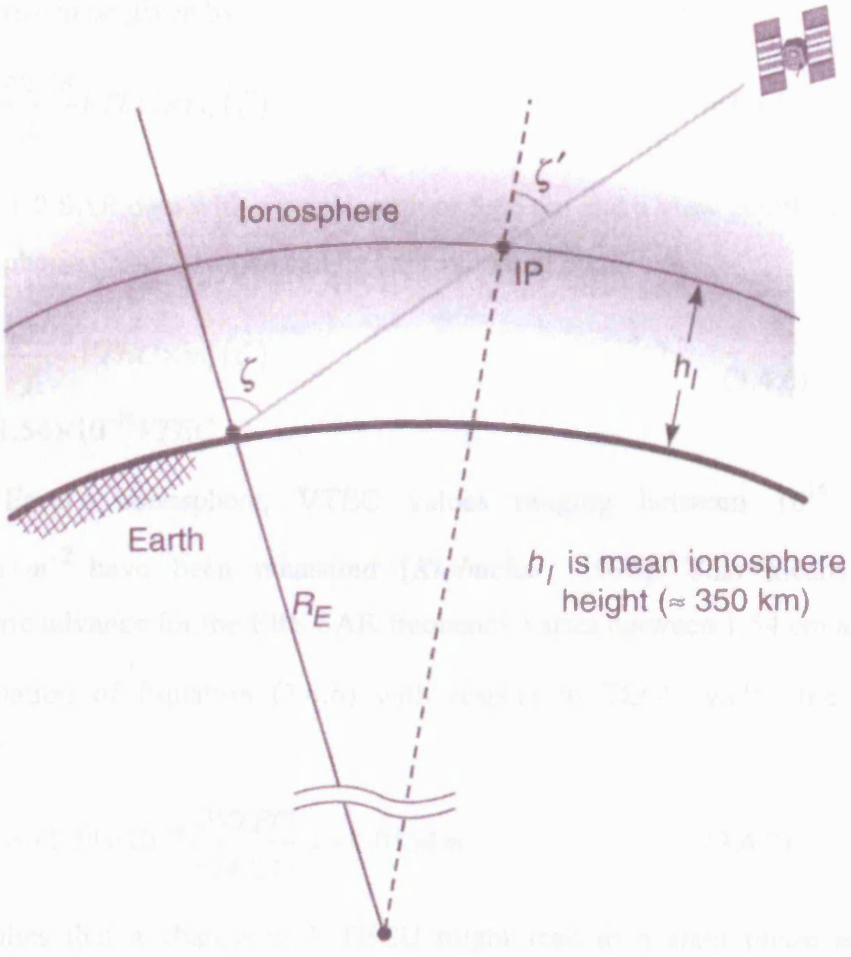

Figure 3.5 Schematic geometry of propagation path of a signal through the ionosphere (From *Misra and Enge* [2001]).

$$m_I(\zeta) = \left[1 - \left(\frac{R_E \sin\zeta}{R_E + h_I}\right)^2\right]^{-1/2} \tag{3.4.3}$$

where R_E is the average radius of the Earth, and h_I is the mean ionosphere height ($h_I \approx 350\,km$). For ERS-1/2 SAR data with an incidence angle of 23° (this means $\zeta \approx 23°$), using $R_E = 6371\,km$ and $h_I = 350\,km$, the mapping function value is $m_I(23°) = 1.07657$.

Therefore, the relationship between OTEC and VTEC can be given by:

$$OTEC = VTEC \times m_I(\zeta) \tag{3.4.4}$$

From Equations (3.4.2) and (3.4.4), the slant phase advance (SPA) due to the ionosphere can be given by:

$$SPA = -\frac{40.28}{f^2} VTEC \times m_I(\zeta) \tag{3.4.5}$$

For ERS-1/2 SAR data with a wavelength of 5.66 cm and a view zenith angle of 23°, the ionospheric phase advance can be approximated by:

$$\begin{aligned} SPA &= -\frac{40.28}{f^2} VTEC \times m_I(\zeta) \\ &= -1.54 \times 10^{-18} VTEC \end{aligned} \tag{3.4.6}$$

In the Earth's ionosphere, VTEC values ranging between 10^{16} and 10^{19} $electrons \cdot m^{-2}$ have been measured [*Klobuchar*, 1996]. This means that the ionospheric advance for the ERS SAR frequency varies between 1.54 cm and 15.4 m.

Differentiation of Equation (3.4.6) with respect to TECU yields the following equation:

$$\frac{\partial SPA}{\partial TECU} = -1.54 \times 10^{-18} \frac{\partial VTEC}{\partial TECU} = -0.0154\,m \tag{3.4.7}$$

This implies that a change in 1 TECU might lead to a slant phase advance of 1.54 cm, so typical diurnal changes of over 12 TECU might result in a SPA variation of 18.48 cm. It should be noted here that, as far as InSAR is concerned, an interferogram is the difference of two SAR images acquired on different days, but at the same local time. Therefore, a very similar SPA impacts on both images, e.g. the diurnal TEC variation, will be cancelled out in the interferogram.

3.4.4 Distinguishing between tropospheric and ionospheric effects

Hanssen [1998] demonstrated very well the relationship between tropospheric and ionospheric effects. Since a phase advance in the master image gives the same result as a phase delay in the slave image, it is impossible to distinguish between phase delay and phase advance based solely on interferometric data for a single interferometric pair. Fortunately, Pair-wise logic, i.e. different interferometric combinations of images, can be utilized to identify such errors (see Section 3.5).

For a local area, the effects of reduced water vapour density appear similar to those of a relative advance of phase. In this case, it is impossible to identify the type of error without any other additional information. So far, several techniques have been developed to measure the ionosphere [e.g. *Schaer*, 1999]. However, the spatial resolution of all available products cannot satisfy the needs of InSAR, because all the ionospheric maps available now are only at a large scale, e.g. 2-hour resolution with 2.5 degrees in latitude by 5 degrees in longitude for the IGS ionospheric products [1], 15-minute resolution with 1°× 1° two-dimensional grids over the Continental US for the US Total Electron Content (US-TEC) product[2].

At present, it is hard to distinguish ionospheric effects from tropospheric ones. Taking into account experience with dual frequency GPS, if dual frequency SAR were available it would have a significant impact on this field. Alternatively, for a SAR system with a wide bandwidth of 50 MHz or more (note: only 15.55 MHz available for ERS and 14.00 MHz for ENVISAT), a split radar bandwidth technique can be used to minimise ionospheric effects [*Wadge and Parsons*, 2003]: 1) Raw data is bandpass filtered into two separate bands with different centre frequencies; 2) Two interferograms are produced from two filtered SAR images with different centre frequencies; 3) The ionospheric phase advance is estimated from the 'recovered' phase differences, assuming the differential integer ambiguities of phase observations can be determined directly from the spatial correlation of the signals of phase differences; 4) Using the estimated phase advance, the ionospheric effects on phase observations can be reduced. It should be noted that, in order to increase the

[1]: http://igscb.jpl.nasa.gov/components/prods.html, 9 November 2004.
[2]: http://www.sec.noaa.gov/ustec/USTEC_PDD.pdf, 9 November 2004.

sensitivity for dispersive estimation of ionospheric phase advance, a bandwidth as wide as possible (up to 80 MHz) is recommended [*Wadge and Parsons*, 2003].

3.4.5 Discussion

On the one hand, from the theoretical analysis in this section, it is clear that: 1) The occurrence of phase scintillation due to small-scale ionospheric disturbances is limited in the equatorial and auroral regions, and extremely rare in mid-latitude regions; 2) Ionospheric effects on InSAR measurements should be ~17 times less at C-band than at L-band; 3) The diurnal TEC variation can be effectively cancelled out in interferograms. On the other hand, knowledge of the spatial characteristics of the ionosphere within spatial scales of less than 100 km is very limited. In other words, there is no ionospheric map having the spatial resolution needed for InSAR. Therefore, like *Hanssen* [2001], an assumption is made in this thesis that ionospheric effects will not significantly affect phase variations in SAR images, although they may lead to long wavelength gradients which can be removed using the baseline refinement technique (see Section 2.3.3).

3.5 Review of atmospheric correction approaches

In this section, a brief review of atmospheric correction approaches, which have been proposed to reduce atmospheric effects (particularly water vapour effects) from SAR interferograms in the last decade, is given.

1. Pair-wise logic or linear combination: *Massonnet and Feigl* [1995] used a pair-wise logic to discriminate atmospheric perturbations from other signatures, in which at least two interferograms that have a common SAR image are required. A shortcoming of this method is that it cannot give an exact measure of the atmospheric effects [*Li et al.*, 2003]. If there is an atmospheric anomaly in the common SAR image, it will contaminate the signal in both interferograms. Therefore, summing or subtracting these two interferograms would result in a complete removal of the atmospheric anomalies [*Hanssen*, 2001]. This approach is usually titled as a linear combination. The disadvantages are: 1) two interferograms with a common SAR image with atmospheric effects are not always available; 2) in order to extract the deformation, the deformation rate has be assumed to be constant during the acquisitions of these SAR images.

2. Stacking: Temporal averaging of N independent interferograms reduces the spatially uncorrelated noise by $1/\sqrt{N}$ [*Zebker et al.*, 1997; *Sandwell and Price*, 1997; *Williams et al.*, 1998]. *Ferretti et al.* [1999] developed a weighted averaging method to construct DEMs taking into account the normal baseline value, the coherence level, and the phase distortion due to atmospheric effects. *Emardson et al.* [2003] have calculated the water vapour spatial variation using zenith atmospheric delays from GPS data from the Southern California Integrated GPS Network (SCIGN). Using these results, they showed the possibility of calculating the number and duration of interferograms required to achieve a desired sensitivity to deformation rate at a given length scale for a given orbit revisit time and image archive duration. Like the linear combination method, the stacking method is based on an assumption that the deformation is constant and is not appropriate for areas with a nonlinear deformation rate. On the other hand, this method differs from the linear combination method in that it requires independent interferograms.

3. Modelling of atmospheric delays based on ground meteorological data: Based on the surface meteorological measurements, a number of different models to determine zenith wet delays (ZWD) have been proposed. The most common and simplest models are based on the assumption of the decrease in temperature with height and the relation between total pressure and water vapour partial pressure [e.g. *Saastamoinen*, 1972]. Some improved models take into account seasons, latitudes and type of climates [e.g. *Baby et al.*, 1988]. More complex models estimate humidity and temperature profiles with statistical regression, and then use numerical integration method to compute the refractivity [e.g. *Askne and Nordius*, 1987]. *Delacourt et al.* [1998] reported that the use of the tropospheric correction model by *Baby et al.* [1988] could account for 2 fringes in ERS interferograms, and that the accuracy of the interferograms was about ±1 fringe after correction. *Bonforte et al.* [2001] demonstrated general agreement between GPS-derived zenith path delays and those estimated from the Saastamoinen model and ground meteorological observations. However, there are two major disadvantages of this method: 1) ZWD can only be derived with an accuracy varying from about 2 cm to 5 cm using surface meteorological measurements [*Baby et al.*, 1988]; 2) It is obvious that such models

can only remove the "stratification effect" and not the "turbulent effect" [*Webley*, 2003].

4. Numerical Atmospheric Model: *Shimada* [2000] evaluated the applications of the global objective analysis data (GANAL) to correcting JERS-1 interferograms, and found that the accuracy of the observed surface deformation improved from 4.04 cm before correction to 2.04 cm after correction. GANAL is a numerical dataset in the Japanese Meteorological Agency, which express the 3-dimentsional structure of the lower atmosphere in terms of temperature, pressure, wind vector, and water vapour's partial pressure with a temporal resolution of 6 hours and a spatial resolution of 1.25 degrees (latitude/longitude). The European Centre for Medium-range Weather Forecasts (ECMWF) operational model with a temporal resolution of 12 hours and a spatial resolution of 2.5 degrees was found to have a comparable accuracy to GANAL for correcting JERS-1 interferograms, taking into account its resolutions [*Shimada et al.*, 2001]. Regional and global numerical models are usually too coarse to represent the km-scale features that might affect the water vapour field over a mountain. *Wadge et al.* [2002] used a local-scale numerical dynamic model (NH3D) to simulate the path delays due to water vapour over Mt. Etna, and found that the NH3D delays were in general agreement with the ERS-2 interferogram and GPS estimates. This NH3D model had a horizontal spatial resolution of 1.7 km, which was a reasonable compromise between topographic representation and computational demands [*Webley*, 2003]. In the case of InSAR atmospheric correction, the most outstanding advantage of the NH3D model is that it is relatively independent of the availability of surface meteorological or other measurements, so that it could be applied widely if its accuracy was good enough. Unfortunately, the NH3D model is currently sensitive to the initial data [*Webley*, 2003].

5. Stochastic filtering: *Crosetto et al.* [2002] developed a stochastic filtering procedure to reduce atmospheric effects on SAR unwrapped phases. Firstly, stable areas need to be identified in the vicinity of the deformation area under consideration using *a priori* information; secondly, based on an autocovariance function (AF), a quantitative analysis is performed to extract the atmospheric signal over the stable areas; thirdly, taking advantage of the correlation characteristics of

AF, the atmospheric effects can be predicted over the deformation area; finally, subtracting the predicted atmospheric effects from the differential phases is expected to reduce the atmospheric effects. A validation over Manresa, Spain showed that the atmospheric effects on the corrected phase decreased to 30% or even less of the original phase [*Crosetto et al.*, 2002]. This method is limited by three factors: Firstly, it can only be applied to small-scale deformation; Secondly, it is based on the availability of stable areas, which might be difficult to find; Thirdly, a possible subsidence inside the supposed stable areas may contaminate the results.

6. Permanent scatterers technique: Permanent scatterers (PS) technique has been developed to detect isolated coherent pixels and estimate (and remove) the atmospheric effects at the expense of a large number of required images (at least 25-30 images) and a sparse pixel-by-pixel based evaluation [*Ferretti et al.*, 2000, 2001]. The phase contribution of topography, deformation, and atmosphere can be estimated by carefully exploiting their different time-space behaviour. Among them, the contribution of atmospheric effects (atmospheric phase screen, APS) is independent of baseline, uncorrelated in time (>1 day), but strongly spatially correlated within each individual interferogram. The atmospheric effects can either be approximated as a linear phase ramp both in range and in azimuth direction [*Ferretti et al.*, 2001] or be handled using spatio-temporal filtering techniques [*Ferretti et al.*, 2000]. The former can only process small areas (less than 5 × 5 km), since the planar approximation becomes less accurate for larger areas. The latter is more flexible but more complicated. *Ferretti et al.* [2000] showed that the RMS values of the atmospheric effects on 41 ERS images over Pomona, California varied from 0.25-1.35 radians. It should be noted that the estimated APS is actually the sum of two-phase contributions: atmospheric effects and orbital error terms [*Ferretti et al.*, 2000]. However, the latter do not change the low wave number character of the atmospheric signal since it only corresponds to low-order phase polynomials [*Colesanti et al.*, 2003]. As mentioned previously, a shortcoming of the PS technique is that a larger number of SAR images, at least 25-30 images, are required to get reliable results. In addition, the performance of the PS technique is highly dependent on the number and the distribution of reliable permanent scatters in the specific deformation area.

7. The use of GPS measurements: Keeping in mind the fact that Global Positioning System (GPS) measurements can be used to provide a high accuracy 3D position, to derive water vapour products, and to map deformation, it will be advantageous to integrate GPS with InSAR measurements: 1) They can be used to validate each other; 2) GPS water vapour products can be applied to reduce atmospheric effects in InSAR measurements; and 3) GPS positioning results can be used as constraints to refine baselines in InSAR processing. The notion of integrating InSAR and GPS was first suggested by Bock and Williams in 1997 [*Bock and Williams*, 1997], and developed as Double Interpolation and Double Prediction (DIDP) by *Ge et al.* [2000]. *Williams et al.* [1998] performed a simulation using the Southern California Integrated GPS Network (SCIGN) to assess the possibility of reducing atmospheric effects on interferograms using GPS data. They demonstrated that atmospheric effects conform to a power law and considered that a reduction in power law noise can be achieved by removing the long-wavelength effects and leaving the higher-frequency, lower power components. Therefore, it is possible to use tropospheric delays estimated from a GPS network to reduce atmospheric effects on SAR interferograms with an appropriate spatial interpolator. They also suggested that the stacking method and the calibration method, with independent data including GPS, are complementary and these two methods should be used simultaneously. On the other hand, the possibility of correction of InSAR measurements is dependent on the spatial distribution of GPS receivers. Since current GPS networks are not optimal for InSAR purposes and GPS-derived zenith delay represents a 5-minute (or else) average along the paths of 4–12 (or more) GPS satellites as they orbit the Earth, which is different from the the atmospheric contribution to the phase observation in interferograms, it will not be possible to remove artefacts with smaller spatial scales than the GPS data is able to determine [*Hanssen*, 2001]. *Bonforte et al.* [2001] suggested that GPS measurements and/or ground-based meteorological data should be used whenever available, and both data sets could be integrated. A comparison between GPS-derived zenith delays estimated from a 14 station continuous GPS (CGPS) network and InSAR measurements was performed over Mt. Etna [*Wadge et al.*, 2002]. The result showed that the equivalent values for InSAR-GPS gave an RMS value of 19 mm with a mean of +12 mm. With 16 GPS stations over Houston, USA, *Buckley et al.* [2003] applied an atmospheric correction to a tandem

interferogram. Although the reduction is marginal, they demonstrated a possible utility in using GPS-derived zenith delays for a priori interferogram atmospheric assessment.

8. The use of space-based radiometer measurement: Space-based monitoring is the only effective way to obtain water vapour distribution on a global basis with relatively high spatial resolution. The Medium Resolution Imaging Spectrometer (MERIS) and the Advanced Synthetic Aperture Radar (ASAR) are on board the ESA ENVISAT satellite and these two datasets can be acquired simultaneously during daytime. This allows the possibility of using the MERIS water vapour product to reduce water vapour effects on ASAR measurements. In addition, the NASA Moderate Resolution Imaging Spectroradiometer (MODIS) instrument is a key instrument on the Terra and Aqua satellites, launched on 18 December 1999 and 4 May 2002, respectively. The Terra platform flies in a near-polar sun-synchronous orbit while ERS-2 is in a sun-synchronous polar orbit, and both have a descending node across the equator at 10:30 am local time. This indicates that there is also a possibility of applying MODIS water vapour data to ERS-2 SAR measurements. A shortcoming is that this method works only in the daytime under cloud free conditions, since both MODIS and MERIS near IR water vapour retrieval algorithms rely on observations of water vapour absorption of near IR solar radiation reflected by land, water surfaces and clouds (Sections 4.3 and 4.4). Moreover, prior to this study, little has been done on the application of such datasets to reducing atmospheric effects on InSAR measurements.

3.6 Conclusions

This chapter gives an overview of atmospheric effects on repeat-pass InSAR. It is shown that tropospheric effect (particularly the part due to water vapour) is a major limitation for the application of repeat-pass InSAR. A brief review of atmospheric correction approaches (particularly water vapour correction) is also given. This thesis focuses on the possibility of using GPS, MODIS and MERIS water vapour products for InSAR correction, and these three techniques will be introduced in Chapter 4.

Chapter 4

Radiosonde, GPS, MODIS, MERIS and precipitable water vapour

As described in Chapter 3, atmospheric water vapour is one of the major error sources in repeat-pass InSAR applications. In this Chapter, the main issues involved in deriving precipitable water vapour (PWV) from GPS, RS, MODIS, and MERIS measurements are presented. Error sources for each method are also discussed.

Meteorologists have defined several different terms to express the amount of atmospheric water vapour. One of the most commonly used is precipitable water vapour (PWV). PWV is defined as the total atmospheric water vapour contained in a vertical column of unit cross-sectional area extending between any two specified levels, commonly expressed in terms of the height to which that water substance would stand if completely condensed and collected in a vessel of the same unit cross-section [*AMS*, 2000]. PWV is also referred to as the total column water vapour [*Ferrare et al.*, 2002]. Currently, measurements of PWV can be obtained in a number of ways including *in situ* measurements and remote sensing from satellites [*Mockler*, 1995; *Chaboureau et al.*, 1998]. The objective of this chapter is to discuss the derivation of PWV from several different instruments, viz. radiosondes (RS), Global Positioning System (GPS), the Moderate Resolution Imaging Spectroradiometer (MODIS), and the Medium Resolution Imaging Spectrometer (MERIS).

The radiosonde network has long been the primary *in situ* observing system for monitoring atmospheric water vapour. Radiosondes provide vertical profiles of meteorological variables such as pressure, temperature, and relative humidity. Sometimes, wind information can be obtained as well. However, the use of radiosondes is restricted by their low temporal resolution, high operational costs, decreasing sensor performance in cold dry conditions, and their poor coverage over oceans and in the Southern Hemisphere. Usually, radiosondes are expected to produce PWV with an uncertainty of a few millimetres, which is considered to be the accuracy standard of PWV for meteorologists [*Niell et al.*, 2001].

GPS is an increasingly operational tool for measuring precipitable water vapour, and it has gained a lot of attention in the meteorological community. GPS signals are delayed when propagating through the troposphere. The total tropospheric delay can be divided into a hydrostatic term caused by the dry gases in the atmosphere and a wet term caused by the refractivity due to water vapour [*Davis et al.*, 1985; c.f. Chapter 3]. GPS measurements provide estimates of the zenith total delay (ZTD) using mapping functions. The Zenith Hydrostatic Delay (ZHD) can then be calculated given the local surface pressure. ZHD subtracted from ZTD yields the Zenith Wet Delay (ZWD) from which PWV can be inferred [*Bevis et al.*, 1992]. The primary advantage of GPS is that it makes continuous measurements possible. Furthermore, the spatial density of the current Continuous GPS (CGPS) network is much higher than that of the radiosonde network, and its capital and operational costs are much lower than for RS. The potential for GPS to detect PWV has been well demonstrated. Agreement at the level of 1-2 mm of PWV between GPS, radiosondes and microwave water vapour radiometers (WVR) has been reported in previous research [*Emardson et al.*, 2000; *Niell et al.*, 2001].

Space-based monitoring is the only effective way to assess water vapour levels on a global basis, and various missions have been implemented to monitor water vapour (e.g. Television and Infrared Operational Satellite (TIROS) Operational Vertical Sounder (TOVS), Special Sensor Microwave/Imager (SSM/I), etc.) [*Chaboureau et al.*, 1998; *Randel et al.*, 1996]. More recently, atmospheric water vapour has been measured with the one MERIS (Medium Resolution Imaging Spectrometer), and the two NASA MODIS (Moderate Resolution Imaging Spectroradiometer) instruments. The first MODIS was launched on 18 December 1999 on board the Terra Platform and the second on 4 May 2002 on board the Aqua platform. The MODIS near Infrared (IR) water vapour products (MOD_05 from the Terra platform and MYD_05 from the Aqua platform) consist of daytime only total column atmospheric water vapour (designated MODIS-PWV hereafter). The technique implemented for the MODIS water vapour retrievals uses ratios of radiance from water vapour absorbing channels centred near 0.905, 0.936, and 0.94 μm with atmospheric window channels at 0.865 and 1.24 μm. MODIS-PWV is claimed to be determined with an accuracy of 5-10% [*Gao and Kaufman*, 2003]. Errors will be greater for retrievals from data collected over dark surfaces or under hazy conditions (with

visibilities less than 10 km) [*Gao and Kaufman*, 2003]. MERIS was launched on 23 March 2002 on board the ESA environmental research satellite ENVISAT. Although the primary mission of the MERIS instrument is to make a major contribution to scientific projects that seek to understand the role of the oceans and ocean productivity in the climate system, MERIS also permits new investigations of the atmosphere, such as water vapour, clouds and aerosols. The ratio of reflected radiances at 0.89 and 0.90 μm has been used as an indicator for the total amount of atmospheric water vapour in the MERIS sensor. The theoretical accuracy of the algorithm is 1.6 mm under cloud free conditions over land [*Bennartz and Fischer*, 2001] and between 1 mm and 3 mm above clouds [*Albert et al.*, 2001]. The accuracy of estimation of the total amount of atmospheric water vapour is expected to be less than 20% over water surfaces [*Fischer and Bennartz*, 1997].

4.1 Radiosondes

A radiosonde is a lighter than air balloon filled with helium, having radio communication capability that can be launched, manually or automatically, to a fixed schedule or on demand. Measurements of pressure, temperature and humidity are made and wind data may be obtained by tracking the position of the balloon.

Data from two types of radiosondes, Vaisala RS90 and Vaisala RS80, were used in this thesis, and the Atmospheric Radiation Measurement (ARM) Southern Great Plains (SGP) and Herstmonceux (HERS) sites are given as examples in the next section.

4.1.1 The ARM SGP and HERS sites

The ARM SGP site is located in northern Oklahoma (36.62°N, 97.50°W, 317.0 m above mean sea level (AMSL), Table 4.1), and Vaisala RS90 radiosondes have been launched four times daily at 05:30, 11:30, 17:30, and 23:30 Greenwich Mean Time (GMT) since 1 August 2001. RS90 relative humidity resolution is quoted as 1%, reproducibility as 2%, and repeatability as 2%, with a 5% uncertainty in soundings [*Vaisala*, 2002b]. The raw data sent from the radiosonde are processed with standard

ARM ground-station software, and quality controlled (i.e. filtered, edited and interpolated) before being output with 2-second resolution[1].

The Herstmonceux (HERS) site is located in East Sussex, UK (50.90°N, 0.32°E, 50.9 m AMSL, Table 4.1). Vaisala RS80-H radiosondes have been launched twice daily at 23:15 and 11:15 GMT since the beginning of December of 2001, and extra launches sometimes occur at 05:15 and 17:15 GMT when greater detail of the atmospheric conditions overhead are needed (J. Jones, private communication, 2003). Measured range and resolution for RS80 relative humidity are the same as for the RS90 but the reproducibility is quoted as <3% [*Vaisala*, 2002]. A general problem with Vaisala RS80 radiosondes is that they have been found to exhibit a dry bias, which results from contamination of the humidity sensor during storage and leads to the reported relative humidity values being lower than the actual ones [*Liljegren et al.*, 1999; *Wang*, 2002]. Vaisala changed the desiccant type in the package from clay to a mixture of active charcoal and silica gel in September 1998 and also introduced a new type of protective shield over the sensor boom in May 2000 for RS80 radiosondes [*Wang et al.*, 2002]. *Wang* [2002] evaluated the performance of the new sensor boom cover and found that RS80-H radiosondes with a sensor boom cover are free of contamination. Therefore, no contamination correction was required but a modelled ground check correction has been used to calibrate the radiosonde humidity sensors for the RS data since May 2000 at the HERS site (J. Jones, private communication, 2003).

4.1.2 Integrated Water Vapour (IWV)

Measurements including pressure, temperature and relative humidity profiles above a radiosonde station can be used to calculate precipitable water vapour. The integrated water vapour (IWV) along the path of the sounding balloon can be calculated by [*Bevis et al.*, 1992]:

$$IWV = \int \rho_v dz \qquad (4.1.1)$$

where ρ_v is the density of water vapour in kg/m^3. According to the gas state equation, the water vapour density (ρ_v) can be calculated by:

[1]: http://www.arm.gov/instruments/static/bbss.stm, 1 November 2004.

$$\rho_v = \frac{e_w}{R_v \cdot T} \tag{4.1.2}$$

where $R_v = 461.495 J \cdot K^{-1} \cdot kg^{-1}$ is the specific gas constant for water vapour, and e_w is the partial pressure of water vapour which can be obtained from the relative humidity using the following formula recommended by the World Meteorological Organization in its Technical Note No. 8 [*Godson*, 1955]:

$$e_w = RH \cdot \exp\left(-37.2465 + 0.213166 \cdot T - 2.56908 \cdot 10^{-4} \cdot T^2\right) \tag{4.1.3}$$

where RH is the relative humidity in percentage, and T is the absolute temperature in degrees Kelvin.

In practice, the profiles from radiosondes are discrete series of temperature and relative humidity at different heights, h, which separates the atmosphere into many layers. If the water vapour density is assumed to vary linearly in each layer, Equation (4.1.1) can be approximated by

$$IWV = \frac{1}{2}\sum\left(\rho_{v,i+1} + \rho_{v,i}\right) \cdot \left(h_{i+1} - h_i\right) \tag{4.1.4}$$

where the subscripts i and $i+1$ denote the bottom and the top of each layer. Obviously, the more observations there are of the profiles of temperature and water vapour pressure, the thinner the layer thicknesses, the better the approximation that can be made using the above expression [*Feng et al.*, 2001].

4.1.3 Zenith Wet Delay (ZWD)

As mentioned in Section 3.3, ZWD can be expressed as:

$$ZWD = \int [n-1] dh = 10^{-6} \int N_w dh \tag{4.1.5}$$

where N_w is the wet refractivity which can be expressed as a function of its temperature, pressure, and water vapour pressure.

$$N_w = k_2' \frac{p_w}{T} Z_w^{-1} + k_3 \frac{p_w}{T^2} Z_w^{-1} \tag{4.1.6}$$

So, assuming that the measurements of pressure, temperature and humidity are obtained along a vertical ascent (although this is not the case for almost all radiosonde profiles, i.e. the horizontal motion of radiosonde trajectories is almost always significant), ZWD can be calculated for each radiosonde profile [*Niell et al.*, 2001]. In this study, ZWD was calculated with a ray tracing program developed by J. Davis, T. Herring and A. Niell of MIT [*Niell et al.*, 2001]. ZWD can be converted into PWV using surface temperature (see Section 4.2.3).

4.1.4 High resolution and standard resolution data

Radiosondes usually take measurements at intervals of approximately 2 seconds. The high-resolution profiles contain all such data. In contrast, the standard resolution profiles only contain measurements re-sampled from the high-resolution data at particular pressure levels. Different providers apply different criteria to select pressure levels for transmission and archiving. For instance, the UK Met Office (UKMO hereafter) standard resolution radiosonde data contain measurements at the so-called standard and significant pressure levels. The standard pressure levels are 1000, 925, 850, 700, 500, 400, 300, 250, 200, 150, 100, 70, 50, 30, 20 and 10 hPa, and the significant pressure levels are calculated according to UKMO criteria and constitute levels at which significant events occur in the profile[1] (e.g. turning points). In contrast, the University of Wyoming standard resolution radiosonde data (UWRS hereafter) comprise some additional levels evaluated with temperature and relative humidity criteria[2].

In order to examine the effect of the radiosonde resolution on ZWD, comparisons among UKMO, UWRS and the high-resolution radiosonde data (HRRS hereafter) were performed over the ARM SGP and HERS sites. All of these data consist of height profiles of pressure, temperature and dew point, but their height resolutions are different. A summary of the radiosonde data employed in this thesis for the comparisons is given in Table 4.1.

As the UKMO profiles contain heights only at mandatory levels, and much higher resolution is given for the meteorological variables [*Mendes et al.*, 2000], two methods were applied to process the UKMO data:

[1]: http://badc.nerc.ac.uk/data/radiosglobe/, 1 November 2004.
[2]: http://weather.uwyo.edu/upperair/sounding.html, 1 November 2004.

The first method eliminated levels within a sounding when there were no observations of height, pressure, temperature or dew point. The exception was for layers above 10 km where only height, pressure and temperature were checked because the ray tracing program employs a model to fill in the missing values (referred to as UKMOEL hereafter).

The second method was the same as the first one except that the missing heights were calculated from reported temperature and pressure using the hypsometric equation (referred to as UKMOHF hereafter) [*Wright,* 1997; V. Mendes, private communication, 2003]. In Table 4.1, it is obvious that UWRS had more levels than the UKMO profiles, and UKMOEL had fewer levels than UKMOHF.

Table 4.1 Summary of RS datasets.

Station	Lat/Lon	RS Type	Period	Datasets	Number of Profiles	Mean number of Pressure levels
ARM SGP	36.61°N 97.49°W	Vaisala VS90	20011202 ~ 20020801	HRRS	964	2898
				UKMOEL	688	13
				UKMOHF	690	31
				UWRS	683	81
HERS	50.90°N 0.32°E	Vaisala VS80-H	20020715 ~ 20021031	HRRS	280	2404
				UKMOEL	291	14
				UKMOHF	291	59
				UWRS	280	101

The ray tracing program developed at MIT was used to calculate ZWD from the HRRS, UKMOEL, UKMOHF and UWRS data over the ARM SGP site. The UKMOEL ZWD was compared to the HRRS ZWD. When the relationship between them was assumed to be linear, i.e. ZWD (UKMOEL) = a × ZWD (HRRS) + b, a least squares fit gave a scale factor of 0.99±0.004 with an offset at zero of 1.5±0.6mm (Table 4.2). The standard deviation was 9.0 mm with a bias of 0.4 mm. The observations are shown in Figure 4.1(a), and a comparison in Figure 4.1(b). In contrast, a linear fit of the UWRS ZWD to the HRRS ZWD for the same time period yielded a relationship of ZWD (UWRS) = 1.00(±0.001) × ZWD (HRRS) - 0.7(±0.2) mm with a standard deviation of 3.1 mm and a bias of −1.3 mm (Table

4.2). Furthermore, a linear fit of the UKMOEL data to the UWRS data had a large standard deviation, 9.8 mm (Table 4.2). This means that the UWRS ZWD was in much closer agreement with the HRRS data than the UKMOEL data was. Similar comparison results at the HERS site are also shown in Table 4.2. As mentioned earlier, there were far fewer pressure levels in the UKMOEL data than in the UWRS data (Table 4.1). It appeared that the UKMOEL data suffered from an "aliasing" artefact, which occurred when the high-resolution data were under-sampled.

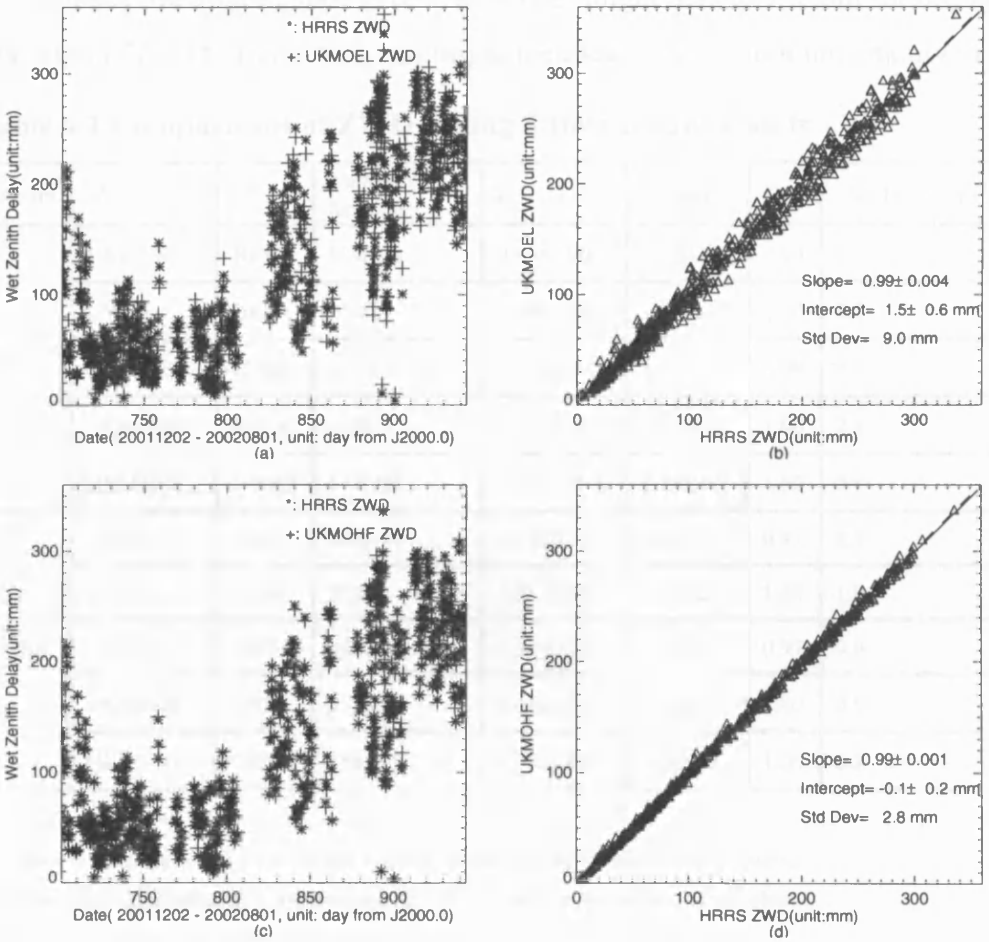

Figure 4.1 Comparisons between High Resolution Radiosonde (HRRS) and UKMO standard resolution radiosonde ZWD estimates above the ARM SGP site during the period from 01 December 2001 to 01 August 2002. (a) ZWD estimates derived from HRRS and UKMOEL; (b) Correlation between HRRS and UKMOEL ZWD estimates; the line of perfect fit (dashed line) and a least squares regression line (solid line) are plotted; (c) ZWD estimates derived from HRRS and UKMOHF; (d) Correlation between HRRS and UKMOHF ZWD estimates.

When the UKMOHF data, i.e. profiles with missing heights filled in, were compared with the HRRS data, the scale factors were close to unity (Figure 4.1, Table 4.2). The standard deviations ranged from 0.9 mm to 2.8 mm with the biases varying from –0.7 mm to –1.0 mm. The UKMOHF data were also in good agreement with the UWRS data.

The above comparisons suggest that some caution needs to be exercised when using the standard resolution data, particularly the UKMO data, to validate other datasets. For instance, the first method (viz. UKMOEL) might lead to 9.0 mm for the standard deviation of ZWD (Table 4.2), and might then lead to a 1.5 mm uncertainty in PWV.

Table 4.2 Comparisons of ZWD among different RS datasets.

Station	A[a]	B[a]	Number of Samples[b]	*a*[c]	*b* (mm)[c]	Corr	Std Dev (mm)[d]
ARM SGP	UKMOEL	HRRS	624(39)	0.99±0.004	1.5±0.6	0.99	9.0
	UWRS	HRRS	656(7)	1.00±0.001	-0.7±0.2	1.00	3.1
	UKMOEL	UWRS	647(23)	1.00±0.005	2.1±0.7	0.99	9.8
	UKMOHF	HRRS	656(7)	0.99±0.001	-0.1±0.2	1.00	2.8
	UKMOHF	UWRS	644(26)	1.00±0.000	0.5±0.06	1.00	0.9
HERS	UKMOEL	HRRS	263(14)	0.94±0.01	9.9±2.0	0.97	8.8
	UWRS	HRRS	272(4)	1.01±0.002	1.1±0.2	1.00	1.0
	UKMOEL	UWRS	262(13)	0.94±0.01	8.7±2.0	0.97	9.0
	UKMOHF	HRRS	272(5)	0.99±0.001	-0.1±0.2	1.00	0.9
	UKMOHF	UWRS	255(20)	0.98±0.001	-1.1±0.2	1.00	0.8

[a] The relation is $A = aB + b$;

[b] Values in brackets in this column refer to those omitted due to the two-sigma exclusion

[c] Uncertainties multiplied by sqrt(chi-square/(N-2)), where N is the number of samples

[d] Standard deviation of the linear least squares solutions

4.1.5 Accuracy

Errors in the measurements of relative humidity and temperature are the main sources of error in the radiosonde estimates of the integrated water vapour.

Numerous factors influence the accuracy of radiosonde temperature measurements, and an excellent review is given in the WMO Guide to Meteorological Instruments

and Methods of Observation [*WMO*, 1996]. Solar and infrared radiation impinging on the sensor can cause errors that depend in complex ways on the configuration of the radiosonde and environmental factors [*Gaffen et al.*, 1999]. Solar effects vary with elevation angles [*McMillin et al.*, 1992]. Infrared effects are both from the environment (air, surface, clouds, aerosols) and from radiosonde components (instrument housing, balloon). Meteorological balloon size influences the rise rate of radiosondes that, in turn, influences sensor lag errors. Moreover, the final height attained by the balloon before it bursts depends both on balloon type and environmental factors.

The quality of humidity data from radiosondes is generally thought to decrease with decreasing water vapour content, temperature, and pressure [*Elliott and Gaffen*, 1991]. A study by *Schmidlin and Ivanov* [1998] indicated that the humidity sensor response is quite poor in cold environments, i.e. no sensor appeared to respond to humidity changes at temperatures colder than -30°C. Some relative humidity sensors (e.g. Vaisala RS-80 A- and H-HUMICAP) have been found to suffer from contamination from the packing material, which causes the relative humidity sensor to indicate lower values than are actually present [*Liljegren et al.*, 1999; *Wang*, 2002]. As mentioned earlier, Vaisala changed the desiccant type in the package from clay to a mixture of active charcoal and silica gel in September 1998 and also introduced a new type of protective shield over the sensor boom in May 2000 for RS80 radiosondes [*Wang et al.*, 2002]. *Wang* [2002] evaluated the performance of the new sensor boom cover and found that RS80-H radiosondes with a sensor boom cover are free of contamination, but new RS80-A sondes still exhibit dry biases.

The major advantage of radiosonde data over some satellite data, e.g. GPS, MODIS and MERIS data, is that it provides a high vertical resolution profile. Moreover, since it has been applied for a long time, it is very reliable and its results have been proven to be dependable and accurate. Finally, ease of collection and efficient processing algorithms are also factors in favour of using radiosonde data.

There are two major drawbacks to the use of radiosondes. On the one hand, the equipment can only be used once, which makes the application of radiosondes very cost inefficient and restricts the spatial resolution of the radiosonde network. On the

other hand, there is a delay of 60-100 minutes in the reception of observation, which limits its application to measuring bad weather or rapidly changing weather.

4.2 GPS

The Navigation Satellite Timing and Ranging (NAVSTAR) Global Positioning System (GPS) is a passive, satellite-based, navigation system operated and maintained by the US Department of Defense (DoD). Its primary mission is to provide passive global positioning/navigation for land-, air-, and sea-based strategic and tactical forces [*USACE, EM 1110-1-1003*, 2003]. Civil use is a secondary objective, and civil users were limited throughout the 1990s to a purposefully degraded subset of the signals [*Misra and Enge*, 2001]. Nevertheless, civil applications of GPS unforeseen by the designers of the system are now thriving and growing at an astonishing rate, and many more are on the way. With the rapid development and operation of permanent global and dense regional GPS ground station networks, and also in view of the rapidly expanding number of Low Earth Orbiting (LEO) satellites carrying GPS or GPS-related instruments for limb sounding measurements, GPS meteorology has been receiving increasing attention from geodesists, meteorologists and others.

The GPS constellation nominally consists of 24 satellites (current total of 29) arranged in 6 orbital planes with a 55° inclination and an altitude of 20,200 km above the Earth's surface. The orbital period is c.12 hours, so a GPS satellite is continuously visible above the horizon for up to about 5 hours dependent on latitude. GPS satellites transmit two L-band radio signals, namely L1 (f_{L1}=1575.42 *MHz*) and L2 (f_{L2}= 1227.60 *MHz*).

In GPS geodesy, the distances between the receiver antenna and the satellites are determined either by measuring the time of flight of the time-tagged radio signals that propagate from satellite to receivers ("pseudoranging") or by finding the associated path lengths by an interferometric technique ("phase measurement"), and the position is determined by tri-lateration. The distances from each satellite are computed by dividing the time taken for transmission by the speed of light. However, the propagation speed of the GPS radio signals is sensitive to the

refractive index of the atmosphere, which is a function of pressure, temperature and moisture.

Like other microwave signals mentioned in Chapter 3, both the ionosphere and the neutral atmosphere of the Earth introduce propagation delays into the GPS signals. The ionospheric delay is dispersive and can be determined by using both of the two frequencies transmitted by GPS satellites with the known dispersion relations for the ionosphere [*Spilker*, 1980; *Gu and Brunner*, 1990]. Ionospheric delays affecting observations recorded by a dual-frequency GPS receiver can be eliminated without reference to observations recorded by other GPS receivers in the same network (if available). The remaining delay, due to the neutral atmosphere, can be divided into two parts: a hydrostatic delay and a wet delay [*Saastamoinen*, 1972; *Davis et al.*, 1985; Section 3.3.1]. The hydrostatic delay reaches about 2.3 m in the zenith direction. Given surface pressure measurements accurate to 0.3 hPa or better, the zenith hydrostatic delay can be determined to better than 1 mm [*Bevis et al.*, 1992, 1996; *Niell et al.*, 2001]. The zenith wet delay can be less than 10 mm in arid regions and as large as 400 mm in humid regions. Although the wet delay is always much smaller than the hydrostatic delay, it is usually far more variable. Significantly, the daily variability of the wet delay usually exceeds that of the hydrostatic delay by more than an order of magnitude in temperate areas [*Elgered et al.*, 1991]. If the position of the receiver is accurately known and the ionospheric delay has been accounted for, an estimate of the zenith wet delay can be derived from GPS signals together with observations of surface pressure [*Bevis et al.*, 1992, 1994; *Neill et al.*, 2001; *Li et al.*, 2003].

4.2.1 Processing strategy

In this thesis, if not specified, the GPS data were analysed separately for each UTC day using the GIPSY-OASIS II software package in Precise Point Positioning mode [*Zumberge et al.*, 1997]. Phase measurements were decimated to 300 s in the analysis. The receiver's clock was modelled as a white noise process with updates at each measurement epoch, and ZWD was modelled as a random walk with a sigma of 10.2 $mm/\sqrt{hour}$. The gradient parameters, G_N and G_E, were modelled as random

walk processes with a sigma of 0.3 $mm/\sqrt{hour}$. Satellite final orbits and clocks were obtained via anonymous FTP[1] from the Jet Propulsion Laboratory (JPL[2]).

The Niell Mapping Function was used in the processing because of its independence from surface meteorology, its small bias and its low seasonal error [*Niell,* 1996; *Niell et al.*, 2001; Section 3.3.5]. *Niell et al.* [2001] evaluated the impacts of the uncertainties of the Niell hydrostatic and wet mapping functions on ZWD. The uncertainty of the hydrostatic mapping function at 5° elevation angle is 1% and results in an uncertainty in the estimated ZWD of about 3 mm (about 0.5 mm of PWV) for the lowest elevation angle 24-hour solutions when the site positions are estimated along with ZWD. For the wet mapping function, the uncertainty at 5° elevation angle is 0.5%. Taking into account the fact that the maximum PWV is usually less than 50 mm, the maximum uncertainty in PWV due to the wet mapping function is 0.25 mm.

On the one hand, there is a loss of sensitivity to ZWD when only high-elevation ray paths are used in the GPS analysis. On the other hand, when low angle elevation data are included in the analysis, the uncertainty of the mapping function increases for very low elevation angles along with the noise of the GPS observations due to effects such as multipath and antenna phase centre variations. A trade-off between the sensitivity of ZWD and the uncertainties of mapping functions and other factors should be made. *MacMillan and Ma* [1994] reported improved VLBI baseline length repeatabilities using an elevation cut-off angle of 7°. *Bar-Sever* [1996] found superior agreement in ZWD estimates between a collocated WVR and a GPS receiver using the same cut-off value. Therefore, an elevation cut-off angle of 7° was used as a compromise in this study.

Tropospheric delay was estimated in two steps [cf. *Niell et al.*, 2001]. First, the tropospheric delay was determined together with the site position and receiver clock. Then the site position was fixed to the average for that day, and only the zenith tropospheric delays and receiver clocks were estimated. This was done because of the high correlation between height estimates and ZWD estimates, i.e. real variations in ZWD may manifest themselves as apparent variations in height. Therefore,

[1]: ftp://sideshow.jpl.nasa.gov/pub, 1 November 2004.
[2]: http://www.jpl.nasa.gov/, 1 November 2004.

retrievals of ZWD will be obtained with less reliability if the height and ZWD need to be estimated simultaneously.

4.2.2 Relationship between IWV and ZWD

Integrated Water Vapour (IWV) gives the total amount of water vapour over a site (or a GPS receiver) in units of kg/m^2 as Equation (4.1.1).

$$IWV = \int \rho_v dz \tag{4.2.1}$$

where ρ_v is the density of water vapour in kg/m^3.

IWV can be calculated from ZWD by [*Askne and Nordius*, 1987; *Schueler et al.*, 2001]:

$$IWV = \frac{ZWD}{10^{-6} \cdot \left(k_2' + \frac{k_3}{T_M} \right) \cdot R_v} = \frac{ZWD}{10^{-6} \cdot \left(k_2' + \frac{k_3}{T_M} \right) \cdot \frac{R_0}{M_v}} \tag{4.2.2}$$

where R_v is the specific gas constant for water vapour, $R_0 = 8.31434 Jmol^{-1}K^{-1}$ is the universal gas constant, M_v is the molar mass of water vapour, k_2' and k_3 are the refractivity constants. T_m is the weighted mean temperature of the troposphere and defined as [*Davis et al.*, 1985]:

$$T_M = \frac{\int_{H_0}^{\infty} \frac{e}{T} \cdot dH}{\int_{H_0}^{\infty} \frac{e}{T^2} \cdot dH} \tag{4.2.3}$$

where H_0 is the surface (antenna) height, e is the water vapour pressure in hPa and T is the absolute temperature in degrees Kelvin. Usually, water vapour pressure e is derived from temperature (T) and relative humidity (RH) using Equation (4.1.3) or as follows [*Liu*, 2000]:

$$e = 6.11 \cdot RH \cdot 10^{\frac{7.5 \cdot T}{T+237.3}} \tag{4.2.4}$$

where T is in degrees Celsius.

4.2.3 Relationship between PWV and ZWD

Precipitable Water Vapour (PWV) expresses the height of an equivalent column of liquid water in units of *mm* [*Bevis et al.*, 1992]. Thus, PWV is IWV scaled by the density of water.

$$PWV = \frac{IWV}{\rho_w} \tag{4.2.5}$$

where ρ_w is the density of liquid water ($\rho_w = 1 \times 10^3 kg/m^3$).

Therefore, the ratio of ZWD and PWV is

$$\Pi = \frac{ZWD}{PWV} = \frac{ZWD}{\left(\frac{IWV}{\rho_w}\right)} = 10^{-6} \cdot \rho_w \cdot \left(k_2' + \frac{k_3}{T_M}\right) \cdot \frac{R_0}{M_w} \tag{4.2.6}$$

where Π, a conversion factor, is dimensionless and usually ranges from 6.0 to 6.5 (and could be up to 7.0 at some areas) [*Bevis et al.*, 1992; *Niell et al.*, 2001; *Li et al.*, 2003]. For the purpose of rough conversion between ZWD and PWV, an average conversion factor of 6.2 can be adopted.

If the mean temperature is known, a conversion factor can be derived from [*Scheuler et al.*, 2001]:

$$\Pi = 0.10200 + \frac{1708.08[K]}{T_M} \tag{4.2.7}$$

It should be noted that T_m is in degrees Kelvin in Equation (4.2.7).

4.2.4 Mean temperature and conversion factor

The most accurate way to obtain the mean temperature is to calculate the integral Equation (4.2.3) using radiosonde profiles or Numerical Weather Models (NWM). In the absence of such NWMs, one can also relate the mean temperature to a local surface temperature by a statistical analysis of many radiosonde profiles. Radiosondes can provide a series of discrete temperature and relative humidity measurements along the weather balloon's ascending path. These discrete values describe temperature and water vapour distribution. Actually, the discrete observations in a profile, such as in a temperature profile, separate the troposphere

into many temperature layers, and two sequential temperature measurements represent the temperature at the bottom and top of each layer. Assuming temperature and water vapour pressure variations in each layer are linear, Equation (4.2.3) can be approximately rewritten by

$$T_m = \frac{\sum \frac{e}{T} \cdot (h_{i+1} - h_i)}{\sum \frac{e}{T^2} \cdot (h_{i+1} - h_i)} \qquad (4.2.8)$$

In the above expression, the subscripts i and $i+1$ denote the bottom and the top of each layer, h is the height above the mean sea level in metres, e and T are the average water vapour pressure and temperature respectively for the corresponding layer.

It is also possible to determine the mean temperature using surface temperatures as demonstrated by numerous authors, e.g. *Bevis et al.* [1992 and 1994], *Emardson* [1998], *Liu* [2000], and *Mendes et al.* [2000].

Bevis et al. [1992] used approximately 9,000 radiosonde observations from the United States and derived the relationship (Model MB):

$$T_m = 70.2 + 0.72 \cdot T_s \qquad (4.2.9)$$

where T_s is the surface temperature in degrees Kelvin. They estimated that using this relationship to compute T_m would produce approximately a 2% error in PWV.

Based on the analysis of 50 sites covering a latitude range of 62° S to 83° N and a height range of 0 to 2.2 km, with a total of around 32,500 radiosonde profiles for the year of 1992, *Mendes* [1999] presented slightly different coefficients (Model VM1):

$$T_m = 50.4 + 0.789 \cdot T_s \qquad (4.2.10)$$

Mendes also found that for high latitudes the mean temperature was better modelled using a cubic relation (Model VM2):

$$T_m = 196.05 + 3.402 \times 10^{-6} \cdot T_s^3 \qquad (4.2.11)$$

Emardson et al. [1998] analyzed 128,649 radiosonde profiles from 38 sites in Europe with a latitude range of 36° N to 79° N during the period from 1989 to 1997,

and developed four different models to obtain the conversion factor Π directly. Three of these models are driven by surface temperature measurements. Only the polynomial expansion of the form is presented here (Model ED1):

$$\Pi = a_0 + a_1 \cdot T_\Delta + a_2 \cdot T_\Delta^2 \qquad (4.2.12)$$

where $T_\Delta = T_s - T_{\bar{s}}$, and $T_{\bar{s}}$ is the mean surface temperature for the region ($T_{\bar{s}} = 283.49K$).

The fourth one is independent of the surface temperature but dependent on site latitude and time of the year (Model ED2):

$$\Pi = a_0 + a_1 \cdot \varphi + a_2 \cdot \sin\left(\frac{2\pi \times t_D}{365}\right) + a_3 \cdot \cos\left(\frac{2\pi \times t_D}{365}\right) \qquad (4.2.13)$$

where φ is the site latitude in degrees, and t_D is the decimal day of year.

Mendes et al. [2000] evaluated the above models by ray-tracing radiosonde profiles of 138 stations covering the globe during the period from Jan 1997 to June 1999. Based on data from Europe, it was shown that all of the models have a small positive bias and similar levels of precision. VM1 and VM2 are less biased than MB. All the above models can be used to compute the mean temperature with a relative precision of ~1.1% (at the one-sigma level). *Mendes et al.* [2000] also indicated that regionally optimised models do not provide superior performance compared to the global models.

In contrast, *Emardson et al.* [1998] found that accuracy can sometimes be further improved by adjusting the values of the model parameters to the area or site of interest in spite of the fact that the benefit of using smaller regions or site-specific models is in general small. Also, *Liu et al.* [2000] proposed different coefficients using a stepwise regression model based on the analysis of radiosonde profiles in Hong Kong (Model YL):

$$T_m = 272.4 + 0.556 \cdot T_s \qquad (4.2.14)$$

It was shown that Model YL mitigates the systematic bias of Model MB in Hong Kong, and the RMS error is 1.7 K. Similarly, *Lijegren et al.* [1999] carried out an extensive comparison of integrated water vapour from a microwave radiometer

(MWR), an ARM balloon-borne sounding system (BBSS) and a GPS at several ARM facilities in Oklahoma and Kansas. They found that the mean temperature calculated from radiosonde profiles, rather than estimated from surface temperatures using Model MB, improved the agreement between GPS and the ARM MWR water vapour.

As a useful rule of thumb, an uncertainty of 5°C in surface temperature could lead to a relative error of 1.7-2.0% in PWV [*Hagemann et al.*, 2003]. For more discussion on surface temperature, see Appendix A. In this thesis, the mean temperature was determined by Model MB, i.e. Equation (4.2.9).

4.2.5 GFZ near real-time GPS PWV products

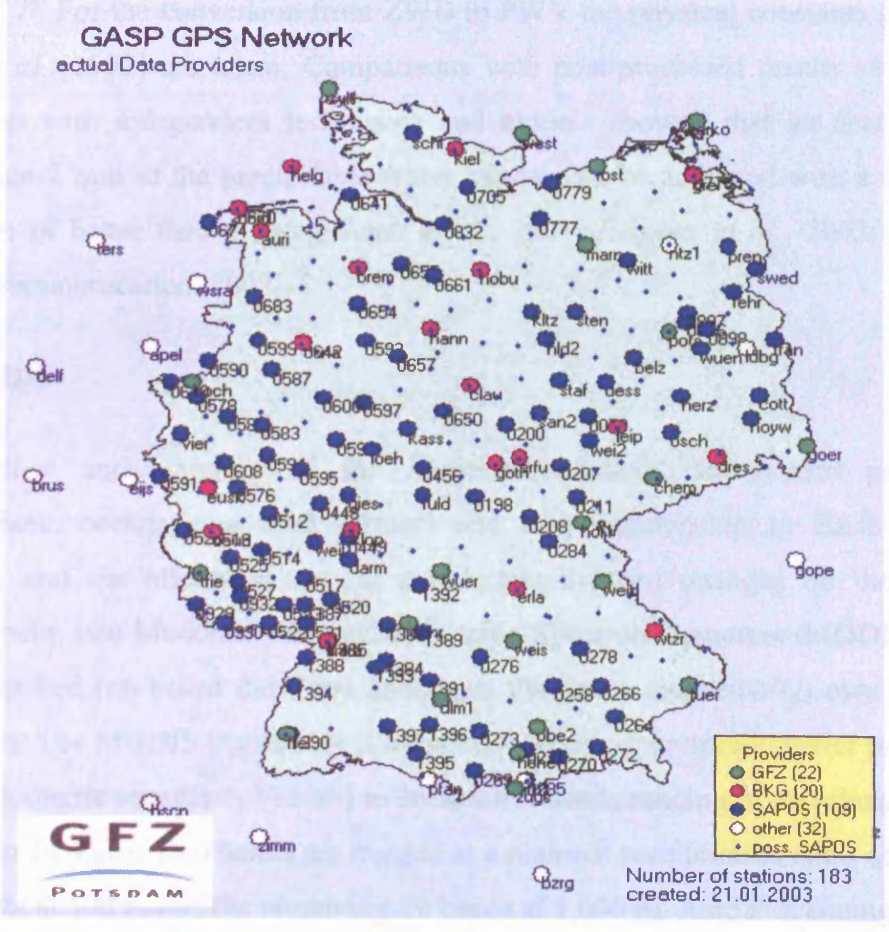

Figure 4.2 The GASP GPS network in January 2003 [*GFZ*, 2003]

In this thesis, the GeoForschungsZentrum Potsdam (GFZ) near real-time GPS PWV retrievals were also used to validate MODIS and MERIS PWV products and to investigate the spatial structure of water vapour. The GPS Atmosphere Sounding

Project (GASP), led by GFZ, utilizes a near real time (NRT) ground-based GPS network of around 183 sites with a spacing of about 50 kilometres all over Germany (Figure 4.2). It should be noted that the total number of GPS stations increased with time, e.g. from 183 sites in January 2003 to 192 sites in April 2004.

In contrast to JPL GIPSY, the GFZ near-real-time (NRT) processor, EPOS.P.V2, uses least squares adjustment instead of a Square Root Information Filter (SRIF). The EPOS.P.V2 is used to handle GPS data in two steps. The first step is to estimate high-quality GPS orbits and clocks from a global network with five GASP stations; the second is to estimate zenith total delay with a resolution of 30 min using Precise Point Positioning based on the fixed orbits and clocks. GFZ currently works on a sliding 12-hour data window with a sampling rate of 150 s and an elevation cutoff angle of 7°. For the conversion from ZWD to PWV the physical constants given by *Bevis et al.* [1992] are taken. Comparisons with post-processed results as well as validation with independent techniques and models showed that an accuracy of better than 2 mm in the precipitable water vapour can be achieved with a standard deviation of better than 1 mm [*Gendt et al.*, 2001; *Reigber et al.*, 2002; Y. Liu, private communication, 2003].

4.3 MODIS

For further understanding of the Earth's interrelated sub-system processes (atmosphere, oceans, and land surface) and their relationship to Earth system changes, and the effects of natural and human-induced changes on the global environment, two Moderate Resolution Imaging Spectroradiometers (MODIS) have been launched (on board the Terra and Aqua Platforms respectively) over the last five years. The MODIS instrument is a passive imaging spectroradiometer providing high radiometric sensitivity (12 bit) in 36 spectral bands ranging in wavelength from 0.4 μm to 14.4 μm. Two bands are imaged at a nominal resolution at nadir of 250 m, five bands at 500 m and the remaining 29 bands at 1,000 m. A ±55° scanning pattern at the Terra (or Aqua) orbit of 705 km achieves a 2,330-km swath and provides global coverage every one to two days dependent on latitude [*Nishihama et al.*, 1997].

The remote sensing method applied to MODIS which is of immediate interest here is based on detecting the absorption by water vapour of the reflected solar radiation after it has transferred down to the surface and back up through the atmosphere [*Kaufman and Gao*, 1992]. For simplicity, the radiance L_s at a downward-looking satellite sensor can be written as the sum of the ground reflected radiance L_{gnd} (including direct and path scattered ground reflected radiance) and the backscattered atmospheric radiance L_{atm} [*Schläpfer et al.*, 1995; *Gao and Kaufman*, 1998]:

$$\begin{aligned} L_s(\rho,\lambda) &= L_{gnd}(\rho,\lambda) + L_{atm}(\lambda) \\ &= L_{sun}(\lambda)T(\lambda)\rho(\lambda) + L_{atm}(\lambda) \end{aligned} \qquad (4.3.1)$$

where λ is the wavelength, L_{sun} is the solar radiance above the atmosphere and is a known value, $T(\lambda)$ is the total atmospheric transmittance, which is equal to the product of the atmospheric transmittance from the Sun to the Earth's surface and that from the surface to the satellite sensor, and contains information about the total amount of water vapour in the combined Sun-Surface-Sensor path. $\rho(\lambda)$ represents the surface reflectance. The backscattered atmospheric radiance L_{atm} is also called the path scattered radiance and is not dependent on the surface reflectance ρ, including effects of single scattering and multiple scattering.

For radiation with a wavelength near 1 μm, Rayleigh scattering is negligible and the main contribution to the path radiance is the scattering of radiation by aerosols through single and multiple scattering processes. When the aerosol concentrations are low, the path scattered radiation near 1 μm can be treated as a fraction of the direct reflected radiation [*Gao and Goetz*, 1990]. This assumption allows the derivation of column water vapour amounts from satellite data without the need to model single and multiple scattering effects, i.e. L_{atm} can be neglected under this assumption.

The reflectance values at a given wavelength are quite different for different types of surfaces, so two or more absorbing or nonabsorbing channels are required to derive the total vertical amount of water vapour. To retrieve the water vapour amount, the so-called differential absorption technique has been applied [*Frouin et al.*, 1990; *Kaufman and Gao*, 1992; *Schläpfer et al.*, 1995]. The goal of this technique is to

eliminate background factors by taking a ratio between channels within an absorption band and other non-absorption bands. Various ratioing methods on the basis of different channels and calculation techniques have been developed.

4.3.1 Differential absorption technique

A differential absorption technique consists of viewing a source of radiative energy at two (or more) wavelengths through the same atmospheric path; the wavelengths are chosen so that the absorption coefficients of a given gas, the amount of which is to be measured, are different [*Frouin et al.*, 1990]. The key advantage of the differential absorption technique is that it requires no *a priori* knowledge of the surface reflectance.

Consider two channels λ_1 and λ_2, which yield:

$$\frac{L_s(\rho_1,\lambda_1)}{L_s(\rho_2,\lambda_2)} = \frac{L^1_{sun}T(\lambda_1)\rho(\lambda_1)}{L^2_{sun}T(\lambda_2)\rho(\lambda_2)} \tag{4.3.2}$$

If the channels are selected such that $\frac{\rho(\lambda_1)}{\rho(\lambda_2)}$ is a constant, $\frac{T(\lambda_1)}{T(\lambda_2)}$ can be calculated when $\frac{L_s(\rho_1,\lambda_1)}{L_s(\rho_2,\lambda_2)}$ is measured ($\frac{L^1_{sun}}{L^2_{sun}}$ is known).

When the two channels are located in a spectral region, e.g. $\lambda_1 = 0.94\mu m$ and $\lambda_2 = 0.865\mu m$, where atmospheric absorption is essentially due to water vapour, the ratio of atmospheric transmittance in two channels, $T_w = \frac{T(\lambda_1)}{T(\lambda_2)}$, can be expressed as a function of an equivalent amount of water vapour along the optical path, or the vertically integrated water vapour (Section 4.3.3).

4.3.2 Continuum interpolated band ratio (CIBR)

If surface reflectances vary linearly with wavelength, one measurement channel can be expressed by a linear interpolation between two reference channels at the same wavelength [*Bruegge et al.*, 1990] (Figure 4.3):

$$T_w = \frac{T_m}{T_1 \cdot \frac{\lambda_2 - \lambda_m}{\lambda_2 - \lambda_1} + T_2 \cdot \frac{\lambda_m - \lambda_1}{\lambda_2 - \lambda_1}} \tag{4.3.3}$$

where T_m is the transmittance at the measurement channel with its central wavelength λ_m and T_1 , T_2 are the transmittances of the reference channels at the central wavelengths λ_1, λ_2.

The path scattered radiance L_{atm} is sensitive to the atmospheric composition, in particular the aerosol amount and the water vapour content, whose values depend on the ground altitude h [*Schläpfer et al.*, 1995]. The current CIBR techniques usually neglect the effects of path radiance.

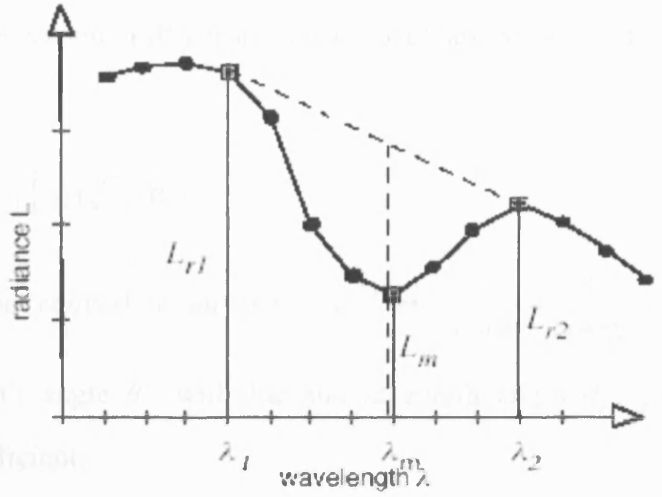

Figure 4.3 Continuum Interpolated Band Ratio (CIBR) [*Schläpfer et al.*, 1995]

In order to improve the accuracy of the differential absorption technique, *Schläpfer et al.* [1995] took the effects of path radiance into account and derived an "Atmospheric Pre-corrected Differential Absorption" (APDA) technique.

Both the 2-channel differential absorption technique and the 3-channel CIBR technique are currently used to drive the total water vapour contents over clear land areas and extended oceanic areas with sun glint for the two MODIS instruments. When clouds are present, the 2-channel ratios provide information about absorptions due to water vapour molecules on the Sun-Cloud-Sensor path instead of the Sun-Surface-Sensor path. The absorption effect is enhanced slightly due to multiple scattering of solar radiation within clouds. The cloud top height (CTH) must be known in order to retrieve the water vapour contents along the path. In the case of MODIS, a CO_2-slicing technique is employed to determine the CTH [*Menzel et al.*, 2002].

Taking into account the possible application of InSAR and D-InSAR techniques, in this study we are only interested in the water vapour content over land surfaces rather than that over cloud. Therefore, only MODIS water vapour estimated under cloud-free conditions will be utilised in this thesis.

4.3.3 Relating ratio values to PWV

The differential absorption technique yields only unquantified ratio values, which have to be transformed to total water vapour amounts.

Frouin et al. [1990] proposed an exponential approach to derive the vertically integrated water vapour (W) from the ratio of atmospheric transmittance in two channels (T_w):

$$T_w = \frac{T(\lambda_1)}{T(\lambda_2)} = \exp\left[-\beta\sqrt{m \cdot W}\right] \qquad (4.3.4)$$

where m is the equivalent air mass, and $m = \frac{1}{\cos\theta} + \frac{1}{\cos\theta_0}$ when viewing the surface at zenith angle θ with the sun at zenith angle θ_0. β is a differential absorption coefficient.

For MODIS, the relationship between the total precipitable water vapour (PWV), the precipitable water vapour along the optical path (PWV^*), and T_w can also be expressed as [*Kaufman and Gao*, 1992]:

$$PWV^* = PWV\left(\frac{1}{\cos\theta} + \frac{1}{\cos\theta_0}\right) \qquad (4.3.5a)$$

$$T_W = \exp\left(\alpha - \beta\sqrt{PWV^*}\right) \qquad (4.3.5b)$$

where θ is the view zenith angle and θ_0 is the solar zenith angle. The coefficients (α and β) for the best fit to T_w as a function of PWV^* for the MODIS water vapour channels are related to the channel wavelengths, the view zenith angle and the solar zenith angle.

4.3.4 MODIS characteristics

The MODIS instrument is a passive imaging spectroradiometer providing high radiometric sensitivity (12 bit) in 36 spectral bands ranging in wavelength from 0.4 μm to 14.4 μm. Five near-IR MODIS channels are useful for remote sensing of water vapour [*Gao and Kaufman*, 1998]. The positions and widths of these channels are given in Table 4.3 and Figure 4.4.

Table 4.3 Positions and widths of MODIS near-IR channels used in water vapour retrievals (adapted from *Gao and Kaufman* [1998])

MODIS Channel	Position (μm)	Width (μm)	Spatial Resolution(m)
2	0.865	0.040	250
5	1.240	0.020	500
17	0.905	0.030	1000
18	0.936	0.010	1000
19	0.940	0.050	1000

The channels at 0.865 and 1.24 μm are non-absorption channels, and the other three are water vapour absorption channels (Figure 4.4). Atmospheric water vapour has very different absorption coefficients over the band pass of MODIS channels centred near 0.936, 0.940, and 0.905 μm. For a very small water vapour content (<< 1 cm), the main error in the remote sensing procedure may result from uncertainty in the spectral surface reflectance. In that case, a more sensitive channel, i.e. a strong absorption channel, should be selected. For water vapour amounts much larger than 4 cm, or for slant view and illumination conditions, the strong absorption channel can partially saturate, resulting in lower sensitivity to water vapour. In this case, a water vapour absorption band in a spectral range corresponding to lower absorption should be preferable. As a result, the strong absorption channel at 0.936 μm is most useful for dry conditions, while the weak absorption channel at 0.905 μm is most useful for humid conditions, or a low solar elevation angle.

Under a given atmospheric condition, the derived water vapour values from the three channels can be different. A mean water vapour value (PWV) is obtained according to the equation [*Gao and Kaufman*, 1998]:

$$PWV = f_1 W_1 + f_2 W_2 + f_3 W_3 \qquad (4.3.6)$$

where W_1, W_2 and W_3 are water vapour values from the 0.936, 0.940, and 0.915 μm channels, respectively, and f_1, f_2 and f_3 are the corresponding weighting functions which are currently defined on the basis of the sensitivity of the transmission (T_i) in each of the channels for MODIS.

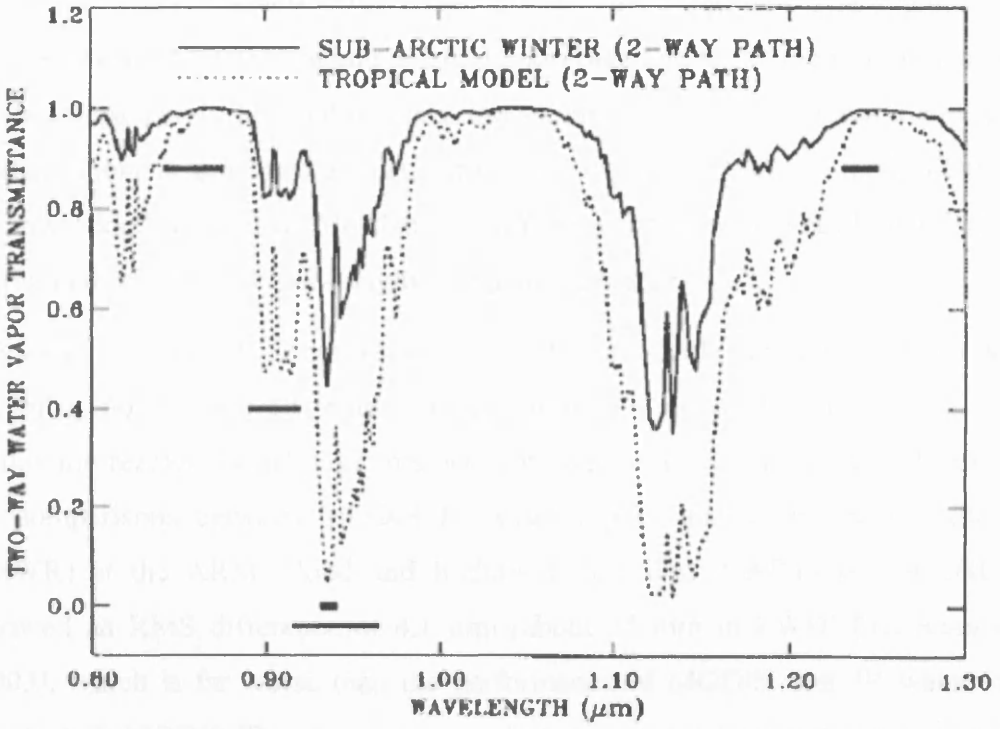

Figure 4.4 Two-way water vapour transmittance spectra for the tropical and subarctic winter models with a solar zenith angle of 45 degrees and a nadir-looking geometry, and positions and widths of five MODIS near IR channels in water vapour retrievals marked in thick horizontal bars (from *Gao and Kaufman* [1998]).

4.3.5 MODIS water vapour product description

The MODIS near IR water vapour product (including MOD_05 and MYD_05) consists of column water vapour amounts. The solar retrieval algorithm relies on observations of water vapour attenuation of reflected solar radiation in the near IR MODIS channels so that the product is produced only over areas where there is a reflective surface in the near IR. As a result, during the daytime, a near-IR algorithm is applied over clear land areas of the globe and above clouds over both land and ocean. Over clear ocean areas, water vapour estimates are provided only over the extended glint area.

To date, both daily Level 2 and daily, 8-day, and monthly Level 3 (Global Gridded) water vapour products have been available to the public at no charge through the MODIS Multiple Data Ordering Page (MDOP)[1]. The Level 2 data are generated at the 1-km spatial resolution of the MODIS instrument using the near IR algorithm during the day, and at 5×5 1-km pixel resolution both day and night using the IR algorithm when at least 9 FOVs (fields of view) are cloud free. The output grid of a single Level-2 MODIS granule is 2,030 1-km pixels in width (across the swath) and 1,354 1-km pixels in length (along the swath). The infrared-derived precipitable water vapour is generated as one component of product MOD07 (or MYD07), and simply added to product MOD05 (or MYD05) for convenience. Level 3 data are computed on $1^{\circ}\times1^{\circ}$ latitude-longitude equal angle grids.

Although MODIS IR water vapour product is available for night-time as well as daytime, no MODIS IR water vapour product is adopted in this thesis for the following reasons, which take into account its poor accuracy and spatial resolution: 1) comparisons between MODIS IR water vapour and a microwave radiometer (MWR) at the ARM Cloud and Radiation Test Bed (CART) site in Oklahoma showed an RMS difference of 4.1 mm (about 25 mm in ZWD) [*Seemann et al.*, 2003], which is far worse than the performance of MODIS near IR water vapour product; 2) MODIS IR water vapour product appeared to be in better agreement with MWR at night-time than during day-time [*Ferrare et al.*, 2002]; 3) the spatial resolution of MODIS IR water vapour product is only 5 km (cf. 1 km for MODIS near IR water vapour product).

4.3.6 Accuracy

Several sources of errors in column water vapour retrievals from MODIS channels have been described by *Kaufman and Gao* [1992] and summarized in Table 4.4.

Because channel ratios are used in the algorithm, only the relative channel-to-channel radiometric calibration is important. Spatial averaging can greatly alleviate the problem of misregistration between channels.

The largest sources of errors are the uncertainties in spectral reflectance of surface targets and in the amount of haze. *Gao and Kaufman* [2003] suggested that the

[1]: http://eosdata.gsfc.nasa.gov/, 2 November 2004.

presence of haze can result in errors of 10% or slightly greater in the current MODIS water vapour values. Typical errors in the derived water vapour values are estimated to be 5-10% [*Gao and Kaufman*, 2003], and errors can be up to 14% under hazy conditions.

Table 4.4 Error sources in MODIS near IR water vapour retrievals (from *Kaufman and Gao*, 1992).

Error Sources	Direct Derivation	Using additional MODIS Channels	Description of the extra MODIS channels
Spectral reflectance of the surface	9.0%	5.5%	Red and near-IR for NDVI
Sensor calibration	3.0%	3.0%	
Mixed pixels	0.7%	0.7%	
Subpixel clouds	5.0%	1.0%	220 m Channels
Shift in the channel location	1.5%	1.5%	
Pixel registration	2.5%	2.5%	
Temperature and moisture profile	4.0%	1.0%	IR channels
Haze effect	6.0%	2.0%	Visible channels
RMS error	13%	7%	

Note: This table shows errors in the derived amount of water vapour for nadir view and a water vapour amount of 4.1 cm. The errors are given for the direct derivation, using the "window" channel (0.865μm) and the water vapour channel (0.940μm), as well as with the assistance of additional MODIS channels that can be used to reduce the uncertainties [*Kaufman and Gao*, 1992].

4.4 MERIS

The Medium Resolution Imaging Spectrometer (MERIS) forms part of the core instrument payload of ESA's environmental research satellite ENVISAT. MERIS is a 68.5° field-of-view push-broom imaging spectrometer that measures the solar radiation reflected by the Earth, at a ground spatial resolution at nadir of 300 m, in 15 spectral bands, programmable in width and position, in the visible and near IR. It allows global coverage of the Earth in 3 days [*ESA-MERIS*, 2002].

The primary task of MERIS is to monitor the marine biophysical and biochemical variables over a large area at a very high spectral resolution. The second mission of MERIS is to provide accurate, reliable information on specific atmospheric constituents, such as water vapour, aerosols, cloud properties, and surface pressure. The third mission is dedicated to land surface processes: global scale vegetation monitoring, distribution, extent and condition.

4.4.1 Algorithm overview

The water vapour retrieval algorithm developed for MERIS is based on a differential absorption method using two spectral channels close to each other. Channel 15 is located at 0.900 μm within the absorption region, channel 14 at 0.885 μm outside the absorption region, and both have a 0.010 μm bandwidth [*Bennartz and Fischer*, 2001]. The algorithm consists of fitting a polynomial of the logarithm of the ratio of radiances measured in channels 14 and 15 [*Fischer and Bennartz*, 1997]:

$$PWV = k_0 + k_1 \log\left(\frac{L_{15}}{L_{14}}\right) + k_2 \log^2\left(\frac{L_{15}}{L_{14}}\right) \qquad (4.4.1)$$

where PWV is the column amount of water vapour, L_{14} and L_{15} are the radiances at channels 14 and 15 respectively, and k_0, k_1 and k_2 are regression constants derived by inverting the results of a radiative transfer model. The regression constants depend on observation geometry, surface type, presence of glints (above water), and/or cloud properties (above clouds), for any given pixel [*ESA-MERIS*, 2002]. The algorithm is applied to land, water and cloud pixels.

For land surfaces, even small variations in surface albedo slope may cause significant systematic deviations of retrieved water vapour content, so a simple correction algorithm based on the ratio between MERIS channel 10 (0.75375 μm) and channel 14 (0.885 μm) was developed. Moreover, the polynomial coefficients take surface pressure into account.

For water surfaces, within the sun glint (i.e. the sparkling appearance of waves on water) region, the land surface algorithm without correction can be applied. The accuracy of retrievals over sun glint is expected to be comparable to land surfaces. Outside the glint region, the effects of variable aerosol optical depth and of variations in aerosol and water vapour vertical profiles are the most significant

factors affecting the retrieval accuracy. This has been accounted for by introducing a dependence of the regression coefficients on the aerosol optical depth. Aerosol optical depth can be derived from MERIS' atmospheric correction channels 12 (0.775 μm) and 13 (0.865 μm) [*Fischer and Bennartz*, 1997]:

$$\delta_A = a + bL_{Ch12} + cL_{Ch13} \qquad (4.4.2)$$

where a, b, and c again are regression coefficients, δ_A is the retrieved aerosol optical depth at 0.900 μm, and L_{Ch12} and L_{Ch13} are the radiances measured at MERIS channel 12 and channel 13 respectively. The aerosol optical depth can be retrieved from Equation (4.4.2) with an absolute accuracy of 0.03. Despite this correction, the retrieval accuracy of the ocean algorithm, outside the sun glint, is still inferior to that over land surfaces.

When cloud is present, the regression coefficients take into account cloud optical thickness and the albedo of the underlying surface [*ESA-MERIS*, 2002].

4.4.2 MERIS water vapour product description

The MERIS products are available with different time scales (i.e. Near Real Time (NRT) and consolidated processing), with different spatial scales depending on the geographical location (i.e. global (1200 m) and regional (300 m) products), and with different levels of processing (i.e. Level 1b and Level 2) [*Bézy et al.*, 2000].

NRT services provide data 3 hours after data acquisition. Consolidation is a gradual process by which more accurate auxiliary data (e.g. precise orbit vectors and calibration information) becomes available through time. The consolidated data products are typically available within a timescale of three weeks. The format of the data products available at these different times does not change; only the quality of the auxiliary data used in their processing is improved.

MERIS products are available at two spatial resolutions: Full Resolution (FR) with a resolution at sub-satellite point of 300 m and Reduced Resolution (RR) with a resolution at sub-satellite point of 1200 m. For the purpose of distribution, the MERIS product is packaged in multiples of scenes of 1150 km ×1150 km for the RR product, and in scenes of 575 km × 575 km or 296 km × 296 km for the FR products.

Error sources in the MERIS water vapour retrievals include signal to noise (SNR), spectral mis-location, observation geometry, aerosol, surface albedo, etc. The theoretical accuracy of the algorithm is 1.6 mm under cloud free conditions over land [*Bennartz and Fischer*, 2001] and between 1 mm and 3 mm above clouds [*Albert et al.*, 2001]. The accuracy of estimation of the total amount of atmospheric water vapour is expected to be less than 20% over water surfaces [*Fischer and Bennartz*, 1997].

4.5 Conclusions

In this chapter, brief reviews of methods to retrieve water vapour using radiosonde, GPS, MODIS and MERIS measurements are given. So far, GPS water vapour products have been well validated using radiosondes and water vapour radiometers [*Dodson and Baker*, 1998; *Emardson et al.*, 2000; *Niell et al.*, 2001]. MODIS near IR water vapour product has been evaluated using PWV measured by microwave radiometer, Raman lidar, and Cimel [e.g. *Ferrare et al.*, 2002; *Gao et al.*, 2003], which are all quite limited. As regards MERIS near IR water vapour product, very few validation results have been available up to now. In Chapter 5, in order to assess the performances of different instruments, viz. radiosondes, GPS and MODIS, for measuring precipitable water vapour, coincident observations collected at the HERS site and the ARM SGP site over a 3 to 8 months period are used for inter-comparisons in time series. More importantly, a first spatial comparison of GPS-PWV and MODIS-PWV is performed using data covering all of Germany and supplied by GFZ, Potsdam. Furthermore, MERIS near IR water vapour product is evaluated temporally and spatially using radiosonde and GPS data.

Chapter 5

Assessment of the potential and limitations of water wapour products to correct InSAR measurements

In order to assess the performance of different instruments, viz. RS, GPS, MODIS and MERIS, for measuring precipitable water vapour (PWV), both temporal and spatial comparisons were performed. It should be noted that the Terra MODIS near IR water vapour product (Collection 3) is examined in this chapter; however, the improved Collection 4 product is discussed in Section 5.5. It should be noted that there is no change in the water vapour retrieval algorithm, but an update of calibration lookup tables for the MODIS Level 1B (L1B) radiances between MODIS-PWV Collections 3 and 4 (B.-C. Gao, private communication, 2003).

As discussed in Section 4.3 and 4.4, both MODIS and MERIS water vapour products are sensitive to the presence of clouds in the field of view. Therefore, using the MODIS cloud mask product, the frequency and the percentage of cloud free conditions are evaluated for Germany and the SCIGN region.

Note that all statistics are given after 2σ elimination, i.e. all differences more than twice the standard deviation are considered to be outliers and are removed. This elimination is mainly required when poor collocations between the data in either time or space are found, or where cloudy pixels are falsely identified as cloud free in the case of MODIS and/or MERIS. The percentage of data removed in this study is around 5% with a range of 4% ~ 10%.

5.1 Effect of atmospheric variation on SAR interferograms

Zebker et al. [1997] developed a model of atmospheric effects in repeat-pass radar interferograms and estimated the interferogram degradation expected from typical atmospheric conditions. Their results showed that the most significant atmospheric effect is induced by water vapour. For simplicity, the total two-way phase delay due

to water vapour for side-looking imaging radars can be expressed as [*Zebker et al.*, 1997; *Williams et al.*, 1998]:

$$\Delta\varphi = \frac{4\pi}{\lambda}\frac{ZWD}{\cos\theta_{inc}} \tag{5.1.1}$$

where $\Delta\varphi$ is the phase shift for the radar echo signal received from a point at an incidence angle θ_{inc}, and ZWD is the zenith wet delay induced by water vapour. The incidence angle of ERS-1/2 varies from 19.35° for near range to 26.50° for far range with a mean incidence angle of 23° at an average altitude of 800 km [*Olmsted*, 1993; *Scharroo and Visser*, 1998]. In this thesis, a nominal incidence angle of 23° is assumed with an uncertainty less than 2.5% for ERS-1/2. It should be noted that: 1) this is not necessarily the case for other space-based SAR sensors (e.g. ENVISAT and RADARSAT). For example, the incidence angle of ASAR varies from 15.0° to 45.2° [*ESA-ASAR*, 2002]; 2) the effects of water vapour on phase shifts increase with incidence angle.

For repeat-pass InSAR, considering that the phase of an interferogram is the difference of phase between two different SLC images, and assuming a standard deviation of σ_{ZWD} on each ZWD measurement, the effect of ZWD on interferograms can be given by:

$$\sigma_{\varphi} = \frac{4\sqrt{2}\pi}{\lambda}\frac{1}{\cos\theta_{inc}}\sigma_{ZWD} \tag{5.1.2}$$

One should keep in mind that Equation (5.1.2) is based on the assumption that ZWD values are uncorrelated for different SLC images when their temporal interval is greater than 1 day, which has been validated by previous work [*Emardson et al.*, 2003]. From Equation (5.1.2), an uncertainty of 1.0 mm in PWV (~6.2 mm in ZWD) could result in an uncertainty of 0.3 fringes (2π) in the resultant interferograms.

For repeat-pass topography mapping, taking into account Equation (3.1.8), the height error σ_h with respect to ZWD error can be given by:

$$\sigma_h = \frac{h_a}{2\pi}\sigma_{\varphi} = \frac{2\sqrt{2}}{\lambda}\frac{h_a}{\cos\theta_{inc}}\sigma_{ZWD} \tag{5.1.3}$$

In order to derive height accuracy better than 20 m, the uncertainty of *ZWD* should be less than 8.2 mm (~1.3 mm of PWV) with an ambiguity height of 45 m (i.e. a perpendicular baseline of 200 m). From Equation (5.1.3), it is obvious that *ZWD* with a larger uncertainty can still meet this goal when used with a smaller ambiguity height. For instance, the uncertainty of ZWD could be up to 16.7 mm (~2.7 mm of PWV) with an ambiguity height of 22 m (i.e. a perpendicular baseline of 400 m).

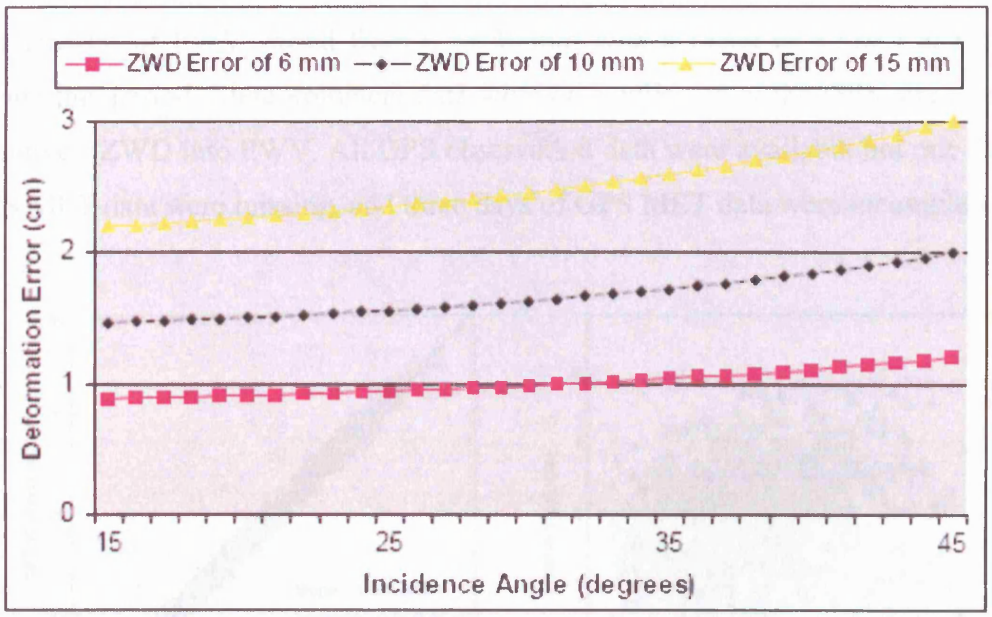

Figure 5.1 Impacts of incidence angles on error propagation from ZWD to deformation.

For repeat-pass deformation mapping, bearing in mind Equation (3.1.9), the deformation error σ_ρ with respect to *ZWD* error can be given by:

$$\sigma_\rho = \frac{\sqrt{2}}{\cos\theta_{inc}}\sigma_{ZWD} \qquad (5.1.4)$$

When a deformation of 1 cm is required, *ZWD* with an uncertainty less than 6.5 mm (~1.0 mm of PWV) is needed. Figure 5.1 shows the impacts of incidence angles on error propagation from ZWD to deformation estimates. It is clear that a smaller incidence angle would reduce atmospheric effects on surface deformation. In order to estimate deformation with an uncertainty less than 1 cm, an incidence angle less than 32 degrees together with ZWD uncertainty of 6 mm is required.

5.2 Temporal comparisons between RS and GPS PWV

Bearing in mind the good agreement between the HRRS and the UKMOHF ZWD as demonstrated in Section 4.1.4, the UKMOHF data were compared with both GPS and MODIS PWV products at the HERS site for the period from 02 December 2001 to 31 October 2002. The HERS International GPS Service (IGS) station is located at (50.87°N, 0.34°E, 76.49 m Ellipsoid), 3.8 km away from the HERS radiosonde site. The amount of PWV varied from 0 to 40 mm with a mean of 17 mm at the site during this period. Meteorological data were also collected at the GPS site in order to convert ZWD into PWV. All GPS observation data were available but one day of GPS MET data were missing, and three days of GPS MET data were incomplete.

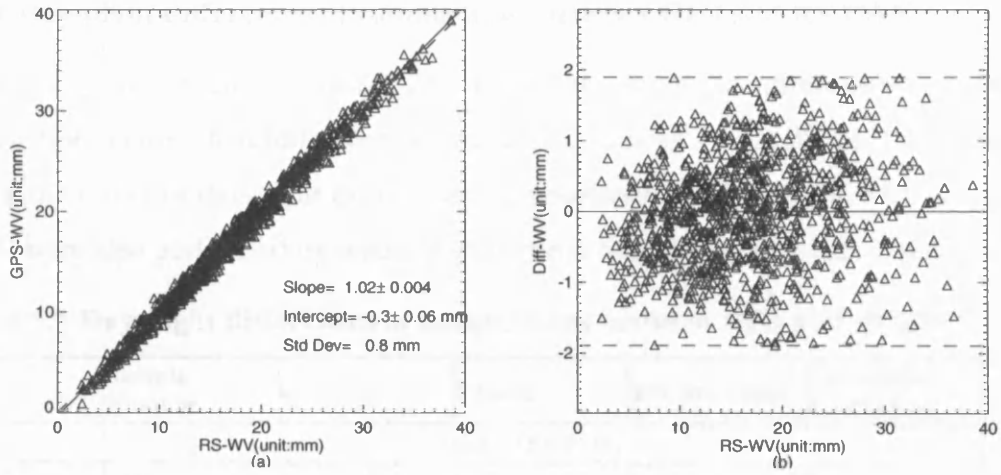

Figure 5.2 Scatter plots of ZWD from UKMOHF RS and GPS for both day-time and night-time at the HERS station from 02 December 2001 to 31 October 2002. (a) The line of perfect fit (dashed line) and a least squares regression line (solid line) are plotted. The number of valid samples was 931, and 54 samples were omitted due to the 2-sigma exclusion; (b) Diff-WV (difference in PWV) = GPS-PWV – RS-PWV. The solid line stands for the zero difference, and the dashed lines for the 2σ values.

For the ARM SGP site, the HRRS data were used in the comparisons during the period from 02 December 2001 to 01 August 2002. The LMNO IGS site is 5.8 km away from the ARM SGP radiosonde site. The amount of PWV ranged from 0 to 55 mm with a mean of 19 mm during this period. There were only 147 days of coincident GPS observation and MET data.

The same algorithm (Equations (4.2.6) and (4.2.9)) was used to convert ZWD into PWV for both GPS and RS data; therefore, this conversion does not add any additional uncertainty for the comparisons between GPS and RS PWV. Consistency was expected with the other comparisons, so that PWV rather than ZWD were compared and the GPS-PWV values were averaged over 30-minute time intervals during the radiosonde launches and flights.

Figure 5.2 shows PWV from the UKMOHF data for the period from 02 December 2001 to 31 October 2002 compared with retrievals from GPS. There were 931 valid pairs. A high correlation coefficient, 0.99, was observed between these two datasets. GPS-PWV was 1.02±0.004 times greater than RS-PWV with a zero-point offset of -0.3±0.06 mm.

5.2.1 Day-night differences of comparisons between GPS and RS PWV

Some previous studies revealed that there are day-night differences in RS90 radiosonde relative humidity measurements [e.g. *Smout et al.*, 2001]. In order to check the effect of day-night differences, comparisons between GPS-PWV and RS-PWV were also performed by separating day-time and night-time cases (Table 5.1).

Table 5.1 Day-night differences of comparisons between GPS and RS PWV

Time	Sample Number	*a*	*b* (mm)	Std Dev (mm)#	Correlation Coefficient
	HERS (RS80-H) *				
All time	931	0.97±0.003	0.5±0.06	0.8	0.99
Day-time	411	0.96±0.006	0.5 ±0.1	0.8	0.99
Night-time	517	0.97±0.004	0.5 ±0.08	0.7	0.99
	ARM SGP (RS90) *				
All time	508	0.99±0.004	1.1±0.1	1.2	0.99
Day-time	263	0.97±0.005	1.0 ±0.1	1.2	0.99
Night-time	245	1.01±0.005	1.1 ±0.1	1.0	1.00

Standard deviation of the linear least squares solutions

* RS-PWV = a × GPS-PWV + b

A linear fit of RS-PWV and GPS-PWV at the HERS site using only the day-time results yielded the relationship, RS-PWV (Day) = 0.96 (±0.006) × GPS-PWV (Day) +0.5 (±0.1) mm. At night-time, a linear relationship, RS-PWV (Day) = 0.97 (±0.004) × GPS-PWV (Day) + 0.5 (±0.08) mm, was found. The scale factor

variation due to day-night differences was only ~1% for RS80 PWV relative to GPS measurements at the HERS site. By comparison, the scale factors for the RS90 PWV relative to GPS-PWV measurements changed from 0.97±0.005 in the day-time to 1.01±0.005 at night-time at the ARM SGP site. A possible cause for the larger scale factor variation at the ARM SGP site is that the RS90 sensors were heated by the Sun's solar radiation during the day, which resulted in lower relative humidity measurements, while there is a cap on the RS80 sensors, which avoids additional uncertainties due to heating by solar radiation [*Smout et al.*, 2001].

5.2.2 Temporal comparisons between GPS and RS PWV in the day-time

As the MODIS and MERIS near IR water vapour retrieval algorithms rely on observations of water vapour attenuation of near IR solar radiation reflected by surfaces and clouds, the product is produced only in the day-time [*Fischer and Bennartz*, 1997; *Gao et al.*, 2003]. For consistency purposes, only day-time measurements were used in Table 5.2.

Table 5.2 Temporal comparisons among RS, GPS and MODIS PWV

Station	Sample Number	*a*	*b* (mm)	Std Dev * (mm)	Correlation Coefficient
GPS-PWV vs. RS-PWV (Day-time) [a]					
HERS	411	1.02±0.006	-0.3±0.1	0.8	0.99
ARM SGP	263	1.02±0.005	-0.9 ±0.1	1.2	0.99
MODIS-PWV vs. GPS-PWV [b]					
HERS	66	1.09±0.02	-0.3±0.3	1.0	0.97
ARM SGP	21	1.14±0.03	-0.1±0.3	0.8	0.99
MODIS-PWV vs. RS-PWV [c]					
HERS	50	1.14±0.03	-0.8±0.5	1.6	0.98
ARM SGP	35	1.20±0.04	-1.4±0.7	2.2	0.96

* Standard deviation of the linear least squares solutions

[a] GPS-PWV = $a \times$ RS-PWV + b

[b] MODIS-PWV = $a \times$ GPS-PWV + b

[c] MODIS-PWV = $a \times$ RS-PWV + b

The mean and standard deviation of the differences between GPS and RS PWV were 0.1 and 0.8 mm at the HERS site and –0.5 and 1.2 mm at the ARM SGP site in the day-time. The larger quantity for the ARM SGP site might be attributable to the longer distance between the RS and GPS stations and the larger PWV range.

5.3 Comparisons between RS, GPS and MODIS PWV

As MODIS-PWV is sensitive to the presence of clouds and only 15%~30% of all observations appear to be cloud free at mid-latitudes in Northern Europe (Section 5.5), long term datasets are required.

5.3.1 Temporal comparisons between MODIS and GPS PWV

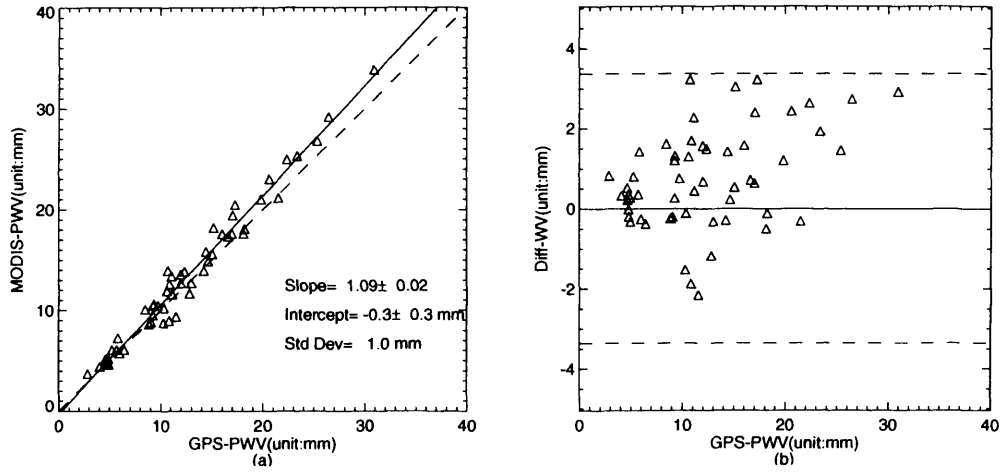

Figure 5.3 Scatter plots of MODIS-PWV and GPS-PWV for cloud free observations at the HERS site from 02 December 2001 to 31 October 2002. (a) The number of valid samples was 66 and 4 samples were omitted due to the 2σ exclusion; (b) Diff-WV (difference in PWV) = MODIS-PWV – GPS-PWV.

Figure 5.3(a) shows the correlation between GPS-PWV and MODIS-PWV at the HERS station during the period from 02 December 2001 to 31 October 2002. It indicates that MODIS-PWV was larger than GPS-PWV by a scale factor of 1.09±0.02. Figure 5.3(b) shows that the differences (MODIS-PWV – GPS-PWV) increased slightly with the amount of PWV. The number of valid pairs was smaller than for the previous comparisons between radiosondes and GPS retrievals because only cloud free observations were kept, and also because there are only two Terra MODIS overpasses a day per location, whereas there can occasionally be up to 4 radiosonde launches a day as mentioned in Section 4.1.1.

The same comparison was performed over 124 GASP GPS stations in Germany (Figure 4.2). There were at least 10 cloud free measurements for 86 out of 124 stations. The average scale factor for MODIS-PWV with respect to GPS-PWV for

these 86 stations was 1.07±0.09 with an average offset at zero of -0.8±1.6 mm. 18 out of 86 scale factors (21%) were smaller than 1 (i.e. MODIS-PWV/GPS-PWV < 1); and 68 out of 86 (79%) were greater than 1 (i.e. MODIS-PWV/GPS-PWV > 1). The average standard deviation of the differences was 1.4 mm.

5.3.2 Temporal comparisons between MODIS and RS PWV

As mentioned in the previous section, radiosondes are usually launched two to four times a day, and MODIS PWV products are only retrieved at most twice a day above one site. Terra MODIS provides global coverage every 1 to 2 days and views the Earth's surface near nadir at 10:30 am local time, so only serendipitous spatio-temporally overlapping data can be found.

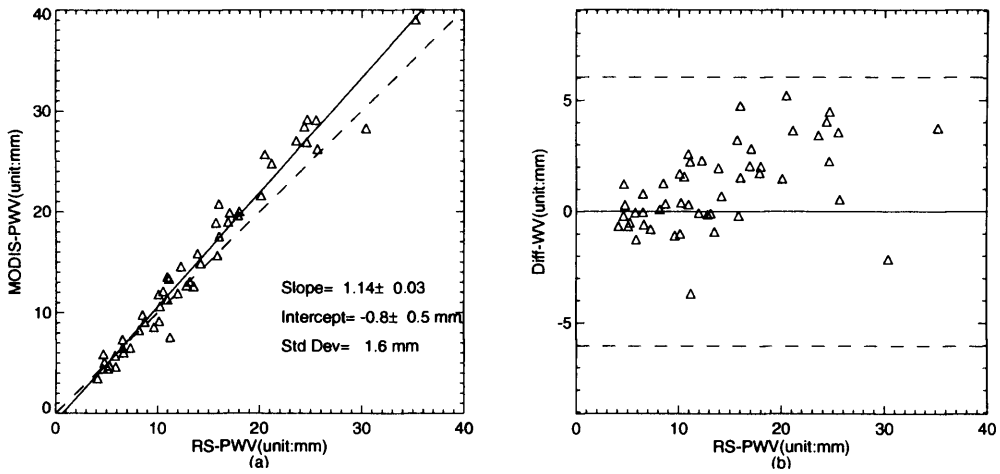

Figure 5.4 Scatter plots of MODIS-PWV and UKMOHF RS-PWV for cloud free observations at the HERS site from 02 December 2001 to 31 October 2002. (a) The number of valid samples was 50 and 2 samples were omitted due to the 2σ exclusion; (b) Diff-WV (difference in PWV) = MODIS-PWV – RS-PWV.

Figure 5.4 shows a comparison of MODIS and RS PWV above the HERS site. The amount of MODIS-PWV was 14%±3% larger than RS-PWV with a zero-point offset of -0.8±0.5 mm. Taking into account the scale factors of GPS-PWV relative to RS-PWV, MODIS-PWV values had a similar linear relationship to RS as to GPS within a 1σ uncertainty. Figure 5.4(b) shows clearly that the differences were dependent on the amount of PWV. In other words, the differences (MODIS-PWV – RS-PWV) increased with the amount of PWV.

5.3.3 Spatial comparisons between MODIS and GPS PWV

For the first time, a spatial comparison of PWV from GPS and MODIS was performed using data collected over Germany (47-55°N, 6-15°E) during the period from 01 May 2002 to 30 June 2002. There were 115 Terra overpasses in total in the day-time for this experimental period, with some just over the German border. For each Terra overpass, the number of GPS stations with cloud free conditions varied from 2 to 64 out of 124. A comparison was only performed when at least 10 GPS stations were cloud free. 59 out of 115 overpasses fulfilled this condition (Table 5.3). The correlation coefficients between GPS and MODIS PWV for each overpass varied from 0.42 to 0.98 with an average of 0.82. 36 out of 59 scale factors (61%) for MODIS-PWV relative to GPS-PWV were greater than 1. More importantly, we derived an average linear fit model between MODIS and GPS PWV in this area: MODIS-PWV = 1.03 (±0.12) × (GPS-PWV) − 0.1 (±2.3) mm. The average scale factor for this spatial-temporal comparison was smaller than that in the time series (1.07±0.09, c.f. Section 5.3.1), but the difference was not significant in terms of their uncertainties (only 1σ).

Table 5.3 Spatial comparisons between MODIS and GPS PWV across Germany

		Number of Passes	Slope	Intercept (mm)	Correlation	Number of Samples	Std Dev (mm) *
Before Correction	Average	59	1.03±0.12	-0.1±2.3	0.82	25	1.7
	Min		0.63±0.41	-8.5±6.0	0.42	10	0.9
	Max		1.44±0.27	8.0±7.9	0.98	69	3.5
After Correction	Average	58	1.01±0.11	-0.1±2.2	0.83	25	1.5
	Min		0.61±0.39	-8.3±5.9	0.34	10	0.8
	Max		1.39±0.26	7.7±7.7	0.98	72	2.8

* Standard deviation of differences

Bearing in mind the good agreements between GPS-PWV and MODIS-PWV in time series, particularly the small standard deviations of the linear least square solutions (See Table 5.2), we used the average linear fit as a model to calibrate MODIS-PWV, and then compared the calibrated MODIS-PWV with GPS-PWV (Table 5.3). After such a correction and 2σ elimination, 58 overpasses fulfilled the requirement that at least 10 GPS stations be cloud free. The average correlation coefficients were almost the same, 0.83 after the correction. However, the average scale factor decreased to 1.01, the average bias from 0.6 mm to 0.2 mm, and the

average standard deviation of the differences from 1.7 mm to 1.5 mm. Figure 5.5 shows the distributions of the standard deviations before and after the correction. It indicates that the correction was encouraging, with more standard deviations less than 1 mm and fewer larger than 2 mm after the correction.

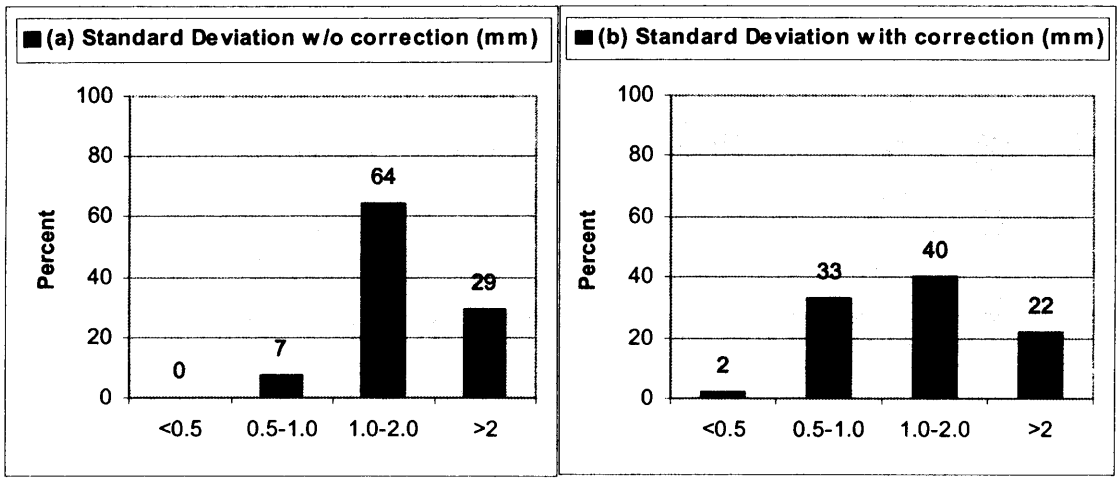

Figure 5.5 Statistics of spatial comparison between MODIS-PWV and GPS-PWV throughout Germany during the period from 01 May 2002 to 30 June 2002. (a) Standard deviations of the differences (MODIS-PWV – GPS-PWV) in millimetres without any correction; (b) Standard deviations of the differences (MODIS-PWV (calibrated) – GPS-PWV) in millimetres after a linear fit model was applied to correct MODIS PWV: MODIS-PWV (calibrated) = 0.97 × (MODIS-PWV) + 0.1 mm.

5.3.4 Discussion

As shown in Table 5.1, the scale factors of RS and GPS measurements agreed within 4%. In contrast, the scale factors of MODIS-PWV varied from 1.09±0.02 to 1.14±0.03 relative to GPS-PWV, and from 1.14±0.03 to 1.20±0.04 with respect to RS-PWV (Table 5.2). In other words, GPS-PWV and RS-PWV agreed better with each other than with MODIS-PWV. Figures 5.2, 5.3 and 5.4 also reveal that the differences relative to MODIS-PWV were larger than those between GPS-PWV and RS-PWV.

The MODIS water vapour amounts are derived from the transmittances based on theoretical calculations and using lookup table procedures. The lookup tables were generated with the HITRAN2000 spectroscopic database and a line-by-line

atmospheric transmittance code [*Gao and Kaufman*, 2003]. The effects of several sources of errors on the MODIS near IR PWV retrieval are shown in Table 4.4. Typical errors in the derived water vapour values are estimated to be 5-10%, and errors can be up to 14% under hazy conditions (with visibilities less than 10 km) or when the surface reflectances near 1 μm are small (less than about 0.1) [*Gao and Kaufman*, 2003]. As described previously, only MODIS-PWV values collected under clear sky conditions were used in this thesis. Therefore, the MODIS scale uncertainty was considered to be 10%. The quadratic sum of the GPS/RS scale uncertainty (4%) and the MODIS typical scale uncertainty (10%) is 11%. The actual scale differences of MODIS/RS are up to 20±4% which is much larger than the combined uncertainty, suggesting that the MODIS errors are larger than those that can be currently accounted for.

Another possible cause for the larger discrepancies of MODIS-PWV relative to GPS/RS could be the different physical principles for the three systems. RS usually takes measurements at intervals of approximately 2 seconds and measurements are acquired for up to 100 minutes after launch. Furthermore RS ZWD is the integration along the flight trajectory, bearing in mind that the horizontal drift of radiosondes might be significant (up to a few kilometres sometimes). GPS can take measurements at rates as high as 20 Hz, although CGPS networks typically record data every 30 seconds; GPS measurements are collected from the whole sky above the cut-off elevation angle (e.g. of 5, 7, 10, or 15 degrees). The GPS ZWD was estimated at 5-minute intervals (30-minute for the GFZ PWV products), so GPS PWV represented a 5-minute (or 30-minute) average along the paths of 4 to 12 GPS satellites as they orbited the Earth. In contrast, one scan of the MODIS mirror takes 1.4771 seconds to observe a swath (also known as a scan line) which is 2200 km long and 10 km wide at nadir, and MODIS-PWV is the instantaneous observation of a 1 km pixel. Furthermore, in this study, the GPS PWV values were averaged over 30 minute intervals during the RS launch time when comparing the PWV values derived from GPS with those from RS, but no such averaging was possible when comparing with MODIS.

The adoption of different mapping functions does not contribute significantly to the larger discrepancies of MODIS-PWV relative to GPS/RS. The mapping functions

(e.g. Niell Mapping Function [*Niell*, 1996]) employed for GPS analysis are usually developed on the basis of the radiosonde profiles, which leads to high correlations between GPS and RS ZWD (or PWV); In contrast, a simple Cosecant Mapping Function (CMF) is employed in the processing of MODIS near IR water vapour products: $PWV^* = PWV\left(1/\cos\theta + 1/\cos\theta_0\right)$, where θ is the view zenith angle and θ_0 is the solar zenith angle [*Kaufman and Gao*, 1992]. The view zenith angles vary between -65 and 65 degrees. The solar zenith angles are typically in the range of 0~70 degrees. At high latitudes, the solar zenith angles can be close to 90 degrees (B. C. Gao, private communication, 2003). From Figure 3.3, the relative difference of CMF with respect to the Niell Wet Mapping Function (NWMF) is 0.3% at 65° view zenith angle and 0.4% at 70° at the HERS site. Therefore, the difference of the NWMF and the CMF could introduce errors of up to 0.5% in this study.

In Table 5.3, the standard deviations of MODIS-PWV with respect to RS-PWV were larger than those with respect to GPS-PWV. This means that MODIS-PWV agreed slightly better with GPS-PWV than with RS-PWV. The different sampling rates and the different observation intervals could be one explanation. As mentioned above, the difference in the observation intervals between RS and MODIS (viz. 60~100 minutes) was much larger than that between GPS and MODIS (viz. ~5 minutes).

5.4 Comparisons between RS, GPS and MERIS PWV

On the one hand, like MODIS, MERIS PWV is sensitive to the presence of clouds in the field of view; therefore, in this study only MERIS PWV collected under clear sky conditions were selected using a cloud mask produced by Freie Universität Berlin (FUB). On the other hand, due to the limited amount of MERIS data, spatio-temporal comparisons were performed in this section rather than the separate spatial and temporal comparisons that were performed in Section 5.3. It should be noted that, due to data availability, the Reduced Resolution (RR) MERIS near IR water vapour product is used for comparisons in this thesis.

5.4.1 Comparisons between RS and MERIS PWV

Ten Vaisala RS-80 radiosonde stations, launched twice daily or more and distributed around Germany, were chosen for this study. In addition to the requirement of cloud free conditions, RS data were chosen only if the time difference between a MERIS overpass and RS was less than 1.5 hours. There were 315 coincident RS and MERIS observations available in total, and 34 cases were omitted due to the 2σ exclusion (Figure 5.6(a)). Assuming the relationship between MERIS and RS PWV to be linear, MERIS-PWV = $a \times$ (RS-PWV) + b, a least squares fit gave a scale factor of 1.09±0.01 with a zero-point offset of -0.4±0.1 mm and a standard deviation of 1.1 mm. The mean difference (MERIS – RS) PWV was 0.7 mm with a standard deviation of 1.4 mm.

5.4.2 Comparisons between MERIS and GPS PWV

The criteria applied to choose GPS observations were different to those applied to RS. Since GPS made continuous observations and PWV was estimated with a resolution of 30 minutes, GPS data covering the scanning time of MERIS measurements were selected, and so the time difference was much smaller than that between MERIS and RS. The spatial distribution of GPS stations is much denser than that of the RS sites in Germany; therefore the number of coincident GPS and MERIS observations was greater than that between RS and MERIS observations. There were 2,261 cases available and 123 cases were omitted due to the 2σ exclusion. The correlation coefficient between MERIS and GPS PWV was 0.99 (Figure 5.6(b)). The mean difference (MERIS – GPS) PWV was –0.2 mm with a standard deviation of 1.1 mm. A linear fit of MERIS-PWV to GPS-PWV yielded a relationship of MERIS-PWV = 1.02 (±0.003) × (GPS–PWV) – 0.5 (±0.05).

In order to validate MERIS PWV under different conditions, viz. dry, moderate or wet conditions, comparisons between GPS and MERIS PWV were performed in different seasons (Table 5.4). It is clear that it was wettest in the summer with a mean PWV of 21.4 mm and driest in the winter with a mean PWV of 5.4 mm. Except for the comparison in the winter, the others showed scale factors greater than unity and negative zero-point offsets. The comparison in the winter showed an apparently worse agreement in terms of the correlation of 0.89, although the positive

offset at zero, the scale factor of significantly less than unity, and the limited ranges of PWV resulted in a small standard deviation of 0.8 mm. Given the error characteristics of MERIS PWV retrievals [*Bennartz and Fischer*, 2001], the large difference in the winter was most likely due to high solar zenith angles. The comparison in the summer showed a larger scale factor and a larger offset from zero. These suggest that MERIS PWV values were slightly greater than GPS values under both dry and wet conditions for the dataset used in the thesis.

Table 5.4 Seasonal comparisons between MERIS and GPS PWV across Germany

Season [a]	Number of Passes [b]	a [c]	b [c] (mm)	Correlation	PWV Range (mm) [d]	Mean PWV (mm) [d]	StdDev (mm) [e]
Spring	879(61)	1.02±0.006	-0.6±0.07	0.98	[1.5,33.5]	11.2	1.0
Summer	707(34)	1.06±0.009	-1.4±0.2	0.97	[5.5, 35.8]	21.4	1.3
Autumn	394(20)	1.06±0.01	-0.9±0.2	0.97	[5.0,26.9]	14.8	1.0
Winter	156(10)	0.89±0.02	0.8±0.1	0.89	[1.4,17.0]	5.4	0.8
All	2138(123)	1.02±0.003	-0.5±0.05	0.99	[1.4,35.8]	14.7	1.1
[5,25]	1654(106)	1.02±0.005	-0.5±0.07	0.98	[5.0,25.0]	14.2	1.0

[a] Spring: March – May 2003; Summer: June – August 2003;
Autumn: October– November 2002 and September 2003;
Winter: December 2002 – February 2003;

[b] The number of valid passes (the number of samples omitted due to the 2σ exclusion);

[c] Here MERIS-PWV = a × GPS-PWV + b;

[d] Derived from GPS measurements;

[e] Standard deviation of the mean differences.

Assuming that PWV varied from 5 to 25 mm under moderate conditions (which is similar to autumn), a linear fit of MERIS-PWV to GPS-PWV yielded a relationship of MERIS-PWV = 1.02(±0.005)× (GPS-PWV)- 0.5(±0.07) with a standard deviation of 1.0 mm (Table 5.4, Figure 5.6(e)). A similar comparison was performed between MERIS and RS PWV (Figure 5.6(d)). The MERIS PWV values were 1.07±0.02 times the RS PWV with a zero-point offset of -0.3±0.2.

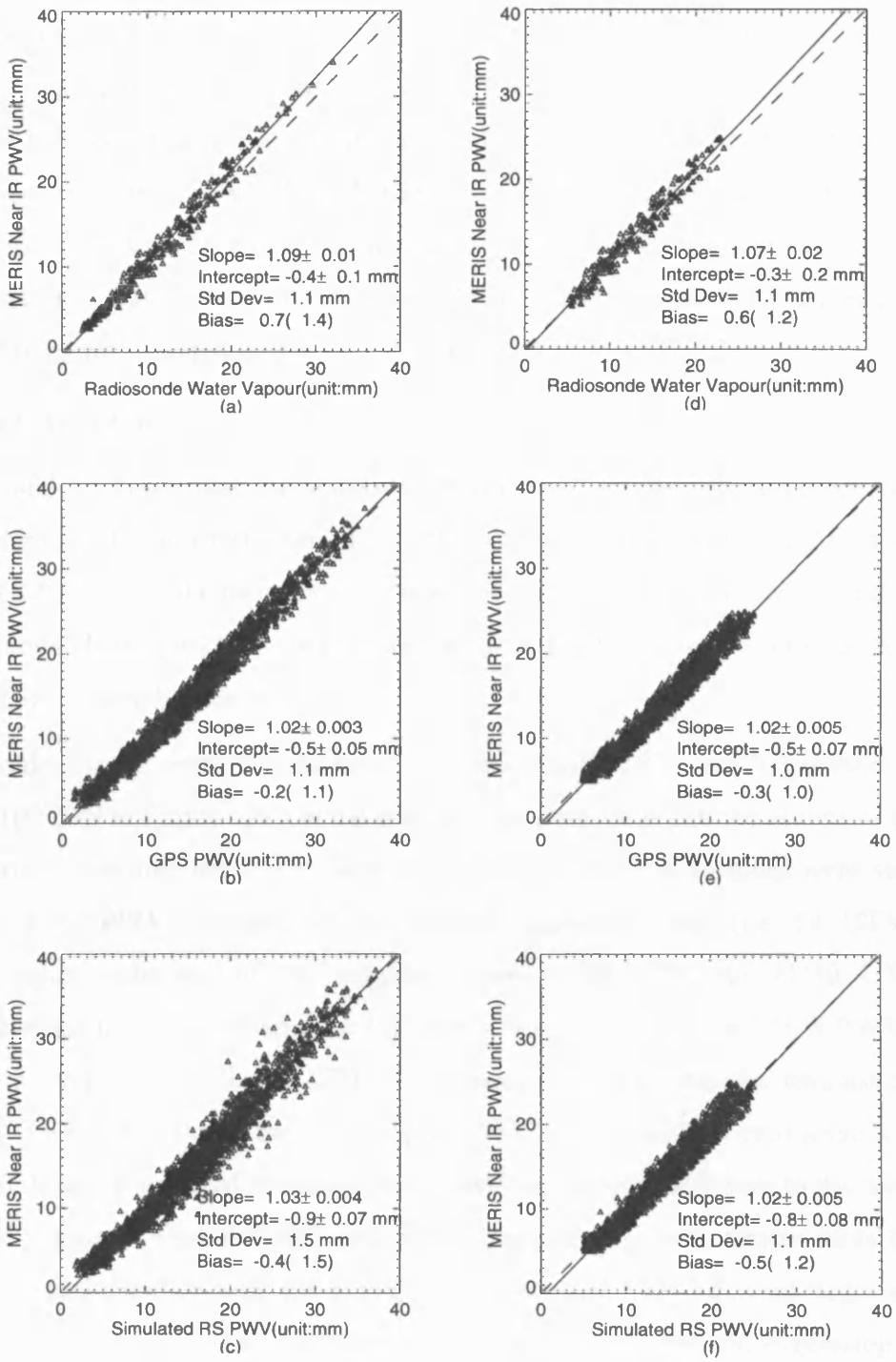

Figure 5.6 (a) Scatter plots of PWV from MERIS and RS under cloud-free conditions. The line of perfect fit (dashed line) and a least squares regression line (solid line) are plotted. The number of valid samples was 281, and 34 were omitted due to the 2σ exclusion. (b) Scatter plots of PWV from MERIS and GPS under cloud-free conditions. The number of valid samples was 2,138, and 123 were omitted. (c) Scatter plots of PWV from MERIS and simulated RS under cloud-free

conditions. The RS PWV values were simulated using the GPS PWV values at the nominal launch time of RS, viz. 11 UTM, with observation intervals of 30 minutes. (d) Scatter plots of PWV from MERIS and RS under moderate conditions with clear sky (PWV: 5-25 mm). The number of valid samples was 217, and 25 were omitted. (e) Scatter plots of PWV from MERIS and GPS under moderate conditions with clear sky (PWV: 5-25 mm). The number of valid samples was 1,654, and 106 were omitted. (f) Scatter plots of PWV from MERIS and simulated RS under moderate conditions with clear sky (PWV: 5-25 mm).

5.4.3 Discussion

It should be noted that the standard deviations of all the above comparisons are smaller than the quadratic sum of both the accuracy of GPS PWV (1-2 mm, or more for RS PWV) and the theoretical accuracy of MERIS PWV (~1.6 mm), and thus the agreement between GPS (or RS) and MERIS PWV is well within the estimated accuracy of each technique.

It should also be noted that the scale factors of MERIS/RS were larger than those of MERIS/GPS in Figure 5.6. On the one hand, in order to check the effects of the time difference between RS and MERIS measurements, RS PWV values were simulated using GPS PWV estimates at the nominal launching time (i.e. 11 UTM) with observation intervals of 30 minutes (from 11:00 UTM to 11:30 UTM). A comparison between the simulated RS PWV values and the 'real' GPS PWV values (which overlapped with the MERIS overpasses) showed that the simulated values were 0.99±0.003 times the 'real' GPS PWV values with a zero-point offset of 0.5±0.04 and a standard deviation of 0.9 mm (not shown). Relative to the 'real' GPS PWV values in Figure 5.6(b) and 5.6(e) respectively, both scatter plots between MERIS and simulated RS PWV in Figure 5.6(c) and 5.6(f) showed larger standard deviations and larger mean differences with similar scale factors, suggesting that the time difference made contributions to the larger standard deviations, but had no significant effects on the larger scale factor of MERIS/RS. On the other hand, bearing in mind that the scale factor of RS/GPS was ~0.95 for Vaisala RS-80 radiosondes [*Niell et al.*, 2001; *Li et al.*, 2003], the division of the scale factors of MERIS/GPS (1.03) and RS/GPS (0.95) was about 1.08 within 1σ of the MERIS/RS scale factor (1.09), when using the whole data sets (Figure 5.6(a) and 5.6(c)). Under

moderate conditions (Figure 5.6(d) and 5.6(f)), the division of the scale factors of MERIS/GPS (1.02) and RS/GPS (0.95) was about 1.07, identical to the MERIS/RS scale factor (1.07). These figures imply that both types of comparisons were consistent with each other.

5.5 Statistics of cloud free conditions

Although precipitable water vapour can be retrieved above the highest cloud level under cloudy conditions for both MERIS and MODIS [*Albert et al.*, 2001; *Gao and Kaufman*, 2003], the interests of InSAR applications lie in the PWV values over land rather than clouds. Therefore, the frequency and the percentage of cloud free conditions need to be evaluated. The frequency of cloud free conditions refers to the probability of cloud free occurrence; the percentage of cloud free conditions is inferred from the density of cloud free pixels. *Wylie et al.* [1999] investigated the frequency, geographical distribution, and seasonal changes of upper-tropospheric clouds using the High resolution Infrared Radiation Sounder (HIRS) over 8 years (1989-1997) and reported that clear skies were found in 27% of all observations of the Earth from 65°S to 65°N latitude in the boreal summer (June-August) and in only 24% during the boreal winter (December-February). It should be noted that the spatial resolution of the cloud product derived from HIRS data is 20 km. Therefore, HIRS may observe broken clouds, overcast transmissive clouds, and/or broken transmissive clouds, which implies an observation where the HIRS radiometer detects radiation from below, as well as above a cloud layer [*Wylie et al.*, 1999].

In this study, the 1 km cloud mask product stored in MODIS near IR water vapour product [*Ackerman et al.*, 1998] has been utilized to produce the statistics of cloud free conditions.

5.5.1 Frequency of cloud free conditions

An area of $4^{o} \times 4^{o}$ in Germany (49–53° N, 8-12° E) was chosen to estimate the frequency of cloud free conditions, and a uniformly spaced grid of 1 km × 1 km was applied. There were 481×481 grid cells in total.

Figure 5.7 shows seasonal frequencies of cloud free conditions over parts of Germany during the period from 1 March 2002 to 28 February 2003. It is clear that

the frequencies varied from place to place in all four figures. For example, the frequency in the south of the test area was higher than that in the centre.

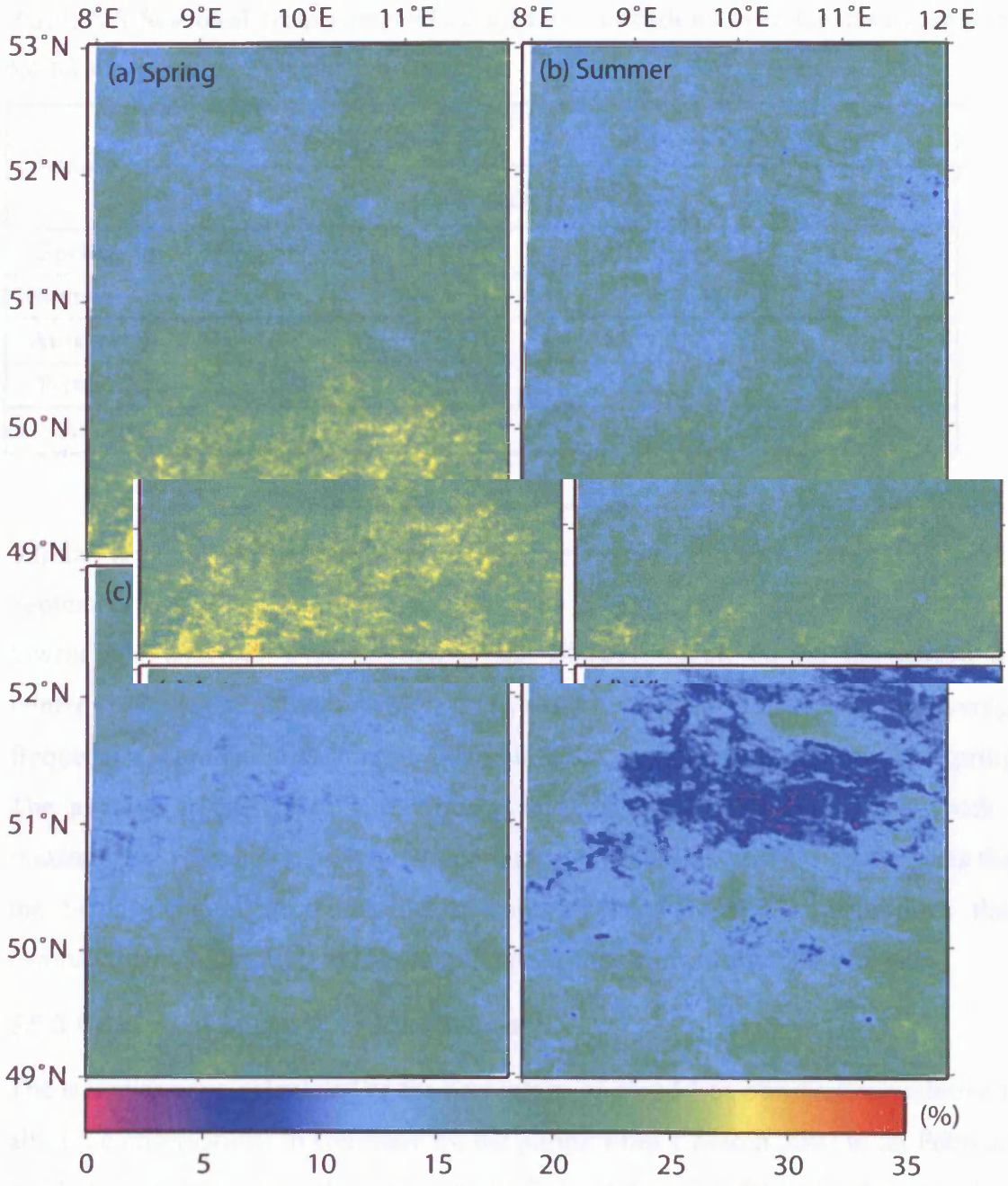

Figure 5.7 Seasonal frequencies of cloud free conditions over Germany during the period from March 2002 to February 2003. Summer spans the months of June–August, and winter the months of December–February.

Table 5.5 shows a summary of seasonal frequency variation: both the highest individual and average frequencies over Germany were found in spring (33% and 19%, respectively) whilst the lowest ones occurred in winter (0% and 13%). The

average frequency of cloud free conditions was found to be 17%, with a maximum of 25% in the area during the whole year.

Table 5.5 Seasonal frequencies of cloud free conditions over Germany and the SCIGN region

Season	Germany (%)			SCIGN (%)		
	Max	Min	Average	Max	Min	Average
Spring	33	7	19	65	21	48
Summer	32	4	18	74	13	58
Autumn	26	6	16	68	27	52
Winter	27	0	13	53	2	36
All	25	7	17	62	26	48

Similar analyses were applied to the SCIGN region during the period from 1 September 2000 to 31 August 2003 (Table 5.5, Figure 5.8). Like Germany, both the lowest individual and average frequencies over the SCIGN region were observed in winter (2% and 36%, respectively). However, the highest individual and average frequencies were found in summer (74% and 58%, respectively) instead of in spring. The average frequency of cloud free conditions was found to be 48%, with a maximum of 62% in the SCIGN region during the whole 3 years. This suggests that the SCIGN region exhibited higher frequencies of cloud free conditions than Germany, which in turn indicates that the frequency varies from place to place.

5.5.2 Percentage of cloud free conditions

The statistics were calculated as the percentage of cloud free observations relative to all of the observations in Germany for the period from 1 March 2002 to 28 February 2003. Figure 5.9 shows the percentage of cloud free conditions with a trendline showing monthly average values. It is obvious that the percentages of cloud free conditions varied widely, even from 0% to 100% on a day-to-day basis. A seasonal variation can also be observed, e.g. there are far fewer cloud free conditions in the late autumn and the early winter in Germany. The average percentage was 22% during the experimental period.

Figure 5.10 shows the percentage of cloud free conditions over the SCIGN region (33–36° N, 116-119° W) with a monthly trendline. The monthly percentages were found to vary mainly between 35% and 80%. Comparing Figures 5.9 and 5.10, it is clear that the trend line in the SCIGN region was different from that in Germany, and the SCIGN region had a relatively higher overall percentage. It is also obvious in Figure 5.10 that the trendline varied from season to season, and from year to year.

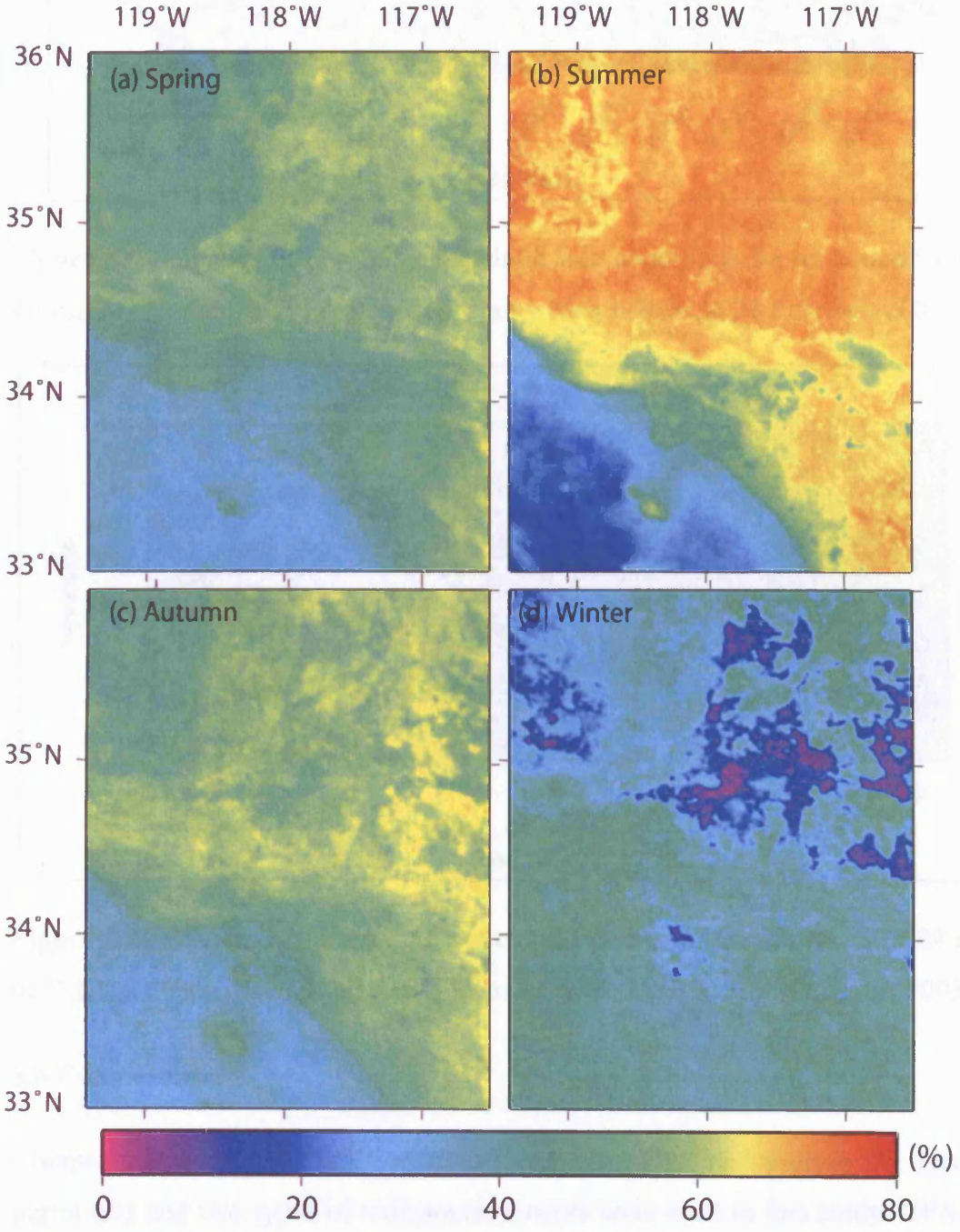

Figure 5.8 Seasonal frequencies of cloud free conditions over the SCIGN area during the period from 1 September 2000 to 31 August 2003.

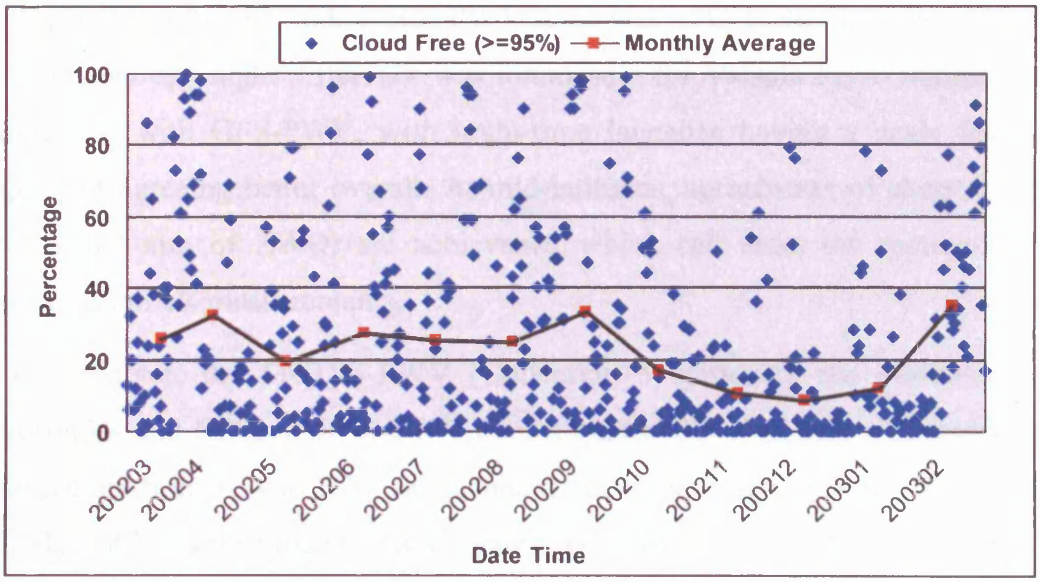

Figure 5.9 Statistics of percentage of cloud free conditions for an area of 4°(lat) x 4°(lon) in Germany during the period from 1 March 2002 to 28 February 2003.

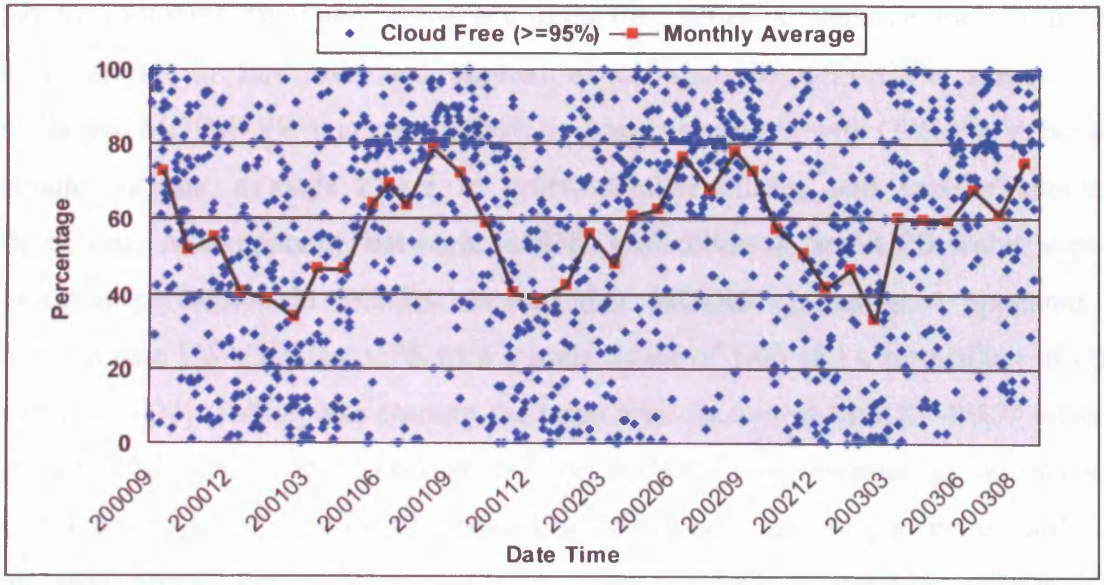

Figure 5.10 Statistics of percentage of cloud free conditions for the SCIGN region of 3°(lat) x 3°(lon) during the period from 1 September 2000 to 31 August 2003.

5.6 Conclusions

Comparisons between PWV values derived from GPS and radiosonde data were performed and two types of radiosonde sensors were used in this study. GPS-PWV was larger than RS-PWV with a scale factor of 0.96±0.006 at the HERS site for the Vaisala RS80-H radiosondes (Table 5.1), which is consistent with *Niell et al.*'s

[2001] findings that the radiosonde PWV scale was ~5% lower than the GPS scale. A significant day-night difference was found only for Vaisala RS90 radiosondes in comparison with GPS-PWV, with night-time launches having a scale factor 4% larger, but agreeing better overall. At mid-latitudes, agreements of about 1 mm of PWV (~6.2 mm of ZWD) are achievable, which can meet the requirement for correcting InSAR measurements.

In this chapter, the MODIS-PWV (Collection 3) products are evaluated using radiosondes and GPS. MODIS-PWV overestimated PWV against radiosondes with scale factors from 1.14 to 1.20, and standard deviations ranging from 1.6 to 2.2 mm. MODIS-PWV overestimated PWV against GPS by a factor of 7% to 14%, with standard deviations varying from 0.8 to 1.4 mm in time series. For the first time, MODIS-PWV (Collection 3) was compared spatially with GPS-PWV using the GASP GPS network in Germany. Taking into account the good linear relationship between MODIS-PWV and GPS-PWV in the time series, an average linear fit model was derived in this area and applied to calibrate MODIS-PWV values. The calibrated MODIS-PWV appeared to be in closer agreement with GPS-PWV, having smaller offsets, a slope closer to unity, smaller biases, and smaller standard deviations. A comparison between MODIS (collection 4) and GPS water vapour products performed in SCIGN showed that MODIS collection 4 appeared to overestimate PWV against GPS with a scale factor of 1.05 and a zero-offset of –0.7 mm [*Li*, 2004]. Taking into account the large scale factors of MODIS-PWV relative to GPS-PWV, it is recommended that the MODIS water vapour products (both Collections 3 and 4) should be updated or calibrated (e.g. using a linear model as proposed above) before being applied to correct InSAR atmospheric effects. The correction method is investigated further in Chapter 7 using MODIS-PWV (collection 4).

To assess the accuracy of MERIS near IR PWV, MERIS near IR water vapour product processed at FUB are evaluated using RS and GPS. The comparison with Vaisala RS-80 radiosondes revealed a strong dry bias of RS measurements for high PWV values with a MERIS/RS scale factor of 1.09 when using the whole data set, or 1.07 under moderate conditions, and the standard deviations were 1.4 and 1.2 mm respectively. A simulation of RS PWV values using GPS data showed that the time

difference between MERIS and RS could contribute to a larger standard deviation, but had no significant effects on scale factors. The comparison of MERIS and GPS PWV showed an excellent agreement with a standard deviation of 1.1 mm, which is well within the estimated accuracy of both techniques. The scatter plots (Figure 5.6(a) and 5.6(b)) showed a slight curvature with positive biases for very low (PWV < 0.5mm) and very high (PWV > 25mm) PWV values, indicating that MERIS PWV overestimated PWV against GPS under both dry (PWV < 0.5mm, mainly in the winter) and wet (PWV > 25mm, mainly in the summer) conditions. In the winter (i.e. under dry conditions), the high solar zenith angle may lead to a decrease of accuracy in the retrieved MERIS PWV. However, in order to assess the accuracy of MERIS near IR PWV under dry/wet conditions, a larger dataset is needed. It should be noted that in any case the standard deviations were very small (within 1.3 mm). Therefore, it appears reasonable to state that MERIS PWV has better accuracy than the theoretical value (viz. 1.6 mm), particularly under moderate conditions with PWV values ranging from 5 mm to 25 mm.

Assuming MERIS water vapour values are independent of each other, a low pass filter with an average width of 2 pixels may improve the accuracy by a factor of 2 at the expense of the spatial resolution (degraded to 2400 m for the FR water vapour product and 600 m for the RR water vapour product respectively). In this case, taking into account the requirements for correcting InSAR measurements (see Section 5.1), MERIS water vapour products can be used for InSAR atmospheric correction.

Since MODIS and MERIS water vapour are sensitive to the presence of clouds, only PWV values above the land are applicable in this study. Therefore, the frequency and the percentage of cloud free conditions were investigated in Germany for 1 year and the Three Gorges area in China for 3 years. The frequencies varied from place to place and the percentages from day to day. Seasonal variations were also observed, and the fewest cloud free observations were found in winter. It appeared that the Three Gorges area had higher frequencies and percentages of cloud free conditions than Germany. Unfortunately, it was found that, even in the Three Gorges area, there was still only 15%~35% cloud free observations for MERIS and MODIS near IR PWV retrievals. Bearing in mind that the global cloud free conditions are about 25%

[*Menzel et al.*, 1996; *Wylie et al.*, 1999], the low percentage of cloud free observations is also a major limitation in applying MERIS and MODIS near IR water vapour products to InSAR atmospheric correction.

Table 5.6 Brief comparisons among GPS, MODIS and MERIS water vapour products

Products	GPS PWV	MODIS near IR PWV	MERIS near IR PWV
Number of Satellites	24	2	1
Coverage*	Regional	Global	Global
Observation Period	Day and night	Day	Day
Spatial Resolution*	A few km to a few hundred km (e.g. 10 km to 25 km over SCIGN)	1 km × 1 km	RR: 1.2km × 1.2km FR: 300m × 300m
Temporal Resolution	Almost continuous (e.g. 5 minutes)	Up to 4 times at some latitudes during daytime	3 days
Sensitivity to Clouds	No	Yes	Yes
PWV Accuracy	~1 mm	5-10% (or 1.6~2.0 mm)	1.6~2.0 mm

*: Both coverage and spatial resolution are relative to current continuous GPS networks in the world.

Table 5.6 gives a brief comparison among GPS, MODIS and MERIS water vapour products. It is clear that these three different types of water vapour products are complementary. On the one hand, GPS water vapour product has higher temporal resolution and much better accuracy than MODIS and MERIS. More importantly, GPS water vapour is not sensitive to the presence of clouds. On the other hand, MODIS and MERIS near IR water vapour products have a much wider coverage and much higher spatial resolution as compared with current Continuous GPS (CGPS) networks.

Due to the relatively limited availability of MERIS data over the last two years (i.e. 2002~2003), only GPS and MODIS data is further investigated in this thesis. The

next two chapters of this thesis aim to produce high accuracy and high spatial resolution 2D water vapour fields for InSAR correction using GPS data only or together with MODIS data, which depends on the data availability:

1) No MODIS data was available before February 2000, but dense CGPS networks have been set up in some areas (e.g. Southern California and Japan) since the early 1990s. Furthermore, MODIS data that is coincident with ERS-2 data may not always be available due to the low percentage and frequency of cloud free conditions. Under such conditions, only GPS data is available to derive 2D water vapour fields, which is the main concern of Chapter 6.

2) When both GPS and MODIS data are available, given the high accuracy and the high temporal resolution of GPS water vapour products as well as the high spatial resolution of MODIS PWV, an integrated method is preferred to produce high accuracy and high spatial resolution 2D water vapour fields, which is presented in Chapter 7.

Chapter 6

InSAR atmospheric correction: I. GPS Topography-dependent Turbulence Model (GTTM)

Integration of InSAR and GPS was first suggested by *Bock and Williams* [1997]. *Williams et al.* [1998] used the Southern California Integrated GPS Network (SCIGN) to assess the possibility of reducing atmospheric effects on interferograms using GPS data. They demonstrated that atmospheric effects appear to conform to a power law and a reduction in power law noise can be achieved by removing the long-wavelength effects (estimated from GPS zenith total (or wet) delays), leaving the higher-frequency, lower power components. Since current GPS networks are generally not optimal for InSAR purposes and GPS-derived zenith total (or wet) delays represent an average along the paths of 4–12 (or more) GPS satellites as they pass the station (which is different from the two-way slant-range propagation in SAR images), it is impossible to remove artefacts with smaller scales than GPS station spacing [*Hanssen*, 2001]. *Wadge et al.* [2002] compared GPS-derived zenith wet delays estimated from 14 continuous GPS (CGPS) and InSAR measurements over Mt. Etna, and found the equivalent delays for InSAR-GPS had an RMS value of 19 mm and a mean bias of +12 mm. With 16 GPS stations over Houston, Texas, *Buckley et al.* [2003] applied atmospheric correction to a Tandem interferogram. Although the artefact reduction was marginal, they demonstrated utility in using GPS-derived zenith wet delays for the assessment of atmospheric effects on interferograms. To date, there have been few satisfactory results for the reduction of atmospheric effects on interferograms. This is usually believed to be due to two factors: 1) the limited spatial resolution of GPS stations; and 2) the lack of an efficient spatial interpolator.

In this chapter, based on an analysis of the spatial structure of water vapour using a spatial structure function, an efficient spatial interpolator is developed and tested along with the traditional Inverse Distance Weighted interpolation method (IDW) [*Shepard*, 1968; Section 7.1.1].

6.1 Spatial Structure Function of water vapour

6.1.1 Spatial Structure Function (SSF)

In order to describe the spatial variation of water vapour as a turbulent medium, a spatial structure function is usually applied. For a random function $x(r_0)$, where r_0 is a spatial coordinate, the spatial structure function for a displacement vector $\vec{L}$ is defined as [*Tatarskii*, 1971; *Treuhaft and Lanyi*, 1987; *Williams et al.*, 1998]:

$$D_x(\vec{L}) = \left\langle \left[x(r_0, \vec{L}) - x(r_0) \right]^2 \right\rangle \tag{6.1.1}$$

where the angle brackets denote an ensemble average. For homogeneous and isotropic random fields, the spatial structure function depends only on the distance $L = |\vec{L}|$ and can be written as:

$$D_x(L) = D_x(\vec{L}) = \left\langle \left[x(r_0, L) - x(r_0) \right]^2 \right\rangle \tag{6.1.2}$$

The spatial structure function is often described as a power law process [*Williams et al.*, 1998]:

$$D_x(L) = C \times L^{\alpha} \tag{6.1.3}$$

where C characterizes the roughness or scale of the process, and α is the power index which expresses the rate at which the random function decorrelates with increasing distance. In the frequency domain, a power law process has a power spectrum:

$$P_x(f) = P_0 \left(\frac{f}{f_0} \right)^{-\beta} \tag{6.1.4}$$

where P_0 and f_0 are normalizing constants, f is the spatial or temporal frequency, and $-\beta$ is the spectral index (often $1 < \beta < 3$). The spatial structure function with the power spectral form of Equation (6.1.4) can be written as [*Hanssen*, 2001]:

$$D_x(L) = C_x \frac{P_0}{f_0^{-\beta}} L^{\beta-1} = C \times L^{\beta-1} \tag{6.1.5}$$

where $C_x = \frac{-\pi^{\beta}}{2^{1-\beta}\Gamma(\beta)\cos(-\beta\pi/2)}$ and $\Gamma(\beta)$ is the gamma function of β. The relationship between the power index α in Equation (6.1.3) and the spectral index $-\beta$ can then be given by:

$$\alpha = \beta - 1 \qquad (6.1.6)$$

When $\alpha = \frac{2}{3}$ (or $\beta = \frac{5}{3}$), it is referred to as Kolmogorov turbulence [*Tatarskii*, 1971].

Based on the spatial structure function (Equations (6.1.2) and (6.1.3)), *Treuhaft and Lanyi* [1987] developed a statistical model (TL hereafter) of water vapour fluctuations to estimate wet tropospheric effects on very long baseline interferometry (VLBI). The TL model relied on two principal assumptions: First, the spatial structure of the fluctuations can be closely approximated by Kolmogorov turbulence theory; Second, temporal fluctuations are caused by spatial patterns which are moved over a site by the wind, i.e. temporal fluctuations are caused by the "frozen" atmosphere being moved by the wind. For simplicity, the TL model also assumed that both the water vapour spatial structure and the wind vector were independent of height up to an effective scale height, and the "frozen" atmospheric water vapour moved across a flat earth. *Treuhaft and Lanyi* [1987] estimated $\alpha = 2/3$ for a distance L of up to 3000 km, whilst $\alpha = 5/3$ for L much smaller than 1 km, with a smooth transition between these two limits. *Williams et al.* [1998] suggested that tropospheric variations conform temporally and spatially to the TL statistical model.

For interferometric observations such as InSAR, its spatial structure function can be simulated by double differencing all possible observable combinations between time t_n and t_m [*Emardson et al.*, 2003]:

$$D_{int}(L,\Delta t) = \left\langle \left\{ \left[x_{t_n}(r_0,L) - x_{t_n}(r_0) \right] - \left[x_{t_m}(r_0,L) - x_{t_m}(r_0) \right] \right\}^2 \right\rangle \qquad (6.1.7)$$

where the subscript *int* represents interferometric observations, and $\Delta t = t_n - t_m$ represents observation intervals. It is clear that a unique temporal change in the

observations leads to $D_x(L,\Delta t)$ equalling zero even when there is strong spatial variation at a given time (t_n or t_m), indicating that atmospheric effects on interferograms are caused by spatio-temporal variations (instead of solely spatial or temporal variations) of the atmosphere (primarily water vapour). See further discussion in Section 6.2.1.

Goldstein [1995] found that the spatial spectrum of atmospheric effects on an SIR-C radar interferogram acquired over the Mojave Desert in California followed a power-law with a spectral index ($-\beta$) of –8/3 for spatial scales between 0.4 km and 6 km. *Hanssen* [2001] studied atmospheric effects on 8 Tandem interferograms acquired over Groningen in the Netherlands during 1995/1996, and found that the noise power spectrum typically has similar power-law behaviour, although the absolute power varied from one interferogram to another. The spectral indices ($-\beta$) varied between –5/3 and –8/3 for the different spatial scales: –5/3 for spatial scales larger than 2 km, –8/3 for intermediate scales between 0.5 km and 2 km, and –2/3 for spatial scales smaller than 0.5 km. *Hanssen* [2001] argued that the –5/3 power-law behaviour represented scales larger than the thickness of the turbulent layer where an approximation of two-dimensional turbulence can be applied, while the intermediate scales were smaller than the thickness of the turbulent layer and the noise structure had a spectral index of –8/3. *Hanssen* [2001] suggested that the –2/3 power-law behaviour at the smallest spatial scales (<0.5 km) was unlikely to have an atmospheric origin, but more likely to result from decorrelation effects or interpolation errors.

6.1.2 Examples of spatial structure function derived from GPS data

Spatial structure functions of ZWD were investigated using the GFZ near real-time GPS water vapour retrievals for one year from 01 June 2002 to 31 May 2003 (see more details on the GFZ NRT GPS water vapour product in Section 4.2.5). The distance from one GPS station to another varied from 7 km to 1705 km. Within this network, only around 2% of the distances were greater than 1000 km.

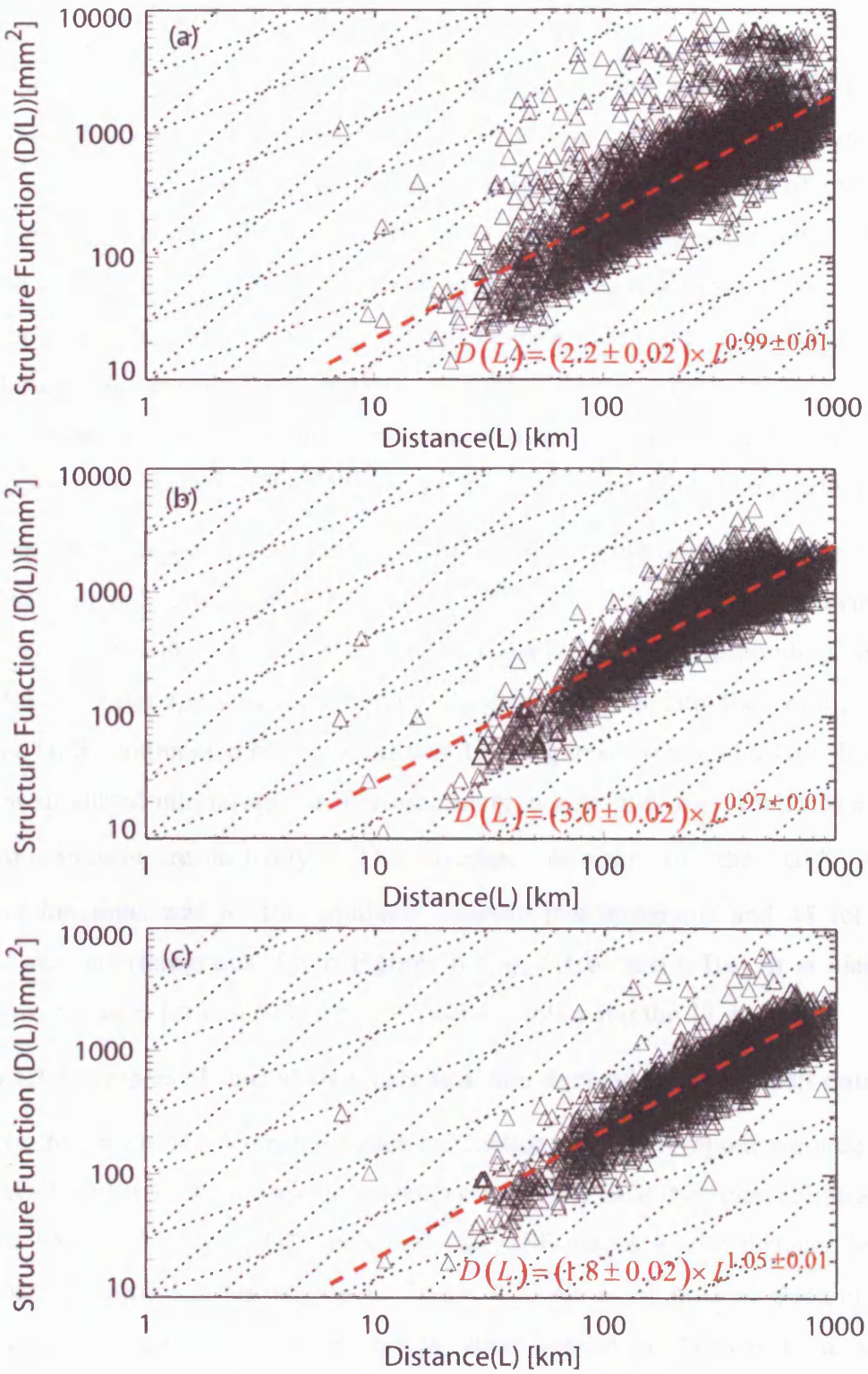

Figure 6.1 Spatial structure functions of ZWD derived from GPS data over Germany during the period from 01 June 2002 to 31 May 2003. a) SSF for simulated 2D ZWD maps; b) SSF for simulated Tandem interferograms (1 day apart); c) SSF for simulated repeat-pass interferograms (35 days apart). The black dotted lines indicate the 2/3 and 5/3 power-law behaviour.

Since *Emardson et al.* [2002; 2003] reported that the water vapour decorrelation range was 500~1000 km based on GPS data from Japan and radiosonde data from Europe, the GPS combination observations (i.e. single differences of ZWD between stations or double differences of ZWD between times after single differences between stations, see Section 6.1.1) were used in this study only if their spacing was not greater than 1000 km. Furthermore, the total number of GPS stations increased during the experimental period, and then the number of GPS observable combinations might be small for some stations. Therefore, another criterion was applied: the number of the GPS observable combinations must be greater than 10.

The spatial structure functions of ZWD across Germany are shown in Figure 6.1. The diagonal dotted lines represent the $2/3^{rd}$ and $5/3^{rd}$ power-law behaviour. Figure 6.1(a) shows the SSF for simulated 2D ZWD maps (corresponding to Equation (6.1.2)). After applying the criteria to the selected GPS data, the average number of the GPS combination observations was 136. Figures 6.1(b) and 6.1(c) show the SSF for simulated interferograms (corresponding to Equation (6.1.7) with $\Delta t = 1$ day and $\Delta t = 35$ days respectively). The average number of the GPS observable combinations was 63 for simulated Tandem interferograms and 44 for simulated 35-day interferograms. From Figures 6.1(a), 6.1(b) and 6.1(c), it is clear that the power indices (α) ranged from 0.97 to 1.09, following the TL model.

6.1.3 Examples of spatial structure function derived from MODIS data

For the first time, the spatial structure functions of water vapour were derived from MODIS near IR water vapour product covering the SCIGN region (Figure 6.2). Like the SSF derived from GPS data, only the SSF values with a distance less than or equal to 1000 km are shown in Figure 6.2. As mentioned in Section 4.3.5, the current resolution of MODIS near IR water vapour products is 1 km x 1 km (at nadir), and the output grid of a single Level-2 MODIS granule is 2,030 1-km pixels in width (across the swath) and 1,354 1-km pixels in length (along the swath). The total number of the observable combinations (corresponding to Equation (6.1.2)) is huge. Therefore, taking into account CPU limitations, all the observable combinations were averaged at a given spatial scale, which is different from Section

6.1.2 where all the observable combinations are shown in Figure 6.1 without averaging. It should also be noted that PWV values were used here instead of ZWD. Since the conversion factor has an impact only on the roughness parameter C, the SSF of PWV can be easily transformed to the SSF of ZWD using:

$$D_{ZWD}(L) = \Pi^2 \times D_{PWV}(L) \approx 6.2^2 \times D_{PWV}(L) \qquad (6.1.8)$$

where Π is the conversion factor defined in Section 4.2.3.

From Figure 6.2, it is clear that the spatial structure function was temporally variable. On the one hand, $D(L)$ started to become relatively flat (despite the variation) from a distance of 200 km in Figure 6.2(a) and (c), indicating that water vapour values were essentially spatially uncorrelated with distances greater than 200 km. However, in Figure 6.2(b), the spatial structure function increased smoothly up to a distance of about 600 km, suggesting that water vapour variations were somewhat correlated within this range. On the other hand, the water vapour variation in Figure 6.2(a) was up to 50 mm^2 at the decorrelation distance of about 200 km, whilst around 40 mm^2 in Figure 6.2(b) and around 60 mm^2 in Figure 6.2(c) at the decorrelation distance.

It should be noted that the power indices lay within the range between 2/3 and 5/3 in Figures 6.2(a) and 6.2(c), but the power index for distances larger than 10 km was smaller than 2/3 in Figure 6.2(b), indicating that water vapour variation might not follow the TL model. However, for the smallest spatial scale (~1 km), the power indices were quite variable, for a reason that currently remains undetermined.

Through the spatial structure analysis, it is shown that the water vapour decorrelation range might be as short as 200 km, which is different from the decorrelation range of 500-1000 km presented by *Emardson et al.* [2002; 2003] based on GPS data from Japan and radiosonde data from Europe. One possible cause for this discrepancy is climate differences at different places and times. Another possible cause lies in the high spatial resolution of the MODIS near IR water vapour fields, which leads to more detailed information on water vapour fields.

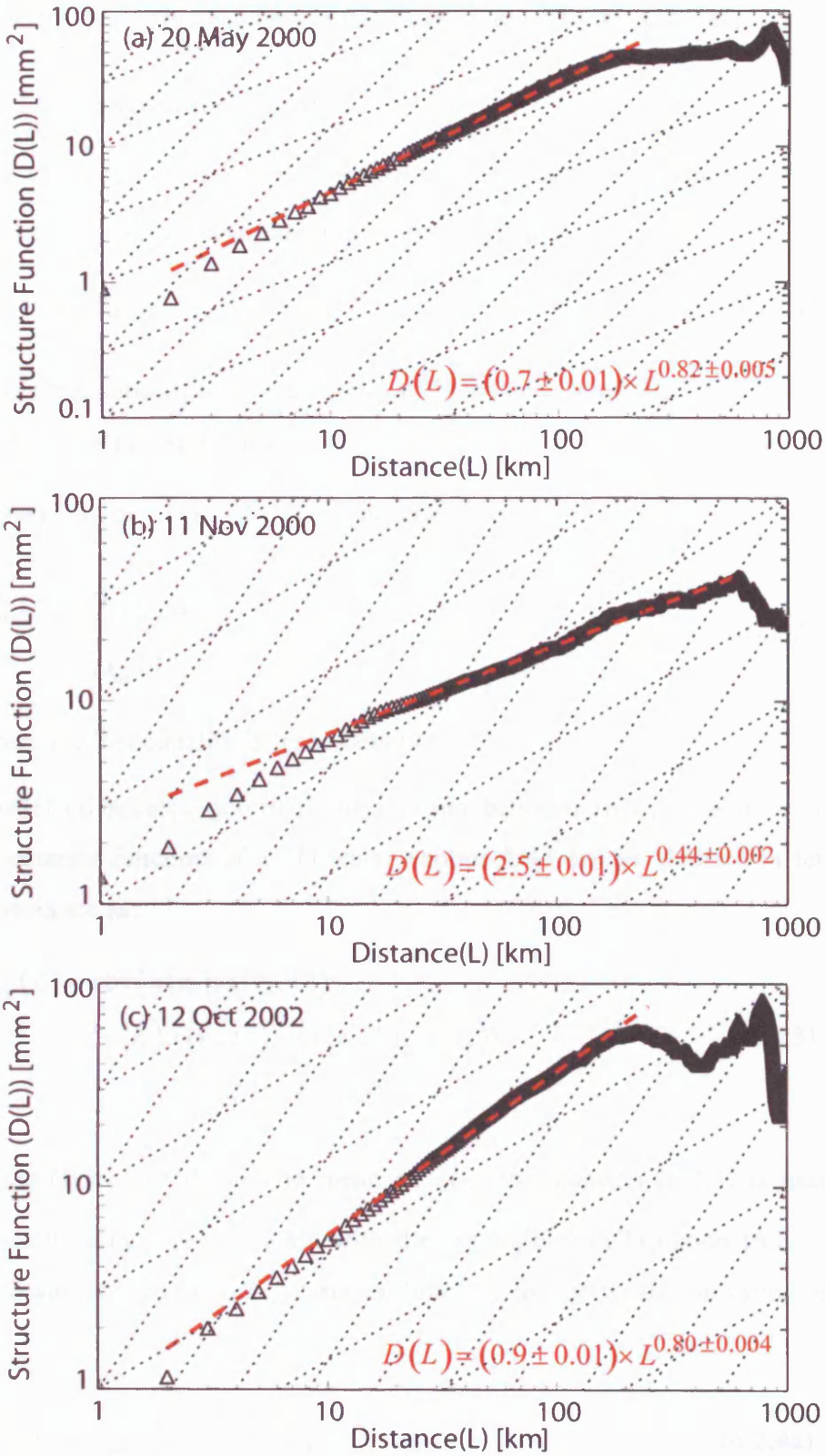

Figure 6.2 Spatial structure functions derived from MODIS near IR water vapour fields. a) Collected at UTC 19:30 on 20 May 2000; b) Collected at UTC 18:45 on 11 November 2000; c) Collected at UTC 18:55 on 12 October 2002. The dotted lines indicate the 2/3 and 5/3 power-law behaviour.

6.2 GPS Topography-dependent Turbulence Model (GTTM)

6.2.1 Variance and covariance

The variance (σ_{wv}^2) of a homogeneous, isotropic and ergodic random water vapour field can be written as a function of distance (L):

$$\sigma_{wv}^2(L) = Var\{[x(r_0, L) - x(r_0)]\} \tag{6.2.1}$$

where the subscript wv represents a 2D water vapour field, and x represents PWV or ZWD values in this thesis.

If the mean of $[x(r_0, L) - x(r_0)]$ is zero, then

$$\begin{aligned} \sigma_{wv}^2(L) &= \left\langle [x(r_0, L) - x(r_0)]^2 \right\rangle \\ &= D_{wv}(L) \end{aligned} \tag{6.2.2}$$

where the last equality is from Equation (6.1.2).

Spatial covariance describes the relation between two points in a 2D image. The covariance function of a 2D water vapour field can be defined in terms of spatial covariance as:

$$\begin{aligned} C_{wv}(L) &= \mathrm{cov}(x(r_0), x(r_0, L)) \\ &= \langle x(r_0) x(r_0, L) \rangle - \langle x(r_0, L) \rangle \langle x(r_0) \rangle \\ &= \langle x(r_0) x(r_0, L) \rangle - (const)^2 \end{aligned} \tag{6.2.3}$$

It should be noted that the mean of $x(r_0)$ in Equation (6.2.3) is assumed to be a constant, which is consistent with the assumption in Equation (6.2.2). Thus, under such an assumption the covariance function can be written in terms of the variance (σ_{wv}^2) as:

$$C_{wv}(L) = C_{wv}(0) - \frac{1}{2}\sigma_{wv}^2(L) \tag{6.2.4a}$$

and in terms of the spatial structure function (SSF, $D_{wv}(L)$) as:

$$C_{wv}(L) = C_{wv}(0) - \frac{1}{2}D_{wv}(L) \tag{6.2.4b}$$

For interferometric observations such as interferograms, the variance (σ^2_{int}) can be written as a function of distance (L) and observation interval (Δt) (also see Equation (6.1.7)):

$$\sigma^2_{int}(L,\Delta t) = Var\left\{\left[x_{t_n}(r_0,L) - x_{t_n}(r_0)\right] - \left[x_{t_m}(r_0,L) - x_{t_m}(r_0)\right]\right\} \quad (6.2.5)$$

where the subscript *int* represents interferometric observations.

If the epochs t_n and t_m are sufficiently separated so that $\left[x_{t_n}(r_0,L) - x_{t_n}(r_0)\right]$ and $\left[x_{t_m}(r_0,L) - x_{t_m}(r_0)\right]$ are uncorrelated, then Equation (6.2.5) reduces to:

$$\begin{aligned}\sigma^2_{int}(L,\Delta t) &= Var\left[x_{t_n}(r_0,L) - x_{t_n}(r_0)\right] + Var\left[x_{t_m}(r_0,L) - x_{t_m}(r_0)\right] \\ &= 2Var\left[x_t(r_0,L) - x_t(r_0)\right]\end{aligned} \quad (6.2.6)$$

As in Equation (6.2.2), if the mean of $\left[x_t(r_0,L) - x_t(r_0)\right]$ is zero, then

$$\begin{aligned}\sigma^2_{int}(L,\Delta t) &= 2\left\langle\left[x_t(r_0,L) - x_t(r_0)\right]^2\right\rangle \\ &= 2D_{wv}(L)\end{aligned} \quad (6.2.7)$$

which is consistent with *Emardson et al.* [2003]. It is clear that the only difference between Equations (6.2.2) and (6.2.7) is a factor of 2.

Under the assumptions of Equations (6.2.6) and (6.2.7), the mean of $\left\{\left[x_{t_n}(r_0,L) - x_{t_n}(r_0)\right] - \left[x_{t_m}(r_0,L) - x_{t_m}(r_0)\right]\right\}$ is zero, so Equation (6.2.5) can also be written as:

$$\begin{aligned}\sigma^2_{int}(L,\Delta t) &= \left\langle\left\{\left[x_{t_n}(r_0,L) - x_{t_n}(r_0)\right] - \left[x_{t_m}(r_0,L) - x_{t_m}(r_0)\right]\right\}^2\right\rangle \\ &= D_{int}(L,\Delta t)\end{aligned} \quad (6.2.8)$$

where the last equality is from Equation (6.1.7).

From Equations (6.2.7) and (6.2.8), it is clear that:

$$D_{int}(L,\Delta t) = 2D_{wv}(L) \quad (6.2.9a)$$

and

$$\sigma^2_{int}(L,\Delta t) = 2\sigma^2_{wv}(L) \quad (6.2.9b)$$

The covariance function of interferometric observations can be written as:

$$\begin{aligned} C_{int}(L,\Delta t) &= \mathrm{cov}\left(\left[x_{t_n}(r_0)-x_{t_m}(r_0)\right],\left[x_{t_n}(r_0,L)-x_{t_m}(r_0,L)\right]\right) \\ &= 2\left\langle x(r_0)\,x(r_0,L)\right\rangle - 2(const)^2 \end{aligned} \tag{6.2.10}$$

where the last equality is derived under two assumptions: 1) The epochs t_n and t_m are sufficiently separated so that $\left[x_{t_n}(r_0,L)-x_{t_n}(r_0)\right]$ and $\left[x_{t_m}(r_0,L)-x_{t_m}(r_0)\right]$ are uncorrelated as in Equation (6.2.6); and 2) The mean of $x(r_0)$ is assumed to be a constant as in Equation (6.2.3). Hence, similar to Equations (6.2.4a) and (6.2.4b), Equation (6.2.10) becomes:

$$\begin{aligned} C_{int}(L,\Delta t) &= C_{int}(0,\Delta t) - D_{wv}(L) \\ &= C_{int}(0,\Delta t) - \frac{1}{2}D_{int}(L,\Delta t) \\ &= C_{int}(0,\Delta t) - \frac{1}{2}\sigma^2_{int}(L,\Delta t) \end{aligned} \tag{6.2.11}$$

6.2.2 GPS topography-dependent turbulence model (GTTM)

Based on the TL model, *Jarlemark and Emardson* [1998] proposed a topography-independent turbulence-based method to spatially interpolate wet delays:

$$\hat{\ell}_e = \sum_i a_i \cdot \ell_i \tag{6.2.12}$$

where $\hat{\ell}_e$ are the estimates of ZWD, ℓ_i are measured values of ZWD, and a_i are the weights of ZWD values.

Using Equations (6.1.3) and (6.2.4b), the covariance matrix $C_{m,m}$ between all measured ZWD values can be calculated as well as the covariance matrix $C_{m,e}$ between the measured and the estimated values, and then all the measured values can be used to construct a Best Linear Unbiased Estimator (BLUE) [e.g. *Kay*, 1993]. The optimal weights can then be written in vector form as:

$$a_{BLUE} = C^{-1}_{m,m}\cdot C_{m,e} + \frac{\left(1 - C^T_{m,e}\cdot C^{-1}_{m,m}\cdot s\right)\cdot C^{-1}_{m,m}\cdot s}{s^T\cdot C^{-1}_{m,m}\cdot s} \tag{6.2.13}$$

where s is a vector of ones whose length is the number of measured values.

Jarlemark and Emardson [1998] reported that the turbulence model produced lower RMS errors when used to interpolate ZWD in different directions at different time-instants as compared with a method that estimates horizontal gradients in the wet delay. *Emardson and Johansson* [1998] demonstrated that it was possible to interpolate ZWD to a particular location with an accuracy of approximately 1 cm, even with a widely distributed (c. 100 km spacing) permanent GPS network using the turbulence model. It should be noted that in their study [*Emardson and Johansson,* 1998] the elevation variation reached a maximum of only 214 metres, and thus this approach might not be applicable in mountain areas such as SCIGN which has an elevation variation of about 3000 metres.

Using GPS data from 126 stations in SCIGN spanning the period from January 1998 to March 2000, *Emardson et al.* [2003] found that the spatio-temporally averaged variance of water vapour depends not only on the distance between observations (L), but also on height difference (H) as follows:

$$\sigma_{int} = c \times L^{\gamma} + k \times H \qquad (6.2.14)$$

where $c = 2.8$, $\gamma = 0.44$, $k = 0.5$ for observation intervals of one day, σ is in millimetres, L and H are in kilometres. It should be noted that the estimate of γ in Equation (6.2.14) corresponds to half of α in Equation (6.1.3), i.e. $\gamma \approx \alpha/2$.

With Equations (6.2.11) and (6.2.14) being used to estimate the covariance matrix for the turbulence model, zenith total delays can be interpolated using Equations (6.2.12) and (6.2.13). It should be noted that typical values of c, α, and k estimated by *Emardson et al.* [2003] were adopted for the SCIGN area in this study. This topography-dependent turbulence model is designated as GPS Topography-dependent Turbulence Model (GTTM in short) in this thesis since only GPS data is required in this turbulence model.

It should be noted that Equation (6.2.14) can only be used with interferometric observations since it was derived from simulated interferometric values [*Emardson et al.*, 2003]. In order to apply Equation (6.2.14) to interpolate PWV or ZWD in a

2D water vapour field, the relationship between σ_{int}^2 and σ_{wv}^2 has to be taken into account (see Equation (6.2.9b)).

6.2.3 Cross validation of the GTTM

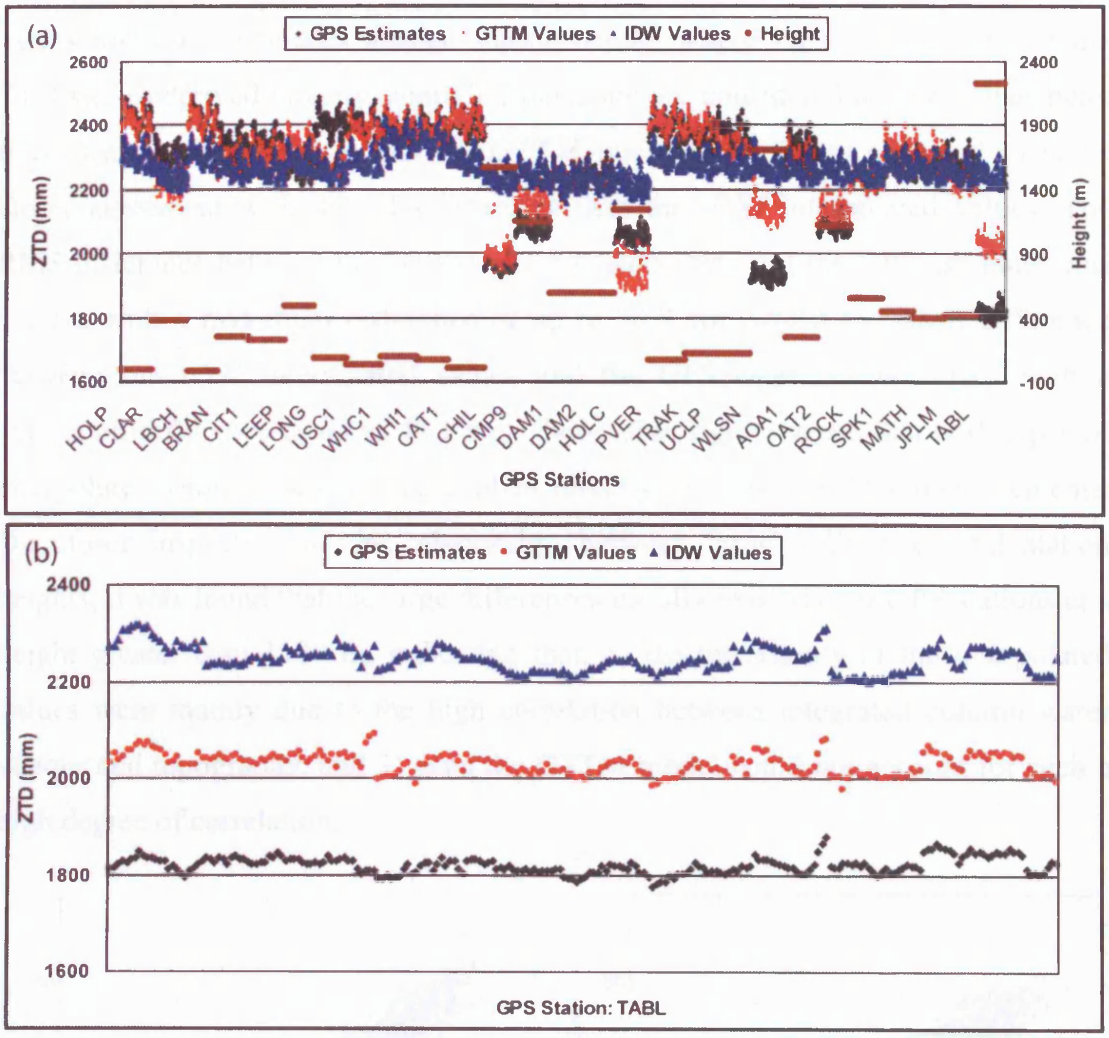

Figure 6.3 Cross validation of the GTTM and IDW methods on ZTD values. (a) The left vertical axis represents ZTD values in mm, while the right vertical axis shows station height in metres; (b) The trend of three ZTD time series derived by different methods over the TABL (Table Mountain) GPS station with a height of 2228 m.

To test the capability of the GTTM, a cross validation test was applied to the GTTM model as well as the traditional Inverse Distance Weighted interpolation method (IDW) [*Shepard*, 1968; Section 7.1.1] with 288 samples over up to 27 CGPS stations during the period from 1995 to 1996, i.e. the total number of cases used in this test was about 288 × 27 = 7776 (actual total of 7164). Cross validation involved

removing a sampled point from the data set and using all the other data to estimate the value at that point [*Williams et al.,* 1998]. This procedure was repeated for all sampled points and the observed data compared with the predicted.

Figure 6.3(a) shows the differences between the GTTM and IDW interpolated values and GPS estimates against station height, where GPS estimates mean the ZTD values derived directly from GPS data, and are considered as true values here. It is clear in Figure 6.3(a) that the GTTM interpolated values appeared to be in closer agreement with the GPS estimates than the IDW interpolated values. The RMS difference between the GTTM interpolated values and the GPS estimates was 5.5 cm with a maximum difference of up to 30.0 cm, whilst the RMS difference between the IDW interpolated values and the GPS estimates was 10.7 with a maximum difference of up to 48.1 cm. These large figures mean that both types of interpolated values could not be applied directly to correct InSAR measurements. On closer inspection of the relationship between large differences and station heights, it was found that the large differences usually existed over GPS stations at a height greater than 1100 m, indicating that: 1) the uncertainty of the interpolated values were mainly due to the high correlation between integrated column water vapour and topography; and 2) even the GTTM model could not account for such a high degree of correlation.

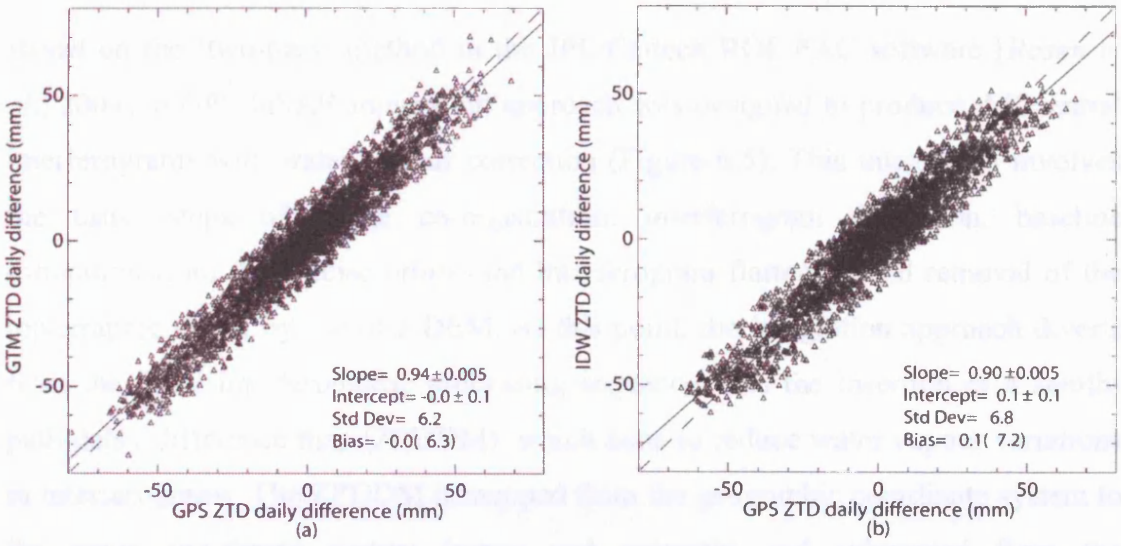

Figure 6.4 Cross validation of GTTM and IDW methods on ZTD daily differences.

In Figure 6.3(b), it is clear that the trends of different ZTD estimates for the TABL (Table Mountain) GPS station were similar though offset by large, but nearly

constant, amounts. Similar trends could be observed over other GPS stations including CHIL (Chilao), CMP9 (Fire Camp 9), HOLC (Holcomb Ridge), WLSN (Mt. Wilson), and OAT2 (Oat Mountain 2) (Figure 6.3(a)). The constancy of this offset implies that elevation effects could be reduced to a large extent when differencing ZTD values from different times. Taking into account the fact that what matters to an interferogram is the change in ZTD from scene to scene, rather than the absolute value of ZTD itself, another cross validation test was performed using the differences between ZTD values one day apart (Figure 6.4). All together, there were 3418 cases in this test. It is shown that the GTTM model was slightly better than the IDW method with a standard deviation of 6.3 mm for the GTTM (Figure 6.4(a)) against 7.2 mm for the IDW (Figure 6.4(b)). Therefore, from Equations (3.1.9) and (5.1.1), the uncertainty introduced by the GTTM model might lead to additional uncertainties of 6.8 mm for deformation estimates when using ERS-1/2 data with incidence angles of 23°, and even the uncertainty introduced by the IDW could only result in additional uncertainties of 7.8 mm, which implies that both the GTTM and IDW methods could be used to produce zenith-path-delay difference maps (ZPDDM) for InSAR atmospheric correction using ZTD (or ZWD) differences between different times.

6.3 A GPS and InSAR integration approach

Based on the 'two-pass' method in the JPL/Caltech ROI_PAC software [*Rosen et al.*, 2004], a GPS/InSAR integration approach was designed to produce differential interferograms with water vapour correction (Figure 6.5). This integration involves the usual steps of image co-registration, interferogram formation, baseline estimation from the precise orbits, and interferogram flattening and removal of the topographic signal by use of a DEM. At this point, the integration approach diverts from the usual interferometric processing sequence with the insertion of a zenith-path-delay difference map (ZPDDM), which aims to reduce water vapour variations in interferograms. The ZPDDM is mapped from the geographic coordinate system to the radar coordinate system (range and azimuth) and subtracted from the interferogram. For longer time intervals, a model for ongoing deformation can also be subtracted in the same way [*Peltzer et al.*, 2001] in this step. This corrected

interferogram can be unwrapped and then used in baseline refinement. The wrapped, water-vapour-corrected interferogram with refined baseline is made by flattening the original interferogram using the refined baseline and precise DEM, and then the differential water vapour field is subtracted from the differential interferogram. In order to obtain the unwrapped water vapour corrected interferogram, a new simulated interferogram is created using the refined baseline and topography, and is subtracted from the unwrapped phase (including orbital ramp) with the water vapour model removed.

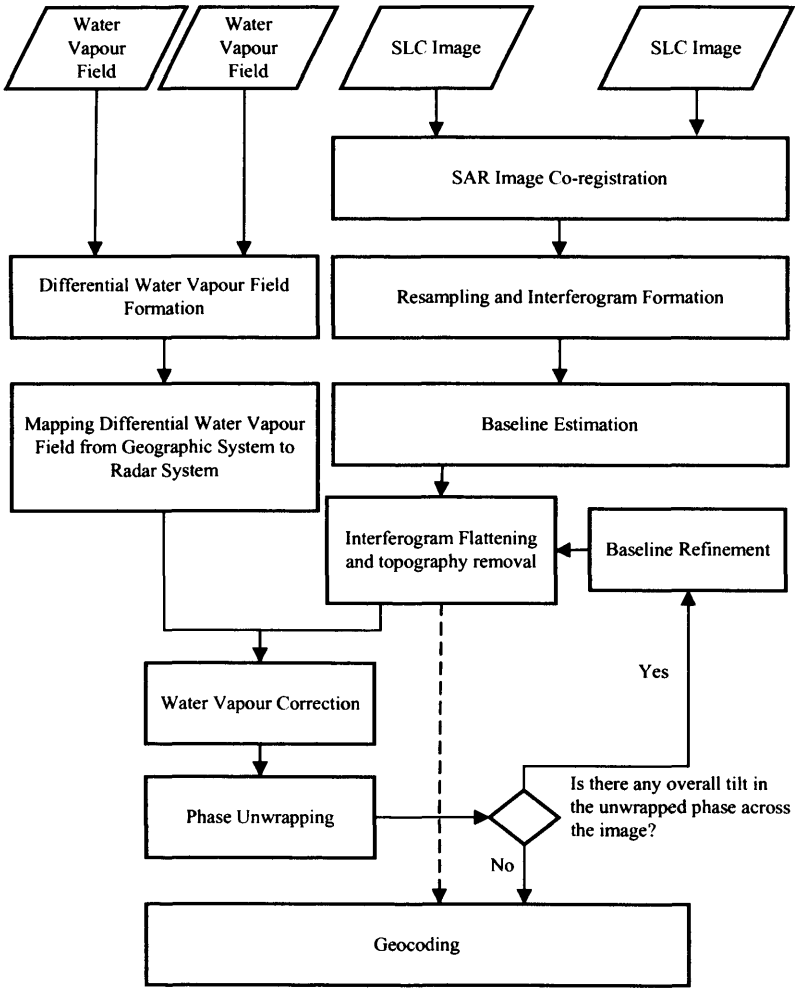

Figure 6.5 2-DInSAR processing flowchart with water vapour correction.

Prior to this study, several studies had been carried out to calibrate water vapour effects on InSAR using atmospheric delay models or independent data sources, including *Delacourt et al.* [1998], *Bonforte et al.* [2001], and *Wadge et al.* [2002]. Among these studies, atmospheric effects were subtracted from (or compared with)

the wrapped (or unwrapped) phase, but these water vapour corrections were not used to improve the InSAR processing, so they were not truly integrated methods. *Buckley et al.* [2003] suggested applying water vapour corrections to the unwrapped phase, and then using the corrected unwrapped phase to refine the baseline. Although the difference between the uncorrected and corrected interferograms was marginal, it was the first time water vapour correction was integrated with InSAR processing. However, this method might suffer from smearing of atmospheric artefacts during the filtering process, widely used in InSAR processing to reduce phase noise [e.g. *Goldstein and Werner*, 1998]. For instance, some topography-dependent water vapour signals, whose wavelength is relatively short but could be estimated using GPS data or other datasets, might be spread over a larger area when a non-linear filter is applied before subtracting water vapour. It is believed that the water vapour correction approach proposed here has advantages over all previous approaches: 1) since the water vapour correction is performed directly on the unfiltered, wrapped interferogram followed by filtering, the performance of the filter does NOT have any unequal impacts on the water vapour correction; 2) reducing the atmospheric effects on the wrapped interferograms may improve phase unwrapping; 3) the corrected unwrapped phase is expected to improve the refined baseline.

6.4 Application to ERS Tandem data over SCIGN

In order to evaluate the efficiency, utility and potential of GTTM, three case studies (Table 6.1) were performed with two processing procedures: 1) the usual 'two-pass' method, and 2) the use of water vapour correction. ERS-1/ERS-2 Tandem data acquired just one day apart was used, so there should be no significant deformation signals in the differential interferograms. The phase remaining in the Tandem interferograms after removing the known topographic and baseline effects should be almost entirely due to changes in the atmosphere between the two acquisitions. The topographic phase contribution was removed using a 1-arc-second (~30 m) DEM from the Shuttle Radar Topography Mission (SRTM) [*Farr and Kobrick*, 2000; Section 2.3.1]. From the elevation sensitivities in Table 6.1, it can be concluded that atmospheric effects should dominate over DEM errors in the differential interferograms (referred to as Ifms hereafter) with short baselines (e.g. Ifm 1 and 3).

Table 6.1 Details of interferograms (Ifms) employed in this chapter

	Track	Frame	Date 1	Date 2	Δt (days)	$B_\perp$ (m)[a]	σ (radians)[b]
Ifm1	442	2925	10-Jan-1996	11-Jan-1996	1	120 to 123	0.59
Ifm2	170	2925	13-Oct-1995	14-Oct-1995	1	-387 to -391	1.89
Ifm3	170	2925	05-Apr-1996	06-Apr-1996	1	96 to 98	0.47

[a] Perpendicular baseline at centre of swath which varies along the track between the values shown.

[b] Possible phase error due to the topographic uncertainty of the SRTM DEM. Note: the average perpendicular baseline was used to estimate the possible phase error.

For the analysis of the spatial variation of unwrapped phase (or water vapour signals), a 2D spatial structure function (2D-SSF) was defined as [*Hanssen*, 2001]:

$$D_x(\Delta r,\alpha)=\left\langle\left[\delta(r_0,\Delta r,\alpha)-\delta(r_0)\right]^2\right\rangle \qquad (6.4.1)$$

where δ is the unwrapped phase (or water vapour signals), r_0 is any random pixel location in the image, Δr is the distance from the denoted pixel, α is the azimuth from the denoted pixel, and the angle brackets indicate an ensemble average. The 2D-SSF gives the expectation value of the squared difference between two pixels at a certain distance Δr and azimuth α in the image, and reveals the spatial phase variation in the interferogram. From the definition of the 2D-SSF in Equation (6.4.1), it can be concluded that:

1) The larger the SSF value, the larger the phase variation at the given distance and azimuth;

2) The 2D-SSF is symmetric about a point at the origin, and the centre of the plot is usually selected as the origin;

3) There are fewer measurements available for the edges and corners of the plot; consequently, some caution needs to be exercised when interpreting the borders [*Hanssen*, 2001].

To make it easy to understand for most people, particularly non-InSAR specialists, the unwrapped phase is employed to show interferograms in this chapter. It should be noted that the unwrapped phase has been converted to range change in millimetres where a positive range change means apparent motion of the ground away from satellite (or an increase in the delay of radar propagation due to the atmosphere).

6.4.1 Interferogram: 10 Jan 1996 – 11 Jan 1996

Figure 6.6(a) shows topography from the 1-arc-second SRTM DEM and 6.6(b) shows the unwrapped phase of the ERS Tandem interferogram 1996/01/10-1996/01/11 (i.e. Ifm1). It is clear that atmospheric signals in Ifm1 appear to be highly correlated with topography.

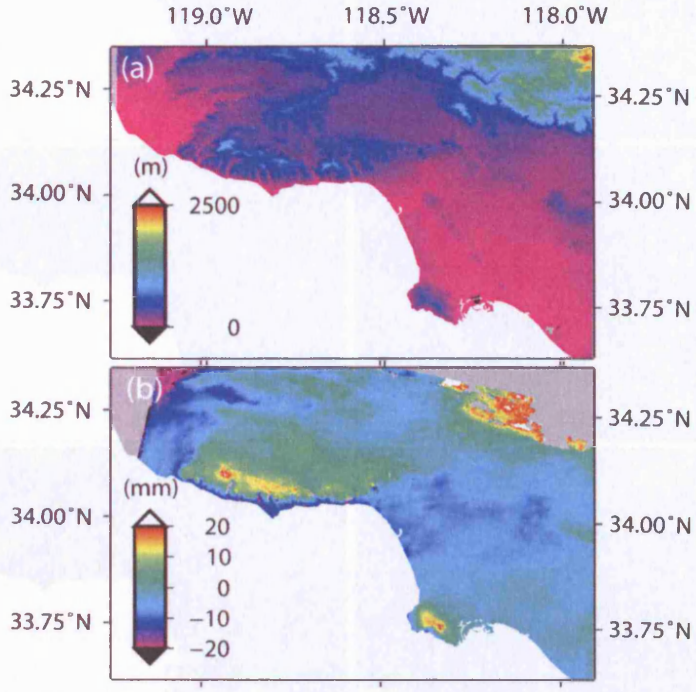

Figure 6.6 Correlation between topography and unwrapped phase. (a) SRTM DEM, elevations in meters; (b) Interferogram 960110-960111.

Figure 6.7 shows the use of the GTTM and IDW methods to correct Ifm1. After applying the GTTM water vapour correction to the original interferogram, it is clear that the Tandem interferogram was significantly improved. Most residual fringes were removed with the RMS decreasing from 1.30 radians (~0.58 cm) (Figure 6.7(a)) to 0.87 radians (~0.40 cm) (Figure 6.7(c)). On the other hand, when the IDW was used, the RMS of the resultant interferogram decreased to only 1.08 radians (~0.49 cm) (Figure 6.7(e)), indicating that the GTTM model works more efficiently than the IDW. On closer inspection of the amount of unwrapped phase over the Palos Verdes hills (indicated by black rectangles), it was found that these signals were significantly reduced after applying the GTTM correction (Figure 6.7(c)), whilst the amount slightly increased after the IDW correction (Figure 6.7(e)), providing strong supporting evidence for the conclusion and suggesting that the

GTTM model can reduce topography-dependent water vapour signals better than the IDW method.

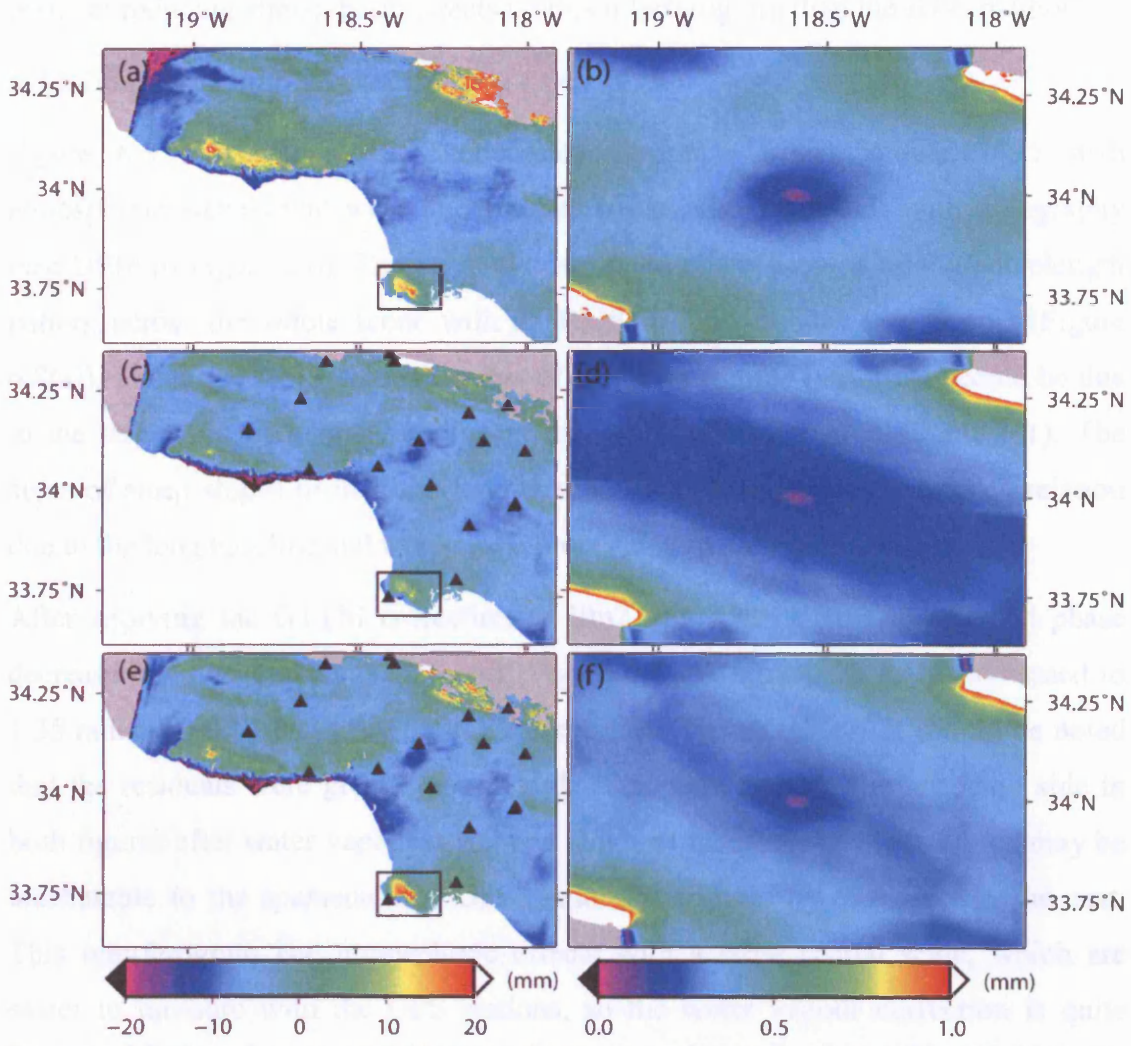

Figure 6.7 Interferogram 960110-960111. (a) Original Ifm1; (b) 2D-SSF for Original Ifm1; (c) Corrected Ifm1 using the GTTM; (d) 2D-SSF for the GTTM-Corrected Ifm1; (e) Corrected Ifm1 using the IDW; (f) 2D-SSF for the IDW-Corrected Ifm1. Note solid black triangles in (c) and (e) represent GPS stations used, and the grey in (f) implies that no valid pair of unwrapped phase existed at the given distance and azimuth.

It should be noted that there is more area of unwrapped phase in the San Gabriel Mountains at the NE corner of Figure 6.7(c) (and/or 6.7(e)) than indicated in Figure 6.7(a), implying that the reduction of the sharp phase gradients due to the atmosphere in the mountains improved the filtering and phase unwrapping.

Comparing the figures for the square root of the 2D-SSF of Ifm1 with and without water vapour correction (Figures 6.7(b), 6.7(d), and 6.7(f)), one can conclude that

the phase variation decreased after both the GTTM and IDW corrections. Comparison between Figures 6.7(d) and 6.7(f) shows that the GTTM model is much better at reducing atmospheric effects on this interferogram than the IDW method.

6.4.2 Interferogram: 13 Oct 1995 – 14 Oct 1995

Figure 6.8 shows an ERS Tandem interferogram from October 1995 with atmospheric signals that were uncorrelated (or poorly correlated) with topography (see DEM in Figure 2.6). The original unwrapped phase showed a long-wavelength pattern across the whole scene with an RMS of 1.56 radians (~0.70 cm) (Figure 6.8(a)). The larger RMS value than that of the first example (viz. Ifm1) could be due to the larger perpendicular baseline in the second interferogram (Table 6.1). The areas of steep slopes in this interferogram had very low interferometric correlation due to the long baseline and were masked out (grey in the figures).

After applying the GTTM correction to Ifm2, the RMS of the unwrapped phase decreased to 1.26 radians (~0.56 cm) (Figure 6.8(c)), whilst the RMS decreased to 1.35 radians (~0.61 cm) after the IDW correction (Figure 6.8(e)). It should be noted that the residuals were greater on the right hand side than on the left hand side in both figures after water vapour correction (Figures 6.8(c) and 6.8(e)), which may be attributable to the sparseness of GPS stations (indicated by triangles) in the east. This interferogram had atmospheric effects with a large spatial scale, which are easier to measure with the GPS stations, so the water vapour correction is quite successful. The masking of the more mountainous areas due to their low coherence also removed the areas where the topography-dependent correction would have the greatest effect.

From the 2D-SSF figures for Ifm2 before and after correction (Figures 6.8(b), 6.8(d) and 6.8(f)), it is obvious that the phase variation decreased after both water vapour corrections, indicating that both the GTTM and IDW methods can reduce topography-independent water vapour effects significantly. A further comparison between Figures 6.8(d) and 6.8(f) shows that the GTTM is slightly better at reducing the topography-independent water vapour effects than the IDW method in this case.

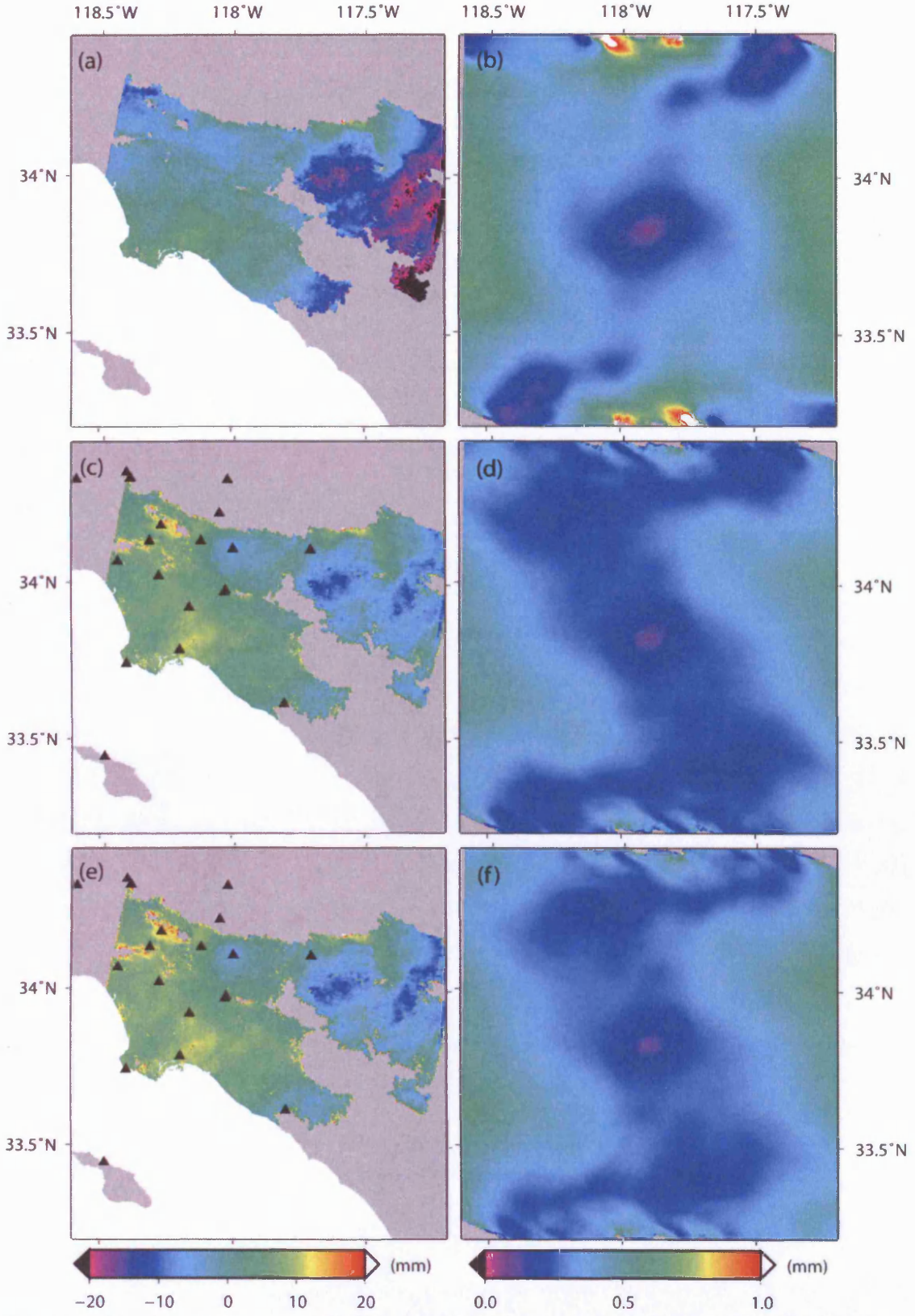

Figure 6.8 Interferogram 951013-951014. (a) Original Ifm2; (b) 2D-SSF for Original Ifm2; (c) Corrected Ifm2 using the GTTM; (d) 2D-SSF for the GTTM-Corrected Ifm2; (e) Corrected Ifm2 using the IDW; (f) 2D-SSF for the IDW-Corrected Ifm2. Note solid black triangles represent GPS stations used.

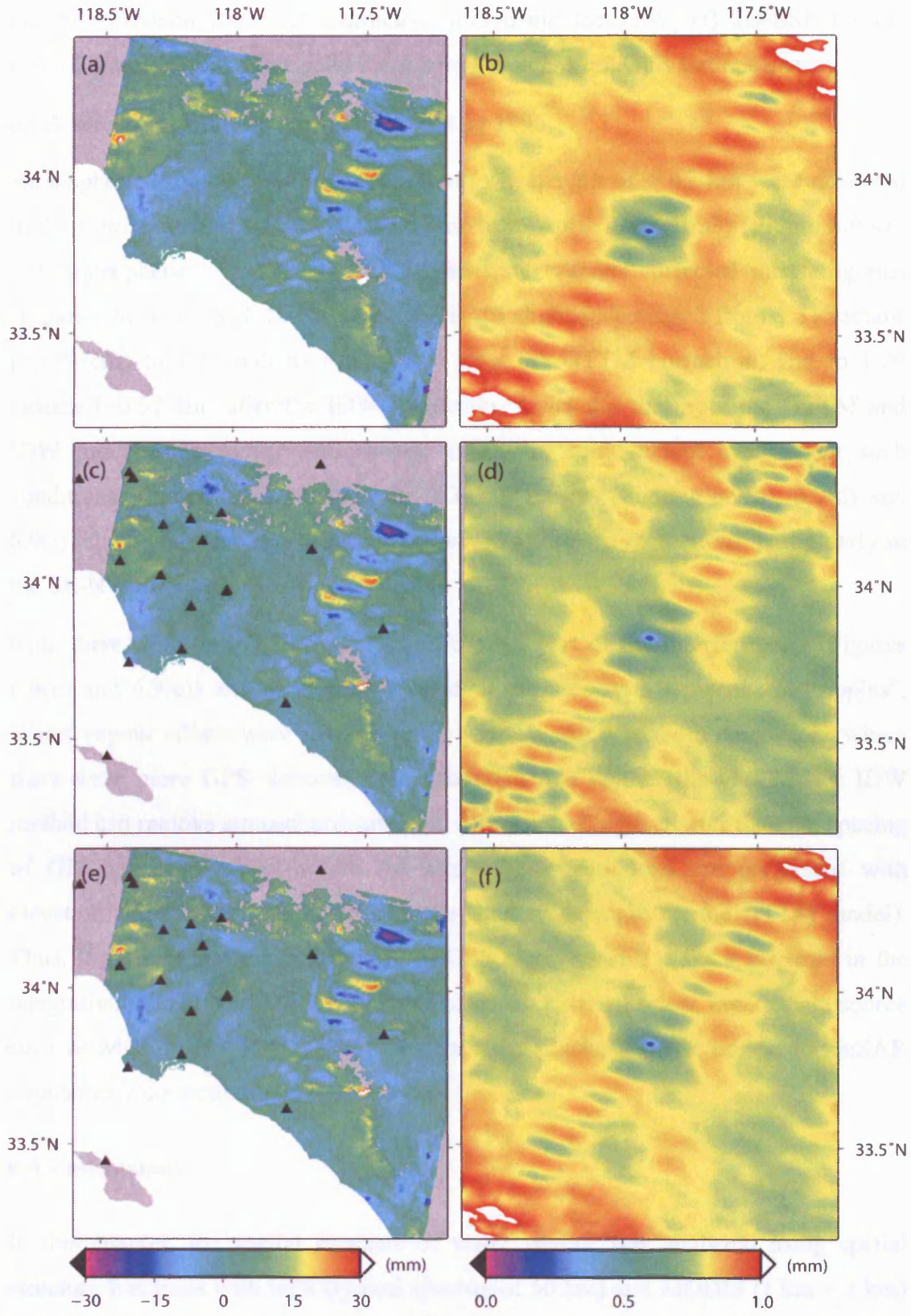

Figure 6.9 Interferogram 960405-960406. (a) Original Ifm3; (b) 2D-SSF for Original Ifm3; (c) Corrected Ifm3 using the GTTM; (d) 2D-SSF for the

GTTM-Corrected Ifm3; (e) Corrected Ifm3 using the IDW; (f) 2D-SSF for the IDW-Corrected Ifm3. Note solid black triangles represent GPS stations used.

6.4.3 Interferogram: 05 Apr 1996 – 06 Apr 1996

Atmospheric "ripples" with a characteristic wavelength of 4~12 km were observed in the third example, an ERS Tandem pair from April 1996 (Ifm3) (Figure 6.9(a)). The atmospheric "ripples" are still in the water vapour corrected interferograms (Figure 6.9(c) and 6.9(e)). However, the RMS slightly decreased from 1.31 radians (~0.59 cm) to 1.22 radians (~0.55 cm) after the GTTM correction, and to 1.26 radians (~0.57 cm) after the IDW correction, indicating that both the GTTM and IDW models can reduce atmospheric effects to some extent even under such conditions. Comparisons between the 2D-SSF images (Figures 6.9(b), 6.9(d) and 6.9(f)) show that the phase variation decreased after both corrections, particularly in the SE-NW direction.

Note there were only 3 GPS stations in the NE part of the interferogram (Figures 6.9(c) and 6.9(e)) and none were located in the area with atmospheric "ripples". Water vapour effects were reduced in the western part after both corrections where there were more GPS stations. It is concluded that neither the GTTM nor IDW method can remove atmospheric artefacts with a wavelength shorter than the spacing of GPS stations (except where the atmospheric variations are correlated with elevation and the topographic relief has a short wavelength for the GTTM model). Thus, it appears that the distribution of GPS receivers still plays a key role in the integration of GPS and InSAR. In these cases, an external water vapour data source such as MODIS [*Li et al.*, 2005; Chapter 7] might be a better option for InSAR atmospheric correction.

6.5 Conclusions

In this chapter, the spatial structure of water vapour was analyzed using spatial structure functions with GPS (typical spacing of 50 km) and MODIS (1 km × 1 km) data. It was shown that: 1) water vapour varied significantly from time to time; 2) the water vapour decorrelation range might be as short as 200 km over SCIGN, which is different from the decorrelation range of 500-1000 km presented by *Emardson et al.* [2003]; 3) water vapour variation might not follow the TL model. It

should be noted here that the water vapour variation shown in Figure 6.2(b) still exhibited a power-law behaviour, although the power index (α) for distances larger than 10 km was smaller than 2/3, outside the range of the TL model (i.e. [2/3, 5/3]).

A topography-dependent turbulence model (i.e. GTTM) has been developed using GPS data only in this chapter. Cross validation tests on the GTTM and IDW methods showed that: 1) In order to produce zenith-path-delay difference maps (ZPDDM) for InSAR atmospheric correction, the GTTM and IDW methods should be applied to ZTD differences (instead of ZTD values). This is crucial to reduce (if not completely remove) the component due to topographic effects; 2) The GTTM model appeared to be better than the IDW, with a standard deviation of 6.3 mm for the GTTM (Figure 6.4(a)) against 7.2 mm for the IDW (Figure 6.4(b)).

A GPS and InSAR integration approach was successfully incorporated into the JPL/Caltech ROI_PAC software. It appeared that this integration approach not only reduces atmospheric effects in interferograms, but also improves phase unwrapping. The application of this integration approach to ERS tandem data showed that the GTTM can reduce significantly not only topography-dependent but also topography-independent atmospheric effects. However, the failure to reduce short-wavelength atmospheric "ripples" using the GTTM and IDW methods indicated that both methods are also limited by the spatial distribution of GPS stations, and only the long-wavelength water vapour variations and some height-dependent effects could be removed through the use of GPS data. Note that the number of Continuous GPS (CGPS) stations in SCIGN has greatly increased since the 1995-1996 time frame covered by the ERS Tandem mission, and it has much better coverage now.

It should also be noted that the model parameters c, α, and k were fixed to the values estimated from the 126 GPS stations over SCIGN during the period from January 1998 to March 2000 [*Emardson et al.*, 2003]. A better reduction might be achieved if the model parameters were estimated from case to case, taking into account the large water vapour variations observed in the spatial structure analysis, which will be an important issue in future work.

Chapter 7

InSAR atmospheric correction: II. GPS/MODIS integrated model

In Chapter 6, a topography-dependent turbulence model (GTTM) was presented which provides 2D zenith path delay fields using GPS data only. A demonstration of the application of GTTM to ERS Tandem data over SCIGN showed that GTTM could reduce water vapour effects significantly. A disadvantage of GPS and InSAR integration is that the required dense GPS network is not usually available, especially in remote areas.

Space-based monitoring is an effective way to obtain measurements of the water vapour distribution on a global basis with a spatial resolution much closer to SAR images. As shown in Table 5.6, MODIS near IR water vapour product has a much wider coverage and much higher spatial resolution as compared with current Continuous GPS (CGPS) networks. In this chapter, GPS and MODIS data are integrated to provide regional water vapour fields with a high spatial resolution of 1 km × 1 km. A water vapour correction model based on the resultant water vapour fields is successfully incorporated into the JPL/Caltech ROI_PAC software and results demonstrated. It should be noted that the Terra MODIS near-IR water vapour product used in this chapter is taken from Collection 4.

7.1 Production of regional 2D 1 km × 1 km water vapour fields using GPS and MODIS data

On the one hand, MODIS near IR water vapour has a scale uncertainty of water vapour (Section 5.3). On the other hand, MODIS near IR water vapour is sensitive to the presence of clouds, and the global cloud free conditions are only about 25% [*Menzel et al.*, 1996; *Wylie et al.*, 1999; Section 5.5]. Therefore, both the accuracy and the missing values limit the application of MODIS near IR water vapour product. In this section, an attempt is made to use GPS data to calibrate the scale of

MODIS water vapour product, and to use an improved Inverse Distance Weighted interpolation (IIDW) to fill in cloudy pixels. It should be noted that the topography-dependent turbulence model developed in Chapter 6 was not applied here due to CPU limitations, even though it is expected that this would improve the interpolation in mountain areas.

7.1.1 Improved Inverse Distance Weighted Interpolation (IIDW)

Inverse Distance Weighted interpolation (IDW) assumes each measured pixel has a local influence on the predicted pixels that decreases with distance [*Shepard*, 1968]. It can be written as:

$$\begin{cases} \hat{D}(\lambda_0,\varphi_0)=\sum_i w_i D(\lambda_i,\varphi_i) \\ w_i=\dfrac{d_{i0}^{-p}}{\sum_i d_{i0}^{-p}} \\ \sum_i w_i = 1 \end{cases} \tag{7.1.1}$$

where D are measured values, i.e. MODIS PWV values under cloud free conditions in this chapter, $\hat{D}$ is the predicted PWV value; λ and φ are longitude and latitude respectively; the subscript 0 denotes the predicted value, the subscript i denotes a measured value; d_{i0} is the distance between the measured pixel and the "missing" pixel; p is a power parameter which influences the weighting of the predicted value. A lower power leads to a smoother surface and a high power results in a more detailed surface. A typical power parameter is 2.

Obviously, when the distance is sufficiently large, water vapour values are uncorrelated with each other. *Emardson et al.* [2003] analyzed 126 GPS stations over SCIGN spanning the period from January 1998 to March 2000, and found that the water vapour variations were uncorrelated at distances greater than ~800 km. In Section 6.1.3, a water vapour decorrelation range as short as 200 km was observed over SCIGN. Therefore, an extent parameter $d_{\max}$ is introduced to the traditional Inverse Distance Weighted interpolation (IDW), referred to as "improved IDW" (IIDW), in this thesis: when d_{i0} is greater than $d_{\max}$, the weight is assigned a value of zero.

$$\begin{cases} \hat{D}(\lambda_0,\varphi_0)=\sum_i w_i D(\lambda_i,\varphi_i) \\ w_i=\dfrac{d_{i0}^{-p}}{\sum_i d_{i0}^{-p}} \quad (d_{i0}\le d_{\max}) \\ w_i=0 \qquad (d_{i0}>d_{\max}) \\ \sum_i w_i=1 \end{cases} \tag{7.1.2}$$

To apply the IIDW, a moving window is defined with a width of $d_{\max}$. The predicted surface is clearly smoother with a large width than that with a small width, which will be discussed later in Section 7.1.3. It is very likely that the quality of interpolation is dependent on the total number and the distribution of measured pixels in such a moving window. As a rule of thumb, only when the percentage of measured pixels was greater than 30% was the IIDW applied to fill in the "missing" pixels due to the presence of clouds.

It should be noted that the extent parameter was not taken into account in Chapter 6, since the width of SAR images (viz. about 100 km) is within the water vapour decorrelation range over the SCIGN area (see Section 6.1.3).

7.1.2 Densification of MODIS near IR water vapour fields

The main steps to densify MODIS near IR water vapour fields are as follows: 1) MODIS PWV values under cloud free conditions were selected using the in-built cloud mask product [*Ackerman et al.*, 1998]; 2) The selected MODIS PWV values were spatially compared with GPS PWV values over GPS stations; 3) A linear correction model was derived from this spatial comparison; 4) This GPS-derived correction model was then applied to calibrate MODIS PWV values; 5) The improved IDW was used to fill in the missing values due to the presence of clouds. It should be noted that Steps 2 and 3 are optional if a GPS-correction model can be derived from a spatio-temporal (or just temporal) comparison, although an updated correction model on a case basis is optimal. However, when the GPS-correction model was updated for each and every case (i.e. using spatial comparisons instead of a spatio-temporal comparison), no obvious further improvement was observed in this study. Therefore, the GPS-correction model derived from a spatio-temporal comparison was used in this section. See further discussion in Section 7.1.3.

The test area is located at (33.20°-34.50°N, 117.2°-118.6°W) in the SCIGN region (Figure 2.6). The range of altitude is from -62 m up to 3,066 m. The total number of GPS stations over this area varied from 71 in March 2000 to 92 in August 2003 as partly shown in Figure 7.1. Surface pressure and temperature measurements were collected at up to 7 GPS stations. A multi-reference differential model was applied to derive surface pressures and temperatures using all the available pressure and temperature measurements, respectively (refer to Appendix A). A temporal comparison over the JPLM (JPL Mesa) GPS station showed that the standard deviation of the mean difference between the modelled pressures and the measured pressures was 0.8 hPa with a bias of 0.7 hPa (modelled value > measured value), suggesting that the uncertainties of modelled surface pressures might result in uncertainties of PWV of less than 0.3 mm. Like surface pressures, a standard deviation of 1.7 °C was observed between the modelled surface temperatures and the measured values with a mean difference of 0.2 °C (modelled value > measured value), indicating that the uncertainties of modelled surface temperatures might result in uncertainties of PWV of around 0.3 mm, even in the worst case (i.e. PWV of 50 mm).

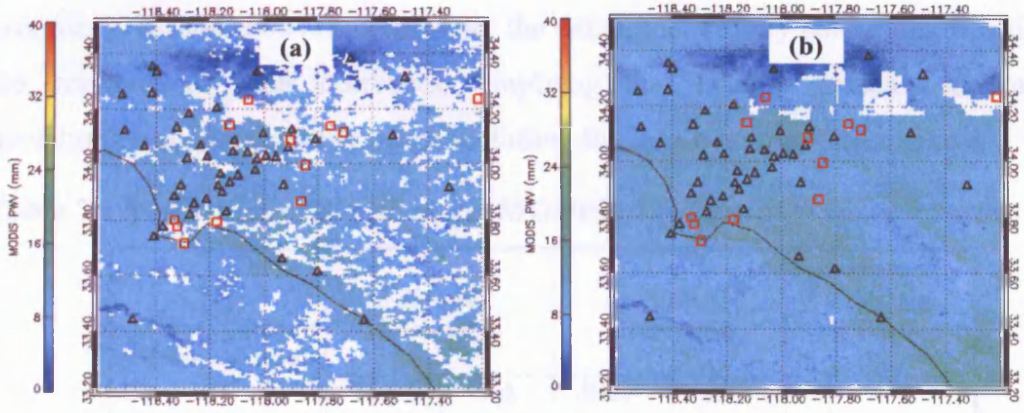

Figure 7.1 (a) MODIS near IR water vapour field collected at 18:50 UTC on 11 November 2000. Black triangles represent GPS stations under cloud free conditions, which were used to derive GPS correction model; Red squares represent GPS stations under cloudy conditions, which were used to validate the interpolated MODIS PWV values. (b) Densified MODIS near IR water vapour field after using the GPS-derived correction model.

Figure 7.1(a) shows the original MODIS near IR 2D water vapour field collected at 18:45 UTC on 11 November 2000, and Figure 7.1(b) shows the densified MODIS near IR 2D water vapour field corrected using GPS measurements. The water vapour field initially had 75.9% coverage; following correction the water vapour field yielded 97.5% coverage, showing an absolute increase of 21.6% of the whole scene (Table 7.1). From Figure 7.1(b), it is clear that there are still some missing pixels (i.e. grey pixels) left in the densified MODIS near IR water vapour field. This is because: 1) an extent parameter of 5 km was used; and 2) the IIDW gave up to interpolate those pixels due to the low percentage of cloud free pixels nearby (<30%).

7.1.3 Validation of the densified 2D MODIS near IR water vapour fields

In order to validate the densified 2D water vapour field, the densified (or interpolated) MODIS PWV values were compared with GPS PWV values under cloudy conditions (red squares in Figure 7.1). Table 7.1 shows a comparison between GPS and the densified MODIS PWV values before and after applying GPS-derived correction models. It is clear that both standard deviations and biases were closer to zero after correction, indicating that GPS-derived correction models were promising. It should be noted that only the data under cloudy conditions was used in the comparisons after correction, implying that smaller biases and standard deviations could be achieved when including the data over cloud free pixels.

Table 7.1 Validation of densified 2D MODIS near IR water vapour fields

Date Time	Extent (km)	Before Correction		After Correction		Increased Coverage Percentage (%)
		Bias* (mm)	Std. (mm)	Bias* (mm)	Std. (mm)	
20001111	5	-0.5	1.2	0.1	0.9	21.6
	10	-0.6	1.2	0.0	0.8	22.9
20021012	5	-2.1	2.7	-1.0	1.6	14.2
	10	-2.1	2.6	-1.4	2.1	16.8

*: Mean difference of (MODIS – GPS);

Note: A power parameter of 1 (i.e. $p = 1$) was used in this table.

The impacts of the extent parameter d_{max} on the interpolated values were also assessed in this study. When an extent parameter greater than 50 km was adopted,

the predicted surface was too smooth and most of the detailed information was missing (not shown). Table 7.1 shows examples with extents of 5 km and 10 km. On the one hand, a larger extent always resulted in a larger increased coverage percentage. On the other hand, for Case 20001111, the extents of 5 km and 10 km resulted in similar standard deviations and biases, whilst the extent of 5 km led to a closer agreement with GPS PWV against the extent of 10 km after correction for Case 20001012. This also implies that a larger extent resulted in a smoother surface with a loss of some detailed information, which in turn indicates that the optimal extent parameter is different from the water vapour decorrelation range presented by *Emardson et al.* [2003] and that observed in Section 6.1.3.

It is noteworthy that the power parameter could be increased to reduce the influences of far-field pixels. Several previous studies have shown that water vapour variations conform temporally and spatially to a power law process with power indices varying continuously from around 5/3 at small distances to 2/3 at large distances [*Treuhaft and Lanyi*, 1987; *Williams et al.*, 1998; *Enardson et al.*, 2003] (also see Section 6.1). There is no compelling reason to adopt a power parameter greater than 2. A power parameter of 2 was also adopted to assess its impacts on interpolation, but no significant difference was observed between power parameters of 1 and 2 in both case studies (not shown in Table 7.1).

It should be noted that this integration approach was developed and tested based on a spatio-temporal correlation analysis using a dense GPS network (viz. SCIGN). The possibility to extend this approach to other situations where only one continuous GPS station is available is examined here. Figure 7.2(a) shows a spatial-temporal comparison between MODIS and GPS PWV over the SCIGN region, from which a linear correction model can be derived to calibrate MODIS PWV values as follows [*Li*, 2004]:

$$MODIS\text{-}PWV\ (calibrated) = 0.95 \times (MODIS\text{-}PWV) + 0.67 \qquad (7.1.3)$$

Figure 7.2(b) shows a temporal comparison between MODIS and GPS PWV over the HOLP (Hollydale) GPS station (Figure 7.4) during the period from 01 September 2000 to 31 August 2003, from which a linear correction model can be given as:

$$MODIS\text{-}PWV\ (calibrated) = 0.94\times\ (MODIS\text{-}PWV) + 0.75 \qquad (7.1.4)$$

Since the phase of an interferogram is the difference of phase measurements between two different SAR images, what matters to the resultant corrected interferogram is the scale factors, rather than the zero-point offsets in Equations (7.1.3) and (7.1.4). Taking into account the typical range of water vapour variation from 0 mm to 40 mm at mid-latitudes, the difference between the calibrated MODIS-PWV values is only up to 0.4 mm when using Equations (7.1.3) and (7.1.4) respectively, and can be neglected. This indicates that the GPS/MODIS integrated approach can also be applied when only one continuous GPS station is available in the MODIS coverage. This goal should be able to be met in most areas in the world taking into account the global distribution of the International GPS Service (IGS) stations and the wide coverage of MODIS near-IR water vapour products (i.e. 2,030 km × 1,354 km). For instance, the HARV IGS station is located at 34.47°N, 120.68°W within the same MODIS coverage as the area of interest in this study. It should be noted that a temporal correlation analysis has to be used in this case instead of a spatio-temporal correlation analysis. In the following sections, Equation (7.1.3) was used to calibrate MODIS near IR water vapour product.

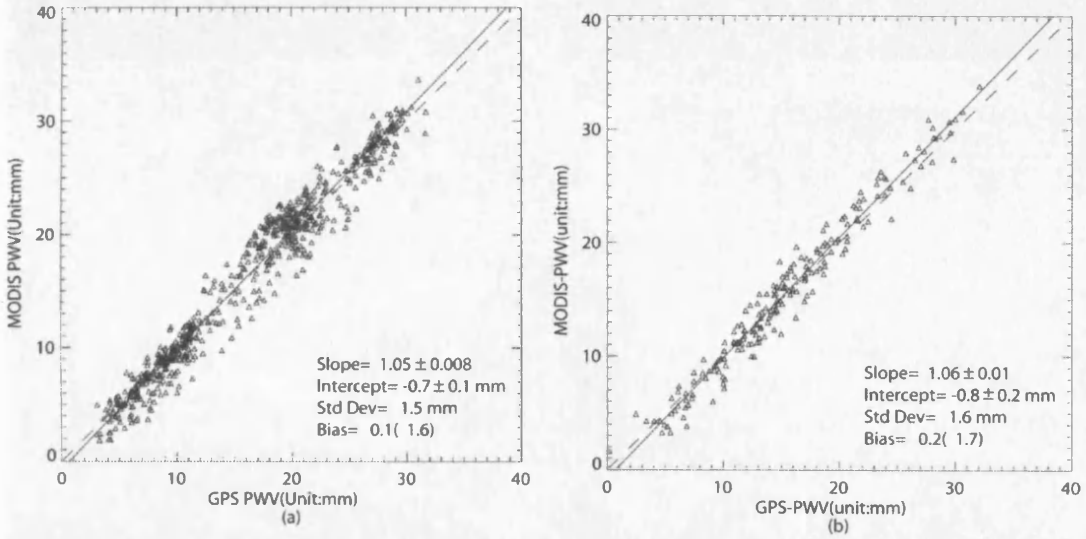

Figure 7.2 (a) Spatio-temporal comparison between MODIS and GPS PWV under cloud-free conditions over the SCIGN area (see *Li* [2004]). The line of perfect fit (dashed line) and a least squares regression line (solid line) are plotted. The number of valid samples was 715, and 37 were omitted due to 2σ exclusion. (b) Temporal comparison between MODIS and GPS PWV under cloud-free conditions over the

HOLP GPS station during the period from 01 September 2000 to 31 August 2003. The number of valid samples was 198, and 13 were omitted due to 2σ exclusion.

7.1.4 Zenith-path-delay difference maps (ZPDDM)

The densified (or interpolated) MODIS 2D water vapour fields were used to derive zenith-path-delay difference maps (ZPDDM). In order to suppress the residual error in a swath of MODIS-PWV, a low pass filter was applied to the ZPDDM with an average width of around 2 km. Assuming pixel by pixel water vapour values were uncorrelated, the accuracy of the ZPDDM increased by a factor of 2 at the expense of the spatial resolution (degraded to 2 km).

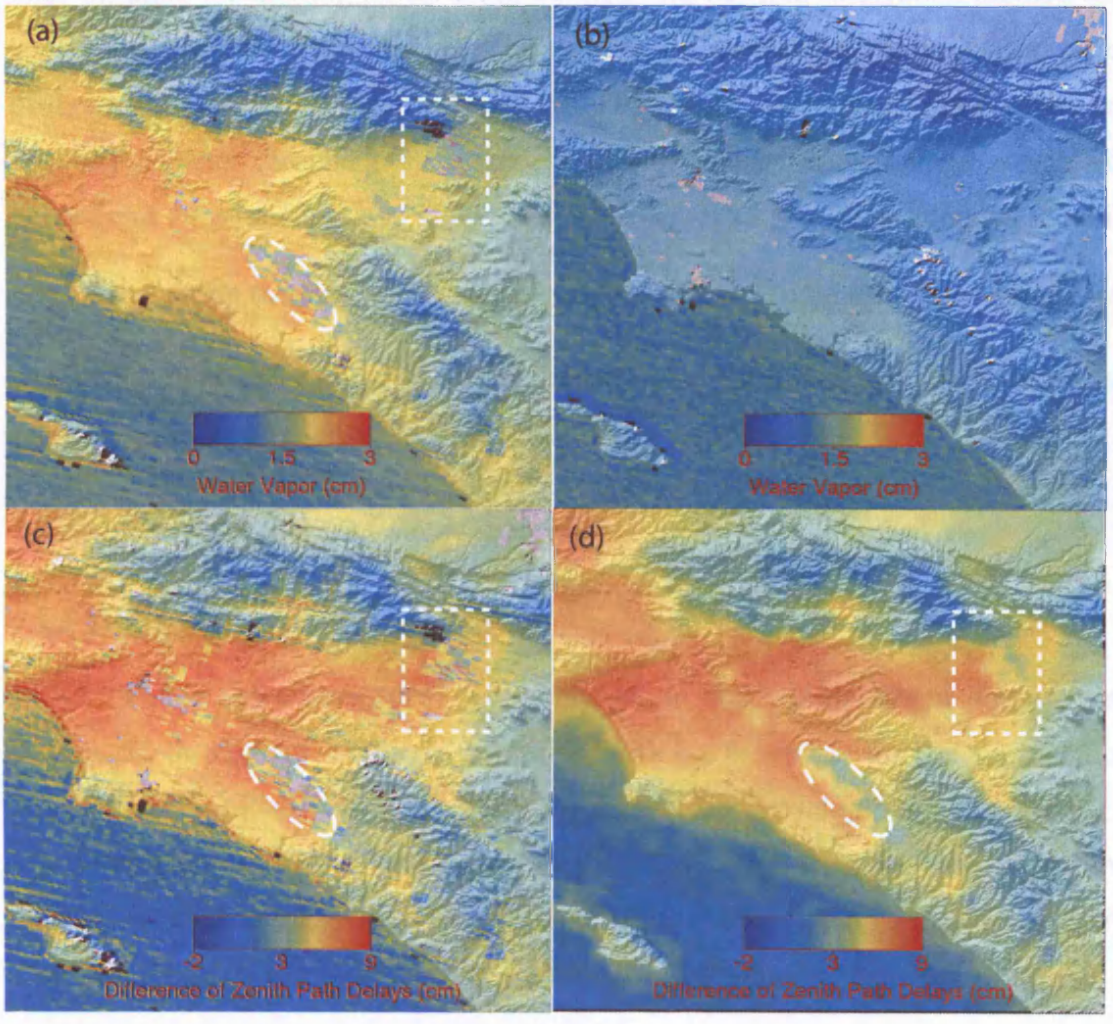

Figure 7.3 MODIS near IR water vapour fields superimposed on a hill-shaded SRTM DEM. Both grey and black imply missing values due to the presence of clouds: (a) water vapour field collected on 02 September 2000; (b) water vapour field collected on 16 December 2000; (c) difference of zenith path delays; (d)

difference of zenith path delays after filling the missing values and applying the low-pass filter. Note: The white dashed ovals and rectangles indicate clouds.

Figures 7.3(a) and 7.3(b) show MODIS near IR water vapour fields collected on 02 September 2000 and 16 December 2000 respectively that were used to generate a zenith-path-delay difference map (ZPDDM) (Figure 7.3(c)). It should be noted that the formula proposed by *Bevis et al.* [1992] (i.e. Equation (4.2.9)) was applied to convert water vapour into zenith wet path delay using an average surface temperature obtained from 7 GPS stations which had local meteorological measurements (Figure 7.4). Figure 7.3(d) shows the difference of zenith path delays after filling in the missing pixels using the GPS and MODIS integration method and applying a low-pass filter. Taking into account the standard deviation of the mean difference between GPS and corrected MODIS water vapour fields (1.6 mm), the conversion factor (around 6.2) to convert precipitable water vapour to zenith wet delays, and the smoothness by a low pass filter with a 2 km x 2 km window, it could be concluded that the uncertainty of ZPDDM is around 5 mm ($\frac{1.6}{\sqrt{2}} \times 6.2 \times \frac{1}{2} \times \sqrt{2} = 5$ mm). Note the GPS-corrected MODIS water vapour fields are assumed to have the same accuracy as GPS-derived precipitable water vapour values.

7.2 Application to ERS-2 data over SCIGN

7.2.1 Test area and processing strategy

SCIGN is the densest regional GPS network in the world, whose stations are distributed throughout southern California with an emphasis on the greater Los Angeles metropolitan region. The SCIGN inter-station spacing varies from only a few kilometres to tens of kilometres (Figure 7.4). The frequency of cloud free conditions is also high in southern California (Section 5.5; *Li et al.*, 2005). Therefore, the Los Angeles region was selected as the principal test area.

The surface of the Los Angeles region is deformed by both tectonic and non-tectonic processes. The most rapid movements are non-tectonic deformation due to groundwater and petroleum fluid level changes as shown by InSAR [e.g. *Bawden et al.*, 2001; *Watson et al.*, 2002]. *Bawden et al.* [2001] reported that parts of the Los Angeles basin are rising and falling by up to 110 mm every year with a large portion

of the Santa Ana city sinking at a rate of 12 mm per year over the period from 1997 to 1999. The seasonal rise and fall of several areas was attributed to annual variations in the elevation of the water table, confirmed by *Watson et al.* [2002] through their analysis of a longer span of data collected by ERS-1 and ERS-2 satellites between June 1992 and June 2000. Therefore, in order to validate the GPS/MODIS integrated water vapour correction model using ERS-2 repeat-pass data, comparisons of deformation derived from InSAR and GPS techniques were performed through the mapping of GPS-derived displacements into the radar line of sight (LOS). Since seasonal horizontal movements of up to 14 mm were detected using GPS data [*Bawden et al.*, 2001], GPS horizontal displacements must be included in the comparisons.

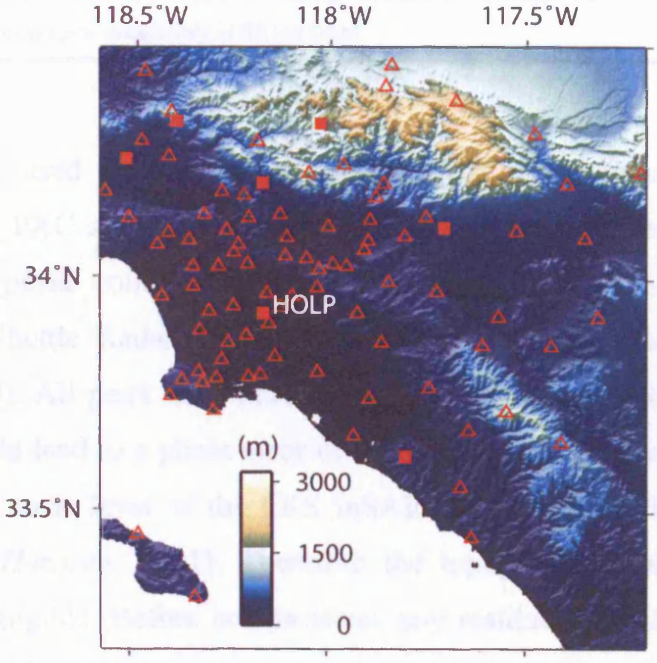

Figure 7.4 GPS stations available on 02 September 2000 superimposed on a 1-arc-second DEM from the Shuttle Radar Topography Mission (SRTM) [*Farr and Kobrick*, 2000]. Red solid squares represent GPS stations with meteorological data, and red open triangles represent GPS stations without meteorological data.

In order to estimate zenith wet delays, GPS data were analyzed as demonstrated in Section 4.2.1. However, to derive the 3D displacements over each GPS station, precise coordinates were obtained from the "Modeled Coordinates by E-Mail Utility" provided by the Scripps Orbit and Permanent Array Center [*SOPAC*, 2004]. These coordinates were based on a refined model including a linear trend, annual

and semi-annual fluctuations, offsets (coseismic or otherwise), and post-seismic exponential decays and rate changes. All parameters are estimated with full white noise + flicker noise covariances based on a noise analysis of a time series of GPS positions. The *a posteriori* RMS noise is claimed to be nearly 1 mm (horizontally) and 3.5 mm (vertically) [*Nikolaidis*, 2002].

Table 7.2 Details of interferograms (Ifms) employed in this chapter

	Track	Frame	Date 1	Time Diff 1 [a] (min)	Date 2	Time Diff 2 [a] (min)	Δt (days)	$B_{\perp}$(m)[b]	σ (radians)[c]
Ifm1	170	2925	20-May-2000	+60	02-Sep-2000	+50	105	13 to 37	0.18
Ifm2	170	2925	02-Sep-2000	+50	16-Dec-2000	+45	105	-45 to -56	0.27
Ifm3	170	2925	02-Sep-2000	+50	23-Aug-2003	+5	1085	88 to 89	0.43

[a] Time difference between ERS and MODIS acquisitions. Positive implies that MODIS over-pass time was later than ERS-2.

[b] Perpendicular baseline at centre of swath which varies along the track between the values shown.

[c] Phase error due to the topographic uncertainty of SRTM DEM.

The ERS-2 data used in this chapter (Table 7.2) were processed using the JPL/Caltech ROI_PAC software [*Rosen et al.*, 2004] as described in Section 6.3. The topographic phase contribution was removed using a 1-arc-second (~30 m) DEM from the Shuttle Radar Topography Mission (SRTM) [*Farr and Kobrick*, 2000] (Figure 7.4). All pairs have reasonably small baselines, and the error in the SRTM DEM might lead to a phase error of up to 0.43 radians, which is well below the typical phase noise level of the ERS InSAR pairs on the order of 40 degrees (~0.70 radians) [*Hanssen*, 2001]. Therefore the topographic contribution can be considered as negligible. Before comparisons, any residual orbital tilts and offsets remaining in interferograms were removed by subtracting a plane fitted to the unwrapped phase.

In this chapter, it should be noted that: 1) the zero phase origin is in the centre pixel of the interferograms; 2) the unwrapped phase has been converted to range change in millimetres and positive range change means ground moving away from satellite (if there is no atmospheric effect and any other error); and 3) the unwrapped phase has been shifted with a mean difference of range changes derived from GPS and InSAR when compared to GPS-derived satellite line-of-sight (LOS) range changes.

7.2.2 Interferogram: 20 May 2000 – 02 Sep 2000

Figure 7.5 shows interferograms spanning the summer from 20 May 2000 to 02 September 2000. It is clear that water vapour effects over several areas (indicated by black rectangles) were significantly reduced after applying the GPS/MODIS integrated water vapour correction technique (Figure 7.5(a) vs. 7.5(b)). In both Figures 7.5(a) and 7.5(b), the Long Beach-Santa Ana basin (indicated by a black oval) showed up to 35 mm of subsidence in the summer of 2000. This result appears to be consistent with subsidence in the summer of 1999 measured by *Bawden et al.* [2001] and the annual cycle measured by *Watson et al.* [2002]. The smaller amplitude (*Bawden et al.* [2001] reported maximum subsidence up to 60 mm) is partly due to the shorter interval of Ifm1.

Phase variation of the unwrapped Interferogram decreased from 2.66 radians without correction to 1.98 radians after applying the GPS/MODIS integrated water vapour correction model, implying that the unwrapped phase was much flatter after correction. Comparisons between GPS and InSAR range changes in the satellite line of sight (LOS) showed that the RMS difference decreased from 1.0 cm before correction to 0.7 cm after correction (Figure 7.5(c)), indicating that the GPS/MODIS integrated water vapour correction model improved the interferogram significantly.

In Figure 7.5(c), the error bars of each technique are shown. In this study, phase standard deviations were calculated by a weighted summation over a 5 x 5 pixel window after removing a local phase gradient from the wrapped differential interferograms after smoothing. The phase standard deviations were determined for both interferograms before water vapour correction and those after water vapour correction. It was observed that the phase standard deviations for both types of interferograms varied from 0.2 mm to 1.3 mm, which was far smaller than the typical phase noise level of ERS InSAR pairs, on the order of 40 degrees (~3.1 mm) reported by *Hanssen* [2001]. This can be expected since a complex multi-look of 8 (in range) × 40 (in azimuth) was applied to the full-resolution interferogram followed by a power spectrum filtering (alpha=0.6, window size 32 x 32) [*Goldstein and Werner*, 1998] to reduce the phase noise in the interferograms. The correlation in the urbanized area of Los Angeles is also quite high so there is little noise coming from low correlation.

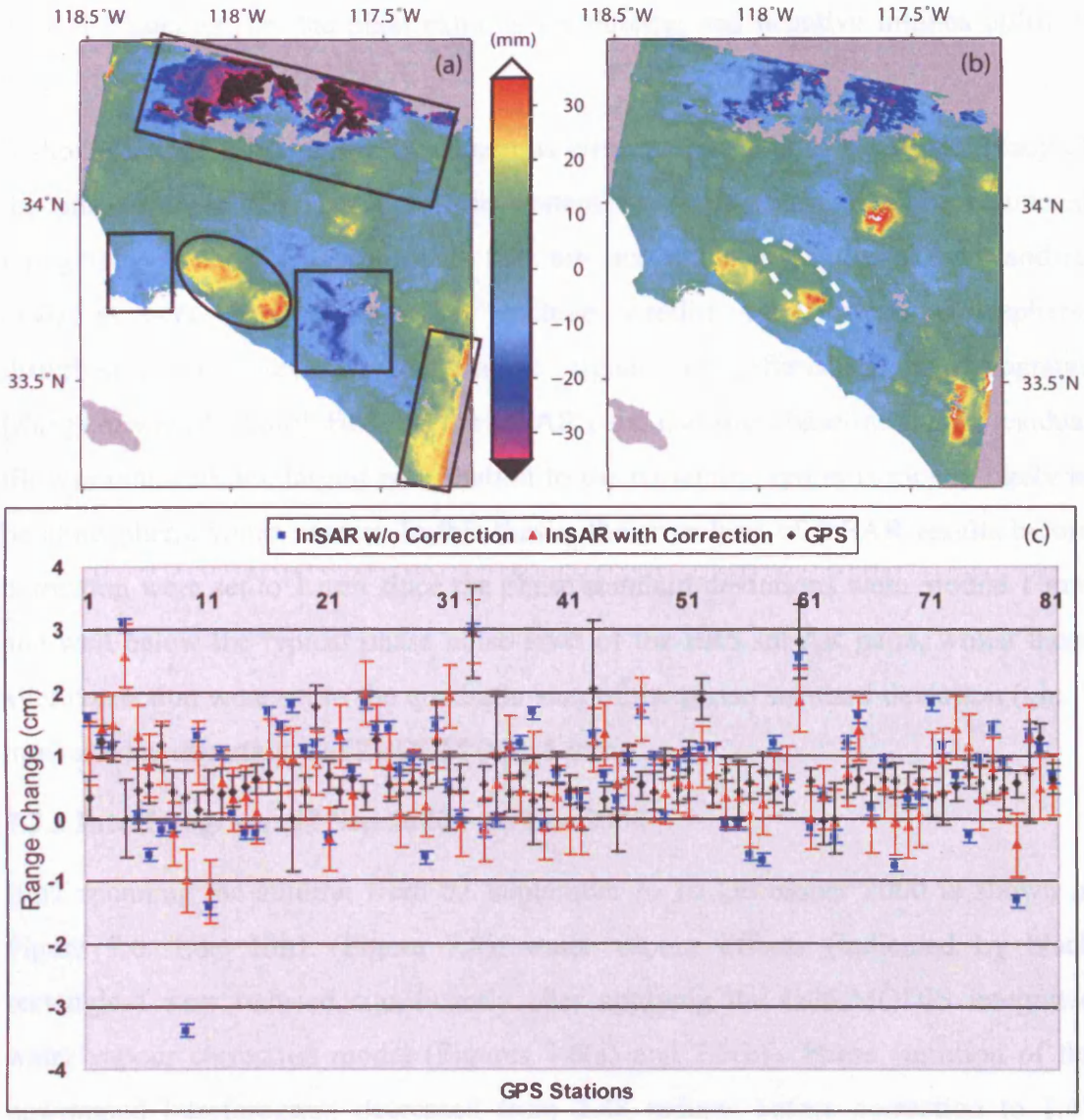

Figure 7.5 (a) Original Ifm: 000520-000902. Red means positive range change (ground moving away from satellite, see text). The black rectangles represent areas affected by water vapour, whilst the black oval indicates the Long Beach-Santa Ana basin exhibiting a subsidence; (b) Corrected Ifm using GPS/MODIS integrated water vapour fields. The white dashed oval indicates an uncertainty due to the presence of clouds; (c) Comparison of range changes derived from GPS and InSAR techniques in satellite line-of-sight (LOS). Note that positive range change means subsidence in the satellite LOS. The error bars imply: 1) phase standard deviations of InSAR measurements (fixed to 1 mm, see text). 2) combined error from phase standard deviation and MODIS water vapour correction. 3) the formal errors of GPS solutions. See discussion in text. Note: Positive implies that the surface moves away

from the satellite, i.e. the pixel exhibits subsidence, and negative implies uplift in LOS.

It should be noted that there are numerous error sources that affect the accuracy of the phase values and may introduce systematic errors (biases) in the estimated topography and deformation fields that are not reflected in the phase standard deviation over small areas. They include satellite orbit errors, atmospheric disturbances, and residual topographic signals in differential interferograms [*Bürgmann et al.*, 2000]. Because the InSAR pairs had short baselines and a residual tilt was removed, the largest contribution to the remaining errors is mostly likely to be atmospheric water vapour. In this thesis, the error bars of InSAR results before correction were set to 1 mm since the phase standard deviations were around 1 mm and well below the typical phase noise level of the ERS InSAR pairs, whilst those after correction were set to the quadratic sum of the phase standard deviation (viz. 1 mm) and the uncertainty of ZPDDM (viz. 5 mm).

7.2.3 Interferogram: 02 Sep 2000 – 16 Dec 2000

Ifm2 spanning the autumn from 02 September to 16 December 2000 is shown in Figure 7.6. Like Ifm1 (Figure 7.5), water vapour effects (indicated by black rectangles) were reduced significantly after applying the GPS/MODIS integrated water vapour correction model (Figures 7.6(a) and 7.6(b)). Phase variation of the unwrapped Interferogram decreased from 2.48 radians before correction to 1.47 radians after correction, and the RMS difference between GPS and InSAR decreased from 1.1 cm before correction to 0.5 cm after correction (Figure 7.6(c)).

Both Figure 7.6 (a) and 7.6(b) show around 35 mm of uplift in the Long Beach-Santa Ana basin (indicated here by a black oval in Figure 7.6 (a)) in the autumn of 2000, which is similar to the 34 mm of uplift in the late autumn in 1997 in *Bawden et al.* [2001].

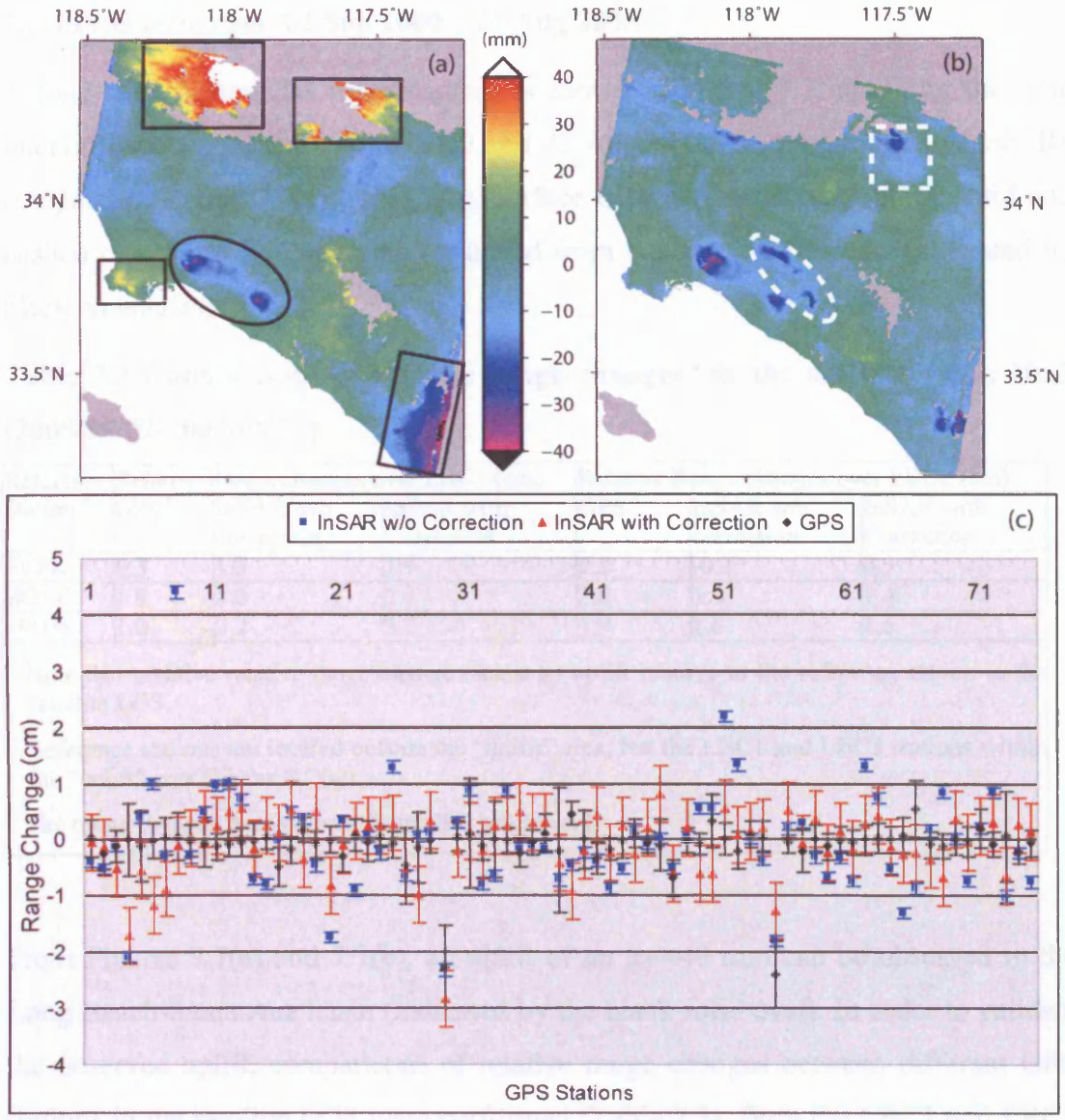

Figure 7.6 (a) Original Ifm: 000902-001216. The black rectangles represent areas affected by water vapour, whilst the black oval indicates the Long Beach-Santa Ana basin exhibiting uplift; (b) Corrected Ifm using GPS/MODIS integrated water vapour fields. Both the dashed rectangle and oval represent uncertainties due to the presence of clouds on 02 September 2000; (c) Comparison of range changes derived from GPS and InSAR techniques in the satellite LOS. Note that positive range change means subsidence in the satellite LOS.

7.2.4 Interferogram: 02 Sep 2000 – 23 Aug 2003

A long-term differential interferogram is shown in Figure 7.7, spanning the time interval between 02 September 2000 and 23 August 2003 (almost three years). By comparing Figures 7.7(a) and 7.7(b), surface deformation signals (black solid and dashed ovals) can be easily discriminated from water vapour effects (indicated by black rectangles).

Table 7.3 Comparisons of relative range changes[a] in the satellite LOS: Ifm3 (2000/09/02-2003/08/23)

Reference Station[b]	Relative Range changes over LBC1 (cm)			Relative Range changes over LBC2 (cm)		
	GPS[c]	InSAR w/o correction	InSAR with Correction	GPS[c]	InSAR w/o correction	InSAR with Correction
FVPK	0.3	1.5	1.9	1.2	-0.1	0.3
HOLP	1.9	3.0	3.1	2.8	1.4	1.4
PMHS	1.0	3.2	3.2	1.9	1.6	1.6

[a] Note that positive relative range change means an uplift relative to the reference station in the satellite LOS.

[b] Reference stations are located outside the "uplift" area, but the LBC1 and LBC2 stations within the "uplift" area (Figure 7.7(a)).

[c] The range changes were derived from GPS heights only.

From Figures 7.7(a) and 7.7(b), an uplift of up to ~40 mm can be observed in the Long Beach-Santa Ana basin (indicated by the black solid oval). In order to validate the observed uplift, comparisons of relative range changes between different GPS stations in the satellite LOS were performed (Table 7.3). Both the LBC1 and LBC2 GPS stations are located within the observed uplift area indicated by the black solid oval, whilst the reference stations, i.e. FVPK, HOLP, and PMHS, are located on the margin of the Long Beach-Santa Ana basin, but outside the uplift area (see locations on Figures 7.7(a) and 7.7(b)). It is clear that, in Table 7.3, all the relative range changes have the same positive sign (+) except for the InSAR result without water vapour correction over the LBC2 station relative to the FVPK station. After water vapour correction, the sign also becomes positive (+). This indicates that both InSAR and GPS techniques can observe the uplift signals. *Bawden et al.* [2001] reported that a two-year interferogram between October 1997 and October 1999 showed a subsidence of about 25 mm within the basin. Despite the fact that the 2000/09/02 and 2003/08/23 SAR images are very close to the same season, the

variations in rainfall in different years might change the phase and amplitude of the seasonal aquifer signal, so that the 3-year interferogram here shows a net uplift over the three-year time interval.

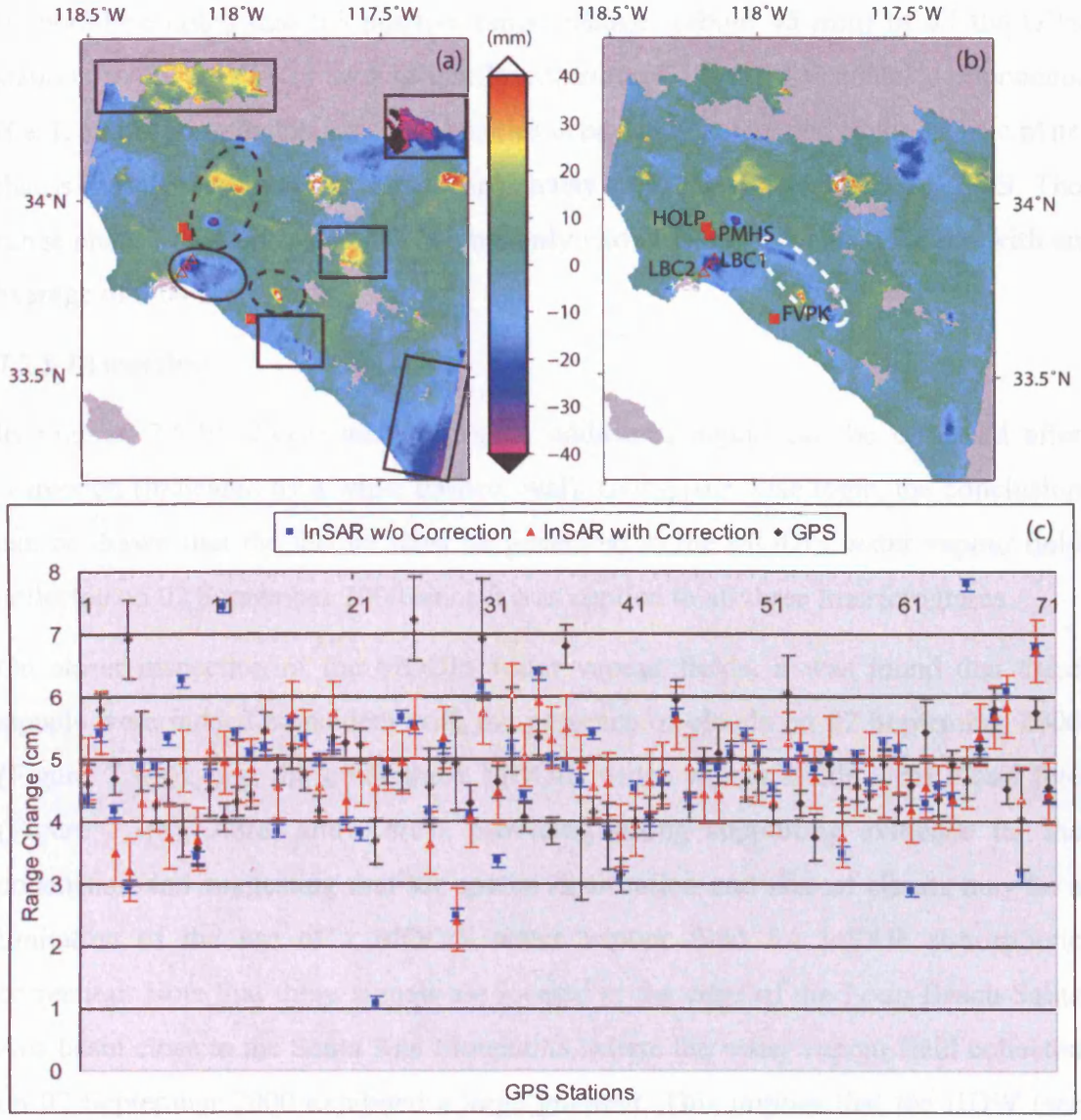

Figure 7.7 (a) Original Ifm: 000902-030823. The black rectangles represent areas affected by water vapour, whilst both the black solid and dashed ovals indicate surface deformation signals; (b) Corrected Ifm using GPS/MODIS integrated water vapour fields. The white dashed oval indicates an uncertainty due to the presence of clouds; (c) Comparison of range changes derived from GPS and InSAR techniques in the satellite LOS. Note that positive range change means subsidence in the satellite LOS.

Phase variation of the unwrapped interferogram decreased from 2.40 radians before correction to 1.60 radians after correction, and the RMS difference between GPS and InSAR decreased from 1.2 cm to 0.8 cm (Figure 7.7(c)).

It should be noted that the positive range change (about 45 mm) of all the GPS stations in Figure 7.7(c) was primarily contributed by the horizontal components (i.e. E and N components), as Los Angeles is basically connected to the Pacific plate that is moving NW relative to the Earth, away from the descending ERS LOS. The range change derived from GPS heights only varied from –1.5 cm to 2.6 cm with an average of 0.04 cm.

7.2.5 Discussion

In Figures 7.5(b), 7.6(b) and 7.7(b), an additional signal can be observed after correction (indicated by a white dashed oval). Using pair-wise logic, the conclusion can be drawn that the feature must be generated in the MODIS water vapour field collected on 02 September 2000 since it was applied to all three Interferograms.

On closer inspection of the MODIS water vapour fields, it was found that these signals were indeed coincident with the presence of clouds on 02 September 2000 (Figure 7.3(a)), and the other three MODIS water vapour fields were cloud free (Figure 7.3(b), 7.8(a) and 7.8(c)), providing strong supporting evidence for the conclusion and suggesting that the spatial distribution and size of clouds may be a limitation of the use of a MODIS water vapour field for InSAR atmospheric correction. Note that these signals are located at the edge of the Long Beach-Santa Ana basin close to the Santa Ana Mountains, where the water vapour field collected on 02 September 2000 exhibited a large gradient. This implies that the IIDW (see Section 7.1.1) may have limited applicability to water vapour fields with large spatial variations, which is commonly the case in mountain areas.

Similarly, the fringes indicated by a dashed rectangle are more likely due to the clouds on 02 September 2000 (Figures 7.6(b) vs. 7.3(a)). Caution therefore needs to be exercised when interpreting the results of the GPS/MODIS integrated water vapour correction model.

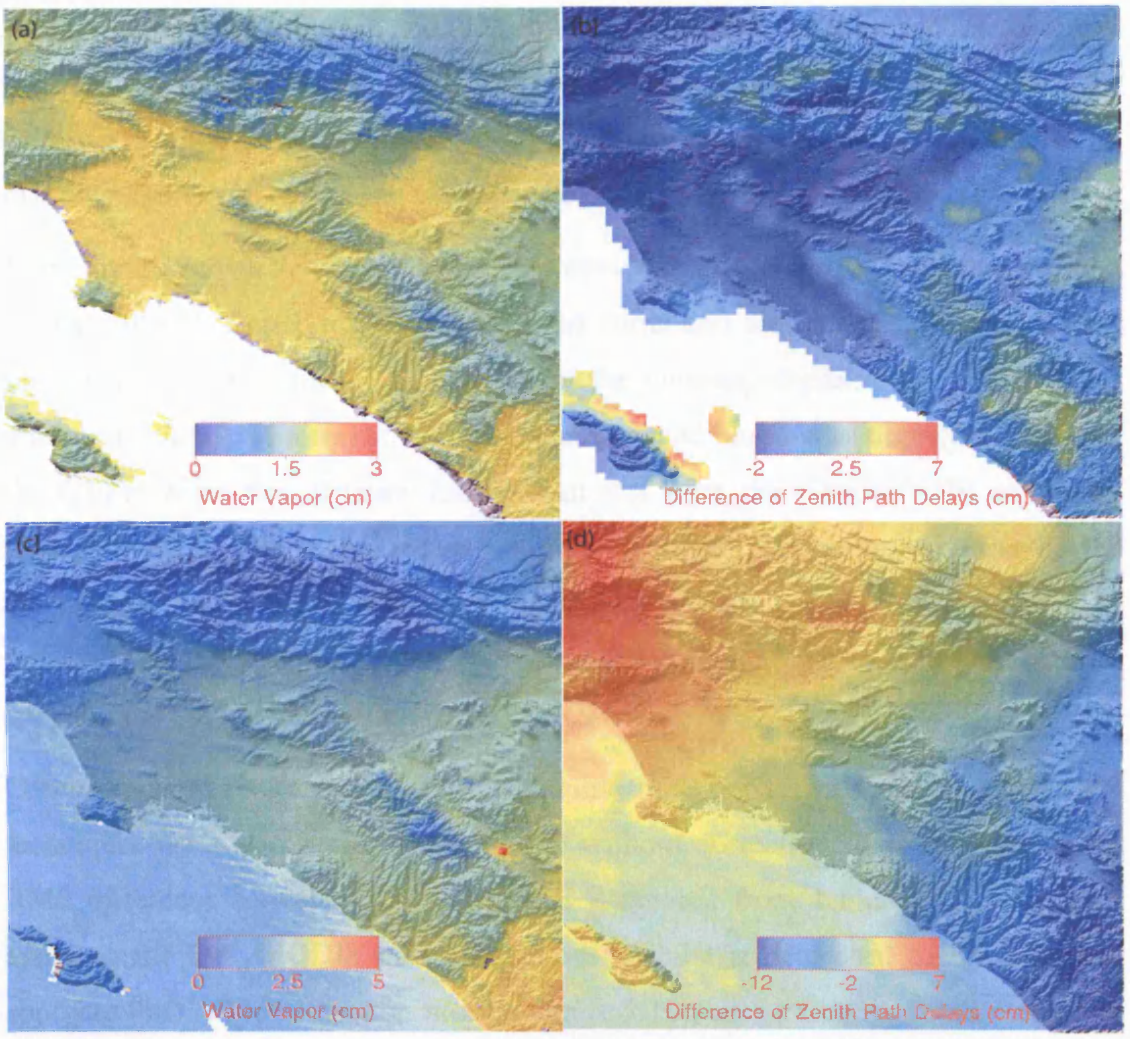

Figure 7.8 MODIS near IR water vapour fields superimposed on a hill-shaded SRTM DEM. Both grey and white imply missing values due to the presence of clouds: (a) water vapour field collected on 20 May 2000; (b) difference of zenith path delays after filling the missing values and applying the low-pass filter (20 May 2000 – 02 September 2000); (c) water vapour field collected on 23 August 2003; (d) difference of zenith path delays after filling the missing values and applying the low-pass filter (02 September 2000 - 23 August 2003).

7.3 Comparison between the GTTM and GPS/MODIS models

In order to assess the performance of the GTTM (See Chapter 6) and GPS/MODIS integrated water vapour correction models, a comparison was performed for Ifm2 (02 Sep 2000 – 16 Dec 2000) (Figure 7.9).

From Figure 7.9(a), 7.9(c) and 7.9(e), it is clear that both correction methods significantly reduced the atmospheric effects in regions labelled A, B, C, D and F.. Comparing Figure 7.9(c) with 7.9(e), one can, once again, come to the conclusion that the features (labelled G and H) must be due to the presence of clouds.

From Figure 7.9(b), 7.9(d) and 7.9(f), it is obvious that the 2D-SSF values decreased dramatically after applying both the GTTM correction model and the GPS/MODIS integrated correction model, implying that the unwrapped phase was much flatter after correction. It is also shown that the unwrapped phase was slightly flatter after the GTTM correction (Figure 7.9(d)) than that after the GPS/MODIS correction (Figure 7.9(f)). This is consistent with the fact that the phase variation of the unwrapped Interferogram decreased from 2.48 radians before correction to 1.47 radians after applying the GPS/MODIS correction model, and to 1.34 radians after applying the GTTM correction model.

Comparisons of range changes in the satellite LOS derived from InSAR and GPS techniques were also performed with and without correction. It is shown that the RMS difference between GPS and InSAR decreased from 1.1 cm to 0.5 cm after applying the GPS/MODIS correction model, whilst it decreased to 0.6 cm after applying the GTTM correction model (Figure 7.10), suggesting that both correction models successfully reduced atmospheric effects on the interferograms.

From this comparison, there is no evidence that one correction model is superior to the other. A brief comparison of the GTTM and GPS/MODIS correction models is shown in Table 7.4.

On the one hand, GPS can collect high temporal resolution (e.g. 30 seconds, even up to 1 Hz) observations day and night, and GPS-derived ZWD (or PWV) estimates are insensitive to the presence of clouds. However, only a few dense continuous GPS networks such as SCIGN operate across the globe, and its spatial resolution is also limited from a few kilometres to a few hundred kilometres.

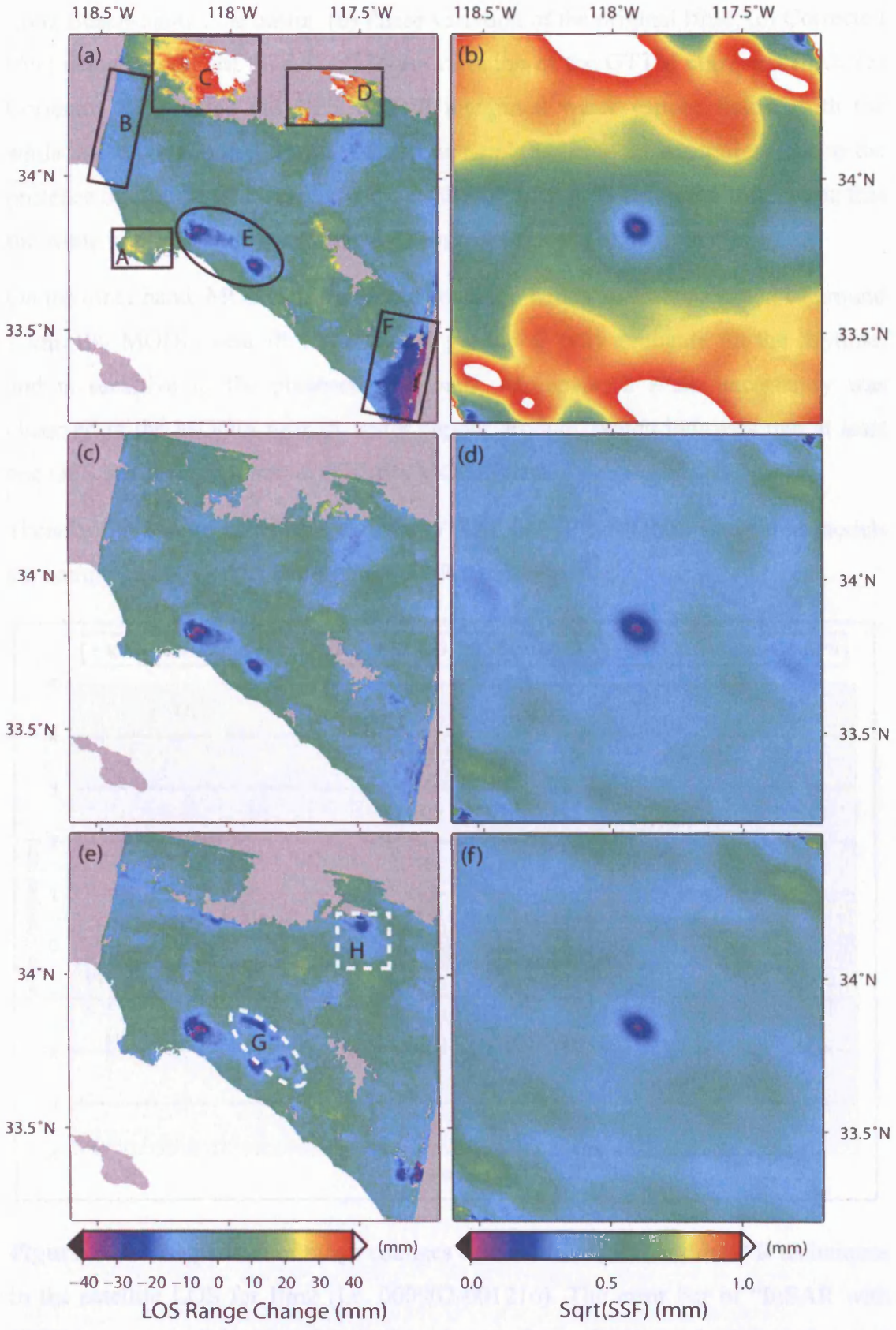

Figure 7.9 (a) Original Ifm2: 000902-001216. The black rectangles represent areas affected by water vapour, whilst the black solid oval indicates an uplift over the

Long Beach-Santa Ana basin; (b) Phase variation of the original Ifm2; (c) Corrected Ifm2 using the GTTM model; (d) Phase variation of the GTTM corrected Ifm2; (e) Corrected Ifm2 using the GPS/MODIS integrated water vapour fields. Both the white dashed oval and the white dashed rectangle indicate an uncertainty due to the presence of clouds; (f) Phase variation of the GPS/MODIS corrected Ifm2. Note that the white implies values greater than 1.5 mm in Figures (b), (d) and (f).

On the other hand, MODIS has a global coverage with a spatial resolution of around 1 km. But MODIS near IR water vapour product is only available for the daytime, and is sensitive to the presence of clouds. Moreover, a scale uncertainty was observed in the MODIS near IR water vapour product, which indicates that at least one GPS station is required to calibrate MODIS data.

Therefore, it can be concluded that the GTTM and GPS/MODIS integrated models are complementary when correcting InSAR measurements.

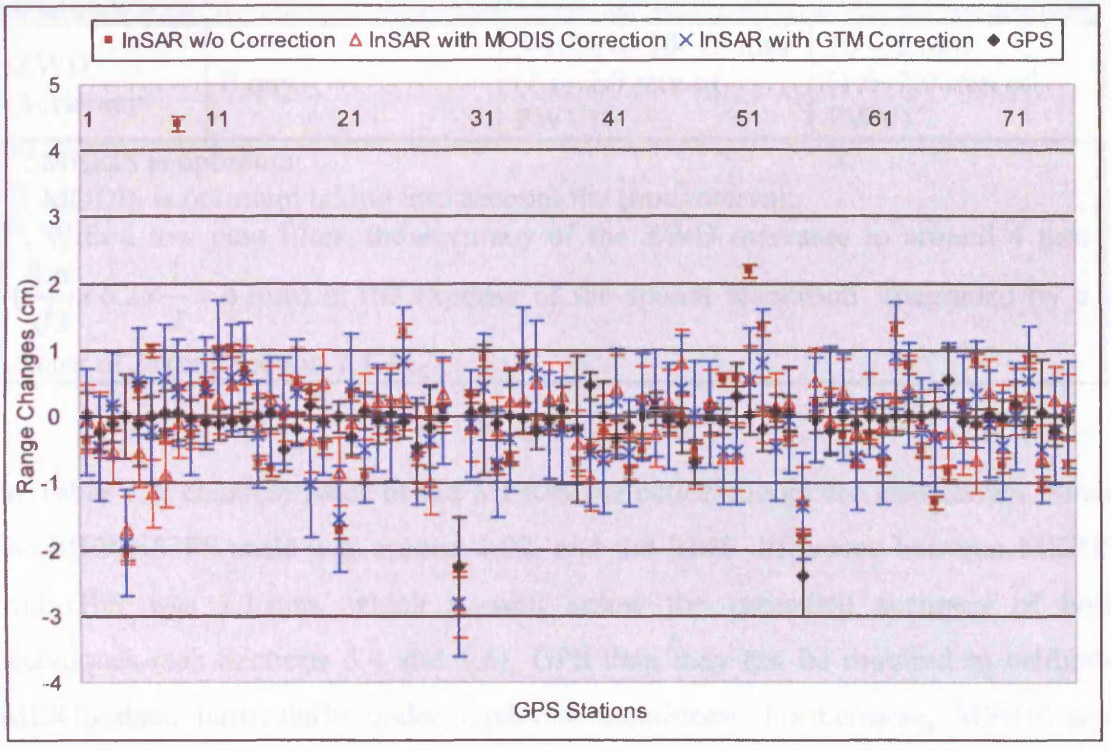

Figure 7.10 Comparison of range changes derived from GPS and InSAR techniques in the satellite LOS for Ifm2 (i.e. 000902-001216). The error bar of "InSAR with GTTM correction" implies the combined error from phase standard deviation and the GTTM correction model.

Table 7.4 A comparison of different correction models

	GTTM Model	GPS/MODIS Integrated Model	MERIS Correction Model
Observable	A dense continuous GPS (CGPS) network	1) At least one GPS station; 2) coincident MODIS data	Coincident MERIS data
Applicability	ERS-1/2, ASAR	ERS-2, ASAR[a]	ERS-2[b], ASAR
Observation Period	Day and night	Day	Day
Coverage	Regional	Global	Global
Spatial Resolution	A few km to a few hundred km (e.g. 7 km to 25 km over SCIGN)	1 km × 1 km	RR: 1.2 km×1.2 km FR: 300 m×300 m
Time interval	Simultaneous	5~60 min	Simultaneous
Sensitivity to Clouds	No	Yes	Yes
ZWD Accuracy	8 mm	5-10% or 10~12 mm (1.6~2.0 mm of PWV)[c]	10~12 mm (1.6~2.0 mm of PWV)[c]

[a]: MERIS is optimum;
[b]: MODIS is optimum taking into account the time interval;
[c]: With a low pass filter, the accuracy of the ZWD increases to around 4 mm ($\frac{1.6}{\sqrt{2}} \times 6.2 \times \frac{1}{2} = 4$ mm) at the expense of the spatial resolution (degraded by a factor of 2) (see Section 7.1.4).

In Table 7.4, characteristics of the MERIS correction model are also shown. Since the MERIS/GPS scale was around 1.02, and the RMS difference between MERIS and GPS was 1.1 mm, which is well below the estimated accuracy of both techniques (see Sections 5.4 and 5.6), GPS data may not be required to calibrate MERIS data, particularly under moderate conditions. Furthermore, MERIS and ASAR are on board the same platform (ENVISAT), and they can collect observations simultaneously. Therefore, the MERIS correction model is much more advantageous to ASAR than the GPS/MODIS integrated model is to ERS-2.

7.4 Conclusions

GPS and MODIS have been successfully integrated with InSAR measurements in this study. Their application to ERS-2 data over the SCIGN area indicates that, even with time differences of up to one hour (shown in Table 7.2) between a MODIS and ERS-2 overpass, this integrated model not only helps discriminate geophysical signals from water vapour effects, but also reduces water vapour effects on Interferograms significantly. Seasonal deformation was observed in the Long Beach-Santa Ana basin, which is consistent with *Bawden et al.* [2001] and *Watson et al.* [2002].

It has also been shown that clouds affected the efficiency of the GPS/MODIS integrated correction approach. Bearing in mind that the frequency of the cloud-free conditions is c. 25% in the global [*Menzel et al.*, 1996; *Wylie et al.*, 1999; Section 5.5], a lack of cloud-free observations may be a major limitation to the application of the GPS/MODIS integrated correction model.

Due to CPU limitations, the topography-dependent turbulence model developed in Chapter 6 was not applied in this study, even though it is expected that this would improve the interpolation in mountain areas. Furthermore, a comparison between the GTTM model and the GPS/MODIS integrated model showed that these two correction models appear to be complementary when correcting InSAR measurements. Future work in this area should therefore be to combine the MODIS (or MERIS) correction demonstrated in this chapter, with the GTTM model of Chapter 6, to estimate seasonal deformation and long-term subsidence rate in the Long Beach-Santa Ana basin.

Chapter 8

Conclusions

Over the last two decades, spaceborne repeat-pass Interferometric Synthetic Aperture Radar (InSAR) has been a widely used geodetic technique for measuring the Earth's surface, including topography and deformation, with a spatial resolution of tens of metres. Like other astronomical and space geodetic techniques, repeat-pass InSAR is limited by the variable spatial and temporal distribution of atmospheric water vapour. The research objective of this thesis is to reduce water vapour effects on repeat-pass InSAR measurements using independent datasets including GPS and Moderate Resolution Imaging Spectroradiometer (MODIS). This thesis is the first successful demonstration of a reduction in water vapour effects on interferograms by using GPS and MODIS near IR water vapour products. The main conclusion is that water vapour effects can be reduced significantly using either of two models developed in this thesis: the GPS Topography-dependent Turbulence Model (GTTM) model or the GPS/MODIS integrated water vapour correction model. The principal contributions of this research are:

1) For the first time, a true integration of GPS and InSAR measurements has been developed that reduces atmospheric effects on interferograms and improves InSAR processing such as phase unwrapping;

2) For the first time, GPS and MODIS data have been integrated to provide regional water vapour fields with a spatial resolution of 1 km × 1 km, and a water vapour correction model based on the resultant water vapour fields has been successfully incorporated into the JPL/Caltech ROI_PAC software.

The conclusions of this research are elaborated in relation to the five specific research questions listed in Chapter 1, followed by a summary of the major contributions of this research as well as recommendations for future work.

8.1 Conclusions of this research

8.1.1 Water vapour products

Specific Research Questions 1: How does water vapour affect InSAR measurements? What is the requirement for the accuracy of individual independent datasets if they are to be used to reduce the atmospheric effects? What is the accuracy of the water vapour product derived from each independent dataset? Are these sufficiently accurate for correcting InSAR measurements?

Atmospheric effects on SAR interferograms have been discussed in Chapter 3. The discussion showed that atmospheric signals in interferograms are mainly due to local changes in the refractive index of the atmosphere, and water vapour is the dominant factor in the atmosphere that causes atmospheric signals in interferograms; its effects are a major limitation in repeat-pass InSAR applications.

The requirement for water vapour products to correct InSAR measurements was investigated in Section 5.1. An uncertainty of 1.0 mm in PWV (~6.2 mm in ZWD) could result in an uncertainty of 0.3 fringes (2π) in the resultant interferograms. PWV with an uncertainty of 1.0 mm is required to detect surface deformation of 1.0 cm. In order to retrieve topography with an accuracy better than 20 m, PWV with an uncertainty of 1.2 mm is needed with a perpendicular baseline of 200 m, i.e. an ambiguity height of 45 m. It should be noted that a nominal incidence angle of 23° is assumed in this thesis, and water vapour effects on SAR interferograms increase with incidence angle. Furthermore, for repeat-pass topography mapping, water vapour effects on SAR interferograms also depend on the ambiguity height: the smaller the ambiguity height (viz. the bigger the perpendicular baseline), the smaller the effects.

In order to assess the performance of different techniques (viz. GPS, MODIS and MERIS) for measuring water vapour, cross-correlation analysis was applied in time and/or in space in Chapter 5. Temporal comparisons between GPS and radiosondes show that agreements of about 1 mm of PWV (~6.2 mm of ZWD) are achievable. This means that GPS water vapour products can meet the requirements for correcting InSAR measurements.

The MODIS near IR water vapour product (Collection 3) appeared to overestimate water vapour against GPS and RS, but with high correlation coefficients. Similar results were observed in the comparisons between GPS and MODIS near IR water vapour (Collection 4) products in spite of having a smaller scale factor and smaller zero-offset. Taking into account the good linear relationship between GPS and MODIS near IR water vapour products, a linear fit model can be used to improve the MODIS near IR water vapour product. After correction, MODIS and GPS water vapour products agreed to within 1.6 mm in terms of standard deviations (see Section 7.1 and *Li* [2004]).

The spatio-temporal comparison of MERIS and GPS PWV showed an excellent agreement with a standard deviation of 1.1 mm, which is well within the estimated accuracy of MERIS PWV (viz. 1.6 mm), particularly under moderate conditions with PWV values ranging from 5 mm to 25 mm. In the winter (i.e. under dry conditions), the high solar zenith angle might lead to a decrease of accuracy in the retrieved MERIS PWV. However, in order to assess the accuracy of MERIS near IR PWV under very wet conditions (i.e. PWV > 25mm, and usually in the summer), further work is required.

Assuming MODIS and MERIS water vapour values are spatially uncorrelated, a low pass filter with an average width of 2 pixels may improve the accuracy by a factor of 2 at the expense of the spatial resolution (degraded to 2 km for the MODIS water vapour product, 2.4 km for the FR MERIS water vapour product and 600 m for the RR MERIS water vapour product). In this case, MODIS and MERIS water vapour products may be able to be used for InSAR atmospheric correction (Chapter 7).

It should be noted that MODIS and MERIS near IR water vapour retrieval algorithms rely on observations of water vapour attenuation of solar radiation reflected by surfaces and clouds in the near IR channels [*Fischer and Bennartz*, 1997; *Gao et al.*, 2003]. As a result, both MODIS and MERIS near IR water vapour products are sensitive to the presence of clouds, and the low percentage and frequency of cloud free conditions is a major limitation in applying MERIS and MODIS near IR PWV for InSAR atmospheric correction (Sections 5.5 and 5.6).

8.1.2 Spatial interpolators

Specific Research Questions 2: What spatial interpolator appears best to take into account the spatial structure of water vapour variation as well as topography? Is there any demonstrable improvement when interpolating 2D GPS water vapour fields using such a spatial interpolator over commonly used interpolation methods such as Inverse Distance Weighting (IDW)?

Integration of InSAR and GPS was first suggested in 1997 [*Bock and Williams*, 1997]. However, before this study, there had been very few satisfactory results for the integration of InSAR and GPS. This is usually believed to be due to the lack of an efficient spatial interpolator to produce 2D water vapour fields using sparsely distributed GPS measurements.

Based on the spatial structure analysis of water vapour using GPS and MODIS data in Section 6.1, it is clear that water vapour variation obeys a power-law relation, although it may not follow the TL model [*Treuhaft and Lanyi*, 1987], i.e. the power indices may lie outside the range between 2/3 and 5/3. Taking into account the power-law relation of water vapour variation as well as topographic effects on water vapour, a GPS Topography-dependent Turbulence Model (GTTM) has been developed in Chapter 6. Since the principal test area of this thesis is SCIGN, for simplicity, the model parameters of the GTTM were fixed to values estimated from the 126 GPS stations over the SCIGN region during the period from January 1998 to March 2000 [*Emardson et al.*, 2003].

A cross validation test to ZTD estimates showed the GTTM interpolated values appeared to be in much closer agreement with the GPS estimates (i.e. the ZTD values derived directly from GPS data) than the IDW interpolated values (Section 6.2.3). However, large but nearly constant offsets were observed between the interpolated values and the GPS estimates over GPS stations at a height greater than 1100 m, implying that: 1) Even the current GTTM model could not account for the high correlation between integrated column water vapour and topography; 2) Those interpolated values from both the GTTM and IDW methods could not be applied directly to correct InSAR measurements; 3) Elevation effects could be reduced to a large extent when differencing ZTD values from different epochs.

It should be kept in mind that what matters to an interferogram is the change in ZTD from scene to scene, rather than the absolute value of ZTD itself. Another cross validation test which applied the GTTM and IDW methods to ZTD daily differences showed standard deviations of 6.3 mm and 7.3 mm respectively for the mean difference between the interpolated values and the GPS estimates, indicating that: 1) Both the GTTM and IDW methods could be used to produce zenith-path-delay difference maps (ZPDDM) for InSAR atmospheric correction using ZTD (or ZWD) differences from different epochs, which is crucial to reduce (if not completely remove) the component due to topographic effects on water vapour distribution (Section 6.2.2); 2) The GTTM model appeared to be slightly better than the IDW method.

In Section 6.4, the application of the GTTM and IDW methods to ERS Tandem data showed that: 1) The phase variation decreased after applying either of the two models: the GTTM model or the IDW method; 2) The GTTM model appeared to be better at reducing atmospheric effects on interferograms than the IDW method, not only for topography-dependent cases (e.g. Interferogram 960110-960111) but also for topography-independent cases (e.g. Interferogram 951013-951014).

It should be noted that the ability of sparse ground-based GPS measurements to produce 2D water vapour fields depends not only on the effectiveness of the spatial interpolator in predicting the value of an unknown point, but also on the distribution (including density) of GPS stations and the accuracy of the measurements themselves.

8.1.3 High resolution water vapour fields

Specific Research Questions 3: Is it possible to produce regional 2D 1 km × 1 km water vapour fields through the integration of GPS and MODIS data? What is the accuracy of the output?

On the one hand, GPS water vapour product has higher temporal resolution and much better accuracy than MODIS. More importantly, GPS water vapour is not sensitive to the presence of clouds. On the other hand, MODIS near IR water vapour product has a much wider coverage and much higher spatial resolution compared with current Continuous GPS (CGPS) networks, but the presence of clouds causes

data gaps. It is clear that these two different types of water vapour products are complementary.

In Chapter 5, it is shown that MODIS near IR water vapour products (both collections 3 and 4) appeared to overestimate water vapour against GPS, but with high correlation coefficients. Taking into account the good linear relationship between GPS and MODIS near IR water vapour products as well as the missing values in MODIS near IR water vapour field due to clouds, a GPS/MODIS integration approach has been developed to produce regional 1 km × 1 km water vapour fields: 1) MODIS near IR water vapour was calibrated using GPS data; 2) An improved inverse distance weighted interpolation method (IIDW) was applied to fill in the cloudy pixels; 3) The densified water vapour field was validated using GPS data. This integration approach was shown to be promising. After correction, MODIS and GPS PWV agreed to within 1.6 mm in terms of standard deviations, and the coverage of water vapour fields increased by up to 21.6% (Section 7.1). There are two factors affecting the increased percentage of the coverage: 1) The extent parameter in the IIDW. Since a large extent results in a smooth surface with a loss of some detailed information, an optimal extent parameter of 5 km was used in the SCIGN area, which in turn indicates that the optimal extent parameter was not the real water vapour decorrelation range, i.e. the extent parameter did not convey a physical meaning. 2) The size of clouds. Obviously, when the size of clouds is larger than 5 km, the missing values due to clouds cannot be filled in using the IIDW with an extent parameter of 5 km.

8.1.4 Integration approach of InSAR with other independent datasets

Specific Research Questions 4: Presently, different calibration methods usually compare between unwrapped phases and independent datasets or models, rather than correct InSAR measurements. Is it possible to design a true integration approach that not only reduces atmospheric effects on interferograms, but also improves InSAR processing such as phase unwrapping?

Prior to this study, several studies had been carried out to calibrate water vapour effects on InSAR using atmospheric delay models or independent data sources. In those studies, atmospheric effects were subtracted from (or compared with) the

wrapped (or unwrapped) phase, but these water vapour corrections were not used to improve the InSAR processing, so they were not truly integrated methods.

The water vapour correction approach developed in this thesis (Section 6.3) involves the usual steps of image co-registration, interferogram formation, baseline estimation from the precise orbits, and interferogram flattening and removal of the topographic signal by use of a DEM. At this point, the integration approach diverges from the usual interferometric processing sequence with the insertion of a ZPDDM (zenith-path-delay difference map), which is mapped from the geographic coordinate system to the radar coordinate system (range and azimuth) and subtracted from the interferogram. This corrected interferogram can be unwrapped and then used in baseline refinement.

From the experiments shown in Chapters 6 and 7, it can be concluded that the water vapour correction approach proposed in this thesis has advantages over all the previous approaches: 1) Additional impact due to filtering can be avoided; 2) Reducing the atmospheric effects on the wrapped interferograms can improve phase unwrapping; 3) The results strongly suggest that the corrected unwrapped phase may improve the refined baseline, but this is a subject for future work.

8.1.5 Validation of water vapour correction models

> *Specific Research Questions 5: How can a particular correction method be assessed? Is there any improvement after water vapour correction using methods developed in this thesis?*

A validation process is crucial to determine whether and to which degree water vapour correction models developed in this study can reduce atmospheric effects on InSAR measurements. Two validation approaches, both of which depend on the characteristics of differential interferograms, were used in this thesis:

1) Differential interferograms without deformation signals, e.g. those produced from ERS Tandem data. Since ERS Tandem data were acquired just one day apart, there should be no significant deformation signals in the resultant interferograms. When a precise DEM is used to remove topographic phase contributions, atmospheric effects should dominate in differential interferograms with short perpendicular baselines. This means that, after water vapour correction, the flatter the differential

interferograms, the better the correction. In Section 6.4, the application of the GTTM correction model to ERS tandem data showed that GTTM can reduce significantly not only topography-dependent but also topography-independent atmospheric effects. After the GTTM correction, the RMSs of residual fringes were of the order of 5 mm in all three case studies shown in this thesis.

2) Differential interferograms with deformation signals, e.g. those produced from 35-day repeat-pass ERS-2 data. The main area of interest of this thesis (viz. the Los Angeles region) exhibits seasonal vertical and horizontal movements of up to 110 mm and 14 mm respectively every year [*Bawden et al.*, 2001]. Therefore, in order to validate water vapour correction models, independent 3D displacements derived from GPS measurements were used to compare with InSAR results in the LOS direction. The application of the GPS/MODIS integrated correction model to ERS-2 data indicated that this integrated model not only helps discriminate geophysical signals from water vapour effects, but also reduces water vapour effects on Interferograms significantly (Section 7.2). After the GPS/MODIS integrated correction, the RMS differences between GPS and InSAR varied from 5 mm to 8 mm with a reduction of up to 6 mm.

Based on the second validation approach, a comparison study between the GTTM and GPS/MODIS correction models is performed in Section 7.3. It is shown that the GTTM model and the GPS/MODIS integrated model are complementary when correcting InSAR measurements.

8.2 Contributions of this research

The contributions to knowledge of the research conducted for this thesis can be summarized as follows:

1) Extensive validation of the MODIS near IR water vapour products has been performed in time and space. It is shown that the MODIS near IR water vapour product appears to overestimate water vapour against GPS and radiosondes, and for the first time a GPS-derived correction model has been developed to calibrate the scale uncertainty of MODIS near IR water vapour products.

2) The spatial structure of water vapour has been analyzed using GPS (typical spacing of 50 km) and MODIS (1 km × 1 km) data. Two findings have been observed which are different from previous research: (i) the water vapour decorrelation range might be as short as 200 km over SCIGN, which is different from the decorrelation range of 500-1000 km presented by *Emardson et al.* [2003]; (ii) water vapour variation might not follow the TL model.

3) Based on the JPL/Caltech ROI_PAC software, a water vapour correction approach has been developed, which truly integrates InSAR and other independent data sets to reduce water vapour effects on interferograms. It is also shown that this water vapour correction approach may improve InSAR processing such as phase unwrapping.

4) For the first time, using GPS data only, a topography-dependent turbulence model (GTTM) has been developed to produce zenith-path-delay difference maps (ZPDDM). Its successful application to ERS Tandem data over the SCIGN area has eventually answered the important question as to: how to use GPS data for InSAR atmospheric correction? This problem has remained unsolved in the InSAR field since 1997.

5) For the first time, GPS and MODIS data have been integrated to provide regional water vapour fields with a spatial resolution of 1 km × 1 km, and a water vapour correction model based on the resultant water vapour fields has been successfully incorporated into InSAR processing.

8.3 Recommendations for future research and applications

A better understanding of water vapour variation will help to improve the effectiveness of the GTTM water vapour correction model developed in this thesis. The availability of high spatial resolution water vapour products (e.g. MODIS and MERIS near IR water vapour products) makes it possible to investigate global and regional water vapour variation. The existing infrastructure of Continuous GPS (CGPS) networks offers the opportunity to examine seasonal and temporal water vapour variation. Future investigations should combine these three different water vapour products (and possibly with new products which are not available yet): 1) to monitor the long-term trends in water vapour variation; 2) to seek a better model

parameter to represent the characteristic of topography-dependent water vapour variation; and 3) to derive specific model parameters c, α, and k for specific areas.

In Section 7.1, an improved inverse distance weighting (IIDW) was developed to fill in the missing values due to the presence of clouds, which was mainly limited by the height effects on water vapour variation. Taking into account the experience with the GTTM in Chapter 6, it is expected that a topography-dependent turbulence model would improve the interpolation, particularly in mountain areas. Due to CPU limitations, the topography-dependent turbulence model is not used to fill in missing values in this thesis, but this should be investigated in the near future.

Although MERIS near IR water vapour product is as sensitive to the presence of clouds as MODIS is, there are several additional advantages for MERIS near IR water vapour product to correct ASAR measurements over MODIS data to ERS-2 (Section 7.4, and Table 7.4): 1) there are usually time intervals of up to 60 minutes between MODIS and ERS data, but MERIS data is acquired at the same time as ASAR data; 2) MERIS has better spatial resolution, up to 300 m against 1 km for MODIS; 3) MERIS near IR water vapour product agrees more closely with GPS than MODIS, particularly under moderate conditions (Sections 5.3, 5.4 and 5.6). From the above discussion, it is expected that MERIS should produce even better water vapour fields than MODIS for the purpose of InSAR atmospheric correction, and it is recommended to be examined further.

Since the GTTM and GPS/MODIS integrated correction models can significantly reduce water vapour effects on interferograms, the application of these techniques to topography and deformation mapping is of great interest to geophysicists using InSAR and/or GPS techniques. As shown in Table 7.4, the GTTM model is limited by the availability of dense GPS networks. At present, the Los Angeles region and Japan are the most suitable areas to apply this technique. With the increasing number of local and regional CGPS networks in the world, the GTTM model is expected to be applicable in some other areas (e.g. Beijing in China) very soon. Due to the high frequency and percentage of cloud free conditions in the area of Tibet (up to 60% with an average of 38% during the period from 01 September 2001 to 31 August 2004), it is an ideal area for the use of MODIS and MERIS data for InSAR

atmospheric correction. Investigation of active faults in Tibet, particularly the Dangxiong Fault, would be a particular interesting application.

Appendix A

Multi-reference differential pressure/temperature models

In order to derive water vapour from GPS measurements, accurate surface pressure and temperature data are required. Unfortunately, although pressure and temperature instruments are not such expensive devices, very few GPS stations are equipped with them. In this appendix, a multi-reference differential model is proposed to interpolate surface pressure and/or temperature values with existing data at various GPS reference stations.

A.1 Multi-reference differential Berg pressure model

The main steps of the multi-reference differential model for interpolating surface pressure are as follows:

1). The modelled pressure is calculated using the Berg model, taking altitude into account over each station [*Webley et al.*, 2002]:

$$P_{s.modelled} = P_0\left(1-0.0000226\cdot\left(h_s - h_0\right)\right)^{5.225} \qquad \text{(A.1)}$$

where $h_0 = 0m$, $P_0 = 1013.25\ hPa$, the subscript s means GPS stations, h_s is the altitude of GPS sites, and $P_{s.modelled}$ is the modelled pressure value.

2). The difference between the observed pressures and the modelled values at each known station was calculated:

$$\Delta P_k = P_{k.observed} - P_{k.modelled} \qquad \text{(A.2)}$$

where the subscript k means station(s) where surface pressure is known, and $P_{k.observed}$ is the observed pressure value.

3). For each unknown station, distances to all known stations are computed: $d_{u.k}$, where the subscript u means station(s) where surface pressure is to be interpolated;

4). Inverse Distance Weighted (IDW) interpolation [*Shepard*, 1968] is used to compute the correction value (offset) for each unknown station: ΔP_u;

5). The surface pressure computed at each unknown station was corrected using the offset:

$$P_{u.interpolated} = P_{u.modelled} + \Delta P_u \qquad \text{(A.3)}$$

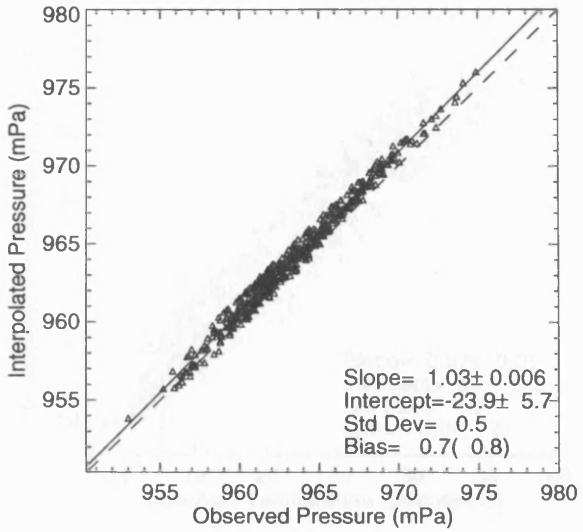

Figure A.1 Scatterplots of interpolated and observed pressure values over the JPLM IGS site from 1 January 2002 to 31 December 2003.

In order to check this multi-reference differential Berg pressure model, a temporal comparison between modelled pressures and measured pressures was performed over SCIGN during the period from 1 January 2002 to 31 December 2003. Surface pressure and temperature measurements were collected at up to 7 GPS stations (Figure 7.4). The JPLM IGS site was selected as a checking station, and the other 6 sites (maybe less) were considered as reference stations to interpolate surface pressure values over the checking station. Figure A.1 shows the scatter plot between interpolated and observed pressures over the JPLM site. A standard deviation of 0.8 hPa was observed with a mean difference of 0.7 hPa (modelled value > measured value). It should be noted that an uncertainty of 1 hPa in surface pressure could result in 0.33-0.37 mm error in precipitable water vapour (PWV) [*Hagemann et al.*, 2003]. Therefore, the uncertainties of modelled surface pressures might result in uncertainties of PWV of less than 0.3 mm.

A.2 Multi-reference differential temperature model

The effect of variations in surface temperature on PWV is much less than that from surface pressure. Uncertainties induced by temperature variations depend on the absolute amount of PWV, and an uncertainty of 5 ºC in surface temperature could lead to a relative error of 1.7-2.0% in PWV [*Hagemann et al.*, 2003].

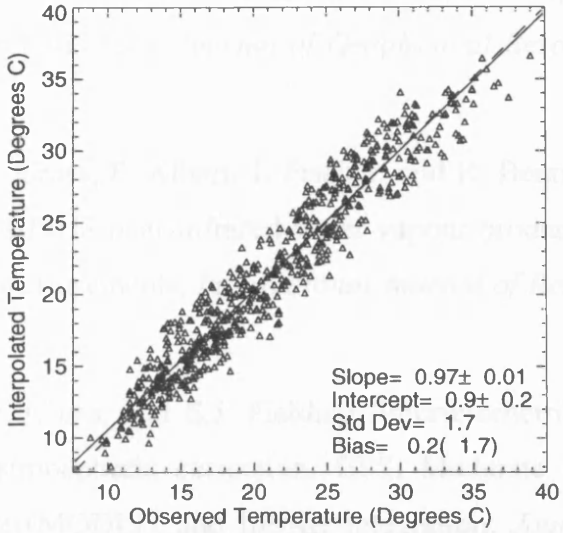

Figure A.2 Scatterplots of interpolated and observed temperature values over the JPLM IGS site from 1 January 2002 to 31 December 2003.

A similar multi-reference differential approach can be applied to interpolate surface temperature values, except that a vertical adiabatic temperature gradient of –6.5 K/km should be assumed [*Stull*, 2000] instead of the Berg Model:

$$T_{s.model} = 288.15 - 6.5 \times H_s \qquad \text{(A.4)}$$

where $T_{s.model}$ is the modelled surface temperature in Degrees Kelvin, and H_s is the height above the geoid in km.

To check this multi-reference differential temperature model, a temporal comparison between modelled and measured temperatures was also performed over SCIGN using the same data set as Section A.1 (Figure A.2). A standard deviation of 1.7 ºC was observed with a mean difference of 0.2 ºC (modelled value > measured value), indicating that the uncertainties of modelled surface temperatures might result in uncertainties of PWV of around 0.3 mm, even in the worst case (e.g. PWV of 50 mm).

Appendix B

List of Publications

Li, Z., E.J. Fielding, P. Cross, and J.-P. Muller, Interferometric synthetic aperture radar (InSAR) atmospheric correction: GPS Topography-dependent Turbulence Model (GTTM), *Journal of Geophysical Research*, under review, 2005.

Li, Z., J.-P. Muller, P. Cross, P. Albert, J. Fischer, and R. Bennartz, Assessment of the potential of MERIS near-infrared water vapour products to correct ASAR interferometric measurements, *International Journal of Remote Sensing*, under review, 2004.

Li, Z., J.-P. Muller, P. Cross, and E.J. Fielding, Interferometric synthetic aperture radar (InSAR) atmospheric correction: GPS, Moderate Resolution Imaging Spectroradiometer(MODIS), and InSAR integration, *Journal of Geophysical Research*, 110 (B3), B03410, doi:10.1029/2004JB003446, 2005.

Li, Z., Production of Regional 1 km × 1 km Water Vapor Fields through the Integration of GPS and MODIS Data (Winner of Student Paper Prize & Best Paper Presentation), in *ION GNSS 2004*, Long Beach, California, September 21-24, 2004.

Li, Z., J. Liu, and C. Xu, Error Analysis in InSAR data processing (in Chinese), *Geomatics and Information Science of Wuhan University*, 29 (1), 72-76, 2004.

Li, Z., J.-P. Muller, and P. Cross, Comparison of precipitable water vapor derived from radiosonde, GPS, and Moderate-Resolution Imaging Spectroradiometer measurements, *Journal of Geophysical Research*, 108 (D20), 4651, doi:10.1029/2003JD003372, 2003.

Li, Z., J. Liu, and C. Xu, Exploration of mathematic model of Differential InSAR (in Chinese), *Journal of Geodesy and Geodynamics*, 23 (2), 88-91, 2003.

Li, Z., J.-P. Muller, and P. Cross, Tropospheric correction techniques in repeat-pass SAR interferometry, in *FRINGE 2003 workshop*, ESA ESRIN, Frascati, Italy, 1-5 December, 2003.

Li, Z., J.-P. Muller, P. Cross, P. Albert, T. Hewison, R. Watson, J. Fischer, and R. Bennartz, Validation of MERIS near IR water vapour retrievals using MWR and GPS measurements, in *MERIS user workshop*, ESA ESRIN, Frascati, Italy, 10-13 November, 2003.

Li, Z., J.-P. Muller, P. Cross, and P. Albert, Comparison of precipitable water vapour derived from GPS, MODIS and MERIS measurements (abstract), in *EGS-AGU-EUG Joint Assembly*, Nice, France, 06-11 April, 2003.

References

Ackerman, S.A., K.I. Strabala, V.B. Mendes, R.A. Frey, C.C. Moeller, and L.E. Gumley, Discriminating clear sky from clouds with MODIS, *Journal of Geophysical Research, 103* (D24), 32,141-32,157, 1998.

Adams, R.J., W.F. Perger, W.I. Rose, and A. Kostinski, Measurements of the complex dielectric constant of volcanicAhrens, C.D., R. Alvelais, and N. Horne, *Essentials of meteorology today: an invitation to the atmosphere*, 464 pp., Brook Cole, 2000. ash from 4 to 19 GHz, *Journal of Geophysical Research, 101* (B4), 8175-8185, 1996.

Ahrens, C.D., R. Alvelais, and N. Horne, Essentials of meteorology today: an invitation to the atmosphere, 464 pp., Brook Cole, 2000.

Albert, P., R. Bennartz, and J. Fischer, Remote Sensing of Atmospheric Water Vapor from Backscattered Sunlight in Cloudy Atmospheres, *Journal of Atmospheric and Oceanic Technology, 18* (6), 865-874, 2001.

AMS, American Meteorological Society Glossary of Meteorology, Boston, Massachusetts, 2000.

Askne, J., and H. Nordius, Estimation of tropospheric delay for microwaves from surface weather data, *Radio Science, 22*, 379-386, 1987.

Baby, H., P. Gole, and J.A. Lavergnat, Model for tropospheric excess path length of radio waves from surface meteorological measurements, *Radio Science, 22*, 1023-1038, 1988.

Bamler, R., A Comparison of Range-Doppler and Wavenumber Domain SAR Focusing Algorithms, *IEEE Transactions Geoscience and Remote Sensing, 30* (4), 706-713, 1992.

Bar-Sever, Y.E., and P.M. Kroger, Strategies for GPS-Based Estimates of Troposphere Delay, in *ION GPS-96*, pp. 615-623, Kansas, Missouri, 1996.

Bar-Sever, Y.E., P.M. Kroger, and J.A. Borjesson, Estimating horizontal gradients of tropospheric path delay with a single GPS receiver, *Journal of Geophysical Research, 103* (B3), 5019-5035, 1998.

Bawden, G.W., W. Thatcher, R.S. Stein, K.W. Hudnut, and G. Peltzer, Tectonic contraction across Los Angeles after removal of groundwater pumping effects, *Nature, 412* (23), 812-815, 2001.

Bennartz, R., and J. Fischer, Retrieval of columnar water vapour over land from back-scattered solar radiation using the Medium Resolution Imaging Spectrometer (MERIS), *Remote Sensing of Environment, 78*, 271-280, 2001.

Bevis, M., S. Businger, S. Chiswell, T. Herring, R. Anthes, C. Rocken, and R. Ware, GPS meteorology: mapping zenith wet delays onto precipitable water, *Journal of Applied Meteorology, 33*, 379-386, 1994.

Bevis, M., S. Businger, T.A. Herring, C. Rocken, R.A. Anthes, and R. H. Ware, GPS meteorology: remote sensing of atmospheric water vapor using the Global Positioning System, *Journal of Geophysical Research, 97* (D14), 15,787-15,801, 1992.

Bézy, J.-L., S. Delwart, and M. Rast, MERIS - A new generation of ocean-colour sensor onboard Envisat, *ESA Bulletin, 103*, 48-56, 2000.

Bock, Y., and C.A. Williams, Integrated satellite interferometry in southern California, *EOS, TRANSACTIONS, American Geophysical Union, 78* (29), 299-300, 1997.

Bonforte, A., A. Ferreti, C. Prati, G. Puglisi, and F. Rocca, Calibration of atmospheric effects on SAR interferograms by GPS and local atmosphere models: first results, *Journal of Atmosphere and Solar-Terrestrial Physics, 63*, 2001.

Bruegge, C.J., J.E. Conel , J.S. Margolis, R. O. Green, G. Toon, V. Carrère , R.G. Holm, and G. Hoover, In-situ atmospheric water vapor retrieval in support of AVIRIS validation, in *SPIE Vol. 1298 Imaging Spectroscopy of the Terrestrial Environment*, pp. 150-163, 1990.

Brussaard, G., and P.A. Watson, *Atmospheric modelling and millimetre wave propagation*, 329 pp., New York: Chapman & Hall, London, 1995.

Buckley, S.M., Radar Interferometry Measurement of Land Subsidence, PhD thesis, The University of Texas at Austin, Austin, 2000.

Buckley, S.M., P.A. Rosen, S. Hensley, and B.D. Tapley, Land subsidence in Houston, Texas, measured by radar interferometry and constrained by extensometers, *Journal of Geophysical Research*, *108* (B11), 2542, doi:10.1029/2002JB001848, 2003.

Bürgmann, R., P.A. Rosen, and E.J. Fielding, Synthetic Aperture Radar Interferometry to Measure Earth's Surface Topography and Its Deformation, *Annual Review of Earth and Planetary Sciences*, *28*, 169-209, 2000.

Carnec, C., and H. Fabriol, Monitoring and modeling land subsidence at the Cerro Prieto geothermal field, Baja California, Mexico, using SAR interferometry, *Geophysical Research Letters*, *26* (9), 1211-1214, 1999.

Carnec, C., D. Massonnet, and C. King, Two examples of the use of SAR interferometry on displacement fields of small spatial extent, *Geophysical Research Letters*, *23* (24), 3579-3582, 1996.

Chaboureau, J.P., A. Chédin, and N. A. Scott, Remote sensing of the vertical distribution of the atmospheric water vapor from the TOVS observations: method and validation, *Journal of Geophysical Research*, *103* (D8), 8743-8752, 1998.

Chen, G., and T.A. Herring, Effects of atmospheric azimuthal asymmetry on the analysis of space geodetic data, *Journal of Geophysical Research*, *102* (B9), 20489-20502, 1997.

Colesanti, C., A. Ferretti, C. Prati, and F. Rocca, Monitoring landslides and tectonic motions with the Permanent Scatterers Technique, *Engineering Geology*, *68* (1-2), 3-14, 2003.

Crosetto, M., C.C. Tscherning, B. Crippa, and M. Castillo, Subsidence monitoring using SAR interferometry: Reduction of the atmospheric effects using

stochastic filtering (DOI 10.1029/2001GL013544), *Geophysical Research Letters*, *29* (9), 26, 2002.

Curlander, J.C., and R.N. McDonough, *Synthetic Aperture Radar: systems and signal processing*, John Wiley & Sons, New York, 1991.

Davis, J.L., G. Elgered, A.E. Niell, and C.E. Kuehn, Ground-based measurement of gradients in the "wet" radio refractivity of air, *Radio Science*, *28* (6), 1003, 1993.

Davis, J.L., T.A. Herring, I.I. Shapiro, A.E.E. Rogers, and G. Elgered, Geodesy by radio interferometry: Effects of atmospheric modeling errors on estimates of baseline length, *Radio Science*, *20*, 1593-1607, 1985.

Delacourt, C., P. Briole, and J. Achache, Tropospheric corrections of SAR interferograms with strong topography. Application to Etna, *Geophysical Research Letters*, *25* (15), 2849-2852, 1998.

Dodson, A., and H.C. Baker, The accuracy of GPS water vapour estimation, in *Proceedings of the ION National Technical Meeting, Navigation 2000*, Long Beach, California, January 21–23, 1998.

Elgered, G., Tropospheric radio path delay from ground-based microwave radiometry, in *Atmospheric Remote Sensing by Microwave Radiometry*, edited by M. Janssen, pp. 215-258, John Wiley, New York, 1993.

Elgered, G., J.L. Davis, T.A. Herring, and I.I. Shapiro, Geodesy by radio interferometry: water vapor radiometry for estimation of the wet delay, *Journal of Geophysical Research*, *96*, 6541-6555, 1991.

Elliott, W.P., and D. Gaffen, On the utility of radiosonde humidity archives for climate studies, *Bulletin of the American Meteorological Society*, *72* (10), 1507-1520, 1991.

Emardson, T.R., Studies of atmospheric water vapor using the Global Positioning System, Technical Report No. 339, Chalmers University of Technology, Goteborg, Sweden, 1998.

Emardson, T.R., G. Elgered, and J. M. Johansson, Three months of continuous monitoring of atmospheric water vapor with a network of Global Positioning

System receivers, *Journal of Geophysical Research*, *103* (D2), 1807-1820, 1998.

Emardson, T.R., J. Johansson, and G. Elgered, The systematic behavior of water vapor estimates using four years of GPS observations, *IEEE Transactions on Geoscience and Remote Sensing*, *38* (1), 324-329, 2000.

Emardson, T.R., and J.M. Johansson, Spatial interpolation of the atmospheric water vapor content between sites in a ground-based GPS network, *Geophysical Research Letters*, *25* (17), 3347-3350, 1998.

Emardson, T.R., M. Simons, and F.H. Webb, Neutral atmospheric delay in interferometric synthetic aperture radar applications: statistical description and mitigation, *Journal of Geophysical Research*, *108* (B5), 2231, doi:10.1029/2002JB001781, 2003.

Emardson, T.R., F.H. Webb, and P.O.J. Jarlemark, Analysis of water vapor spatial variability using GPS, InSAR, microwave radiometer, and radiosonde data, JPL IOM 335-02-01-L, Jet Propulsion Laboratory, Pasadena, California, 2002.

ESA-ASAR, ASAR Product Handbook, Issue 1.1 (available online at http://envisat.esa.int/dataproducts/asar/CNTR.htm), 2002.

ESA-MERIS, MERIS Product Handbook, Issue 1.1 (available online at http://envisat.esa.int/dataproducts/meris/CNTR.htm), 2002.

Farr, T.G., and M. Kobrick, Shuttle Radar Topography Mission produces a wealth of data, *EOS, TRANSACTIONS, American Geophysical Union*, *81*, 583-585, 2000.

Feigl, K.L., F. Sarti, H. Vadon, S. McClusky, S. Ergintav, P. Durand, R. Burgmann, A. Rigo, D. Massonnet, and R. Reilinger, Estimating slip distribution for the Izmit mainshock from coseismic GPS, ERS-1, RADARSAT, and SPOT measurements, *Bulletin of the Seismological Society of America*, *92* (1), 138-160, 2002.

Feng, Y., Z. Bai, P. Fang, and A. Williams, GPS water vapour experimental results from observations of the Australian regional GPS network (ARGN), in *A*

Spatial Odyssey: 42nd Australia Surveyors Congress, Brisbane, Australia, 25-28 September 2001.

Ferrare, R., L. Brasseur, M. Clayton, D. Turner, L. Remer, and B.C. Gao, Evaluation of TERRA aerosol and water vapor measurements using ARM SGP data, in *American Meteorological Society 11th Conference on Atmospheric Radiation*, Ogden, Utah, 3 – 7 June 2002.

Ferretti, A., C. Prati, and F. Rocca, Multibaseline InSAR DEM reconstruction: The wavelet approach, *IEEE Transactions on Geoscience and Remote Sensing, 37* (2), 705-715, 1999.

Ferretti, A., C. Prati, and F. Rocca, Nonlinear subsidence rate estimation using Permanent Scatterers in Differential SAR Interferometry, *IEEE Transactions on Geoscience and Remote Sensing, 38* (5), 2202-2212, 2000.

Ferretti, A., C. Prati, and F. Rocca, Permanent Scatterers in SAR Interferometry, *IEEE Transactions on Geoscience and Remote Sensing, 39* (1), 8-20, 2001.

Fielding, E.J., R.G. Blom, and R.M. Goldstein, Rapid subsidence over oil fields measured by SAR interferometry, *Geophysical Research Letters, 25* (17), 3215-3218, 1998.

Fischer, J., and R. Bennartz, Retrieval of total water vapour content from MERIS measurements, ESA reference number PO-TN-MEL-GS-005, ESA-ESTEC, Noordwijk, Netherlands, 1997.

Franceschetti, G., and R. Lanari, *Synthetic Aperture Radar Processing*, 284 pp., CRS Press, New York, USA, 1999.

Frouin, R., P.-Y. Deschamps, and P. Lecomte, Determination from space of atmospheric total water vapor amounts by differential absorption near 940 nm: Theory and airborne verification, *Journal of Applied Meteorology, 29*, 448-460, 1990.

Fujiwara, S., P.A. Rosen, M. Tobita, and M. Murakami, Crustal deformation measurements using repeat-pass JERS 1 synthetic aperture radar interferometry near the Izu Peninsula, Japan, *Journal of Geophysical Research, 103* (B2), 2411-2426, 1998.

Gabriel, A.K., R.M. Goldstein, and H.A. Zebker, Mapping small elevation changes over large areas: Differential Radar Interferometry, *Journal of Geophysical Research, 94* (B7), 9183-9191, 1989.

Gaffen, D., Radiosonde observations and their use in SPARC-related investigations, in *SPARC Newsletter 12*, 1999.

Gao, B.C., and A.F.H. Goetz, Column atmospheric water vapor and vegetation liquid water retrievals from airborne imaging spectrometer data, *Journal of Geophysical Research, 95*, 3549-3564, 1990.

Gao, B.C., and Y.J. Kaufman, ATBD-MOD-05: The MODIS near-IR water vapor algorithm (available online at: http://ltpwww.gsfc.nasa.gov/MODIS-Atmosphere/_docs/atbd_mod03.pdf), pp. 25, 1998.

Gao, B.C., and Y.J. Kaufman, Water vapor retrievals using Moderate Resolution Imaging Spectroradiometer (MODIS) near-infrared channels, *Journal of Geophysical Research, 108* (D13), 4389, doi:10.1029/2002JD003023, 2003.

Ge, L., S. Han, and C. Rizos, The double interpolation and double prediction (DIDP) approach for InSAR and GPS integration, in *19th International Society of Photogrammetry & Remote Sensing Congress & Exhibition*, pp. 205-212, Amsterdam, Holland, 16 - 23 July 2000.

Gendt, G., C. Reigber and G. Dick, Near real-time water vapor estimation in a German GPS network-first results from the ground program of the HGF GASP project, *Physics and Chemistry of the Earth, Part A: Solid Earth and Geodesy, 26* (6-8), 413-416, 2001.

Gesch, D., M. Oimoen, S. Greenlee, C. Nelson, M. Steuck, and D. Tyler, The national elevation dataset, *Photogrammetric Engineering and Remote Sensing, 68* (1), 2002.

GFZ, GASP Subproject 1: Water vapor estimation from ground GPS networks and assimilation into atmospherical models (available online at http://www.gfz-potsdam.de/pb1/pg1/gasp1/index_GASP1.html), 12 February 2003.

Ghiglia, D.C., and M.D. Pritt, Two-dimensional phase unwrapping: theory, algorithms, and software, 493 pp., Wiley, New York, 1998.

Godson, W.L., Atmospheric Radiation (Current Investigations and Problems), Technical Note No 8,WMO No 38, pp. 32, 1955.

Goldstein, R., and H. Zebker, Interferometric radar measurements of ocean surface currents, *Nature*, *328*, 707-709, 1987.

Goldstein, R.M., Atmospheric limitations of repeat-track radar interferometry, *Geophysical Research Letters*, *22* (18), 2517-2120, 1995.

Goldstein, R.M., H. Zebker, and C. Werner, Satellite radar interferometry: Two-dimensional phase unwrapping, *Radio Science*, *23* (4), 713-720, 1988.

Graham, L.C., Synthetic Interferometer Radar for topographic mapping, *Proceedings of the IEEE*, *62* (6), 763-768, 1974.

Hagemann, S., L. Bengtsson, and G. Gendt, On the determination of atmospheric water vapor from GPS measurements, *Journal of Geophysical Research*, *108* (D21), 4678, doi:10.1029/2002JD003235, 2003.

Hall, M.P.M., L.W. Barclay, and M.T. Hewitt, *Propagation of radiowaves*, 446 pp., The institution of Electrical Engineers, London, United Kingdom, 1996.

Hanssen, R., *Atmospheric heterogeneities in ERS tandem SAR interferometry*, 136 pp., Delft University Press, Delft, the Netherlands, 1998.

Hanssen, R.F., *Radar interferometry: data interpretation and error analysis*, xviii, 308 pp., Kluwer Academic, Dordrecht; Boston, 2001.

Hartl, P., K.-H. Thiel, X. Wu, C. Doake, and J. Sievers, Application of SAR interferometry with ERS-1 in the Antarctic, *Earth Observation Quarterly*, 1-4, 1994.

Ifadis, I.M., and P. Savvaidis, The accurate prediction of the zenith atmospheric delay as a factor of accuracy on delay modeling at low elevation angles, in *Proceedings of International Symposium on "Geodetic, Photogrammetric and Satellite Technologies - Development and Integrated Application"*, pp. 36-55, Sofia, 2001.

Ifadis, I.M., and P. Savvaidis, Space to earth geodetic observations: Approaching the atmospheric effect, *Physics and Chemistry of the Earth, Part A: Solid Earth and Geodesy*, *26* (3), 195-200, 2001.

Jarlemark, O.J., and T.R. Emardson, Strategies for spatial and temporal extrapolation and interpolation of wet delay, *Journal of Geodesy*, *72*, 350-355, 1998.

Joughin, I.R., D.P. Winebrenner, and M.A. Fahnestock, Observations of ice-sheet motion in Greenland using satellite radar interferometry, *Geophysical Research Letters*, *22* (5), 571-574, 1995.

JPL, Shuttle Radar Topography Mission - the mission to map the world (available oneline at http://www2.jpl.nasa.gov/srtm/), 23 June 2004.

Kaufman, Y.J., and B.C. Gao, Remote sensing of water vapor in the near IR from EOS/MODIS, *IEEE Transactions on Geoscience and Remote Sensing*, *30* (5), 871-884, 1992.

Kay, S.M., *Fundamentals of statistical signal processing: Estimation theory*, 595 pp., Prentice Hall International, Inc., Englewood Cliffs, New Jersey, 1993.

Kerker, M., The scattering of light and other electromagnetic radiation, Academic Press, New York, 1969.

Klees, R., and D. Massonnet, Deformation measurements using SAR interferometry: potential and limitations, *Geologie En Mijnbouw*, *77* (2), 161-176, 1999.

Klobuchar, J.A., Ionospheric effects on GPS, in *Global Positioning System: Theory and Applications (Volume I)*, edited by B.W. Parkinson, and J.J. Spilker Jr., pp. 485-515, American Institute of Aeronautics and Astronautics, Washington, DC, 1996.

Klobuchar, J.A., and P.H. Doherty, A look ahead: expected ionospheric effects on GPS in 2000, *GPS Solutions*, *2* (1), 42-48, 1998.

Kwok, R., and M.A. Fahnestock, Ice sheet motion and topography from radar interferometry, *IEEE Transactions Geoscience and Remote Sensing*, *34*, 189-200, 1996.

Li, F.K., and R. Goldstein, Studies of multibaseline spaceborne interferometric Synthetic Aperture Radars, *IEEE Transactions Geoscience and Remote Sensing*, *28* (1), 88-97, 1990.

Li, Z., J.-P. Muller, and P. Cross, Comparison of precipitable water vapor derived from radiosonde, GPS, and Moderate-Resolution Imaging Spectroradiometer measurements, *Journal of Geophysical Research*, *108* (D20), 4651, doi:10.1029/2003JD003372, 2003.

Li, Z., J.P. Muller, P. Cross, P. Albert, J. Fischer, and R. Bennartz, Assessment of the potential of MERIS near-infrared water vapour products to correct ASAR interferometric measurements, *International Journal of Remote Sensing, under review*, 2004.

Li, Z., J.-P. Muller, P. Cross, P. Albert, T. Hewison, R. Watson, J. Fischer, and R. Bennartz, Validation of MERIS near IR water vapour retrievals using MWR and GPS measurements, in *MERIS user workshop*, ESA ESRIN, Frascati, Italy, 10-13 November, 2003.

Li, Z., J.-P. Muller, P. Cross, and E.J. Fielding, Interferometric synthetic aperture radar (InSAR) atmospheric correction: GPS, Moderate Resolution Imaging Spectroradiometer(MODIS), and InSAR integration, *Journal of Geophysical Research*, 110 (B3), B03410, doi:10.1029/2004JB003446, 2005.

Li, Z.W., X.L. Ding, G.X. Liu, and C. Huang, Atmospheric effects on InSAR measurements - A review, *Geomatics Research Australasia*, *79*, 43-58, 2003.

Liebe, H.J., T. Manabe, and G.A. Hufford, Millimeter-wave attenuation and delay rates due to fog/cloud conditions, *IEEE Transactions on Antennas and Propagation*, *37* (12), 1617-1623, 1989.

Liljegren, J., B. Lesht, T. VanHove, and C. Rocken, A comparison of integrated water vapor from microwave radiometer, balloon-borne sounding system and Global Positioning System, in *the 9th Atmospheric Radiation Measurement Program Science Team Meeting*, San Antonio, TX, 1999.

Liu, J.G., A. Black, H. Lee, H. Hanaizumi, and J.M. McMoore, Land surface change detection in a desert area in Algeria using multi-temporal ERS SAR coherence images, *International Journal of Remote Sensing*, *22* (13), 2463-2477, 2001.

Liu, Y., Remote sensing of atmospheric water vapor using GPS data in the Hong Kong region, PhD thesis, The Hong Kong Polytechnic University, Hong Kong, 2000.

Lu, Z., R. Fatland, M. Wyss, S. Li, J. Eichelberger, K. Dean, and J. Freymueller, Deformation of New Trident volcano measured by ERS-1 SAR interferometry, Katmai National Park, Alaska, *Geophysical Research Letters*, *24* (6), 695-698, 1997.

Lutgens, F.K., and E.J. Tarbuck, *The atmosphere: An introduction to meteorology*, 508 pp., Pearson Education, Inc., New Jersey, 2004.

Lyons, S., and D. Sandwell, Fault creep along the southern San Andreas from interferometric synthetic aperture radar, permanent scatterers, and stacking, *Journal of Geophysical Research*, *108* (B1), 2047, doi: 10.1029/2002JB001831, 2003.

MacMillan, D.S., Atmospheric gradients from very long baseline interferometry observations, *Geophysical Research Letters*, *22* (9), 1041-1044, 1995.

MacMillan, D.S., and C. Ma, Evaluation of very long baseline interferogmetry atmospheric modeling improvements, *Journal of Geophysical Research*, *99* (B1), 637-651, 1994.

Marshall, J., and W. Palmer, The distribution of raindrops with size, *Journal of Meteorology*, *5*, 165-166, 1948.

Mason, N., P. Hughes, P. McMullan, R. Reynolds, L. Simmonds, and J. Twidell, *Introduction to environmental physics: planet earth, life and climate*, Tylor & Francis, London, 2001.

Massonnet, D., P. Briole, and A. Arnaud, Deflation of Mount Etna monitored by spaceborne radar interferometry, *Nature*, *375*, 567-570, 1995.

Massonnet, D., and K. Feigl, Satellite Radar interferometric map of the coseismic deformation field of the M=6.1 Eureka Valley, California earthquake of 17 May 1993, *Geophysical Research Letters*, *22* (12), 1541-1544, 1995.

Massonnet, D., K. Feigl, M. Rossi, and F. Adragna, Radar interferometric mapping of deformation in the year after the Landers earthquake, *Nature*, *369*, 227-230, 1994.

Massonnet, D., and K.L. Feigl, Discrimination of geophysical phenomena in satellite radar interferograms, *Geophysical Research Letters*, *22* (12), 1537-1540, 1995.

Massonnet, D., and K.L. Feigl, Radar interferometry and its application to changes in the Earth's surface, *Reviews of Geophysics*, *36* (4), 441-500, 1998.

Massonnet, D., T. Holzer, and H. Vadon, Land subsidence caused by the East Mesa Geothermal Field, California, observed using SAR interferometry, *Geophysical Research Letters*, *24* (8), 901-904, 1997.

Massonnet, D., M. Rossi, C. Carmona, F. Adragna, G. Peltzer, K. Feigl, and T. Rabaute, The displacement of the Landers earthquake mapped by radar interferometry, *Nature*, *364*, 138-142, 1993.

Mather, P.M., *Computer processing of remotely-sensed images: An introduction*, John Wiley & Sons Ltd, Chichester, West Sussex, England, 2004.

McMillin, L.M., M. Uddstrom, and A. Coletti, A procedure for correcting radiosonde reports for radiation errors, *Journal of Atmospheric and Oceanic Technology*, *9* (6), 801-811, 1992.

Mendes, V.B., Modeling the neutral-atmosphere propagation delay in radiometric space techniques, PhD thesis, University of New Brunswick, Fredericton, New Brunswick, Canada, 1999.

Mendes, V.B., G. Prates, L. Santos, and R.B. Langley, An evaluation of models for the determination of the weighted mean temperature of the atmosphere, in *Proceedings of The Institute of Navigation 2000 National Technical Meeting*, pp. 433-438, Anaheim, CA, U.S.A., 26-28 January 2000.

Menzel, W.P., B.A. Baum, K.I. Strabala, and R.A. Frey, ATBD_MOD_04: Cloud top properties and cloud phase: Algorithm Theoretical Basis Document (available online at: http://ltpwww.gsfc.nasa.gov/MODIS-Atmosphere/_docs/atbd_mod04.pdf), NASA Goddard Space Flight Center, 2002.

Menzel, W.P., D.P. Wylie, and K.I. Strabala, Seven years of global cirrus cloud statistics using HIRS, in *IRS Symposium: Current Problems in Atmospheric Radiation*, pp. 719-725, Fairbanks, AK, 1996.

Misra, P., and P. Enge, *Global Positioning System: Signals, measurements, and performance*, 390 pp., Ganga-Jamuna Press, Lincoln, Massachusetts, 2001.

Mockler, S.B., Water vapor in the climate system (Special Report, December 1995) (available online at: http://www.agu.org/sci_soc/mockler.html), American Geophysical Union, Jekyll Island, Georgia, 1995.

Muller, J.-P., and D. Backes, Quality assessment of X- and C-SRTM with ERS-tandem DEMs over 4 European CEOS WGCV test sites, in *FRINGE 2003 workshop*, ESA ESRIN, Frascati, Italy, 1-5 December, 2003, 2003.

Niell, A.E., Global mapping functions for the atmospheric delay at radio wavelengths, *Journal of Geophysical Research*, *101*, 3227-3246, 1996.

Niell, A.E., Improved atmospheric mapping functions for VLBI and GPS, *Earth Plantets Space*, *52*, 699-702, 2000.

Niell, A.E., Preliminary evaluation of atmospheric mapping functions based on numerical weather models, *Physics and Chemistry of the Earth, Part A: Solid Earth and Geodesy*, *26* (6-8), 475-480, 2001.

Niell, A.E., A.J. Coster, F.S. Solheim, V.B. Mendes, P.C. Toor, R.B. Langley, and C.A. Upham, Comparison of measurements of atmospheric wet delay by radiosonde, water vapor radiometer, GPS, and VLBI, *Journal of Atmospheric and Oceanic Technology*, *18*, 830-850, 2001.

Niell, A.E., and L. Petrov, Using a Numerical Weather model to improve Geodesy, in The State of GPS Vertical Positioning Precision: Separation of Earth Processes by Space Geodesy, in *Proceedings of the International Association of Geodesy*, European Center for Geodynamics and Seismology, Luxembourg, 2-4 April 2003.

Nikolaidis, R., Observation of geodetic and seismic deformation with the Global Positioning System, PhD thesis, University of California, San Diego, 2002.

NIMA, NIMA Technical Report TR8350.2: Department of Defense World Geodetic System 1984, Its definition and relationships with local geodetic systems (Third Edition) (available online at: http://earth-info.nga.mil/GandG/tr8350/tr8350_2.html), 4 July 1997, 1997.

Nishihama, M., R. Wolfe, D. Solomon, F. Patt, J. Blanchette, A. Fleig, and E. Masuoka, MODIS Level 1A Earth Location: Algorithm Theoretical Basis Document Version 3.0, pp. 147, the MODIS Science Data Support Team, 1997.

Odijk, D., Fast precise GPS positioning in the presence of ionospheric delays, PhD thesis, Delft University of Technology, Delft, 2002.

Olmsted, C., Scientific SAR User's Guide (available online at: http://www.asf.alaska.edu/SciSARuserGuide.pdf), pp. 53, Alaska SAR Facility, Fairbanks, Alaska, 1993.

Owens, J.C., Optical refractive index of air: Dependence on pressure, temperature and composition, *Applied Optics*, *6*, 51-58, 1967.

Peltzer, G., F. Crampé, S. Hensley, and P. Rosen, Transient strain accumulation and fault interaction in the Eastern California shear zone, *Geology*, *29* (11), 975-978, 2001.

Peltzer, G., and P. Rosen, Surface displacement of the 17 May 1993 Eureka Valley, California, earthquake observed by SAR interferometry, *Science*, 1333, 1995.

Price, E.J., and D.T. Sandwell, Small-scale deformations associated with the 1992 Landers, California, earthquake mapped by synthetic aperture radar interferometry phase gradients, *Journal of Geophysical Research*, *103* (B11), 27,001-27,016, 1998.

Pruppacher, H.P., and K.V. Beard, A wind tunnel investigation of the internal circulation and shape of water drops falling at terminal velocity in air, *Quarterly Journal of the Royal Meteorological Society*, *96*, 247-256, 1970.

Rabus, B., M. Eineder, A. Roth, and R. Bamler, The shuttle radar topography mission - a new class of digital elevation models acquired by spaceborne

radar, *ISPRS Journal of Photogrammetry and Remote Sensing*, *57* (4), 241-262, 2003.

Randel, D.L., T.J. Greenwald, T.H. Vonder Haar, G.L. Stephens, M.A. Ringerud, and C.L. Combs, A new global water vapor dataset, *Bulletin of the American Meteorological Society*, *77* (6), 1233-1254, 1996.

Rees, M.H., *Physics and chemistry of the upper atmosphere*, Cambridge University Press, Cambridge, 1989.

Reigber, C., G. Gendt, G. Dick, and M. Tomassini, Water vapor monitoring for weather forecasts, *GPS World*, January 2002.

Ries, J.C., J.J. Bordi, and T.J. Urban, Precise orbits for ERS-1 using Laser Ranging and Altimeter crossovers (CSR-TM-99-02) (available online at: http://podaac.jpl.nasa.gov/ers1_alt/doc/techmemo99_02.pdf), pp. 28, Center for Space Research, the University of Texas at Austin, Austin, Texas, 1999.

Rigo, A., and D. Massonet, Investigating the 1996 Pyrenean earthquake (France) with SAR Interferograms heavily distorted by atmosphere, *Geophysical Research Letters*, *26* (21), 3217-3220, 1999.

Rogers, A.E.E., and R.P. Ingalls, Venus: Mapping the surface reflectivity by radar interferometry, *Science*, *165*, 797-799, 1969.

Rosen, P.A., S. Hensley, I.R. Joughin, F.K. Li, S.N. Madsen, E. Rodriguez, and R.M. Goldstein, Synthetic aperture radar interferometry - Invited paper, *Proceedings of the IEEE*, *88* (3), 333-382, 2000.

Rosen, P.A., S. Hensley, G. Peltzer, and M. Simons, Updated Repeat Orbit Interferometry package released, *EOS, TRANSACTIONS, American Geophysical Union*, *85* (5), 47, 2004.

Rosen, P.A., S. Hensley, H.A. Zebker, and F.H. Webb, Surface deformation and coherence measurements of Kilauea volcano, Hawaii, from SIR-C radar interferometry, *Journal of Geophysical Research*, *101* (E10), 23,109-23,125, 1996.

Saastamoinen, J., Atmospheric correction for the troposphere and stratosphere in radio ranging of satellites, in *Geophysics monograph 15, 3rd Int. Symp. Use of Artificial Satellites for Geodesy, AGU*, pp. 247-251, Washington DC, 1972.

Sandwell, D.T., and E. Price, Sums and differences of interferograms: Imaging the troposphere, *Eos Trans. AGU, Fall Meeting Supplement, F144, 78* (46), 1997.

Schaer, S., Mapping and Predicting the Earth's Ionosphere Using the Global Positioning System, PhD thesis, University of Berne, 1999.

Scharroo, R., and P. Visser, Precise orbit determination and gravity field improvement for the ERS satellites, *Journal of Geophysical Research, 103* (C4), 8113-8127, 1998.

Schläpfer, D., C.C. Bore, J. Keller, and K.I. Itten, Atmospheric pre-corrected differential absorption techniques to retrieve columnar water vapor: Application to AVIRIS 91/95 data, in *Summaries of the Sixth Annual JPL Airborne Earth Science Workshop*, pp. 209-217, JPL, Pasadena (CA), 1995.

Schmidlin, F.J., and A. Ivanov, Radiosonde relative humidity sensor performance, in The WMO inter-comparison, September 1995. Preprint volume, 10th Symposium on Meteorological Observations and Instrumentation, American Meteorological Society, pp. 68-71, 1998.

Schueler, T., A. Pósfay, G.W. Hein, and R. Biberger, A global analysis of the mean atmospheric temperature for GPS water vapor estimation, in *Proceedings of ION-GPS 2001*, Salt Lake City, Utah, USA, 2001.

Seemann, S., J. Li, W.P. Menzel, and L. Gumley, Operational retrieval of atmospheric temperature, moisture, and ozone from MODIS infrared radiances, *Journal of Applied Meteorology, 42*, 1072-1091, 2003.

Shepard, D., A two-dimensional interpolation function for irregularly-spaced data, in *Proceedings of the 23rd National Conference ACM, ACM*, pp. 517-524, 1968.

Shimada, M., Correction of the satellite's state vector and the atmospheric excess path delay in SAR Interferometry - Application to surface deformation detection, *International Geoscience and Remote Sensing Symposium, 5*, 2236-2238, 2000.

Shimada, M., M. Minamisawa, and O. Isoguchi, Correction of atmospheric excess path delay appeared in repeat-pass SAR Interferometry using objective analysis data, *International Geoscience and Remote Sensing Symposium, 5*, 2052-2054, 2001.

Smout, S., J. Elms, D. Lyth, and J. Nash, Met Office RS90 humidity sensor evaluations, Met Office, Berkshire, UK, 2001.

Solheim, F.S., J. Vivekanandan, R.H. Ware, and C. Rocken, Propagation delays induced in GPS signals by dry air, water vapor, hydrometeors and other particulates, *Journal of Geophysical Research, 104*, 9663-9670, 1999.

Spilker, J.J., Jr., GPS signal structure and performance characteristics, in *Navigation Vol 1*, edited by P.M. Janiczek, pp. 29-54, The Institute of Navigation, Washington D. C., 1980.

Spilker, J.J., Jr., and B.W. Parkinson, Overview of GPS Operation and Design, in *Global Positioning System: Theory and Applications (Volume I)*, edited by B.W. Parkinson, and J.J. Spilker, Jr., pp. 29-55, American Institute of Aeronautics and Astronautics, Washington, DC, 1996.

Spoelstra, T.A.T., A climatology of quiet/disturbed ionospheric conditions derived from 22 years of Westerbork interferometer observations, *Journal of Atmosphere and Solar-Terrestrial Physics, 58* (11), 1229-1258, 1996.

Spoelstra, T.A.T., and Y. Yang, Ionospheric scintillation observations with radio interferometry, *Journal of Atmosphere and Solar-Terrestrial Physics, 57* (1), 85-97, 1995.

Stull, R., *Meteorology for scientists and engineers (Second Edition)*, 502 pp., Brooks/Cole, Thomson Learning, Pacific Grove, CA, 2000.

Talebian, M., E.J. Fielding, G. Funning, M. Ghorashi, J.A. Jackson, H. Nazari, B.E. Parsons, K. Priestley, P.A. Rosen, and R. Walker, The 2003 Bam (Iran) earthquake: Rupture of a blind strike-slip fault, *Geophysical Research Letters, 31* (11), L11611, doi:10.1029/2004GL020058, 2004.

Tarayre, H., and D. Massonnet, Atmospheric propagation heterogeneities revealed by ERS-1 interferometry, *Geophysical Research Letters*, *23* (9), 989-992, 1996.

Tatarskii, V.I., *The effects of the turbulent atmosphere on wave propagation*, 472 pp., Israel Program for Scientific Translations Ltd., 1971.

Thayer, G.D., An improved equation for the radio refractive index of air, *Radio Science*, *9*, 803-807, 1974.

Tranquilla, J.M., and H.M. Al-Rizzo, Range errors in Global Positioning System during ice cloud and snowfall periods, *IEEE Transactions on Antennas and Propagation*, *42* (2), 157-165, 1994.

Treuhaft, R.N., and G.E. Lanyi, The effect of the dynamic wet troposphere on radio interferometric measurements, *Radio Science*, *22*, 251-265, 1987.

USACE, Engineering and design: NAVSTAR Global Positioning System surveying (EM 1110-1-1003) (available online at: http://www.usace.army.mil/usace-docs/eng-manuals/em1110-1-1003/toc.htm), pp. 469, US Army Corps of Engineers, 2003.

van de Hulst, H.C., *Light scattering by small particles*, 470 pp., John Wiley & Sons, New York (reprinted by Dover Publications, New York, 1981), 1957.

Vivekanandan, J., R. Raghavan, and V.N. Bringi, Polarimetric radar modeling of mixtures of precipitation particles, *IEEE Transactions on Geoscience and Remote Sensing*, *31* (5), 1017-1030, 1993.

Wadge, G., and B. Parsons, Definition of the interferometric requirements in support of the TerraSAR-L phase 0 study, Final Report for TSR.PP.00003.EU.ASTR, pp. 42, EVINSAR Science Team, 2003.

Wadge, G., P.W. Webley, I.N. James, R. Bingley, A. Dodson, S. Waugh, T. Veneboer, G. Puglisi, M. Mattia, and D. Baker, Atmospheric models, GPS and InSAR measurements of the tropospheric water vapour field over Mount Etna, *Geophysical Research Letters*, *29* (19), 1905, doi: 10.1029/2002GL015159, 2002.

Wang, J.H., Understanding and correcting humidity measurement errors from Vaisala RS80 and VIZ radiosondes, in *Radiosonde Workshop*, Hampton University, Hampton, Virginia, 21–23 May 2002, 2002.

Wang, J.H., H.L. Cole, D.J. Carlson, E.R. Miller, K. Beierle, A. Paukkunen, and T.K. Laine, Corrections of humidity measurement errors from the Vaisala RS80 radiosonde: Application to TOGA COARE data, *Journal of Atmospheric and Oceanic Technology*, *19*, 981-1002, 2002.

Watson, K.M., Y. Bock, and D.T. Sandwell, Satellite interferometric observations of displacements associated with seasonal groundwater in the Los Angeles basin, *Journal of Geophysical Research*, *107* (B4), 2074, 10.1029/2001JB000470, 2002.

Webley, P.W., Atmospheric water vapour correction to InSAR surface motion measurements on mountains: Case Study on Mount Etna, PhD thesis, The University of Reading, Reading, 2003.

Webley, P.W., R.M. Bingley, A.H. Dodson, G. Wadge, S.J. Waugh, and I.N. James, Atmospheric water vapour correction to InSAR surface motion measurements on mountains: results from a dense GPS network on Mount Etna, *Physics and Chemistry of the Earth, Parts A/B/C*, *27* (4-5), 363-370, 2002.

Williams, S., Y. Bock, and P. Fang, Integrated satellite interferometry: Troposphere noise, GPS estimates, and implications for synthetic aperture radar products, *Journal of Geophysical Research*, *103* (B11), 27051-27067, 1998.

WMO, Guide to meteorological instruments and methods of observation, WMO-No. 8, Sixth Edition, World Meteorological Organization, Geneva, 1996.

Wright, T.J., Crustal deformation in Turkey from synthetic aperture radar interferometry, PhD thesis, University of Oxford, Oxford, 2000.

Wright, T.J., Z. Lu, and C. Wicks, Source model for the Mw 6.7, 23 October 2002, Nenana Mountain Earthquake (Alaska) from InSAR, *Geophysical Research Letters*, *30* (18), 1974, doi:10.1029/2003GL018014, 2003.

Wylie, D.P., and W.P. Menzel, Eight Years of High Cloud Statistics Using HIRS, *Journal of Climate*, *12* (1), 170-184, 1999.

Zebker, H., P. Rosen, R. Goldstein, A. Gabriel, and C. Werner, On the derivation of coseismic displacement fields using differential radar interferometry: the Landers earthquake, *Journal of Geophysical Research, 99* (B10), 19,617-634, 1994.

Zebker, H., and J. Villasenor, Decorrelation in interferometric radar echoes, *IEEE Transactions Geoscience and Remote Sensing, 30* (5), 950-959, 1992.

Zebker, H.A., and R.M. Goldstein, Topographic mapping from interferometric synthetic aperture radar observations, *Journal of Geophysical Research, 91* (B5), 4993-4999, 1986.

Zebker, H.A., S.N. Madsen, J. Martin, K.B. Wheeler, T. Miller, Y. Lou, G. Alberti, S. Vetrella, and A. Cucci, The TOPSAR interferometric radar topographic mapping instrument, *IEEE Transactions Geoscience and Remote Sensing, 30* (5), 933-940, 1992.

Zebker, H.A., P.A. Rosen, and S. Hensley, Atmospheric effects in interferometric synthetic aperture radar surface deformation and topographic maps, *Journal of Geophysical Research, 102* (B4), 7547-7563, 1997.

Zilkoski, D.B., NAVD 88 GPS-derived orthometric heights, part 1, *Point of Beginning (Mar 2001)*, 34, 2001.

Zisk, S.H., A new Earth-based radar technique for the measurement of lunar topography, *Moon, 4*, 296-300, 1972.

Zumberge, J.F., M.B. Heflin, D.C. Jefferson, and M.M. Watkins, Precise point positioning for the efficient and robust analysis of GPS data from large networks, *Journal of Geophysical Research, 102* (B3), 5005-5017, 1997.